POLYURETHANES IN RIGID AND FLEXIBLE ELECTRONICS
NOVEL HYBRID PROCESSING TECHNIQUES AND REAL-TIME MONITORING OF MATERIAL PROPERTIES

A Dissertation

Presented to

The Graduate Faculty of The University of Akron

In Partial Fulfillment

of the Requirements for the Degree

Doctor of Philosophy

Işık Işıl Nugay

August, 2014

POLYURETHANES IN RIGID AND FLEXIBLE ELECTRONICS

NOVEL HYBRID PROCESSING TECHNIQUES AND REAL-TIME MONITORING

OF MATERIAL PROPERTIES

Işık Işıl Nugay

Dissertation

Approved:

_____
Advisor
Dr. Mukerrem Cakmak

_____
Committee Member
Dr. Alamgir Karim

_____
Committee Member
Dr. Darrell H. Reneker

_____
Committee Member
Dr. David Simmons

_____
Committee Member
Dr. Chrys Wesdemiotis

Accepted:

_____
Department Chair
Dr. Robert Weiss

_____
Dean of the College
Dr. Stephen Z. Cheng

_____
Dean of the Graduate School
Dr. George R. Newkome

_____
Date

ABSTRACT

The bistable liquid crystal displays are multilayer devices composed of external layers of flexible conductive biaxially stretched PET and highly compressible interior phase separated droplets of liquid crystal (90+%) dispersed in a thermosetting polymer. The objective of this research was to carry out fundamental understanding of the thermo-mechanical behavior of this display and its individual layers as a polyurethane lens encapsulation is applied on both sides using insert injection molding. In this process the display undergoes spatio-temporally varying heating and cooling that causes considerable problems including thermal expansion, shrinkage and compression of individual layers. To address these, we have developed an instrumented insert injection mold to monitor the temperature and pressure development during the course of insert injection molding. As the encapsulation layers, low viscosity, low melting, polyurethane material was selected to avoid LCD exposure to high temperature and pressures.

While the introduced film-insert injection compression molding process for encapsulation of cholesteric liquid crystal displays with flexible and rigid lenses replaces the PSA-lens or cover glass lamination technique that fails to fully protect the display parts, still remains complex and requires optimization of multiple process conditions.

Display substrate material selection criteria for lowered warpage were defined with supporting thermal characterizations. During the lens encapsulation, the pressure changes were evaluated with screw and mold movements using position detection via displacement transducers attached to track the mold closure and screw forward motion. Among the process parameters, mold temperature was found to be the most influential parameter on warpage, followed by pin gate opening time, packing pressure, and cooling time. Flexible display substrate encapsulation flow simulations are completed in Moldex3D software to help pre-visualize the changing process parameters affecting part quality. The experimental and simulation results for temperature and pressure profiles as well as melt front were found to be in good agreement.

In order to understand the thermo mechanical behavior of the electrode PET layers, real-time optical properties during biaxial stretching and heat setting of PET films were investigated elucidating its shrinkage behavior during heating/cooling cycle typically experienced during insert injection molding process. The optimum samples with reduced final and maximum shrinkage/expansion values as well as MD to TD variations were obtained by using 3x1 UCW stretched and heat set at 190°C for 9 hours.

Finally, real-time segment specific rheo-optical properties (ultrafast IR dichroism and birefringence coupled with true mechanical measurements) during stretching and relaxation of polyurethane(urea)s (PUU)s varying PEO soft segment lengths were investigated. Low molecular weight PEO based PUUs have shown phase mixing whereas, mid and high molecular weight PEO based ones phase segregation of hard and soft segments. Each grade exhibited different rheo-optical behavior and the initial morphologies governed the segment specific orientation at low and high strain values.

ACKNOWLEDGEMENTS

During my undergrad, the two months I spent at the University of Akron, Polymer Engineering Department for my summer internship was an assurance that I really wanted to accomplish my doctorate degree in this place. This thesis is a product of inspiringly challenging five years of my life. I have been given very unique opportunities which helped me develop a refined skillset. The work and effort I put into this thesis was greatly supported, encouraged and endorsed by many remarkable people I would like to acknowledge.

First, I would like to thank my advisor, Distinguished Professor, Dr. Miko Cakmak, for giving me the opportunity to build and work with one of a kind, state of art equipments at the National Polymer Innovation Center. I owe him my deepest gratitude for his academic guidance and emotional support through this arduous journey. The experience I gained working with him opened the doors of a dream career for me. He helped me to aim always higher fearlessly and feel the joy of accomplishment. Thank you for everything Dr.Cakmak.

I would like to also thank my proposal and dissertation committee members. Dr. Alamgir Karim, Dr. Chyrs Wesdemiotis, Dr. Darell Reneker, Dr. David Simmons and Dr. Robert Weiss for their guidance and taking time-off from their busy schedules.

I would like to also acknowledge, Kent Displays Inc. help and support for this work. My substantial first chapter was supported by Ohio State Third Frontier Program through them. Many great people I had the privilege to meet and work with including Erica Montback, R&D Manager and Asad Khan, CTO. Thank you all for the inspiration to continue to work on display electronics.

During my thesis, I couldn`t stop myself in getting into flow simulations and I would like to thank the Moldex3D team, especially Susan Lin who taught me so much about solid meshing and software details.

I would like to thank tons of other people starting with all the group members and Polymer Engineering Department family. Special acknowledgements goes to Gamze Bas, true friend who helped me get through the roughest last year, Bart Hamilton who became my co-signer first time I moved to Akron, always helped me in the lab and created absolute fun times, Emre Unsal, my older brother who teached me a lot, Amy Blake, my good friend who helped me relax with yoga brakes, Deb Wilhite and Sarah Thorley whom I call my university moms. Thank you all for the support and making this place my second home.

I would like to thank also the Society of Women Engineers especially, the University of Akron section, Dr. Mary Verstraete and Heidi Hoffman for the great cause and opportunity to meet many inspiring great Women Engineers at the National

Meetings. Another rewarding membership to the Society of Plastics Engineers: it was a priviledge to work as UA Polymer Engineering Department liason in 2010 for the Akron Section of SPE.

I would like to thank Emel Akozer and Mehmet Akozer for reading through my dissertation, your feedback and corrections. I will always admire the amount of knowledge you both possess.

I would like to dedicate this work to my family who unconditionally supported every single moment of my life. They all sacrificed priceless time to be together and encouraged me enormously in every way. My assertiveness, positivity and courage are all thanks to them. Dedication is especially to my mother Nihan Nugay and my father Turgut Nugay. Mom and dad, thank you for everything you thought me, your endless support and love. You both are my role models and my origin of inspiration.

Finally, my soul mate and best friend, Rifat Emrah Ozel, I am beyond grateful that we found each other, your support this five years going through the same rough pad was so valuable. We both learned and shared a lot through this journey, thank you for your commitment and encouragements.

TABLE OF CONTENTS

Page

LIST OF TABLES

LIST OF FIGURES

Figure Page

KEYWORDS

Birefringence, curing kinetics, dichroism, DOE, drying, film insert injection molding, flow simulation, heat setting, injection compression molding, mechano-optical properties, orientation, polyurethanes, real-time URS-FTIR, rheo-optical properties.

LIST OF ABBREVIATIONS

ABS – Acyrlonitrile-butadiene-styrene

ACF– Anisotropic Conductive Film

ASTM– American Standards for Testing Materials

FIM – Film Insert Injection Molding

FTIR– Fourier-transform Infrared Spectra

HDI– Hexamethylene diisocyanate

IPDI– Isophorone diisocyanate

MD– Machine direction

MDI– Diphenylmethane diisocyanate

PC– Polycarbonate

PEDOT:PSS – Poly(3,4-ethylenedioxythiophene) poly(styrenesulfonate)

PET– Polyethylene Teraphtalate

PIPS – Photopolymerization Induced Phase Separation

PMMA– Polymethylmethacrylate

PNLC– Polymer Network Liquid Crystal

PU– Polyurethane

TD– Transverse direction

TDI– Toluene diisocyanate

TFCF – Transparent, flexible, conductive film

TMA– Thermo-mechanical Analysis

TPU– Thermoplastic polyurethane

URS– Ultra Rapid Scan

UV – Ultraviolet

WRP– Warpage Reversal Phenomenon

CHAPTER I

INTRODUCTION

Polyurethanes are unique materials with combined variety of properties such as elasticity, toughness, transparency and chemical resistance. Engineers use this material in many applications as they are available in a broad hardness range.

Current displays are hand laminated by glass or plastic lenses for protection. This process is a labor intensive process, increasing the production time and failing to encapsulate the edges of the displays as it involves only adhesion of the lens on the display. Combination of film-insert injection molding and injection compression methods to encapsulate displays with a lens without damaging the liquid crystal layer and the electronics of the display is possible. Polyurethane lens encapsulation can be used in current rigid market applications and for flexible future applications.

While the introduced film-insert injection compression molding process for encapsulation of cholesteric liquid crystal displays with flexible and rigid lenses replaces the PSA-lens or cover glass lamination technique that fails to fully protect the display parts, still remains complex and requires optimization of multiple process conditions. Process monitoring instrumentation is a must to understand challenges arising from an insert multilayer display with 90+% liquid crystal content as well as different thermal

expansion coefficients between the layers and the lens material with delamination and warpage potential. Display substrate material selections as well as shrinkage control are crucial for warpage minimization attempts.

The shrinkage behavior of substrate material will be governed by its processing history, therefore the biaxial stretching and heat setting of amorphous PET film has to be carefully examined. The biaxial stretcher and heat setting system equipped with real-time optical property tracking was designed and built by our group [1].

Investigations on thermoplastic polyurethanes (PU) segmental orientation are also very important to understand their final optical and mechanical behaviors and performance. Changing properties of PU films (solvent cast) can be monitored during drying, uniaxial stretching and relaxation by two powerful equipment developed again by our group [2, 3]. First equipment is a wind tunnel capable of real-time monitoring of weight, temperature, thickness, in-plane and out-of-plane birefringences of solvent cast films during drying. Second is a uniaxial stretcher equipped with real-time birefringence as well as specific chain orientation monitoring.

The main goal of this thesis is to introduce polyurethanes in novel applications in display electronics manufacturing as protection lens materials and to develop advance understanding of material behavior under changing processing conditions. The challenges encountered during this development process led to deeper-dive studies on display substrate material preparation process and controlled shrinkage.

CHAPTER II

LITERATURE REVIEW

2.1. Injection Molding

Injection molding is a manufacturing process for producing parts from both thermoplastic and thermosetting plastic materials. During injection molding, molten plastic is injected at high pressure into a mold, which is the inverse of the final product's shape. Most of the injections molding machines are in-line reciprocating screw type, as shown in Figure 2.1. Two-stage injection molding machines are also used (shown in Figure 2.2), where polymer melt is produced in an extruder and exits into a reservoir connected to a hydraulic piston device, which is cyclically pressurized to deliver the melt into the cold mold cavity [4].

Injection molding process usually divided into two parts, the injection molding machine and the injection mold.

Injection molding machine can be divided into the following components (Figure 2.3); Plasticating/injection unit, clamping unit, control system, tempering devices for the mold.

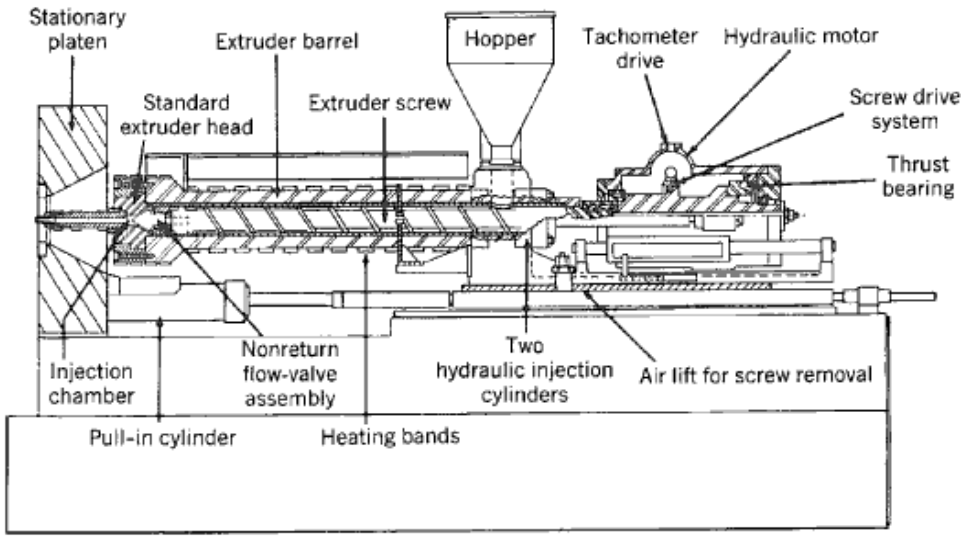

Figure 2.1. Reciprocating-screw machine, injection end [4].

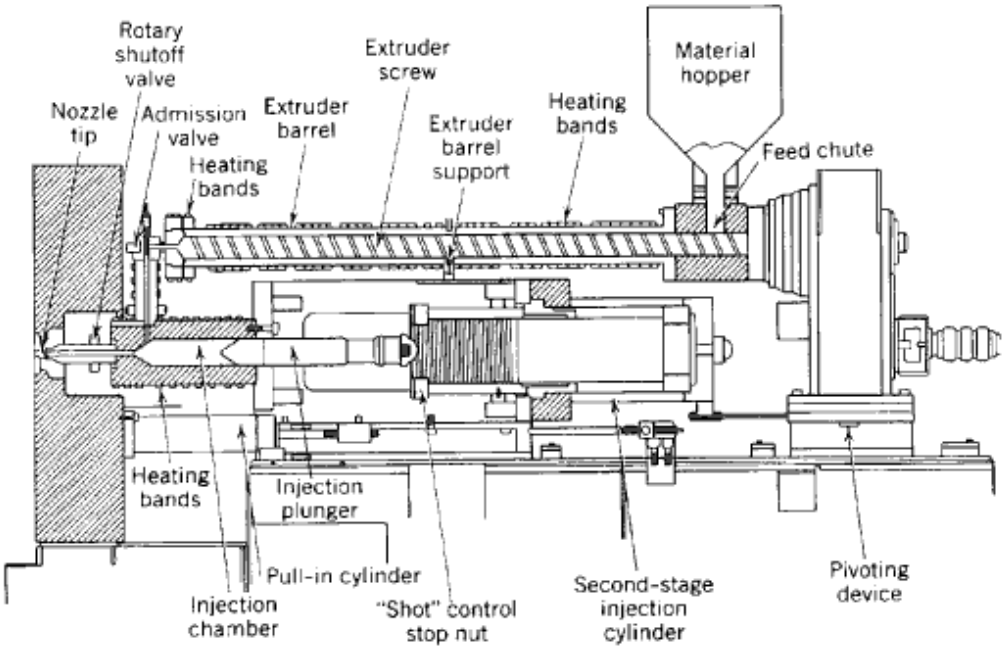

Figure 2.2. Two-stage screw-plunger machine [4].

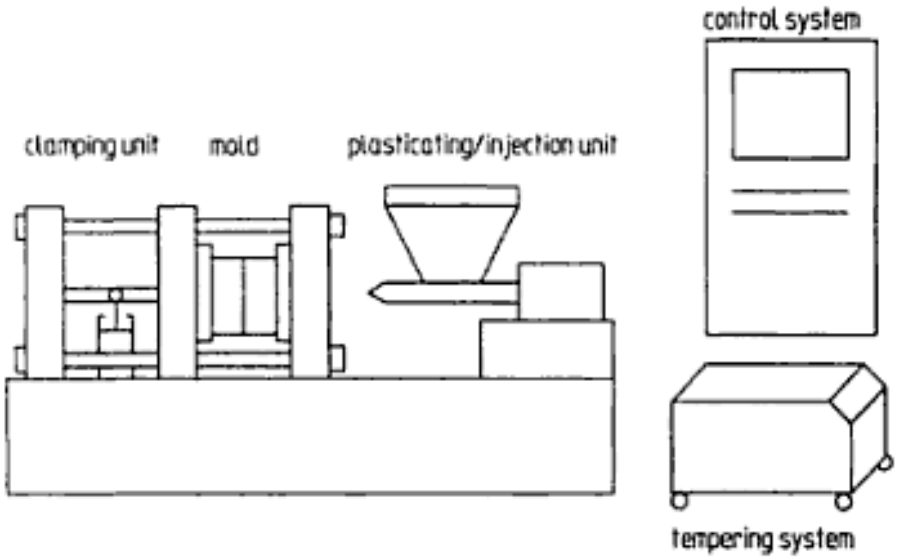

Figure 2.3. Design of an injection molding machine [5].

A. Plasticating Unit:

The plasticating system includes the same components as the extrusion system; a barrel with a rotating screw controlled by a motor. The major tasks of the plasticating unit are to melt the polymer, to accumulate the melt in the screw chamber, to inject the melt into the cavity, and to maintain the holding pressure during cooling. The main parts of the plasticating unit are hopper, screw, heating bands, check valve, nozzle (See Figure 2.4.) [6].

A feeder drops the resin at a predetermined rate into the hopper. From Figure 2.5 it is clear that hopper usually has tapered sides to facilitate dropping material by gravity into the barrel. The base of the hopper should contain a magnet that can be pulled out and cleaned while the machine is running its normal cycles. The purpose of the magnet is to catch any loose metal particles that may have been placed in the raw plastic [7, 8].

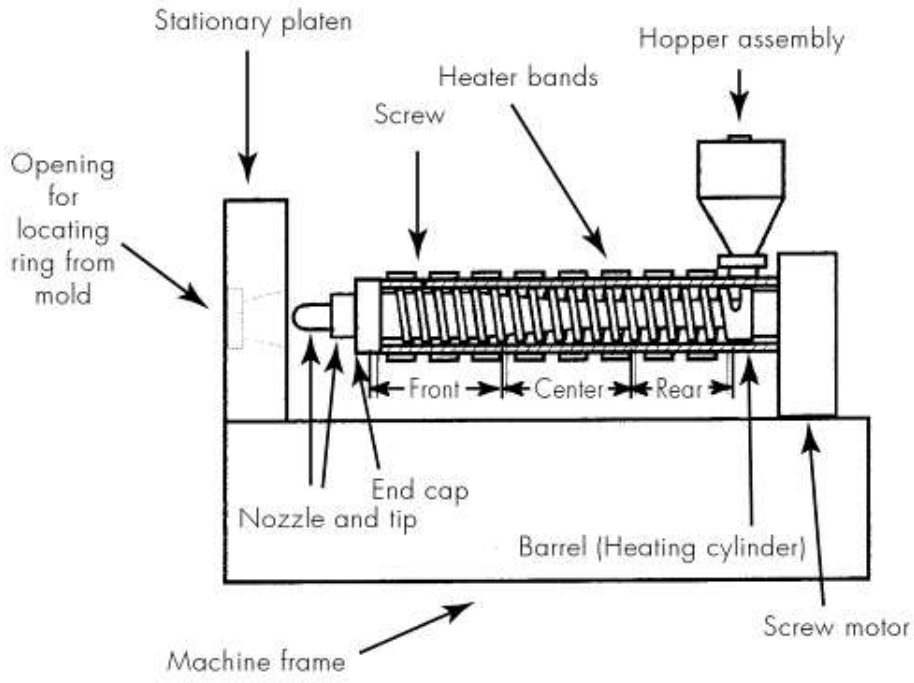

Figure 2.4 Injection unit components [7].

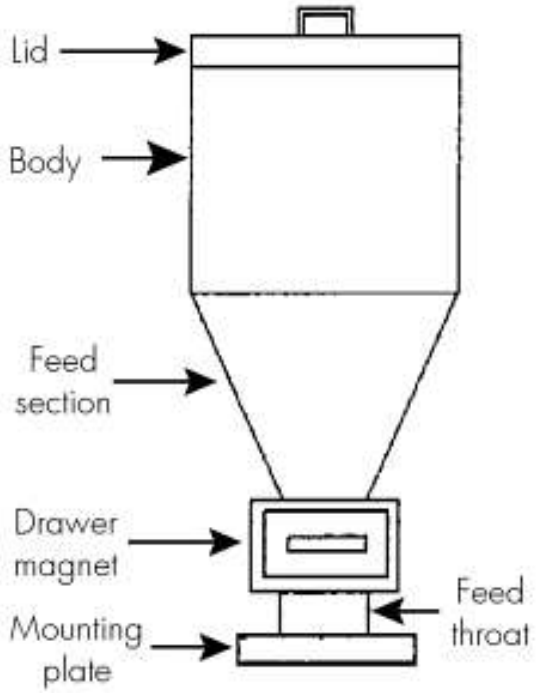

Figure 2.5 Basic hopper unit [7].

The hopper, heating bands, and the screw are similar items found in a plasticating single screw extruder. However, in an injection molding machine screw can slide back and forth to allow melt accumulation and injection. Because of this characteristic, it has the name reciprocating screw. Screw is a long cylinder with one or more helical flights wrapped around it and non-return valve at the end. Screw determines conveying, heating, mixing, and in some cases degassing of the plastic [6].

Important characteristics of this unit are; good plasticating performance, efficient conveying (low residence time), effective melting and mixing (homogeneity of temperature and additives), and good self-cleaning ability. Screw plasticating unit and injection units are shown in Figure 2.6 [5].

Screw consists of three different zones; feeding zone, compressing zone, and metering zone. And there are different types of screws; universal thermoplastic screws, screws for thermosets, screw for elastomers, preplastication screws, and special types [5].

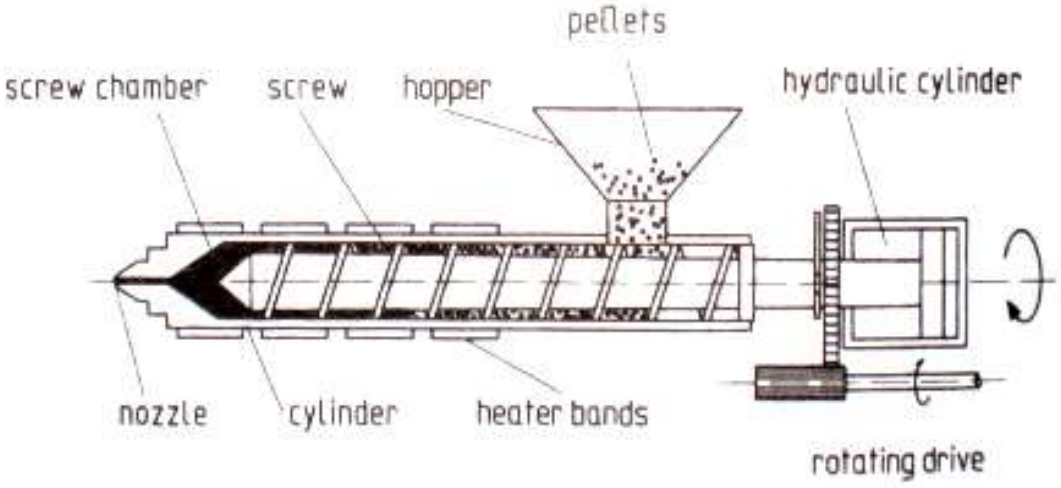

Figure 2.6 Screw plasticating and injection unit.

The barrel is a straight cylinder that closely fits around the screw. The radial difference between screw and barrel is usually 0.20 mm or 0.008 inches; extruders 40 mm in size and smaller have space of about 0.15 mm or 0.006 inches. The barrel is generally produced with a bimetallic liner that is centrifugally cast into barrel. When the plasticating unit is vented, barrel has a vent opening [6]. Outside of the barrel has heater bands strapped to it. The bands are electrically activated and are placed along the entire length of the barrel with minimal space between them. In Figure 2.4 there are three zones, rear, center, and front, and each zone includes three or more heater bands and each zone is individually controlled by an electrical unit located in the control panel of the machine [7].

Injection screws generally includes additional element that turns the screw into a piston like element during the injection and holding pressure phases called check valve (or non-return valves see Figure 2.7). It prevents any backflow of melt into screw channels. There are many different types of shut-off systems; the most common designs are ball check valve and the sliding ring check valve [5, 6].

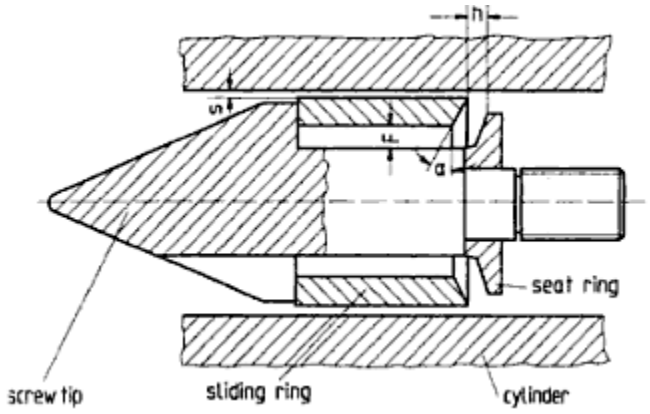

Figure 2.7 Non return valve with sliding retainer ring [5].

The main demands on non-return valves are high efficiency, short closing time, high mechanical strength, and good self-cleaning ability. Here efficiency means the ratio of injected volume to plasticated shot volume and it ranges between 95% and 97%, so 3-5% flows back into the screw channels as the valve closes [5].

The second transition point between the barrel and the mold is the nozzle: a tube providing a mechanical and thermal connection from the hot barrel to the much colder injection mold with a minimum pressure and thermal loss. Nozzle adjusts the cross section of the cylinder to that of the sprue bushing of the mold, and if required, closes the cylinder during plastication and cooling phases [5, 9].

The nozzle tip has a radius that is slightly smaller than the mating radius of sprue bushing for a good seal. It also has to be large enough to avoid excessive wear. Nozzles may be either open or shut-off, and the latter can be self-controlled or externally controlled. Figure 2.8 shows the fit of a nozzle tip to the sprue bushing. Incorrect fit could allow the nozzle to back away during the high pressure of injection allowing plastic to leak [5, 6, 9].

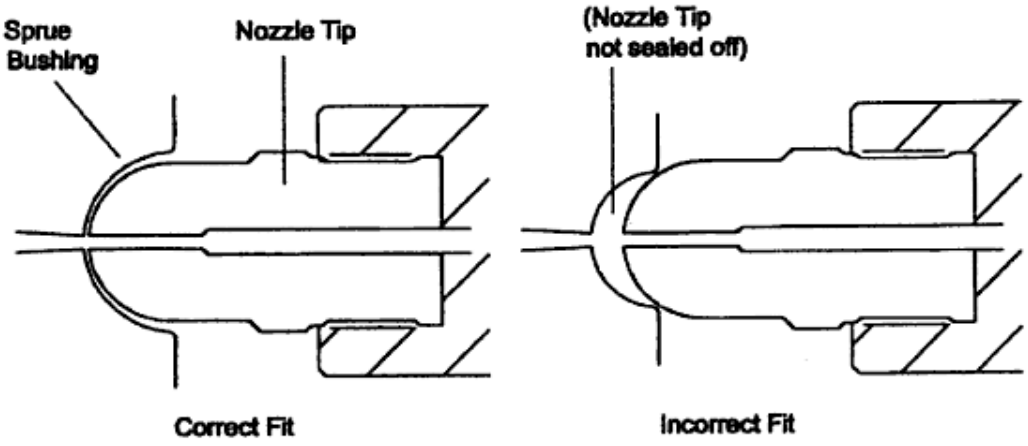

Figure 2.8 Illustration of the fit of a nozzle tip to the sprue bushing [9].

B. Clamping unit

Injection molding process also requires molds that open and close and are held closed with considerable force against injection pressure. As injection molding is a discontinuous process, machine should be able to open the mold for ejection of the product and close it again for the next turn. The clamping unit must afford this (see clamping unit in Figure 2.9) [5, 6].

Clamping units can be divided into groups; mechanical clamping units, hydraulic clamping units, and hydraulic mechanical clamping units. For mechanical clamping units the required motions and clamping forces are provided by the kinematics of the mechanical system. The single-toggle lever system is the cheapest one of mechanical clamping units (shown in Figure 2.10). On the other hand, hydraulic clamping unit has totally different design. The hydraulic clamp mechanism uses direct acting hydraulic cylinders to achieve the closing and clamping of the mold (shown in Figure 2.11). The hydraulic oil reservoir is mounted in a position that allows the oil to flow by gravity or by pumping pressure into the main cylinder. Furthermore, to reduce the volume of oil being moved, especially for larger machines, additional mechanical elements are putted in the clamping systems, which are called hydraulic mechanical clamping units [6, 9].

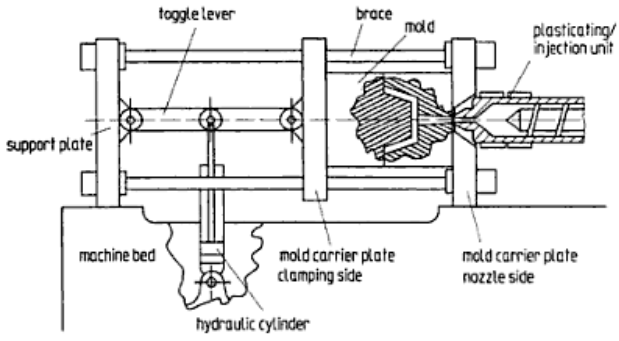

Figure 2.9 Clamping unit of an injection molding machine [5].

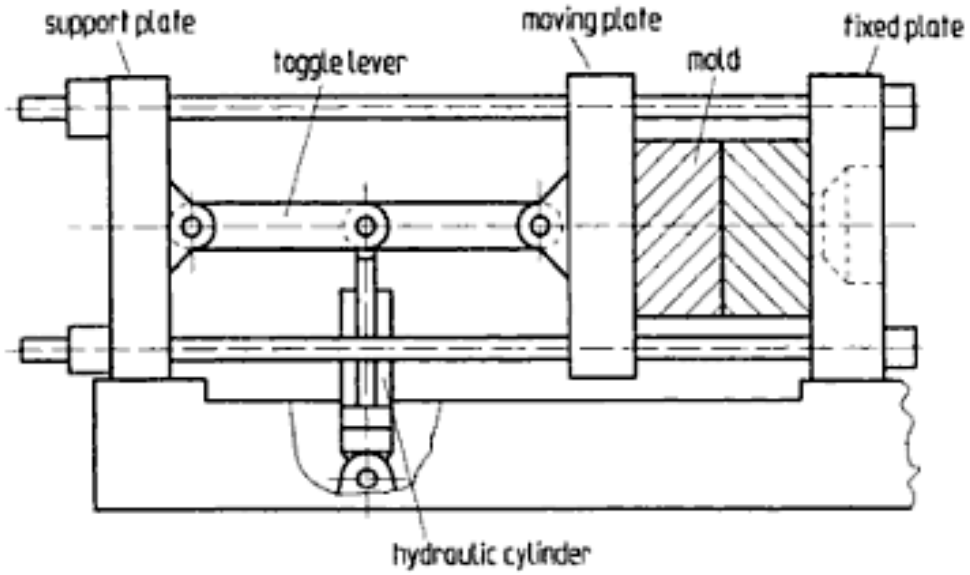

Figure 2.10 Clamping system with single-toggle lever.

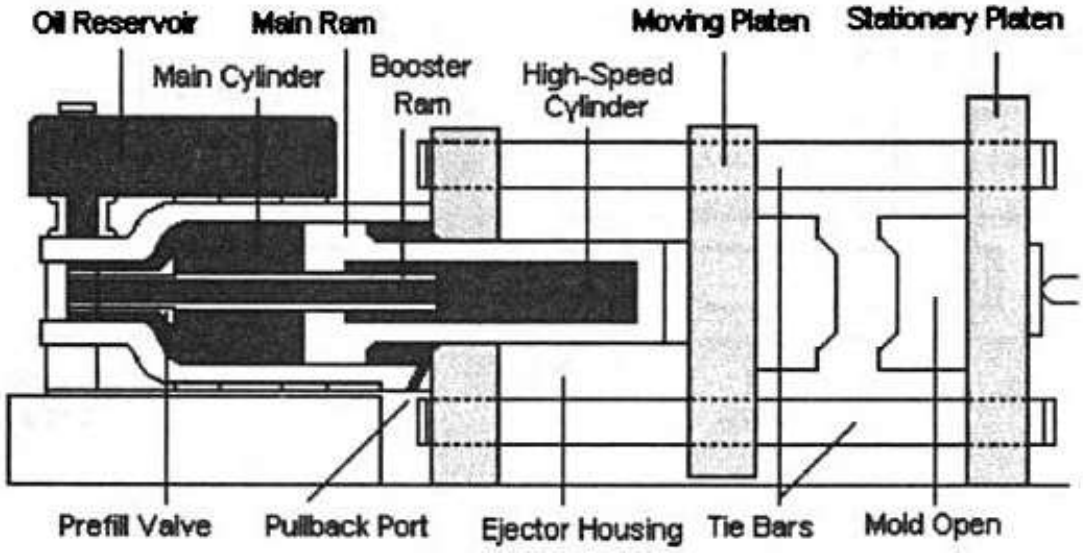

Figure 2.11 Injection molding machine hydraulic clamp unit.

C. Mold:

The mold includes a cavity that forms the features of the plastic part it will produce. A mold must accommodate and distribute the melt, form the melt into the final part geometry, cool melt and eject the finished molded part. Molds can be divided into two main groups like hot-runners and cold-runners, where cold runner is simple and has low cost, and hot runner is expensive and provides higher productivity [5, 6, 9, 10]. Elements of an injection mold are shown in Figure 2.12.

Molten plastic injected from the nozzle of the injection molding machine flows in the sprue, runner, and finally reaches the cavity. Figure 2.13 shows runner system of an injection molding. During injection the nozzle of the plasticating unit is in close contact with the sprue bushing and presses hot melt into the sprue. The runners should be designed to generate low flow resistance and resistant to cooling down. In the case of

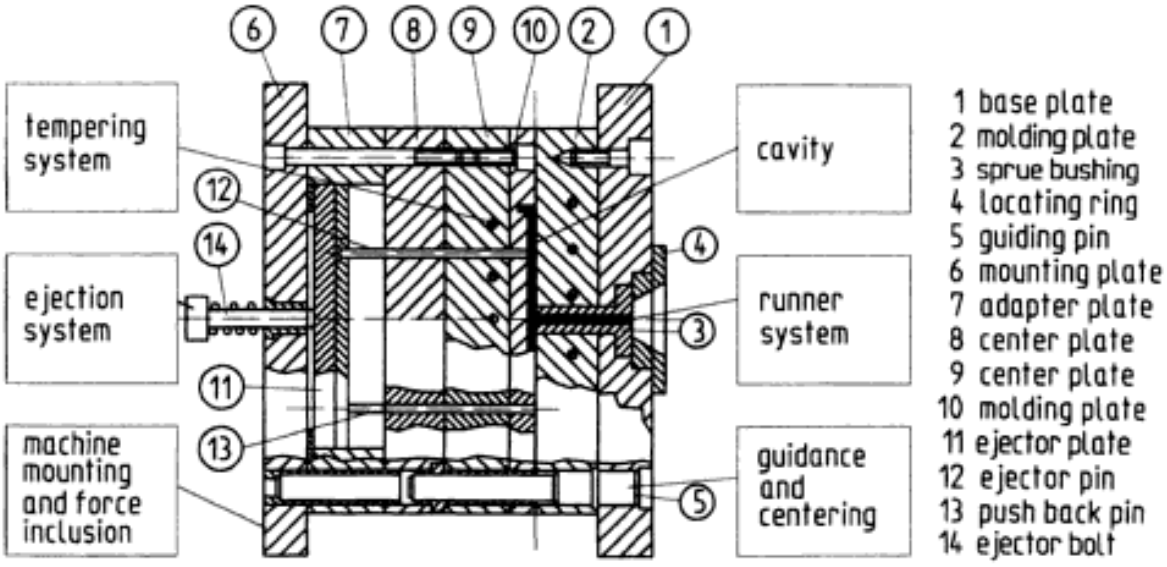

Figure 2.12 Elements of an injection mold.

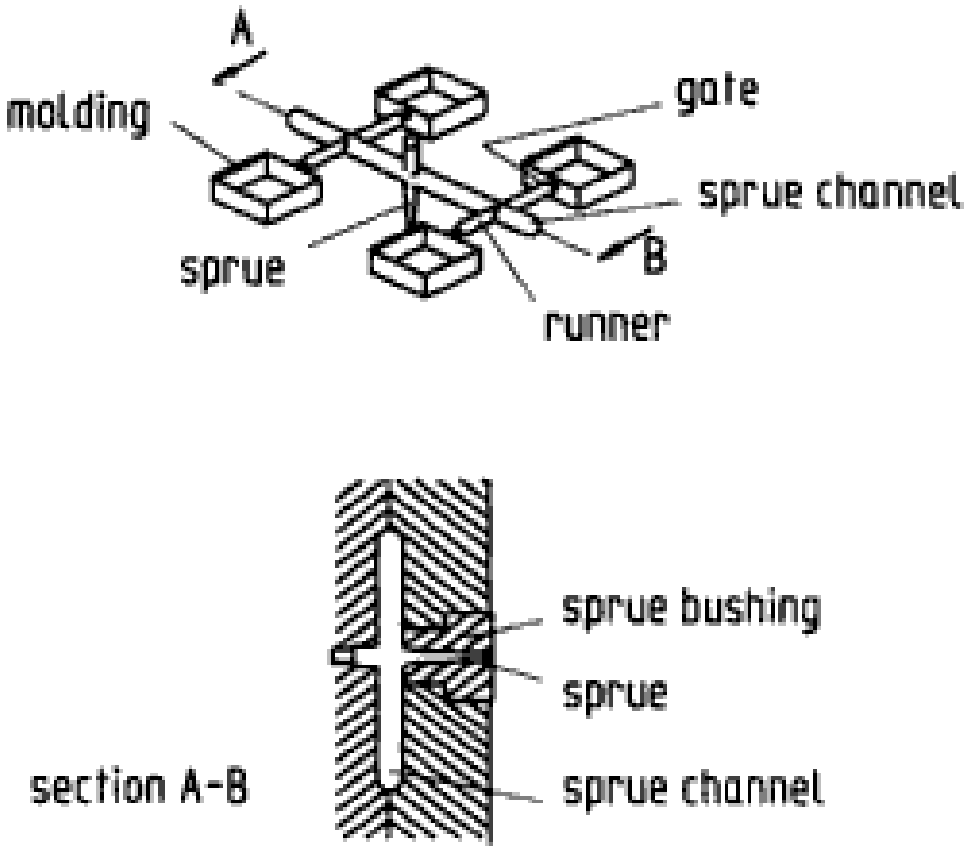

Figure 2.13 Runner system of an injection molding.

multicavity mold, the melt then reaches the sprue channel and is distributed via runners and gates to the various cavities [5, 8].

The gate is the link between the part and the runner system, and it is normally restricted area that facilitates separation of the runner from the part. Gates are generally classified into restricted and unrestricted types; direct gate as unlimited gate, and slide gate, tab gate, film gate, pin gate as limited gate are shown in Figures 2.14, 2.15, 2.16, and 2.17 below [6, 8].

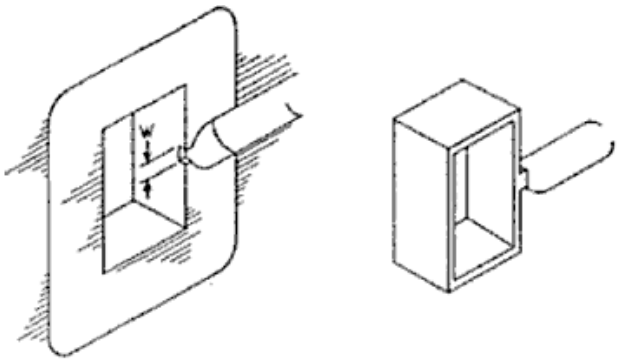

Figure 2.14 Slide gate structure

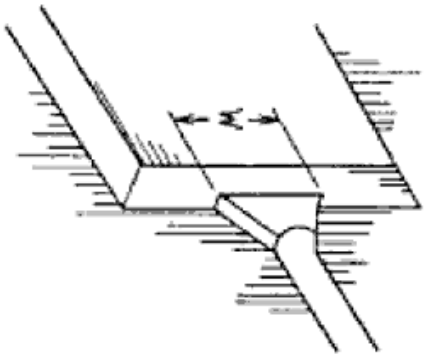

Figure 2.15 Fan gate structure

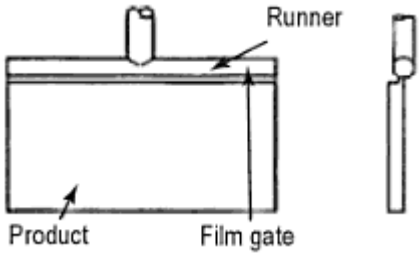

Figure 2.16 Film gate structure

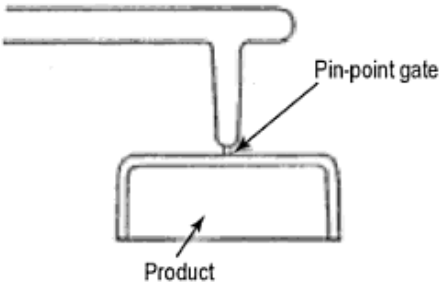

Figure 2.17 Pin-point gate structure

It is desirable that the gate design allows for easy removal from the part. A gate design that is too small might inhibit packing of the part and cause over shearing of the material, jetting, and other gate related defects [6].

Cavity distributes the melt, forms it and gives it the final shape of the molding. It represents the negative shape of the molding walls. Injection moldings are often very complex geometries with undercuts (shown in Figure 2.18). In such cases cavity must be formed by movable mold walls that slide into their final position to build up the cavity walls as the mold closed [5].

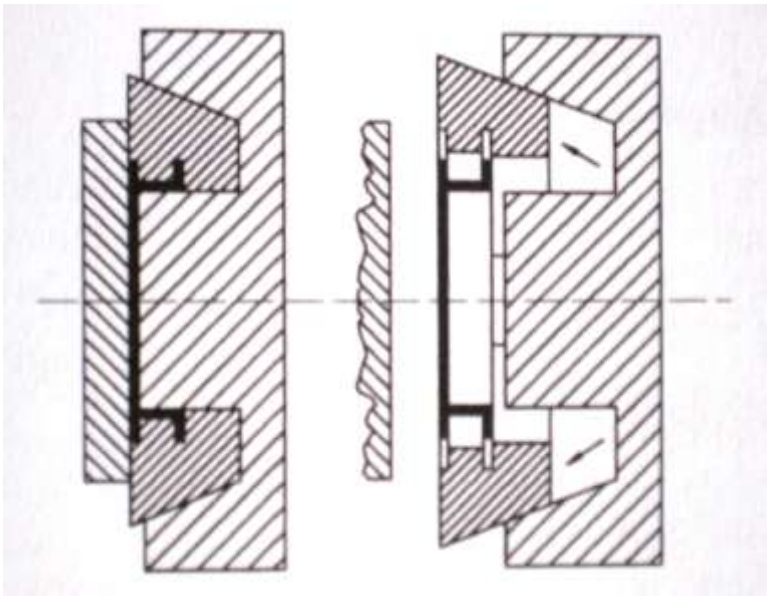

Figure 2.18 Undercuts.

The finished molded part can be removed manually from the open mold, or it can be pushed out by an ejector system as the mold is being opened. The most influential elements for smooth ejection are the shape and the rigidity of plastic products, and product ejection mechanism should be well designed so that no distortion, scratches, or cracks occur on the molded products. Depending on the part geometry, ejectors may consist of pins or rings embedded in the mold that can be pushed forward when the mold is open [5, 8].

Prototyping molds can have additional features such as interchangeable molding tools. Those interchangeable molding tools can be also called removable inserts. The main objective in using these on the core and cavity side of the mold is to allow the user quickly and easily remove and replace parts to make changes on the ejected parts without having to remove the mold base. It is very convenient especially for the prototyping as it eliminates the need for a new mold for both minor and major differences on the parts.

Another advantage of using those inserts is reduced part and storage costs compared to bulky and heavy mold bases [9]. The interchangeable molding tools are even used for making entirely different parts and claimed to increase the speed of each production run [11].

D. Control System:

Physical values such as temperature of plasticating unit and the mold, position of the plasticating unit, screw and mold, velocity of the screw, pressure during the holding phase in the clamping system should be monitored carefully. Physical values are recorded with special sensors (thermocouples, pressure transducers etc.) and those readings than transferred by computers [5, 6]. Based on these input data, the control program can be setup to optimize the process. The linkage between process variables and quality attributes in molded products are essential for precision, as well as technical and economic feasibility.

E. Tempering System:

Tempering is used for cooling the melt so it can solidify and subsequently be removed. Tempering systems of molds for thermoplastics differ from the other types of polymers. For thermoplastics, short cooling times are obtained by low melt and mold wall temperatures as well as by part ejection temperatures as high as possible [5].

F. Injection Molding Cycle:

The sequence of events during the injection molding is shown in Figure 2.19. First, screw moves forward and fills the mold with melt and maintains the injected melt under high pressure. During hold time additional melt is injected. Later, the gate freezes, thus isolating the mold from the injection unit. The melt within the mold is still at high pressure, and as the melt cools and solidifies, pressure drops. After gate freezing, screw rotation starts. Flow rate is controlled by back pressure. After sufficient melt generation for the next turn, screw rotation ends. The filling, packing, and holding stages follow subsequently until the molded part is ejected. The material in the cavity undergoes solidification either due to cooling, in the case of thermoplastics, or curing, in the case of thermosets [4, 8].

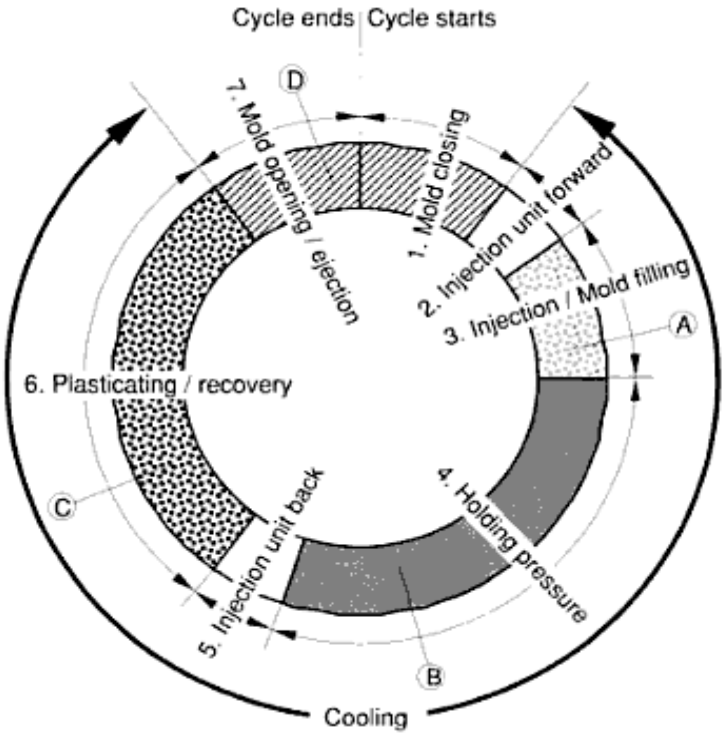

Figure 2.19 Injection molding cycle.

2.1.1 Injection compression molding

In the recent years, the manufacturing of precision plastic optical parts for high-quality parts such as lenses and disk substrates by injection compression molding processes gain importance. This process is actually a combination of the traditional injection molding process and compression molding process.

There are many devices produced by injection molding from automotive parts to medical sensors however, there are also many disadvantages in using a traditional injection molding for making optical parts [12]. The high injection and packing pressure, uneven shrinkage, warpage, residual stress and sink marks are only some of those disadvantages. The optical birefringence due to residual stress is an outcome that significantly reduces the optical performance (e.g. double-vision) of an optical electronic device such as liquid crystal display.

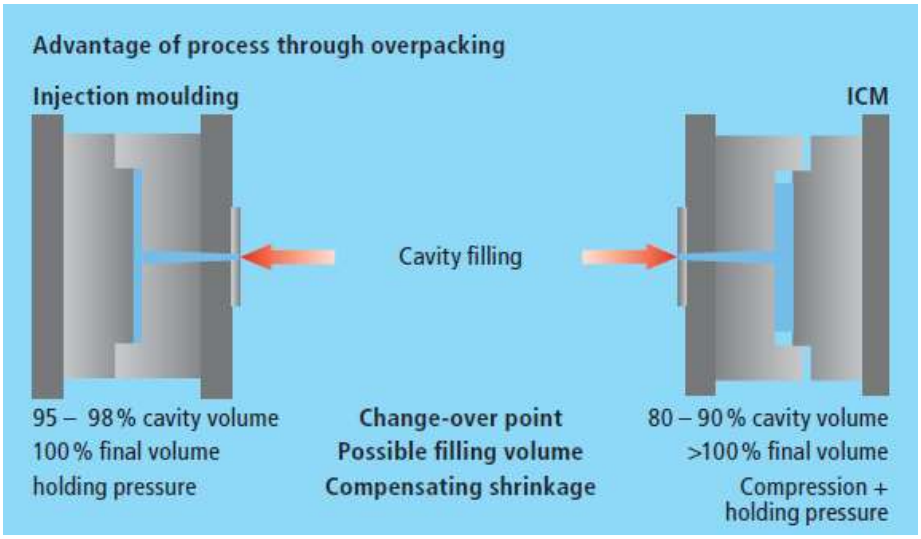

Figure 2.20 Injection versus injection compression molding for packing [13].

In compression molding process, the polymer melt is compressed by the moving platen to flow into the cavity. The pressure produced in this process is more uniform along the cavity wall and lower for post filling stage and therefore results less residual stress as well as less part warpage [12, 14]. The drawbacks for this method are low productivity due to time consuming charging step and limitation for producing large complex shaped parts.

The combination of these two processes, the injection compression molding provides many advantages. The injection compression molding differs from traditional injection molding in terms of cavity filling where there is further melt flow and reduction of cavity volume during the packing phase (see Figure 2.20). The compression stage after the partial melt filling of the cavity decreases the mold pressure and clamp tonnage (20 - 50 % lower see Figure 2.22), reduces the cycle time and residual stresses [6]. The process is also claimed to allow even packing thus, lower uneven shrinkage and warpage [15]. The accuracy of the dimensions and part shape is very important for high precision optical parts therefore, the injection compression molding is good manufacturing process for those parts.

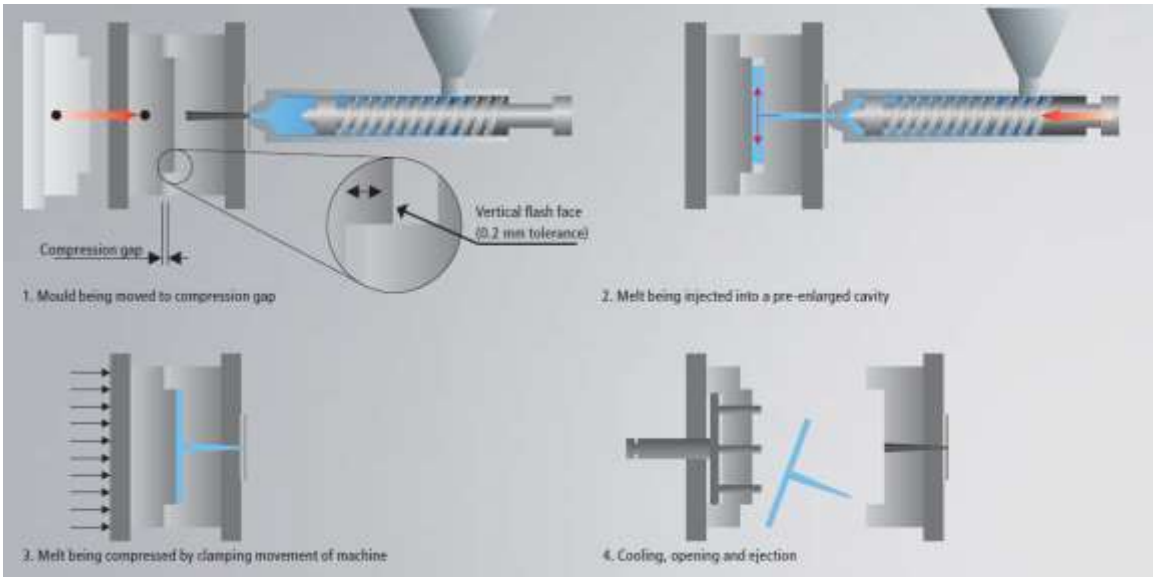

Figure 2.21 Stamping injection compression molding.

There are three types of injection compression techniques [16]. The initial thickness of the mold cavity and the thickness of the part are the main factors leading to this categorization. Two stage sequential (stamping) injection compression molding (see Figure 2.21) is the first type where the thickness of the mold cavity is larger than the thickness of the part. This design allows the polymer melt to reach extremities of the cavity at low pressures. The mold pre-closing and closing positions are set on the machine indicating the injection and compression stages respectively. The disadvantage of this type is the marks due to flow stagnation over the transition period between stages. The second type is the continuous injection compression molding. In this case, those injection and compression stages occur almost simultaneously. The melt is injected into the cavity while the mold is still moving for compression. Melt flow is continuous in this process therefore; there is no flow stagnation mark or surface defect. The coining (selective) injection compression molding is the final type

and the mold cavity thickness is less than the part thickness. As the mold movement depends on the cavity pressure and force exerted on machine plate, the key is the machine communication for this type. Once the force exerted by the mold cavity is higher than the clamp force due to incoming polymer melt mold is opened to decrease the cavity pressure. It is a balance between the mold cavity pressure and clamp force; the mold closes when the latter is higher than the former. This set of movement is also called "mold breathing" At the set point position for the part thickness the machine applies the packing pressure.

High precision optical parts (see Figure 2.23) making via injection compression molding is presented in both experimental and numerical forms on the literature for various cases. The studies conducted on molding optical lenses concluded that the parts had better quality compared to the without compression parts at the same cooling time [17, 18]. The injection compression molded disks (e.g. CD-R) are shown to have enhanced dimensional accuracy on the direction perpendicular to the compression, as

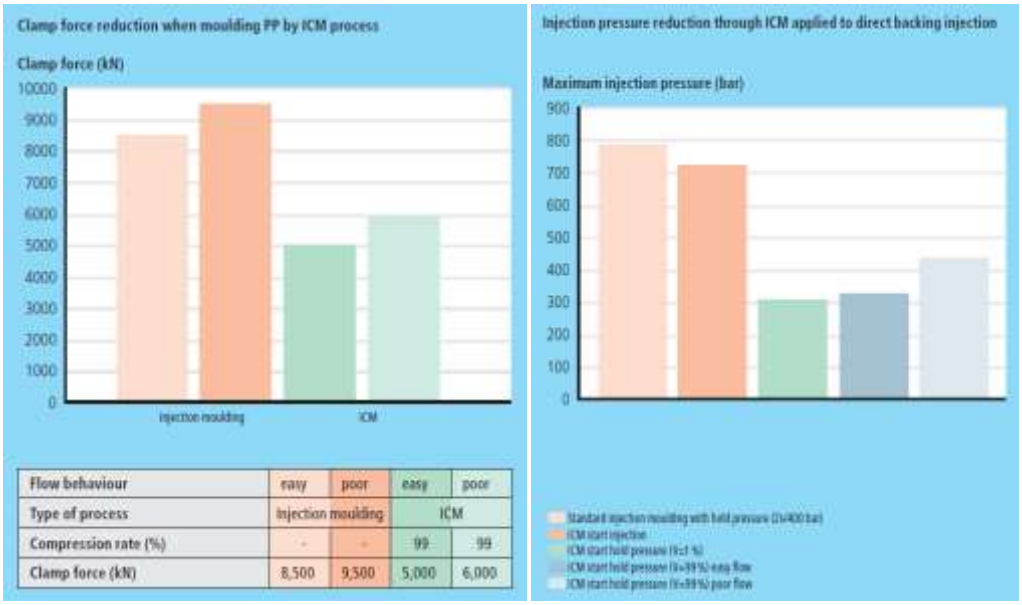

Figure 2.22 Clamp force and injection pressure comparisons [13].

Figure 2.23 Injection compression molded optical parts [13].

well as improved conformity to cavity profile and reduced warpage [19, 20]. Properties like birefringence changing depending on the processing conditions of the parts are also tracked [21]. They concluded on that study that the mold temperature and the cooling time were the two processing parameters affecting the birefringence the most.

These experimental findings were compared to the numerical analysis by modeling the process. Young *et al*. studied the shrinkage and residual stress simulation of injection compression molded pickup lens with large thickness variations [22]. Cross-WLF Equation for viscosity and modified Tait Equation for density were used to simulate the process. The surface profile deviation due to shrinkage is found to be mostly affected by mold temperature and compression time. Kwon *et al*. have shown numerical birefringence distribution on injection compression center-gated disk using the Leonov viscoelastic fluid model [22, 23]. Park *et al*. used the same model for

simulating the same process with the finite difference method and addition of the Tait Equation of state [24]. Chen et al. simulated the filling stage of stamping injection compression molding with a new numerical algorithm [25-28]. They found the measured cavity pressure and simulated pressure are in agreement and switch time changes the pressure profiles. The reduced and more uniform shrinkage in molded parts, smaller birefringence at higher melt temperatures and lower mold closing velocity are reported. On the other hand, the flow rate and mold temperature is shown to have no significant effect on birefringence.

2.1.2. Film Insert Injection Molding

In recent years, film-insert injection molding (FIM) in which molten polymer is injected into the mold cavity after a film is attached on one side of the mold wall (see Figure 2.24) has become a popular method. The adhesion between the film and the substrate may be enhanced using this process as the injected hot molten resin can partially melt the film. It is a cost and time effective technique eliminating various post processing (screen printing, spray painting, laminations etc.) and improving surface quality and durability. Many products such as automotive interior parts, cellular phone cases, logo designs on plastic products are produced using FIM method [29, 30].

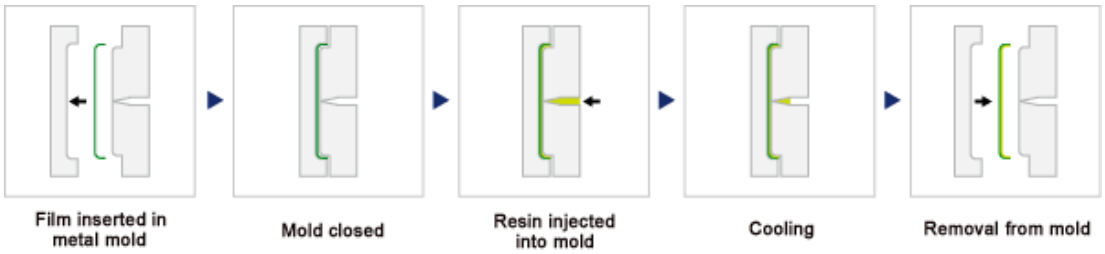

Figure 2.24 Film insert injection molding process steps.

The disadvantages of the FIM process are the possibility of washing off the printed ink on the film, unexpected weld line, wrinkling of the film, warpage and uneven part shrinkage (see Figure 2.25)[29].

Injection molding process creates residual stresses due to shear and extensional flows during processing, high pressure imposed during packing and thermal stresses during solidification and cooling on the part as previously mentioned and it causes

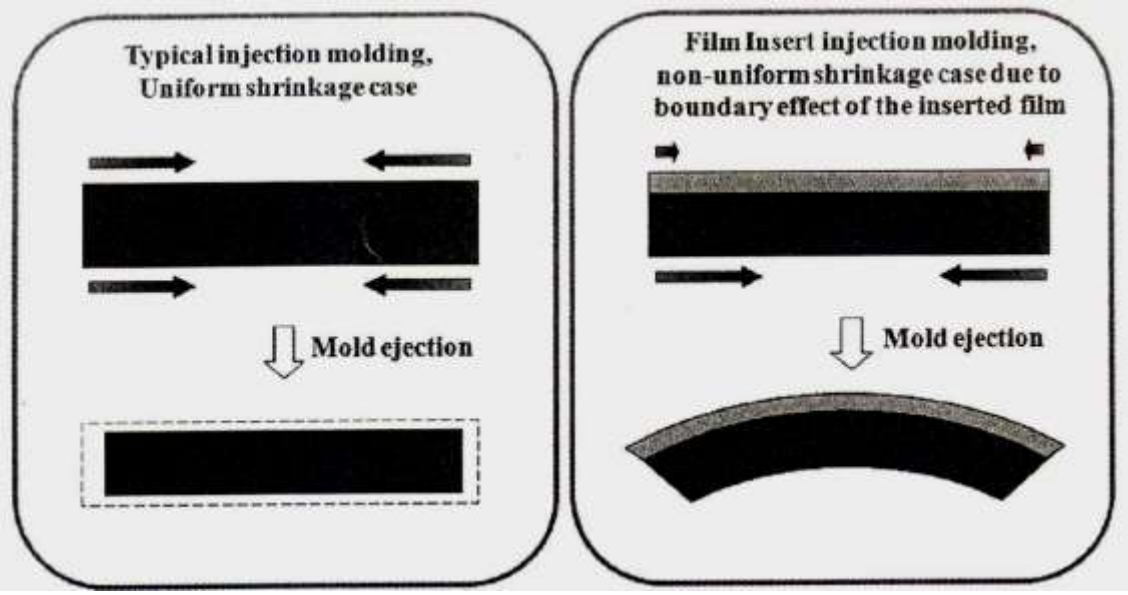

Figure 2.25 Schematic representations of shrinking behavior in injection molding and warpage behavior in FIM [29].

deformation. The FIM process interrupts heat transfer in perpendicular direction to the cavity wall which develops very severe residual stresses on the part. This asymmetric residual stress distribution results in extreme warpage and non-uniform shrinkage. For this reason, investigation of precise residual stress distribution and prediction of the viscoelastic deformation is important for practical applications [29, 30].

2.1.2.1. Film Insert Molded Part Geometry and Viscoelastic Behavior

The effects of injection molding conditions such as injection speed, melt temperature, mold temperature, packing time and pressure on viscoelastic behavior and deformation of film insert molded parts are investigated in many studies. Beak et al. has shown that warpage decreases monotonically with increasing injection speed and exhibits a bell shaped curve as function of melt temperature however, the packing time did not have an effect on warpage of polycarbonate, acrylonitrile-butadiene-styrene (ABS) substrates and polymethylmetacrylate (PMMA) films. The warpage analysis with changing processing conditions is conducted on four different sets of FIM parts of annealed and not-annealed film and substrates. The film insert is annealed at higher temperatures to minimize the effects of thermal shrinkage and residual stress on warpage of the final parts [10, 30, 31]. Not annealed and annealed films dimensional variations are measured to determine the linear thermal expansion coefficient, α, using the Equation below.

$$\alpha = \frac{\Delta l}{l_0 \Delta T} \qquad (1)$$

Where Δl is change in length, l_0 is the initial length and ΔT is the temperature difference.

In these studies, a warpage reversal phenomenon (WRP) where warpage variation generated by annealing not annealed film containing part was observed (see Figure 2.26). The annealing is found to affect the warpage variation more than any other injection molding parameter. During annealing, the part with not annealed film warpage is reversed gradually to concave film side. This phenomenon occurs due to the combined effect of thermal shrinkage of inserted film and relaxation of residual stresses in FIM part during annealing [10].

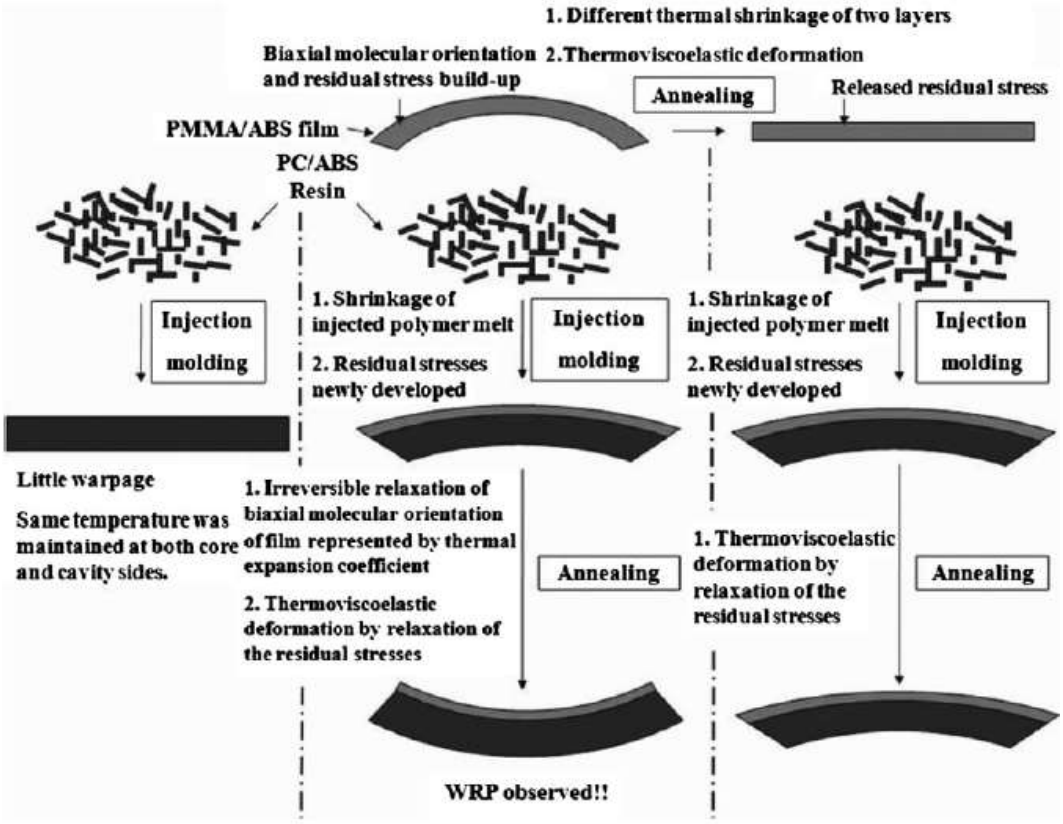

Figure 2.26 Schematic diagram showing predicted different geometry of injected and annealed parts and WRP [10].

The effect of film and substrate thickness on warpage was investigated. The warpage due to non-uniform temperature distribution was increased with increasing film thickness and with decreasing substrate thickness (see Figure 2.27, 2.28).

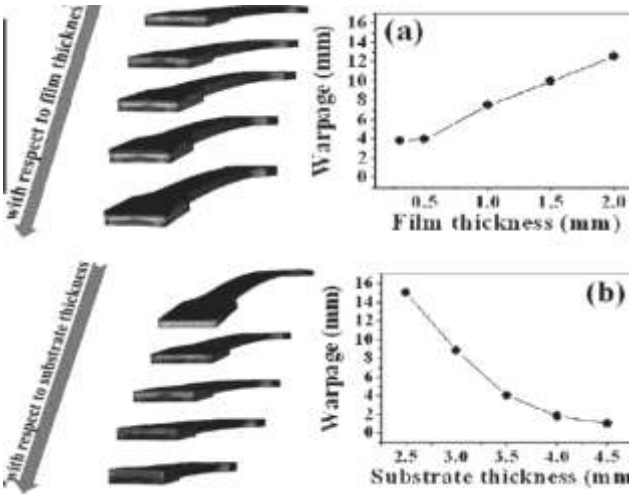

Figure 2.27 Warpage of parts after ejection with respect to (a) film and (b) substrate thickness [29].

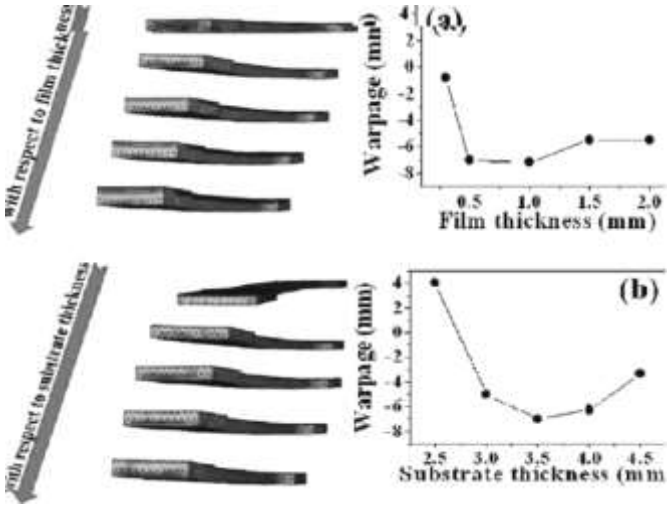

Figure 2.28 Warpage of parts after annealing with respect to (a) film and (b) substrate thickness [29].

Numerical analyses were also conducted in order to understand the processing procedure and physical properties of final products. Kim et al. performed numerical analysis by using three dimensional finite element analysis with Moldflow equipped with part insert option and time dependent viscoelastic analysis were completed with ABAQUS stress analysis code [30]. Beak et al. used a mesh generation program, HyperMesh, to generate two dimensional finite elements for film and substrate domains and carried out the three dimensional analysis in Moldflow program [10]. For the flow analysis, under non-isothermal conditions during filling and post filling stages Hele-Shaw model for compressible viscous fluid is used, rheological behavior of polymer melt is assumed to follow modified Cross model with Williams-Landel-Ferry Equation and PVT relationship is represented by Tait Equation. The material is assumed transversely isotropic for long-term viscoelastic behavior with temperature effect on material behavior explained by thermo-rheological simplification and generalized Kelvin model was selected as constitutive Equation for linear thermoviscoelastic material in stress analysis [29, 30, 32].

The stress numerical analysis results are compared with the experimental results; found in good agreement by Kim et al. [31] (see Figure 2.29). The hole-drilling method is used as semi destructive stress measurement technique. A hole is drilled onto the part for localized stress relaxation and deformation around the hole.

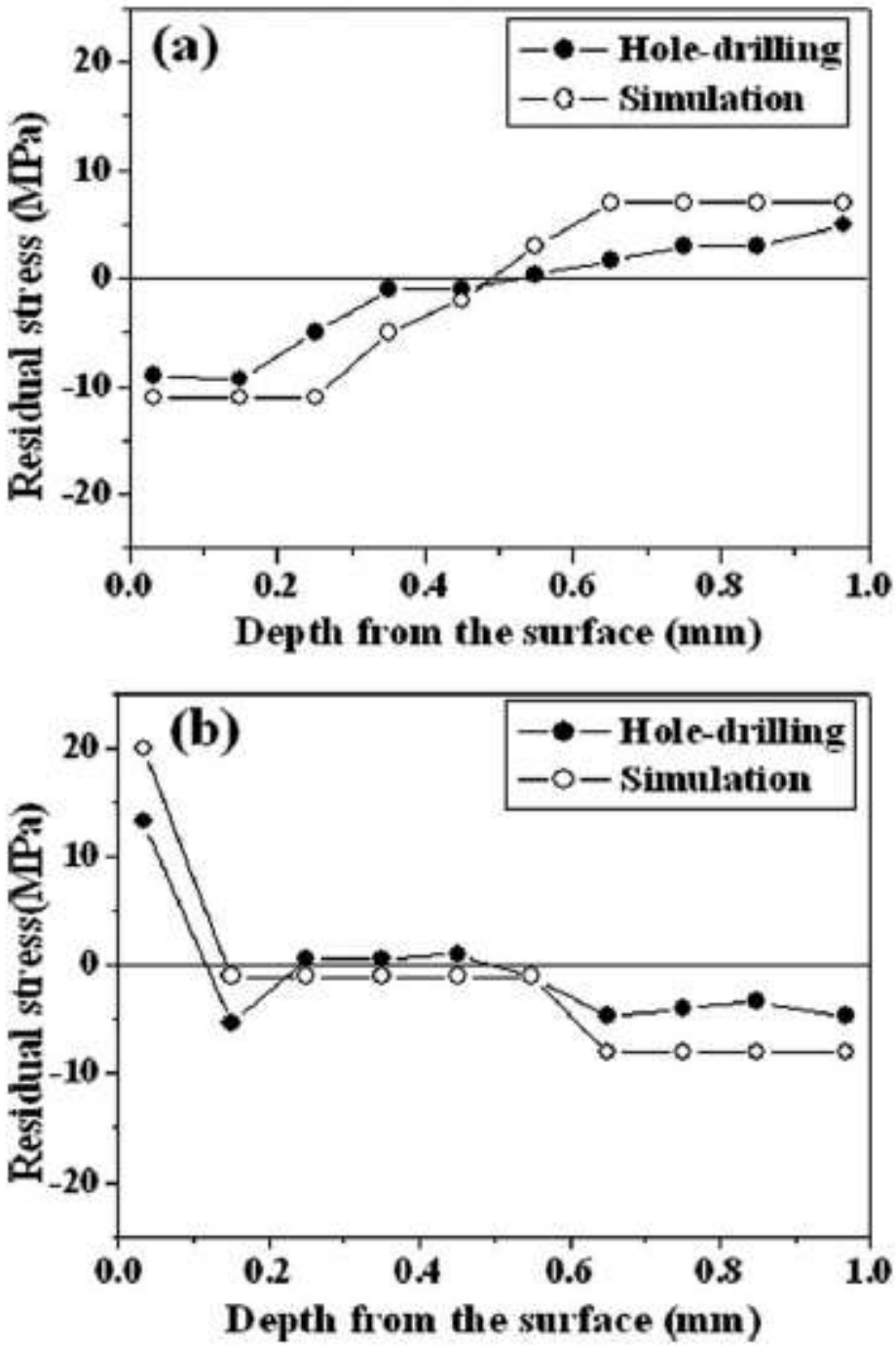

Figure 2.29 Residual stress distributions obtained numerically and experimentally after (a) ejection and (b) annealing [29].

The strain distribution is measured using a specially designed strain gauge. The residual stress distribution in the part is reported to vary from compression to tension in thickness direction from film surface as the shrinkage of injected polymer was larger than of the insert film. For the annealed part, the observed behavior was reversed. The tensile residual stress was observed at film surface after annealing due to large thermal shrinkage in early stages of annealing.

The extent of orientation induced crystallization of polyethylene teraphtalate (PET) has been studied by Leong et al. for PET film-insert moldings. The molded parts are exposed to isothermal annealing to investigate the influence of interfacial molecular reorganization and crystallization on film-substrate interfacial properties. They have observed drastic increases in dichroic ratios of specimens molded at 500 mm/sec injection speed after 1 min of annealing which is explained to be caused by residual stresses particularly localized in high shear regions. They have also seen that lower injection speeds gave rise to better film-substrate adhesion [10].

2.2. Polyurethane Chemistry & Properties

Polyurethanes are polymers obtained combining two multi-functional monomers with isocyanate (-NCO) and hydroxyl groups (-OH) forming urethane linkages. The chemical reaction is shown in the formula below:

ROH + R'NCO → ROC(O)N(H)R' (R and R' are alkyl or aryl groups)

The process is poly-addition reaction which requires presence of a catalyst. Polyurethanes are highly used in manufacturing of foam insulation panels, seals and gaskets, elastomeric wheels and tires, high performance adhesives, coatings, fibers, electronic instruments etc. They exhibit the best properties of both rubber and plastic, allowing a wide variety of application area.

The first important component of polyurethane is the isocyanate. Isocyanates can be aromatic such as diphenylmethane diisocyanate (MDI) or toluene diisocyanate (TDI) and aliphatic such as hexamethylene diisocyanate (HDI) or isophorone diisocyanate (IPDI) (see Figure 2.30). Isocyanates are further modified by partially reacting with a polyol forming a prepolymer.

The second important component of polyurethane is the polyol. A polyol is formed by base-catalyzed addition of propylene oxide, ethylene oxide onto a hydroxyl or amine containing initiator (polyester polyols) or by polyesterification of a di-acid such as adipic acid with glycols such as ethylene or dipropylene glycol (polyether polyols) (see Figure 2.31).

Polycaprolactones are used as other type of polyesters, produced by ring-opening polymerization of ε-caprolactone and having lower viscosity than polyadipates of the same molecular weight due to their narrower molecular weight distribution. They are also more water resistant than polybutanediol adipate [33].

The catalysts used might be tertiary amines such as dimethylcyclohexylamine or organometallic complexes such as dibutyltin dilaurate or bismuth octanoate.

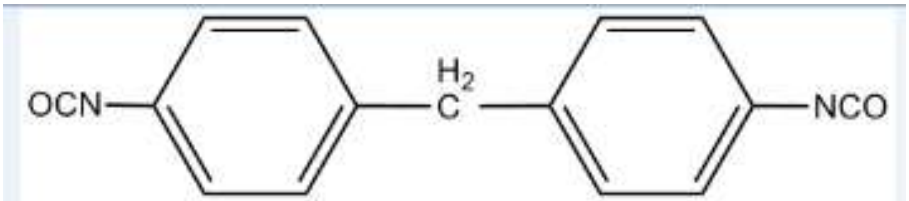

MDI (diphenylmethane-4,4-diisocyanide)

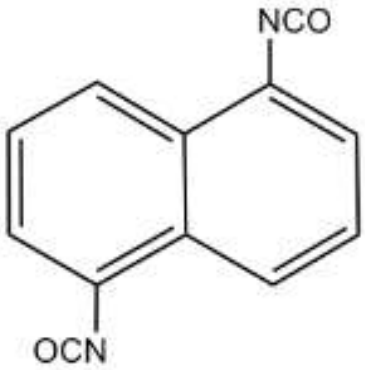

NDI (naphthalene-1,5-diisocyanide)

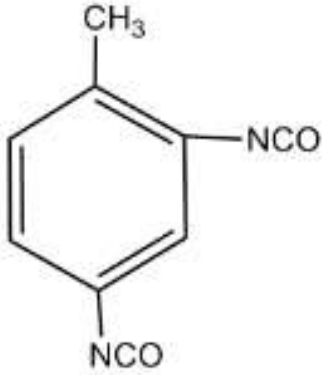

TDI (toluene-2,4-diisocyanide)

$OCN(CH_2)_6NCO$

HDI (hexamethylene diisocyanide)

Figure 2.30 Chemical structures of some isocyanates.

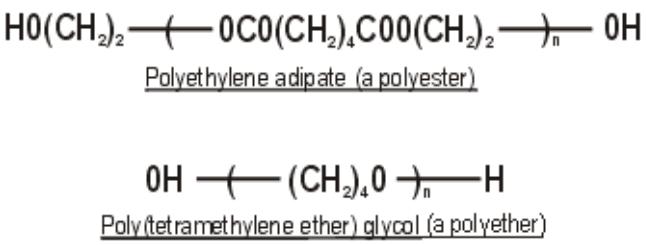

Figure 2.31 Chemical structures of some glycols.

The elastomeric properties is highly dependent on the phase separation of hard and soft copolymer segments of the polymer as urethane hard segment domains serve as crosslink between the amorphous polyether and polyester soft segment domains. The mainly non-polar, low melting soft segments are incompatible with the polar, high melting hard segments, therefore phase separation occurs. The polyol soft segments have high molecular weight and are mobile and in coiled formation whereas, isocyanate and chain extender hard segments are stiff and immobile. The covalently coupled hard segment to the soft inhibit plastic flow of the polymer chain, thus creates elastomeric resiliency. High tensile strength, elongation and tear resistance values can be obtained with these materials due to hard segments aligned in stress direction and consequent powerful hydrogen bonding during mechanical deformation while a portion of soft segments are stresses by uncoiling. The flexible chains contribute to the elongation characteristic of the polymer. The soft domains also provide the material a very low Tg compared to the polymers with same hardness, maintaining the elasticity at very low temperatures. Soft and hard segments can be presented as in the Figure 2.32 below for thermoplastic polyurethanes:

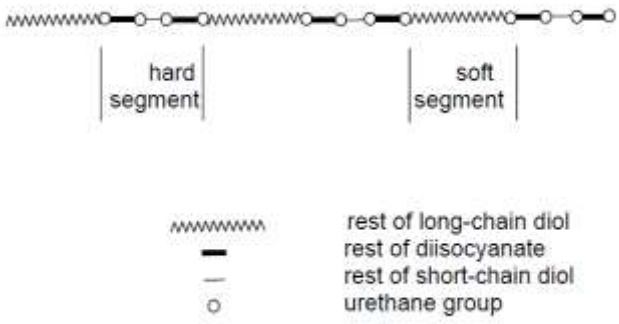

Figure 2.32 General structure of thermoplastic polyurethanes [33].

Polyurethanes are highly versatile, meaning they can be a combination of a variety of soft and hard segments with their respective ranges of molecular weights. Different grades from very soft (80 Shore A) to very hard (60 Shore D) polyurethanes with different degrees of crystallinity can be obtained depending on the application.

The crosslink ("pseudocrosslink") in thermoplastic polyurethanes can be broken reversibly by raising materials temperature via injection molding, calendaring or classical extrusion. In other words, the thermoplastic polyurethanes can be reprocessed easily. The molecular weight can be decreased using these processes for example if lowering the viscosity of the material is desired. Once the polyurethane is cold again the crosslinks reappear again, thus the elastic properties are reestablished [34].

Solvent dissolving, also break up those crosslinks. Therefore, using polyurethanes in solution for classical methods of coating applications is possible as they form the crosslinks back after solvent evaporation [34].

2.3. FTIR Spectroscopy

Infrared spectroscopy is a vibrational spectroscopy technique for characterization of materials in which polymers are major constituents. Identification of materials and determination both of molecular microstructure and morphology of complex polymers are possible using infrared spectroscopy. This method can also be used for quantitative analysis in polymers as the infrared absorbance is linearly proportional to the number density of species giving rise to that band. The method is sensitive to properties such as copolymer sequence, tacticity, molecular conformation, molecular orientation and configuration of the material. Therefore, quantitative method development must be made accordingly [35-37].

A FTIR instrument uses interferometer to generate and collect spectrum of samples. The interferometer consists of a light source, a beam splitter, a detector, one stationary and one moving at a constant velocity mirror. The working principle of the interferometer can be seen in Figure 2.33.

The beam splitter splits the light coming from the source into two identical beams; one will travel and reflect back from the stationary mirror and the other will travel a different path and reflect back from the moving mirror. The reflected beams recombine

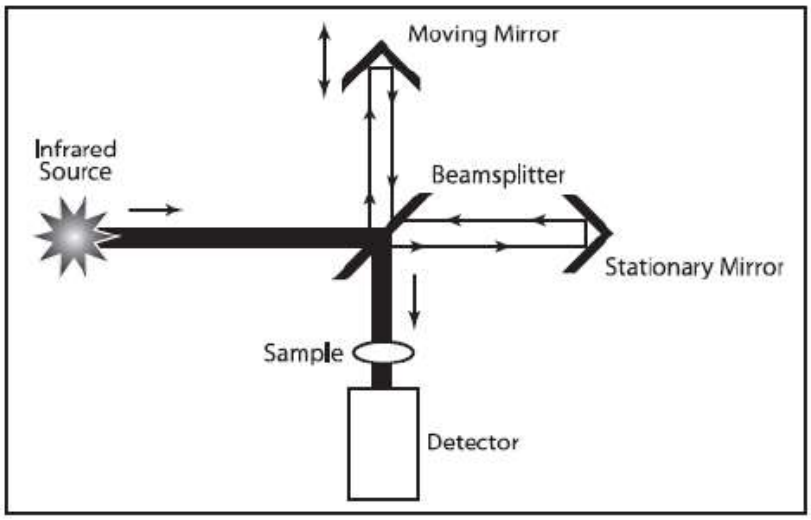

Figure 2.33 Schematic of interferometer.

at the beam splitter. The difference in the optical paths travelled creates a phase difference between two waves so, during the recombination at the beam splitter the results can be destructive or constructive. The interferogram which is the recombined waves interacts with the sample by which will be partially absorbed. The remaining portions are transmitted to the detector. The signals transmitted to the computer, Fourier transform and subtraction of the background spectrum steps are performed to obtain the transmittance spectra of the sample.

2.3.1 Dichroism and Orientation Development

Polymer products such as films, fibers are oriented in selective directions during processing, with techniques such as stretching, fiber spinning etc. Many desired properties like directional stiffness, gas permeability and optical properties are obtained by this directional orientation.

Post processing techniques cause anisotropy in polymers which can be investigated by polarized infrared spectroscopy due to the nature of the interaction between the incident infrared radiation and transition moment vector of the vibration bands. The interaction of the electric field vector of the incident radiation, E, with the transition moment vector, M, of a particular vibration mode causes the absorption of the infrared radiation. In linearly polarized radiation case, the absorbance Ai for the band association with the vibration *i* is proportional to the square of the scalar product of Mi and E:

$$A_i \alpha \sum (M_i \bullet E)^2 \alpha \sum (M_i E)^2 \cos^2 \gamma \qquad (2)$$

ϒ: angle between transition moment and electric field vector

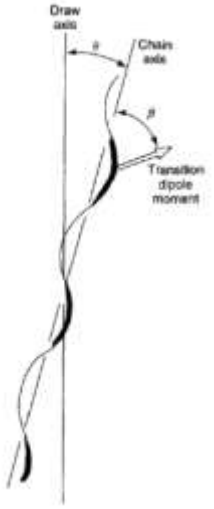

Figure 2.34 Angle in chain orientation function and dipole transition angle in uniaxially oriented polymer.

Considering the relation in Equation 2, highest absorbance is obtained when M and E are parallel and zero absorbance when perpendicular. The angle between

transition moment and electric field vector is calculated summing up the θ and β angles shown in Figure 2.34.

The orientation of various polymer chain directors with respect to the macroscopic reference axes is described by total averages of the angles which can be determined by infrared spectroscopic technique. Oriented samples are examined with horizontally or vertically polarized infrared beam by reference to the sample reference axes which are aligned parallel to the spectrometer axe. The sample reference axe is found using cross polarizers where it coincides with principal axes of refractive index ellipsoid. The axes of interests are draw direction or perpendicular to the draw direction in uniaxially oriented samples. However, in biaxially oriented samples axes in film plane are considered machine direction (MD) and transverse directions (TD) [37].

The dichroism is the anisotropic optical absorption of the oriented samples. The infrared linear dichroism (IRLD) experiments where spectra is measured by using light polarized parallel and perpendicular to the fixed reference direction can be conducted to analyze the anisotropic optical absorption. The dichroic ratio, D, (Equation 3) and dichroic difference, ΔA, (Equation 4) are parameters calculated for this characterization.

$$D = \frac{A_{//}}{A_{\perp}} \tag{3}$$

$$\Delta A = A_{//} - A_{\perp} \tag{4}$$

in which, $A_{//}$ and $A_{\perp}$ are absorbances from investigated band which are measured with beam polarized parallel and perpendicular to the reference direction, z, and the intensities are calculated using the following Equations:

$$A_{/} = \left[ME_{//}\cos\gamma\right]^2 \tag{5}$$

$$A_{\perp} = \left[ME_{\perp}\cos\gamma\right]^2 \tag{6}$$

where, $E_{//}$ and $E_{\perp}$ are parallel and perpendicular electric field vector of incident radiation, M is the transition moment vector and ϒ is the angle between draw axis and transition moment vector described earlier and can be seen geometrically in the Figure 2.35 below [38].

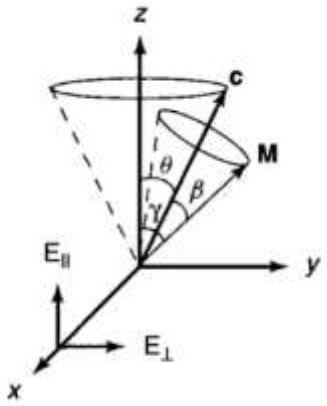

Figure 2.35 Geometrical representation of electric field vectors $E_{//}$ and $E_{\perp}$, transition moment, M, molecular axis c and reference direction z.

The degree of chain orientation can be estimated using orientation function f for the uniaxially oriented samples knowing the dichroic ratio (see Equation 7).

$$f = \frac{3\langle \cos^2 \theta \rangle - 1}{2} = \frac{(D-1)}{(D+2)} \times \frac{2}{(3\cos^2 \beta - 1)} = \frac{(D-1)}{(D+2)} \times \frac{(D_0+2)}{(D_0-1)} \quad (7)$$

Where, dichroic ratio for perfect alignment is $D_0=2\cot^2\beta$ [39].

The orientation of each chemical group in the matrix can be determined from the dichroism as the infrared spectra are selective to the chemical groups.

In industrial investigations, the main goal is to characterize the effects of the process variables such as draw rate, ratio and temperature on molecular orientation. The absorbance of orientation sensitive bands are measured with infrared radiation electric field vectors parallel and perpendicular to the draw axis for uniaxially drawn samples dichroic ratio and subsequently orientation function determination. These measurements are reported in both offline –after deformation performed on samples- and online –real-time, during deformation- forms. For the online measurement systems an ultra-rapid scan FTIR method has been developed and used by Griffits and Manning [40, 41]. Pellerin et al. also evaluated the same system by measuring the real time orientation behavior of PET, PS and PS/PVME blends during irreversible macroscopic deformation and relaxation behaviors [42].

2.3.2. Infrared Studies on Mechanical Deformation of Polyurethanes

The infrared dichroism is a powerful technique allowing monitoring the orientation of specific polymer chain segments. The qualitative analysis of the appropriate infrared absorption bands allows the orientation of polymer segments in different domains of polyurethane systems to be determined.

The hard and soft segments in the PU matrix are both deformed under stress being semi-continuous and interpenetrating. However, each segment deformation has a different effect on the overall material. At least one well-characterized absorption must be available of each segment to use infrared dichroism for the orientations of different segments for polyurethanes. Usually, the N-H stretching vibration located in urethane linkage is used to characterize the orientation of hard segments and the asymmetric C-H stretching is used to describe the prepolymer segments (polyether, polyester etc.) which form soft segments. The stretching absorptions for N-H and C-H respectively, appear around $3320cm^{-1}$ and $2935cm^{-1}$ (other groups vibrational bands are given in Table 2.1).

In order to calculate the orientation function, N-H and C-H bond direction values (β in Equation 7) must also be known. For both N-H and C-H, the bond direction angle is 90°. C=O and C-O-C bond direction values are given in table 2.2 below along with the corresponding peak positions.

After calculation of the orientation functions, resultant values can be evaluated: for randomly oriented groups f is equal to 0, for groups at which the main chain is aligned parallel to the deformation axis to 1 and for perpendicular alignment to -0.5.

In nonoriented state of sample (Figure 2.36 a), the orientation function is zero for all groups. At low strain levels below the yield point, polyureas hard segments chain axis is shown orient transverse to the deformation axis where the orientation function is negative and no orientation in soft segments (Figure 2.36 b). Above the yield point, a different behavior has been observed where hard segments chain axis oriented parallel to the deformation axis showing positive orientation function and soft

segments aligning in direction of deformation (Figure 2.36c). The reasons of these two behaviors has been explained as high aspect ratio of hard segments in first stage and later, the fragmentation of hard domains to allow reorientation [45].

Estes *et al*. designed a set of experiments to monitor polyether based polyurethanes segments behavior after nominal strain level stretching, relaxation at zero load and extension of step increments [43]. Both orientation function at different strain levels and residual orientation functions has been reported (Figure 2.37). At low strain levels soft segments CH orientation is greater than hard segment orientations and this behavior is reversed after 150% strain. In relaxed state hard segments exhibit noticeably higher orientation functions than soft segments due to different stresses acting on the separate domains.

Table 2.1 Assignment of Vibrational Bands for Polyurethane [44].

Observed bands (cm^{-1})	Relative intensity	Assignment
3442	w	NH stretching (nonbonded)
3344	m	NH stretching (bonded)
3290	w	NH stretching (bonded)
3186	vw	CH stretching (aromatic)
3122	vw	CH stretching (aromatic)
3043	vw sh	CH stretching (aromatic)
2957	s	CH_2 stretching
2930	s	CH_2 stretching
2900	m	CH_2 stretching
2876	m	CH_2 stretching
1750–1710	vs	C=O stretching
1614	m sh	C=C aromatic stretching
1598	m	C=C aromatic stretching
1534	s	CN stretching coupled with NH bending
1514	w sh	
1476	w sh	CH_2 scissoring
1465	m	CH_2 scissoring
1453	vw sh	CH_2 scissoring
1415	m	CH_2 scissoring
1402	w	CH_2 scissoring
1370	w	CH_2 wagging
1362	w	CH_2 wagging
1320	w	CH_2 twisting
1311	w	CH_2 twisting
1258	vs	C—O—C stretching (soft segment)
1223	s	C—C, C—O—C stretching (soft segment)
1205	s	
1170	s	C—O—C stretching (hard segment)
1142	s	C—O—C stretching (hard segment)
1068	m	C—O—C asymmetric stretching (soft segment)
1042	w sh	C—O—C symmetric stretching (soft segment)
1018	vw	CH bending
960	w	CH bending
936	vw	CH bending
912	w	CH bending
873	m	CO_3^{2-} out-of-plane bending
865	vw sh	CH out-of-plane bending
852	w	CH out-of-plane bending
820	w	CH out-of-plane bending or C=O—C wagging
770	w	CCO bending
750	vw	CH out-of-plane bending
736	w	C=O wagging
722	vw sh	C=O wagging
714	vw	CO_3^{2-} out-of-plane bending
617	vw	C=O wagging, CCC bending
586	vw	C=O wagging, C=O in-plane bending
510	vw	CH out-of-plane bending

s = strong; m = moderate; w = weak; v = very; sh = shoulder.

Table 2.2 Vibrational Bands and Corresponding Bond Directions for Polyurethane [44].

peak position (cm^{-1})	assignment	block	α (deg)
3325	N−H stretching	hard	90
1615	C═O stretching	hard	78
1110	C−O−C stretching	soft	0

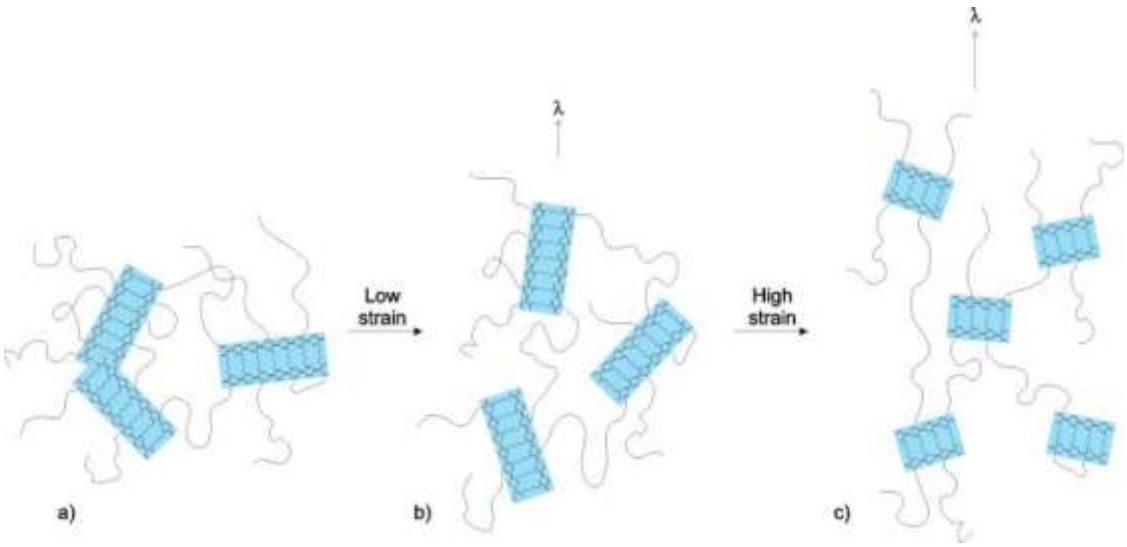

Figure 2.36 Schematic representation of molecular orientation during tensile testing at (a) non oriented, (b) below yield point and (c) above yield point [45].

Different effects on orientation by experiment conditions, material properties and additives are discussed in many studies. The hard segments orientation is highly dependent on strain history while the soft segments orientation is insensitive to it. The effect of temperature is reported being similar on both soft and hard segment orientations increasing gradually with increasing temperature up to 90°, the maxima after which decreases rapidly [45]. Annealing at submelting temperatures is found to enhance phase separation and lower average orientation of both segments [46].

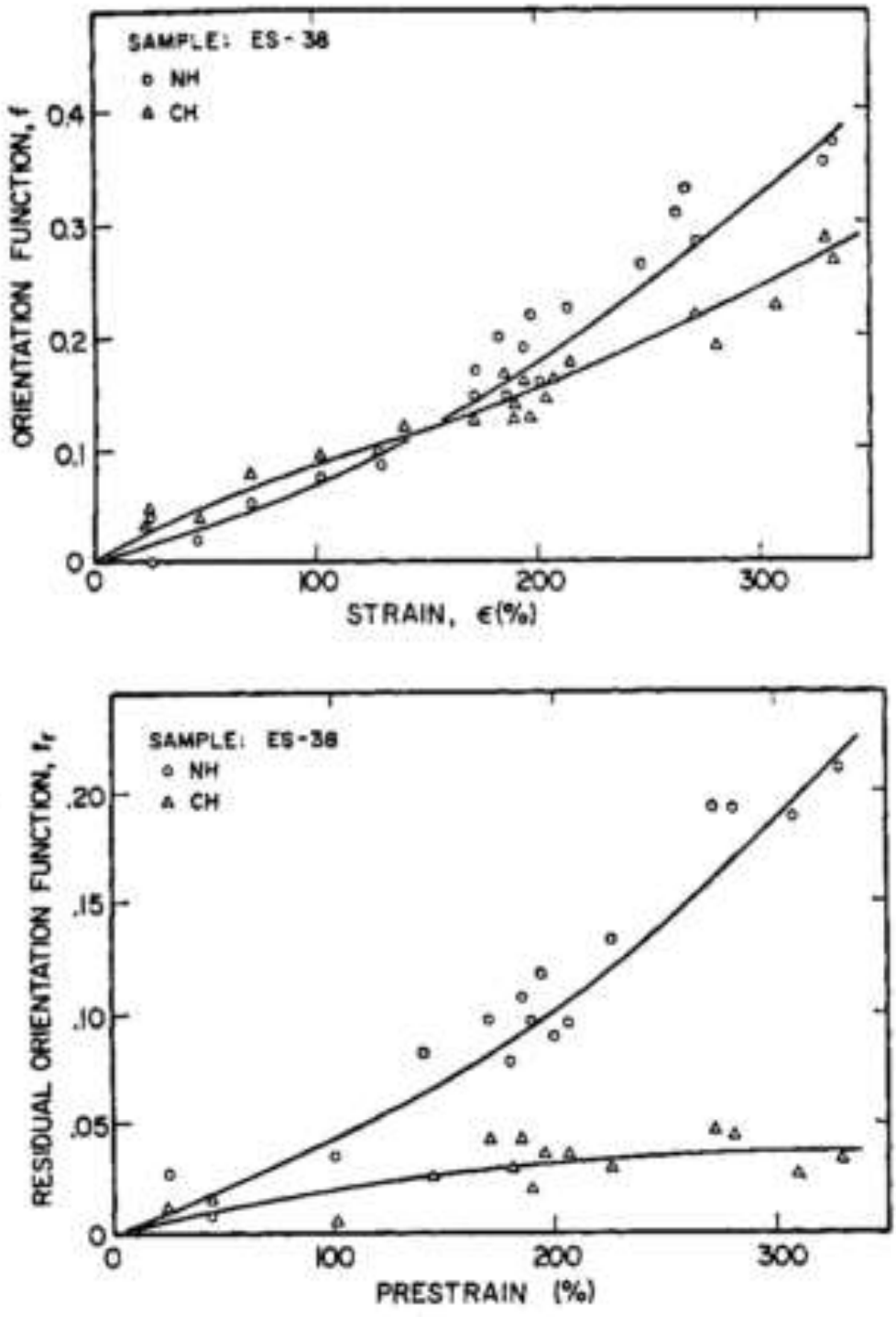

Figure 2.37 Orientation function versus strain levels for stretching experiments and prestrain levels for relaxation experiments [43].

The film thickness and nanoparticle presence are shown not to effect significantly the alignment of hard or soft segments [44]. Wang et al. investigated the effect of added plasticizer in polyurethane which disrupted hydrogen bonding in hard segment and decreased glass transition of soft domain and diminished ability of either domain to reorient [47]. All these orientation studies are done measuring samples after stretching or relaxation.

2.5 Biaxially Oriented and Heat Stabilized PET Films

PET is a condensation homopolyester made from dimethyl terephthalate (DMT) and ethylene glycol (EG). The molecular structure of PET is given below in Figure 2.38. Polyethylene terephthalate (PET) exists both as an amorphous and a semi-crystalline thermoplastic form, and can be made into a resin, fibre or film using various processing techniques. The semi-crystalline PET has good strength, stiffness and hardness while the amorphous PET has better ductility [48]. The amorphous PET can be prepared by quenching from molten state. The density of amorphous PET varies between 1.328 g/cm^3 and 1.341 g/cm^3 depending on the DEG content ranging between 1.83 and 14.90 mol % [49].

The PET crystal structure was determined first by Daubeny et al. [50]. The unit cell is triclinic and contains one chemical repeat unit as shown in Figure 2.39.

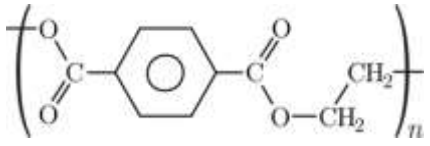

Figure 2.38. PET molecular structure.

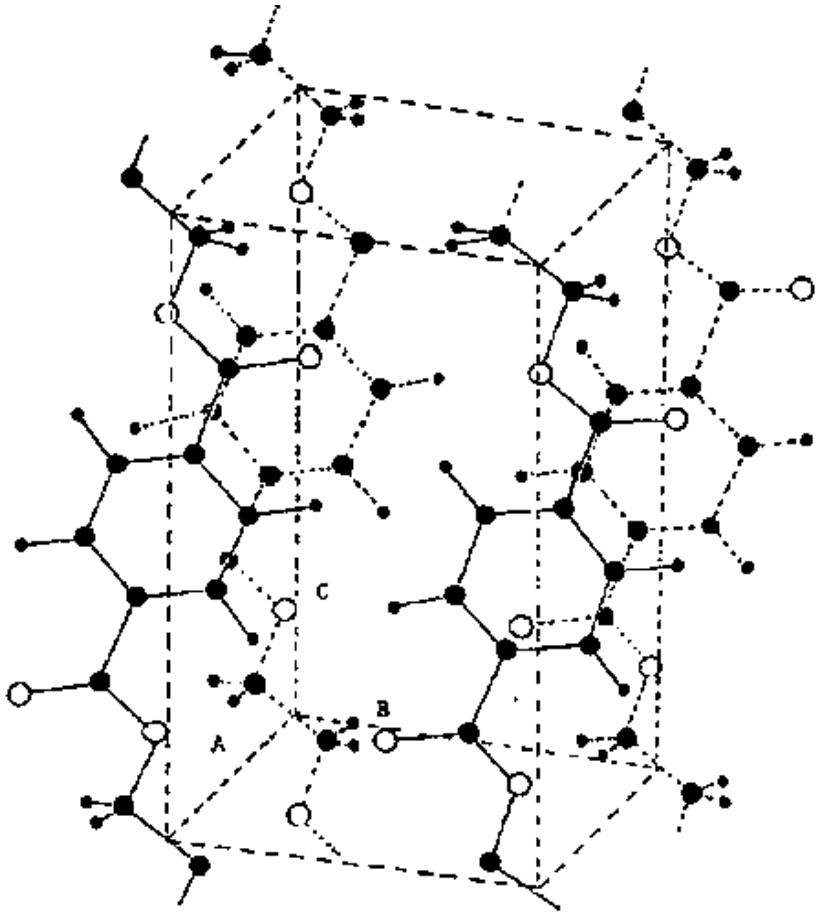

Figure 2.39 Unit cell of polyethylene terephthalate [51].

The unit cell density reported to be between 1.495 g/cm^3 to 1.515 g/cm^3 [52]. Fakirov`s studies on PET resulted the following unit cell parameters: a = 0.448 nm; b = 0.585 nm; c = 1.075 ± 0.004 nm; $\alpha = 99.5°$; $\beta = 118.4°$; and $\gamma = 111.2°$.

The glass transition temperature (T_g) ranges between 67° to 75°C and the melting peak occurs around 250°C for commercial PET. The melting point of virgin, fully annealed PET is 280°C [53]. Starting with amorphous PET, T_g increases up to a medium degree of crystallinity and thereafter drops with the further increase of

crystallinity [54]. Amorphous PET crystallization happens between 95° to 145°C. Higher orientation samples have lower crystallization temperature. Annealed at temperatures between the melting and cold crystallization temperatures additional endothermic peaks are observed as a result of melting and recrystallization of preexisting imperfect crystals to higher perfection and/or larger sized crystals [55, 56]. This peak is observed about 10 to 20°C above annealing temperature.

PET belongs to slow crystallizing polymer group. In this category polymer with relatively stiff chains with ordered chemical architecture. The overall kinetics of crystallization depends on the combination of nucleation density and crystal growth rate and one can always promote the nucleation density to increase the overall crystallization rate under the influence of flow (taking into account the effect of orientation on the change in entropy which in turn influenced the overall crystallization by reducing the critical nucleus size at a given temperature). However, under this condition the structure and properties of these polymers will resemble those of the rapidly crystallizing polymers like PE or PP. It is the influence of the slowly crystallizing kinetics plus the stress- induced crystallization on the structure and properties of the final products that is the determining factors for structural evolution. The crystallization rate of the slowly crystallizing polymers typically show a maximum at a temperature between the melting point and the so-called cold crystallization temperature which is the exothermic peak temperature during a heating scan of the differential scanning calorimeter. In the absence of nucleating agents and plasticizers, PET crystallizes slowly and is best used as fibers, biaxially oriented films,

and soft drink bottles, all of which presume a high degree of final orientation that imparts a satisfactory mechanical behavior to the finished articles.

PET as a slow crystallizing material has the ability to crystallize under strain. The crystallization induced by straining causes the film to be of a higher uniformity, increases its toughness and barrier properties. In order to monitor the effects of stress and strain on the PET behavior, many off-line and on-line techniques have been used.

Crystallization of polyethylene terephthalate has been investigated extensively in literature. One early example is studied in 1953 by Cobbs *et al*. They obtained infrared spectra and x-ray diffraction patterns on samples of PET films before and after heat treatment for 45 minutes at 195°C. Figures 2.40. and 2.41. show comparative results. The straight line in Figure 2.42. was found by the least squares method and shows proportionality between optical density and density for crystallization process [57].

Crystallization kinetics was studied by Avrami of the situation in terms of the probability of the appearance of nuclei per unit time and the rate of growth. On the other hand, typical DSC thermogram of non-isothermal crystallization of polyethylene terephthalate is shown in Figure 2.43 by Jeziorny [58]. He concluded that the morphology of crystalline structures forming as a result of non-isothermal crystallization, and the decisive factor is the cooling rate. By making appropriate changes in the cooling rate, the polymer morphology can be determined in a specific manner.

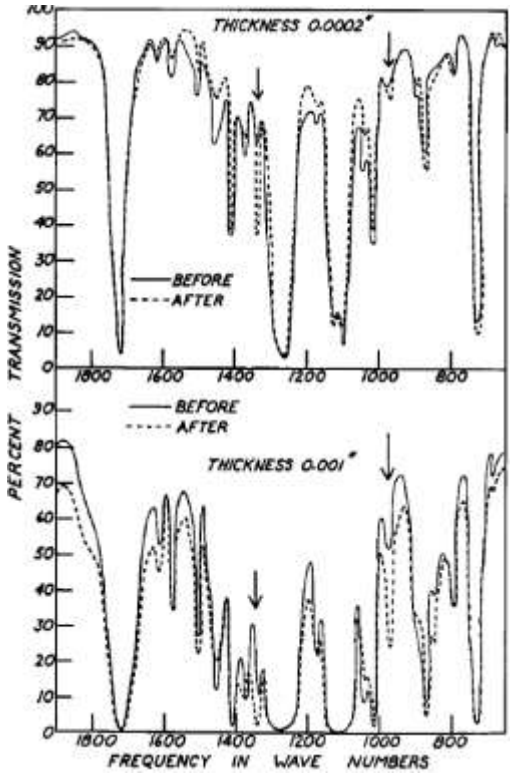

Figure 2.40. Infrared spectra of polyethylene terephthalate before and after crystallization

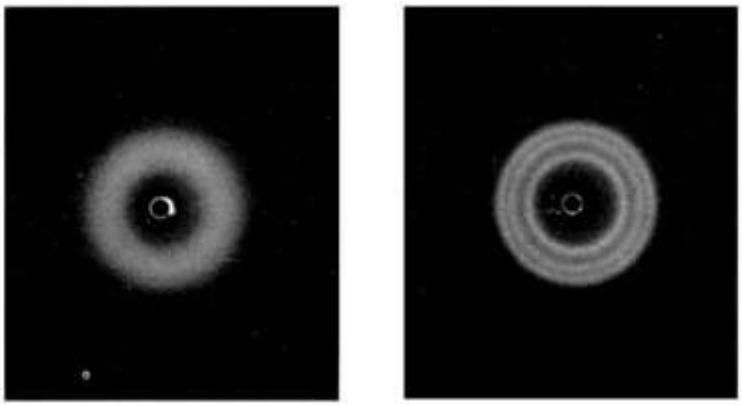

Figure 2.41. X-ray diffraction pattern of polyethylene terephthalate before and after crystallization.

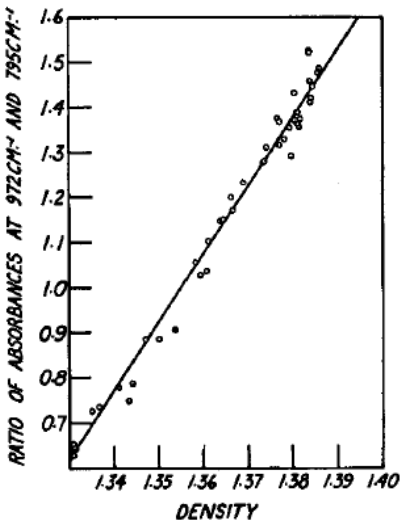

Figure 2.42. Relation between infrared absorption and crystallinity of polyethylene terephthalate, as measured by the density.

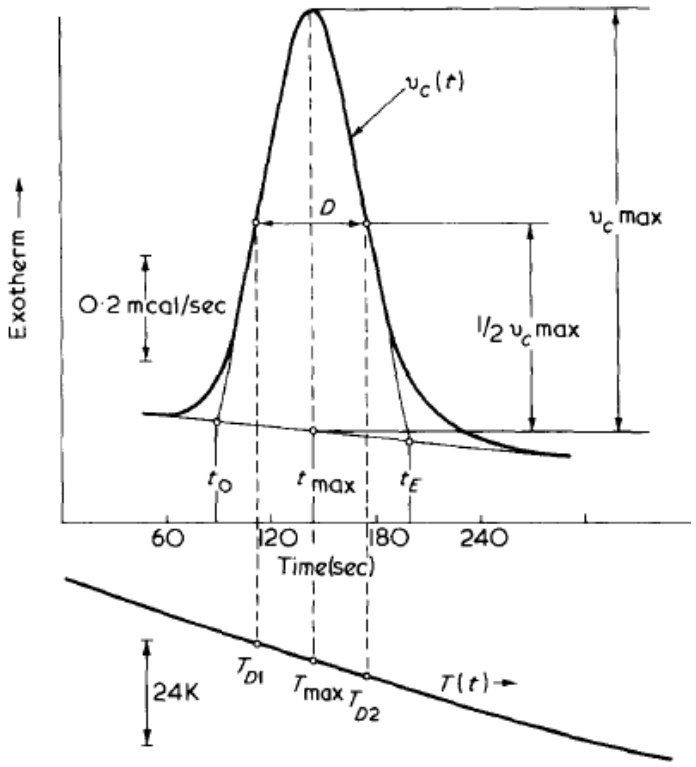

Figure 2.43. Typical DSC thermogram of non-isothermal crystallization of polyethylene terephthalate.

Yeh and Geil reported rotation, alignment and perfection on prefolded, paracrystalline structures present initially in amorphous domain as the result of PET crystallization [59].

Tentering process is used for processing predictable orientation PET film substrates to be used in electronics applications with strict specifications. Tentering process scheme is given in Figure 2.44.

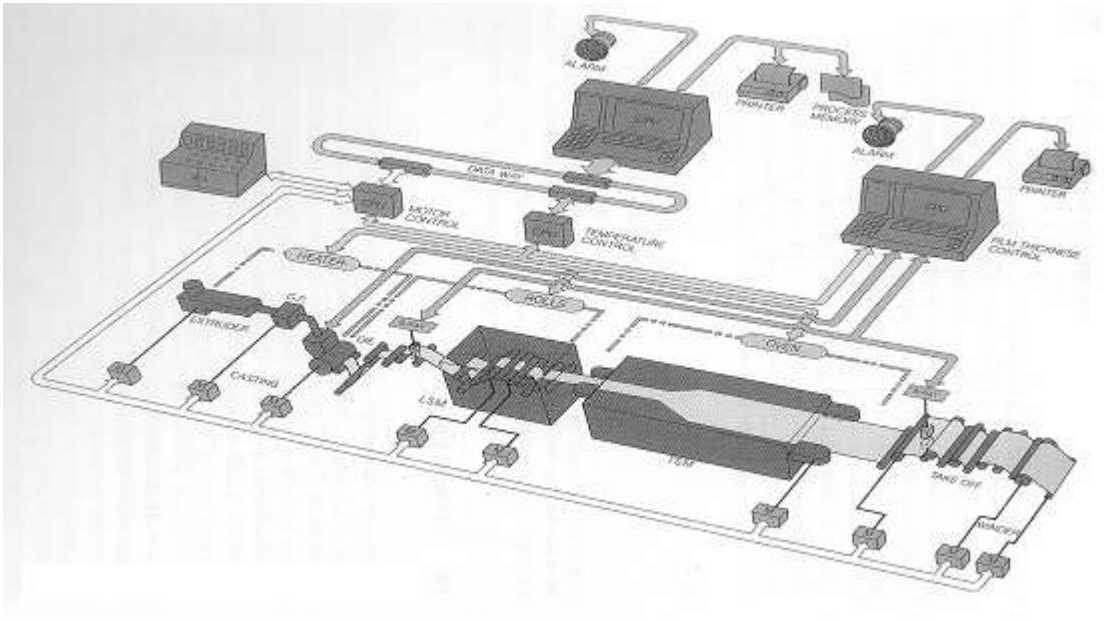

Figure 2.44. Schematic view of the tentering process [60].

In this process involves the following steps:

- PET extrusion from a sheet die;

- Quenching/cooling step;

- Orientation in machine direction between cooled rolls;

- Orientation in transverse direction grasped by tenterhooks into an oven.

The major difference with film blowing process is the ability to control orientation at each direction with limited the polymer rheology contribution. The long tenter oven residence time allows effective production for slow crystallization rate PET.

Sakamoto reported the changes of refractive ellipsoids in each part of stretched sample. The no orientation as cast film having sphere shaped ellipsoid changed to a side elongated structure in longitudinal stretching zone, axis of which rotates in transverse direction later with transverse stretching in Figure 2.45. Given this structure, Sakamoto concluded that isotropic film cannot be achieved with the process as local variations will be present even after heat setting [61].

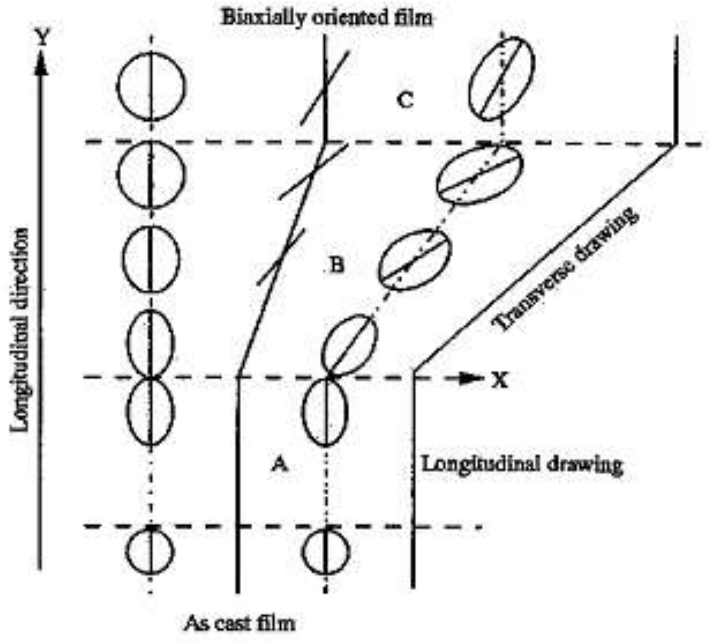

Figure 2.45 Changes of refractive index ellipsoids in each unit process.

Considering this process stretching PET at higher than its Tg, at low stretch rates the molecules can relax during orientation therefore, only limited internal stress can drive orientation and crystallization. Mostly, relaxation phenomenon dominates over orientation phenomenon and the strain hardening modulus is low. Spriuell show that at high stretch rates molecular orientation results in crystallization even if the crystallization rate is low compared to the disorientation action of low stretch rates [62].

Grolier *et al*. stated that there is a minimum strain level at which crystallization begins and develops in stages [63]. Figure 2.46 was suggested in this study to show microstructure formation and included strain hardening controlled by first stages of crystallization. The fully developed crystallization was shown to occur until relaxation end.

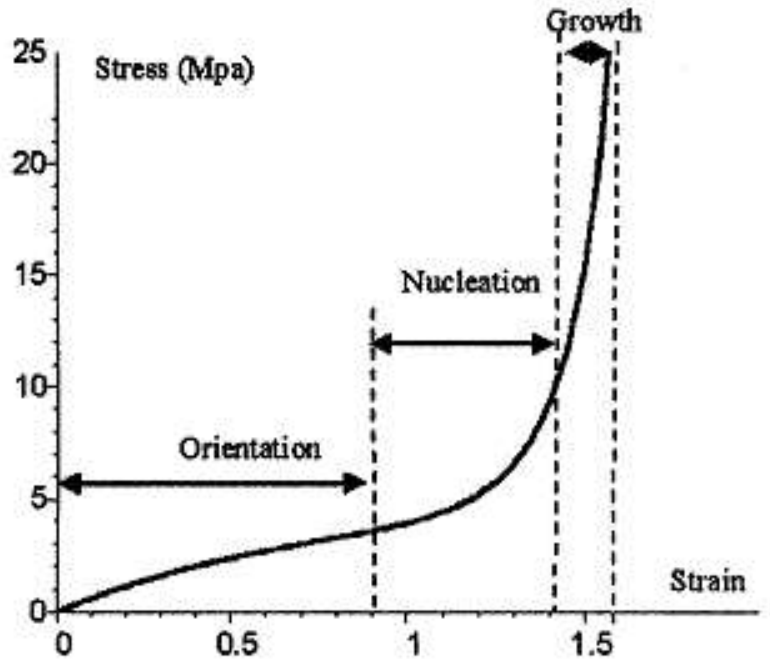

Figure 2.46 Schematic kinetics of microstructure development in PET [63].

Spriuell *et al*. showed that strain induced crystallites grow further with thermal crystallization [62]. This nucleating effect and orientation is reported to decrease by the strain rate applied prior to annealing. Constrained samples are also pointed out to have higher crystallization rates during this process than free shrinkage samples. Tereda and co-workers have reported the initial sheat-like structure in samples changes to rod-like fibrillar structures in annealed samples [64].

The annealing effect on PET has been also studied extensively to assess transition mechanisms of oriented amorphous structures to crystalline state, controlled orientation and structure-property relationships. Many researchers observed an increase of long spacing of drawn and annealed PET with annealing temperature [52, 63, 65]. Annealing was shown as source for increase in chain folding which was causing decrease in strength.

Cakmak showed that annealing does not cause a major reorganization of the structure only slightly perfects the structures developed initially by stress-induced crystallization [51]. SAXS patterns observations combined with WAXS analysis, he suggested staggered crystallite formation in the solid state due the phenyl planes becoming parallel to the surface of the films with deformation.

Thermal shrinkage control is very important for substrate films used in display electronics industry. Thermal expansion coefficient match of substrate layer with the display base material is desired to avoid delamination during thermal cycling tests performed to check device reliability. Most commonly these substrate materials are

prepared through biaxial stretching followed by heat setting, typically by tenter frame processes as mentioned before for mass production in industry.

Currently, PET retardation films for LCD applications are prepared with sequential biaxial stretching. Optical properties are tailored through the combination of deformation in machine (MD) and transverse (TD) directions at optimum stretching rate and temperature [66, 67].

The display substrate material candidates are also expected to meet many specifications for optical clarity, surface smoothness, good barrier as well as thermal performance especially minimal shrinkage [68]. The latter property can be minimized by dimensional stabilization using heat setting (annealing) as also previously mentioned. Processing conditions affect [69-74], morphology-orientation contribution [75, 76] to shrinkage as well as its kinetics [77] and models [78, 79] has been reported for various PET applications.

Sharma and Misra stated that the annealing increased crystallinity but added that the orientation trend and mechanical properties did not show any deviation from un-annealed samples [69]. Maruhashi and Asada evaluating structure-property relationship of biaxially stretch and heat set samples indicated that the draw rate governs crystallization properties [70]. Low draw ratio drawn sample do not show crystallinity increase with heat setting, mid draw ratio increase significantly and high ones only slightly increase with constant number of crystallites. Gupta studied constant length heat setting of stretched fiber and films to evaluate effect of thermomechanical response up to 20 seconds [71]. Shrinkage stress values were

shown to change based on draw speeds proportionally. Haworth characterized shrinkage in oriented PET films using thermomechanical analysis and concluded that magnitude of shrinkage increases with draw ratio but the heat setting effect was not discussed [72]. Panagiotis *et al*. recently reported on thermomechanical shrinkage measurements of annealed films [73]. Vallat and Plazek studied thermal treatment of biaxially stretched samples from room temperature to 140°C and reported shrinkage and coefficient of thermal expansion in different axis [74]. Reversible physical aging cooling down PET from Tg to low temperatures, creep rates decreasing with residence time below Tg were discussed for semi-crystalline samples. Two different probe penetration behavior: first related to shrinkage at glass transition temperature and second to continuous softening and reorganization of sample. Murthy et al summarizes the role of oriented amorphous phase on fiber strength and shrinkage using x-ray diffraction [75]. They concluded that shrinkage is determined by amorphous phase orientation but also their connectivity to crystalline phase governs the strength. Gohil studied simultaneous and sequentially biaxially stretched PET film morphology property relationship [76]. He stated two important factors, in-plane crystalline orientation and the nature of crystallites plays important role in obtaining isotropic in-plane shrinkage/expansion properties. Pakhamov *et al*. determined molecular mechanism of shrinkage for amorphous oriented PETP using IR technique [77]. They conducted shrinkage kinetics analysis and found cooperative conformational regrouping in an intermolecular force field. Shih modelled shrinkage behavior of oriented PETG shrink films [78]. The effect of stretch temperature, stretch ratio, and stretch rate on the shrinkage characteristics of oriented PETG film was also studied.

The stretch temperature was found to have highest influence on the shrinkage. Bhatt and Bell also studied thermal shrinkage of oriented PET filaments. Thermal shrinkage force and optical anisotropy was given as a function of stretch and the behavior explain based on theory of rubberlike elasticity [79]. However, none of these previously reported works to understand shrinkage are coupled with real-time mechano-optical property monitoring technique.

CHAPTER III

INSTRUMENTED FILM-INSERT COMPRESSION MOLDING FOR LENS ENCAPSULATION OF LIQUID CRYSTAL DISPLAYS

3.1 Introduction

Full color, reflective, bistable, lightweight and flexible cholesteric liquid crystal displays were introduced to the market offering numerous applications such as electronic skins with real time switchable colors for consumer device cases, walls and windows. They add an ultimate personalization feature to the application area and device by providing a discrete color with the advantage of low power consumption. For the current use, plastic/glass film lenses are hand laminated on the displays with a pressure sensitive optical adhesive for increased protection and ease of application. However, this process is a labor intensive process, increasing the production time and failing to encapsulate the edges of the displays as it involves only adhesion of the lens on the display. Therefore, there is a need for a more economically viable process to create fully protective display encapsulations allowing use in rigid and flexible applications. The injection molding process can be considered as a good candidate for encapsulating the displays, although

the process complexity is likely to cause challenges to be resolved. Encapsulation application demands for the film-insert injection molding technique however, the traditional injection molding would generate over the limit pressure values on the delicate display elements.

In the film-insert injection molding (FIM) process, the molten polymer is injected into the mold cavity where one side of the mold wall is insulated by a pre-attached film. FIM is a cost and time-effective technique eliminating various post-processing procedures (screen printing, spray painting, laminations etc.) and improving surface quality as well as durability. Many products such as automotive interior parts, cellular phone cases, logo designs on plastic products are produced using FIM method [29, 30]. Adhesion between the film and the substrate may be enhanced using this process as the injected hot molten resin can partially melt the film [80].

Disadvantages of the FIM process include the possibility of washing off the printed ink on the film, unexpected weld line, wrinkling of the film, warpage, and uneven part shrinkage [29]. Traditional injection molding process creates residual stresses due to shear and extensional flows within the process. During packing, high pressure and during solidification and cooling, thermal stresses are imposed on the part as previously mentioned; and thus, it causes deformation. The FIM process interrupts heat transfer in perpendicular direction to the cavity wall, which causes very severe residual stresses on the part. This asymmetric residual stress distribution is shown to result in extreme warpage and non-uniform shrinkage [29, 30]. The effects of injection molding conditions such as injection speed, melt temperature, mold temperature, packing time, and pressure on viscoelastic behavior and deformation of film insert molded parts, were investigated in

many studies [10, 29-31]. Beak *et al*. reported their work on warpage of polycarbonate, acrylonitrile-butadiene-styrene (ABS) substrates, and polymethylmetacrylate (PMMA) films [10]. Film inserts were annealed at higher temperatures to minimize the effects of thermal shrinkage and residual stress on warpage of the final parts; the thermal expansion coefficients were calculated and compared for annealed and non-annealed films [10, 29-31]. Effects of film and substrate thicknesses on warpage were investigated in detail. In the above mentioned studies, warpage reversal phenomenon (WRP) was also observed and presented as the combined effect of the thermal shrinkage of inserted film and the relaxation of residual stresses in FIM part during annealing. Annealing was found to affect warpage variation more than any other injection molding parameter [10]. It is clear that warpage will be a major problem for the rigid lens encapsulation of displays. As a solution to this problem, injection compression molding (ICM) process was introduced to reduce the pressures exerted on the part.

In recent years, manufacturing of precision plastic optical parts for high-quality parts such as lenses and disk substrates by injection-compression molding processes gained popularity. These are a combination of the traditional injection molding process and the compression molding process. There are many devices produced by traditional injection molding, from automotive parts to medical sensors; however, there are disadvantages involved in using this technique for making optical parts, such as high injection and packing pressure, uneven shrinkage, warpage, residual stress, and sink marks [12]. Optical birefringence is an outcome that significantly reduces optical performance (*e.g*. double-vision) of an optical electronic device -for instance, liquid crystal display- due to residual stresses brought about during the process. In the

compression molding process, the molten polymer is compressed by the moving platen to flow into the cavity. The pressure produced in this process is more uniform along the cavity wall, and lower for post filling stage, and therefore results in less residual stress as well as less part warpage [12, 14]. Drawbacks for this method include low productivity due to the time-consuming charging step, and the limitation for producing large complex shaped parts. The injection compression molding differs from traditional injection molding in terms of cavity filling, where there is further melt flow and reduction of cavity volume during the packing step. The compression stage after the partial melt filling of the cavity decreases the mold pressure and clamp tonnage by 20 to 50 %, and reduces the cycle time and residual stresses [81]. The process is also reported to allow even packing, and thus, lower uneven shrinkage and warpage [15]. High-precision optical parts manufacturing via injection compression molding is presented in both experimental and numerical forms in the literature for various cases [17-20]. Studies conducted on molding optical lenses concluded that the parts had better quality compared to the traditional injection molded parts at the same cooling time [17, 19]. The injection compression molded disks (e.g. CD-R) are shown to have enhanced dimensional accuracy on the direction perpendicular to the compression, as well as improved conformity to cavity profile and reduced warpage [18, 20].

The objective of this research is to introduce a new combination of processing method, film-insert injection compression molding (FICM) for lens encapsulating displays and to investigate the process effect on transparent polyurethane lens encapsulation of cholesteric liquid crystal displays (Figure 3.1). The displays are composed of an electrical tab with kapton tape, a PET layer, a conductive coating,

polymerization induced phase separated LC layer, a conductive coating, a PET layer and a thin layer of carbon coating for light absorption. A hybrid method developed to encapsulate displays is considered to reduce production time and allow full protection of the display, including display edges, as a better alternative to the currently used hand lamination technique. The goal is to encapsulate displays with a lens without delamination or damage to the liquid crystal layer and the electronics of the display. Therefore, our primary focus is to optimize processing conditions while maintaining the integrity of potentially compressible display layer of 80 + % liquid crystal domains. For this purpose, a highly instrumented interchangeable cavity mold was designed and built; the effect of different process conditions on final part quality was investigated along with the design of experiments for warpage optimization. A variety of grades for polyurethane lens encapsulations are presented to find use among the current rigid market applications and to foster flexible future applications of these liquid crystal displays. The potential display substrates, PET and PEN, and their thermomechanical properties were also discussed to explain lower warpage results.

3.2 Experimental

3.2.1 Materials

3.2.1.1 Display

The display PET layers were heat stabilized and supplied by Dupont. The 51 μm PET film was used as substrate material in all displays except the optional 127 μm PEN substrate displays. In some displays, 178 μm PET or 127 μm PEN was laminated for extra protection of the liquid crystal layer. The conductive coating

on the substrate layers, carbon the black back coating, and the acrylate encapsulated cholesteric LC with spacers for the entire display device assembly, were prepared by Kent Displays Inc. The substrate layers were laser singulated for complete sealing of the device.

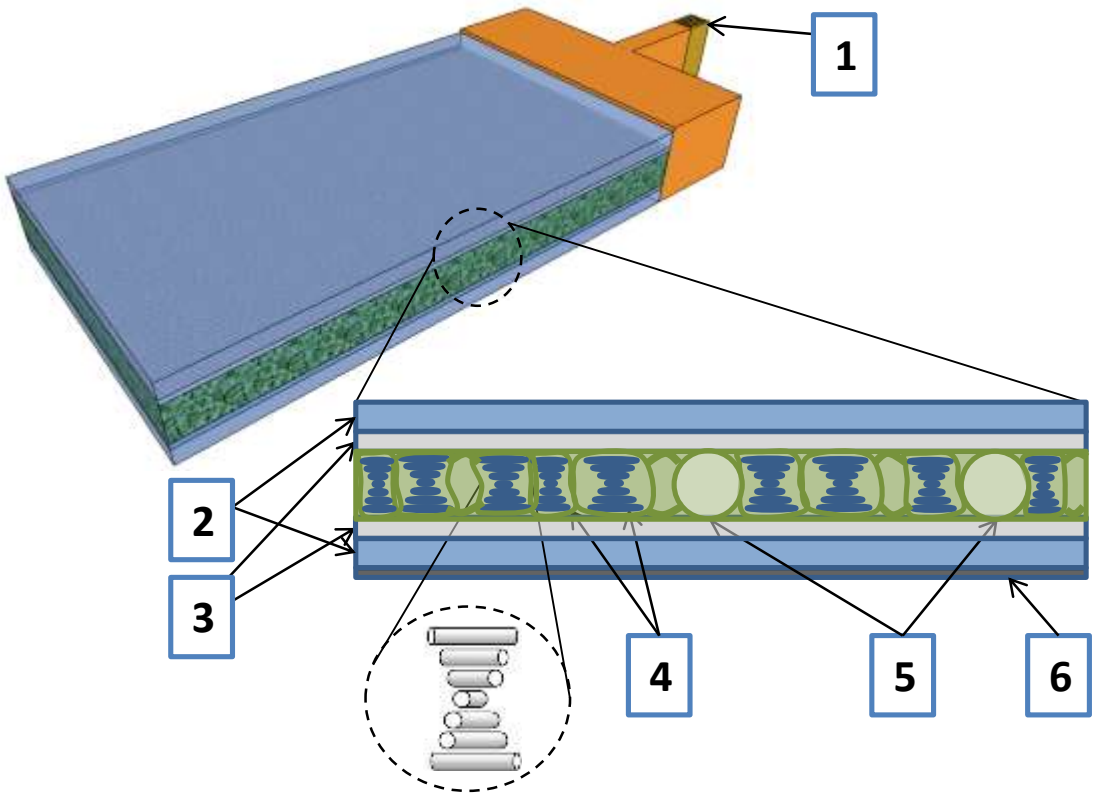

Figure 3.1. Components of the LCD display: cross-sectional view of rectangular (8 x 4 cm) display with one has electronic "tab" for electronic switching (1), PET (2) and conductive layer (3), acrylate encapsulated cholesteric LC(4), separator beads (5) and absorbing carbon black coating (6).

3.2.1.2 Injection Molding Materials

In order to encapsulate the LCD display, a range of thermoplastic polyurethane from flexible to rigid was used as lens material. Three grades of ε-captolactone based thermoplastic polyurethanes with 87A, 57D, and 65D shore hardness were supplied by Lubrizol Corporation (Table 3.1). These TPUs were selected in order to ensure good adhesion to PET and PEN display substrates through polar interactions such as hydrogen bonding. The reported surface energies of 43.9 mJ/m^2 and 39 mJ/m^2, respectively for the PET substrate and the selected TPU, support this information [82]. This class of materials also has excellent low temperature properties, high transparency, low melt temperature, hydrolysis and UV resistance.

Table 3.1. Some properties of thermoplastic polyurethanes as lens material [83].

Lens Material	**Hardness**	**Melt Flow Index** (g/10min @175°C, 2160g load)	**Specific Gravity**	**Tensile Strength (psi)**
Low viscosity TPU	87A	5.00	1.12	9350
Medium viscosity TPU	57D	3.20	1.15	9350
High viscosity TPU	65D	2.00	1.11	9200

3.2.2 Methods

3.2.2.1 Mold Design and Instrumentation for Data Acquisition

A prototyping mold was designed as shown in Figure 3.2 to be used both as film insert and injection compression mold. The mold had a female (Mold A) and a male (Mold B) part to prevent flashes during injection compression molding. Mold A consists of an interchangeable female cavity with inner edge vacuum vents for holding the display on the cavity wall, and adjustable shims allowing the production of center or edge gated lens encapsulations with different thicknesses ranging from 0.5 mm to 2 mm. The vents on this side are also used with air compression to eject the sample at the end of process, instead of ejector pins that would potentially damage the device. Mold B consists of an interchangeable male core with Teflon squeeze insert to prevent flushes onto electronic circuit attachment of the display, and a hydraulic three zone pin gated hot runner. A PETS hot runner system with flush mount small diameter pin gate was used in the system. The center gated lenses were designed to be used in parts having logos in the center to close the gate mark. The PETS hot runner system allows the melt to be at lowest viscosity when it reaches the cavity to exert reduced flow pressure on displays. The mold temperatures can also be controlled with water mold heating/cooling units from Polymer Processing Equipment. In order to investigate the dynamics of injection molding parameters during the full cycle of injection /compression molding, an instrumented injection molding machine and the mold cavity shown in Figure 3.2 (1 - 4) were designed.

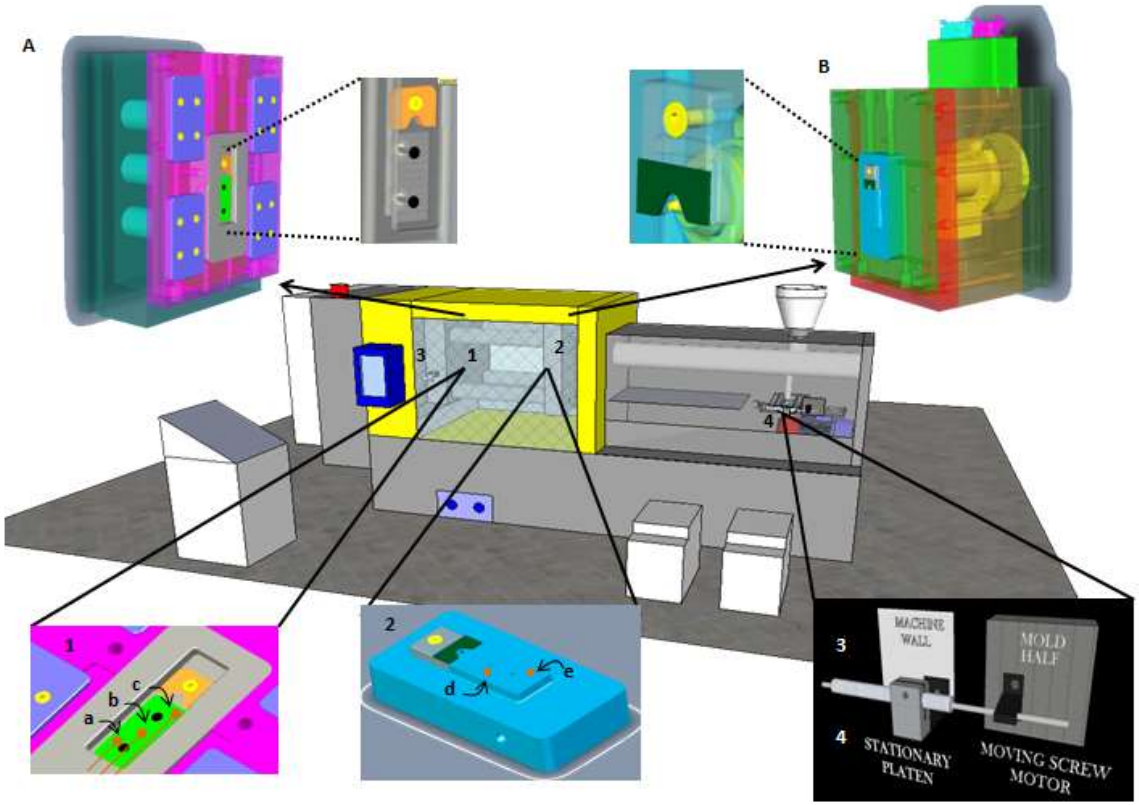

Figure 3.2. Film insert injection compression molding unit: (A) interchangeable female cavity with inner edge vacuum/air compression vents and adjustable shims, (B) interchangeable male core with Teflon squeeze insert and hydraulic 3-zone pin gated hot runner and the instrumentation of (1) thermal monitoring of the display with 3 thermocouples at the cavity side, (2) melt pressure monitoring with 2 pressure transducers and (3) mold and screw movement monitoring LVDTs.

The real time process control hardware and software consists of:

- three 0.08 mm Omega Insulated Thermocouples with Stripped Leads (Figure 3.2 (1)) that can be placed on Mold B cavity wall-PET substrate (a), PET substrate-LC layer (b), PET substrate-PU melt (c) interfaces for temperature monitoring on every layer. These locations are expected to show the temperature changes in each layer of the display during the injection process, which helped us identify and solve the problems caused by the experienced complex thermal history.
- two Kistler flush mounted Unisens® Quartz Cavity Pressure Sensors (Figure 3.2 (2)) controlled by an ICAM voltage amplifier unit for pressure monitoring, flush mounted on the mold core side.
- two Schaewitz LVDTs placed respectively, on mobile mold half (Figure 3.2 (3)) and screw motor (Figure 3.2 (4)) for compression and material flow monitoring.
- a Labview program software to get the signal outputs and plot the results.

The Milacron Roboshot S2000i110B electric injection molding machine with these modifications was used in pre-injection mode to work as an injection compression system where the material is injected while the mold continues to close after designated pre-touch point.

3.2.2.2 Processing Steps

The single and double side encapsulation steps are shown on Figures 3.3 (A) and (B). The display is first placed and held in the cavity by the vacuum system. The injection cycle starts with the mold movement, when the desired pre-touch

mold position as set parameter is reached; then the clamp compression starts, and material is injected at the touch position set on the software (Table 3.2). The melt is compressed during and after injection until the mold is entirely closed. The pin gate movement for the hot runner is controlled by a hydraulic system according to the preset time (Table 3.2). After the cooling cycle, the mold reopens and the sample is ejected out of the cavity using compressed air from the vents. The single side encapsulated sample is reversed when a double side encapsulation is required, and the shim thicknesses are adjusted to inject the second side with the same process steps.

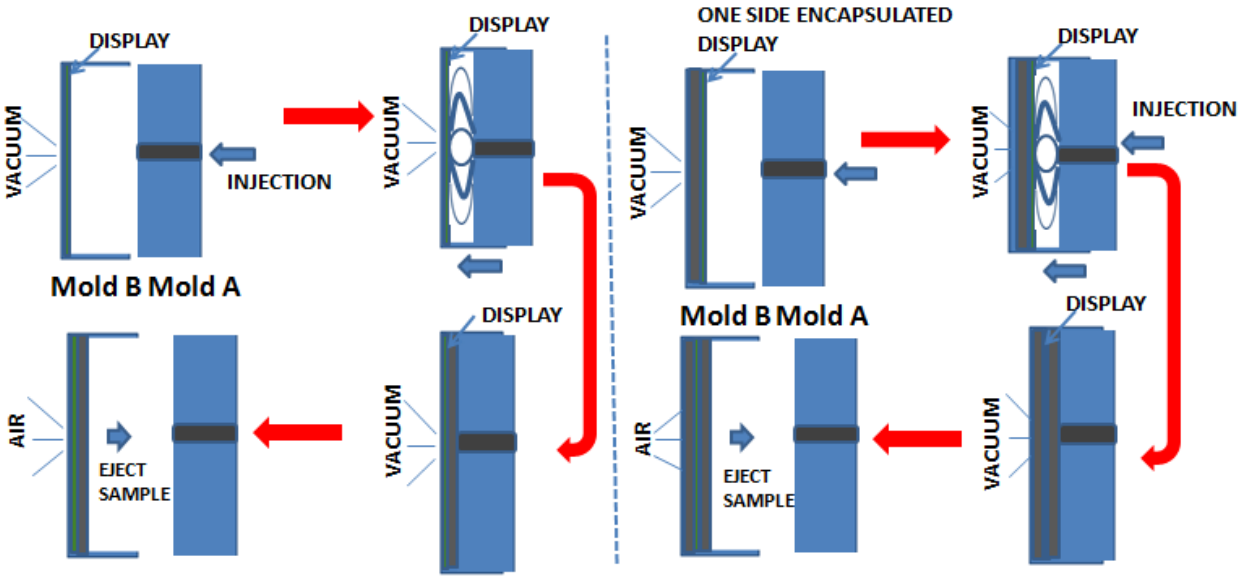

Figure 3.3. Single (A) and double side (B) display encapsulation steps

3.2.2.3 Process Conditions

The processing conditions used in these experiments are summarized on Table 3.2. The "standard conditions" designated on the table with an asterisk (*) were kept constant while others were altered in ranges for various optimization experiments in Milacron Roboshot S2000i110B electric injection molding machine software.

The mold temperatures are different for plate A and B due to the fact that mold A is insulated by the plastic display insert, and therefore, cools down slower than mold B. The mold B is always kept at a higher temperature to approach near symmetrical cooling.

Table 3.2. Processing conditions

TPU Type	**Low Viscosity**	**Medium Viscosity**	**High Viscosity**
Melt Temperature, (°C) *	180	185	190
Mold Temperature, (°C), (A/B plate) *	30/60		
Injection/Packing Pressure, (psi) *	15000/7500		
Injection Speed, (mm/sec)	10/20*/30		
Shot Size, (mm), (first side/second side)	10-15*/8-12*		
Pin Gate Opening Time, (sec)	2*-7		
Compression Positions, (mm)	0-1*		

*Standard conditions

3.2.2.4 Thermal Analysis

A TA Instruments Q400 thermal mechanical analyzer (TMA) was used for measuring dimensional changes in the substrates of 7 mm length and 3.5 mm width as a function of temperature. The force applied to the sample was 0.05 N, and heating and cooling rate during the TMA scan was 25°C per minute and 3 °C per minute, respectively, to simulate the in-mold temperature change kinetics. The results are normalized for real display sizes of 7 cm length to 3.5 cm width.

3.2.3 Warpage Calculation

The samples were stored for 48 h at the ambient temperature in order to relax residual stresses after injection molding. The warpage was measured by a micrometer with an accuracy of 0.01 mm. The calculation for radius of curvature is shown in equation (1) where L is the length of the sample from one end of the curved edge to the other, and H is the warpage measured. Average value from three samples was recorded for each molding condition for accuracy of measurement.

$$R = \frac{\frac{1}{4}L^2 + H^2}{2H} \qquad (1)$$

Higher radii of curvature mean flatter samples, and thus, lower warpages. On Figure 3.4, the arc 2 has a smaller curvature compared to arc 1 and a higher radius of curvature, explaining the inversely proportional relation in the previous statement.

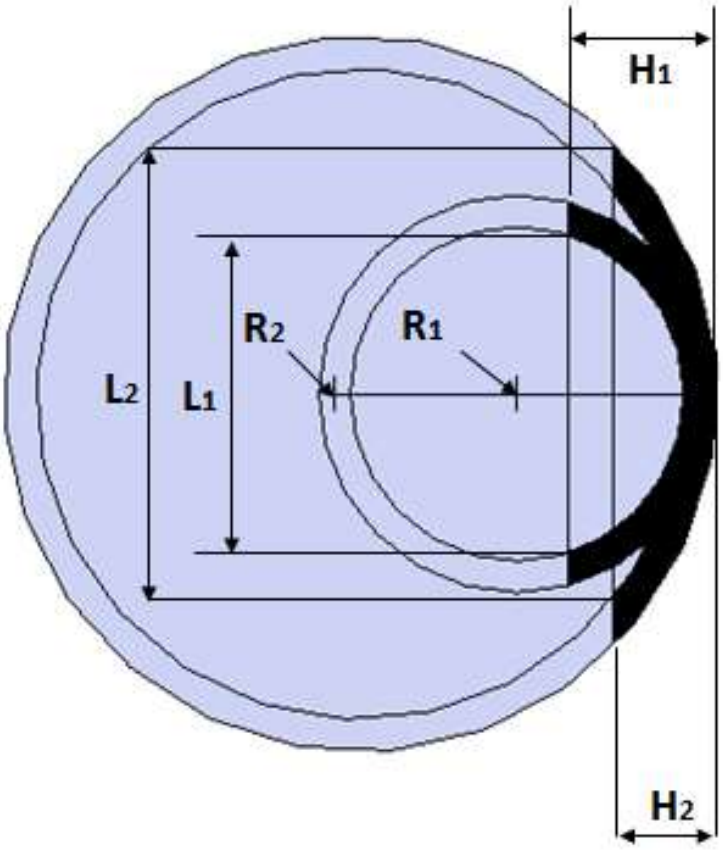

Figure 3.4. Radius of curvature comparison

3.2.4. Taguchi Method

Taguchi method is used in order to locate optimum parameter settings for quality improvement of this application. As warpage is a major problem especially for thin wall parts with non-symmetric cooling, this optimization technique is a common way to get effective process parameters [84-86]. The orthogonal array experiments produce a reduced variance for the experiment consisting of the selected optimum parameters with a small number of experimental trials. The quality indicator in these experiments is the signal to noise ratio reflecting both average and variation of desired property of

the product. It is used to evaluate effect of changing parameter on the product performance. Evaluation of the S/N ratio is based on the standards of "lower the better", "nominal the best" or "higher the better". In this study, lower warpage therefore, higher radius of curvature is expected. Thus, lower the better standard is chosen for the S/N ratio characteristic calculated as below.

$$S/N = -10\, log_{10}\left(1/n \sum 1/y_i^2\right)$$

Where y_i is the value from the performance/quality characteristics, radius of curvature in this case, for i^{th} trials, n is the number of repetitions for one trial.

Considering eight controllable processing parameters with three levels (Table 3.3), the L18 orthogonal array was used for this experiment.

Table 3.3. Process parameters and their levels.

Parameter #	Parameter	Level 1	Level2	Level3
1	Melt Temperature (°C)	185	190	195
2	Mold Temperature (°C)	50	60	70
3	Injection Speed (mm/sec)	25	30	35
4	Packing Pressure (psi)	7000	7500	8000
5	Packing Time (sec)	5	7	9
6	Cooling Time (sec)	25	30	35
7	Compression Position (mm)	0	0.5	1
8	Pin Gate Open Time (sec)	2	4	7

3.3 Results and Discussion

In this research, the LCD device was placed on the wall of the mold core cavity, held in by vacuum (Figure 3.5) and a melt stream was injected either from electrical tab end or from display center, the mass of material flows along the cavity until complete filling with the action of injection and compression. Since the cavity side is insulated by the display, the frozen layer formation becomes asymmetric and thinner against this surface due to slower cooling compared to the core mold wall side where melt directly contacts the mold surface as it flows into the cavity. Therefore, the mold core side

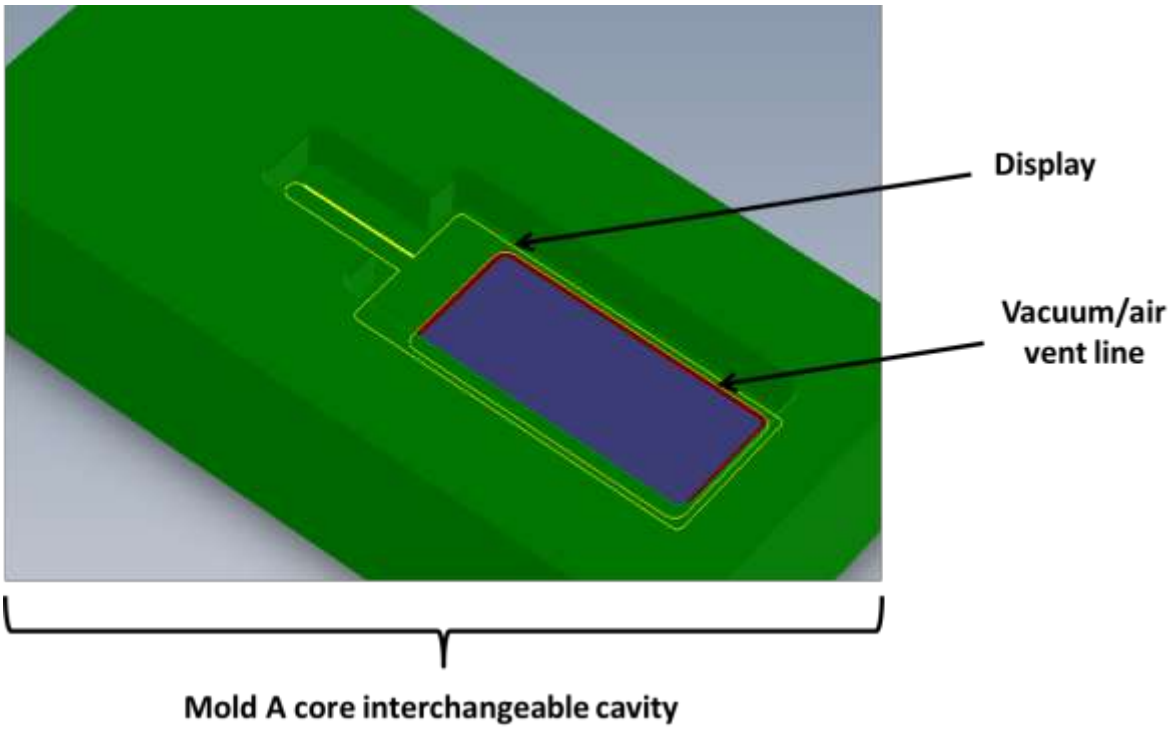

Figure 3.5. LCD device inserted in core cavity (yellow contour) and held by vacuum vents (red line).

temperature was set 20°C higher than the cavity side to be able to reduce the asymmetrical heat distribution and resulting warpage.

The real-time process monitoring elements in this mold allowed us to monitor each step of the process closely as stated previously. The mold and screw movements and pressure changes are shown on Figure 3.6 below for standard process conditions of the flexible low viscosity TPU. The process starts with mold closing (Stage I). A and B sides gets engaged (Stage II), pin gate opens at set cavity gap and material flows into the cavity where the first pressure transducer records the first peak (Stage III). The material continues to flow with compression towards the end of cavity and pin gate closed (Stage IV). Finally, the pin gate opens for a second cycle, where the pressure rises for both sensors near gate (up) and flow end (down) locations, and the mold closes (Stage V). For later stages, pin opening and mold closure can be modified according to the selected material, maximum pressure allowance, and packing criteria. Pressure peak profiles are closely related with the pin gate open/close cycles as seen here in Stages VI and VII where the pin gate closes first and an immediate pressure decrease is observed and followed by a new pressure peak at reopening. Peak values can be controlled easily by changing shot size, pin gate open/close cycles, cavity gap, lens thickness, and material (Figure 3.7). The higher viscosity TPU injection generated a higher pressure profile as expected. The selection of a lower viscosity TPU has the advantages of getting lower pressure profiles as well as lower melt temperatures compared to higher viscosity TPU. Shot size and pin gate cycle adjustments have a significant impact on the pressure control, and by varying them not only the profile height but also the width can be controlled. The comparison of single and double side lens encapsulation cases justifies

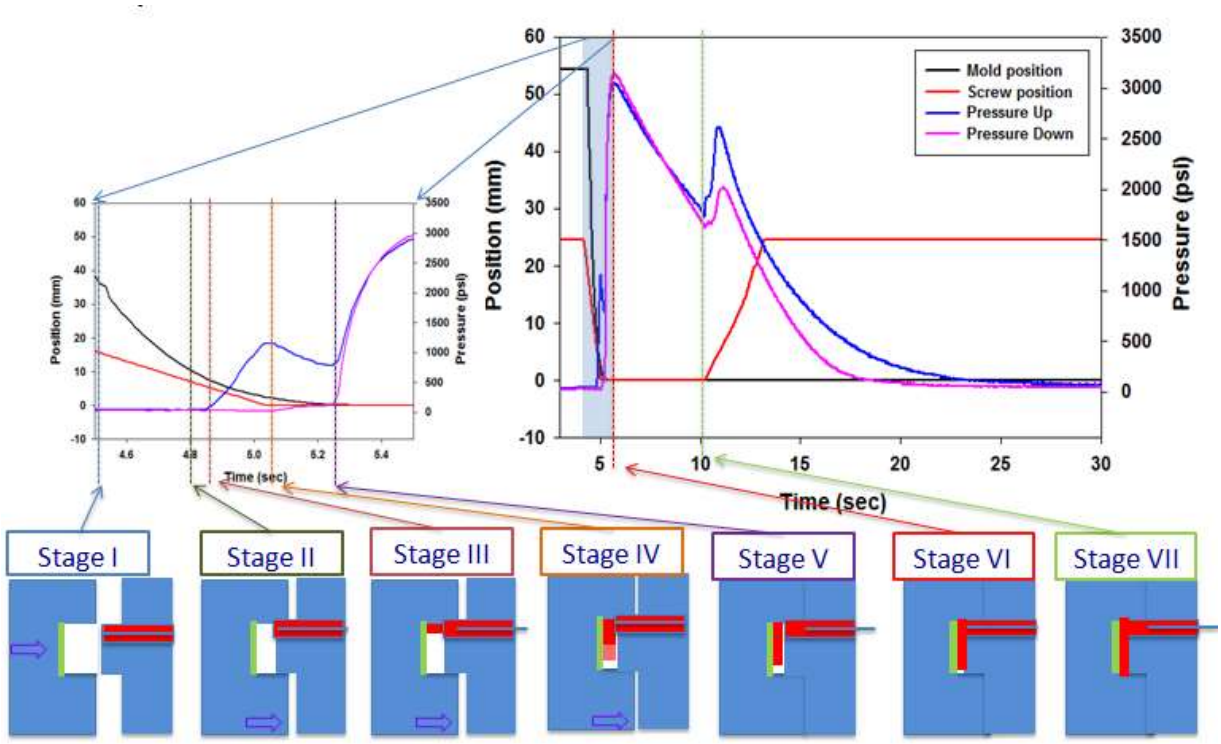

Figure 3.6. Process steps monitored by implemented instrumentation in FICM.

that pressure exposure can be diminished by a factor of two if the pin gate cycle and the shot size is reduced as shown on Figure 3.7 graph (b). The final lens thickness effect on pressure profiles is shown on Figure 3.7 graph (c) where with higher lens thickness, higher pressure trend behavior is observed. Although for the thicker lens there is more space in the cavity gap, the increased amount of material (shot size) that enters in the cavity causes increased pressure values. Similarly, thinner the display to be encapsulated for a fixed final lens thickness (Figure 3.6(d)), lower is the pressure profile recorded. These observations allowed us to understand the residual stress development on parts depending on the pressure history. Detailed comments on the warpage behavior will be found further below.

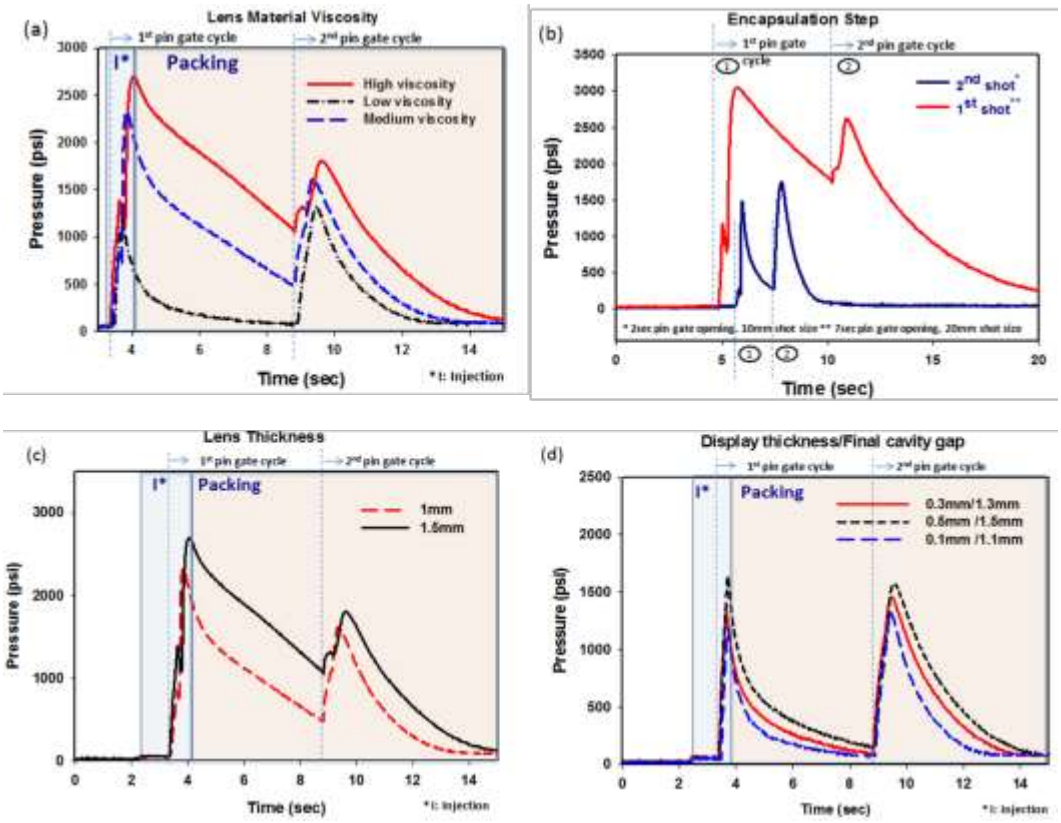

Figure 3.7. Pressure profiles for different lens materials (a), process settings such as pin opening time and shot size (b), lens thicknesses (c), display substrate thicknesses (d).

Pressure control is crucial since the LC display contains as much as 80% low molecular weight liquid crystal in compartments surrounded by an acrylate polymer matrix, and therefore does not exhibit high mechanical integrity under compression. The acrylate encapsulated LCs may be damaged if pressure exceeded the separator bead support tolerance (Figure 3.8). It is observed that the maximum pressure that can be used in this process to maintain the display integrity, or in other words, to prevent liquid crystal destruction, is 3000 psi for regular displays and 4500 psi for displays with PEN

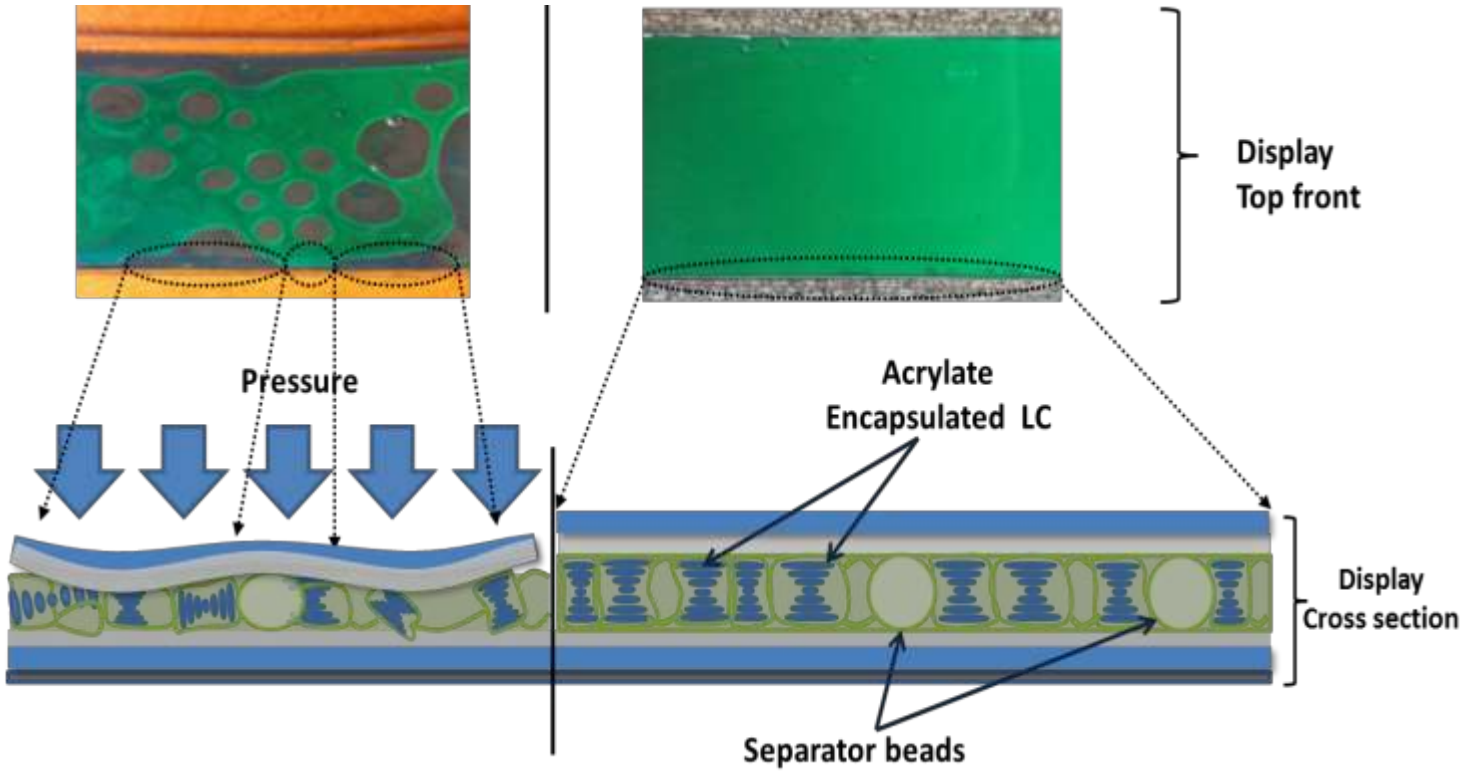

Figure 3.8. Pressure effect on the liquid crystal display.

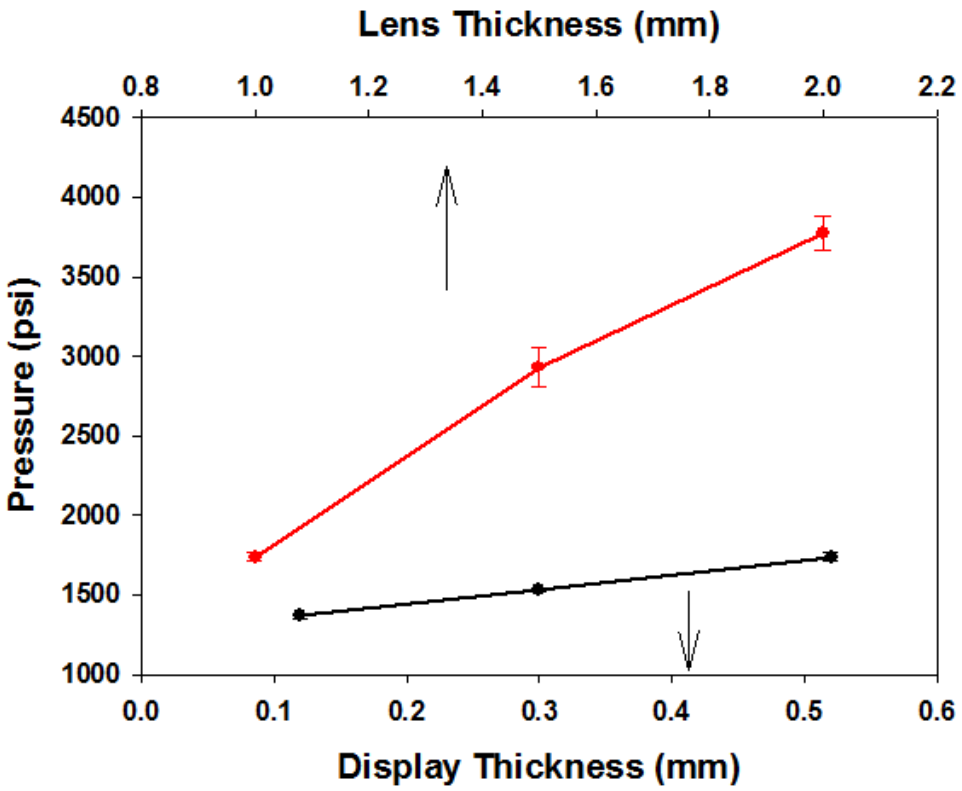

Figure 3.9. Maximum pressures experienced on successful parts for different lens and display thicknesses.

substrate. The highest pressure experiment at 6500 psi did not cause any damage on the extra 178 µm PET or 127 µm PEN laminated samples. Maximum pressure experienced on successful parts for different lens and display thicknesses are given on Figure 3.9.

During this process, a spatio-temporally complex series of events occurs. The surface facing the melt heats up, sets up a thermal gradient across the thickness with one side being the insulating molten plastic insert and the other side the metal mold wall. Furthermore, the rest of the surface is heated as the melt flows along the cavity, establishing thermal gradients. The temperature varies along the display length and through the thickness direction and is monitored by the real-time temperature

measurements showing this complex thermal history (Figure 3.10 and 3.11). Near gate and middle sections of the display substrate faces temperatures higher than its glass transition temperature (72°C) during the injection step. In contrast, the end section receives melt flow at lower temperatures as shown on Figure 3.10. Additionally, a comparison of Graph A and Graph B reveals that the inner layer point of the display experiences lower temperatures than the outer layer at same location at the same time frame. This causes differences in expansion/shrinkage behavior at different layers in the thickness direction of the display. The complex thermal history in this process, combined with differences in thermal expansion/shrinkage behavior of different layers of display, can lead to delamination.

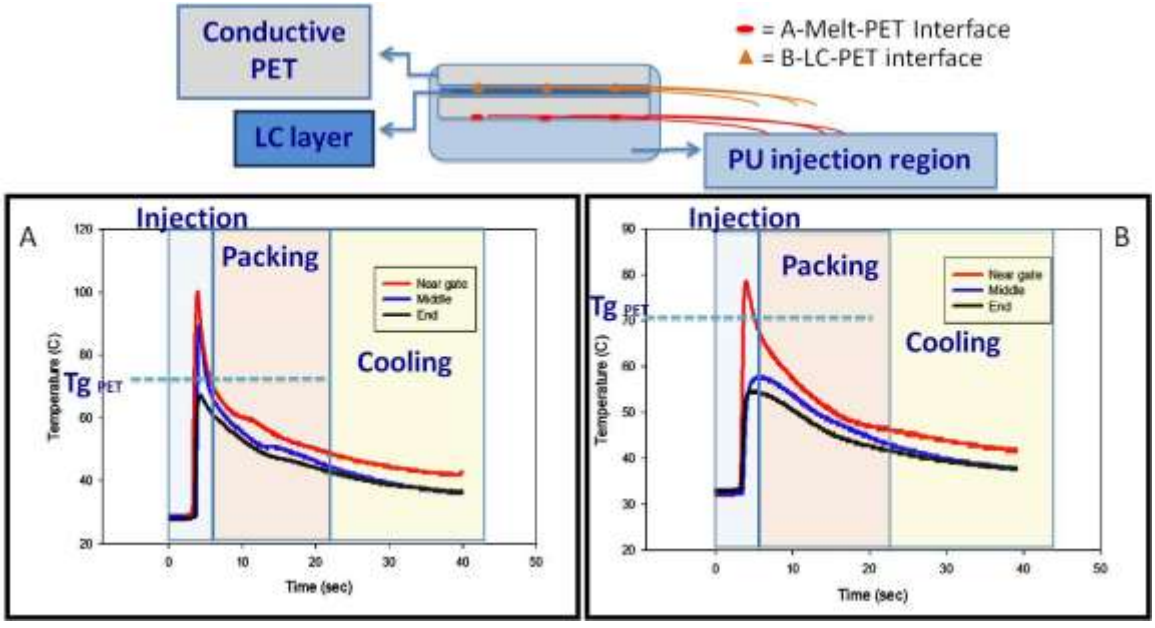

Figure 3.10. Real-time temperature profiles from thermocouple locations on the display-melt interface (A) and on PET-LC interface (B).

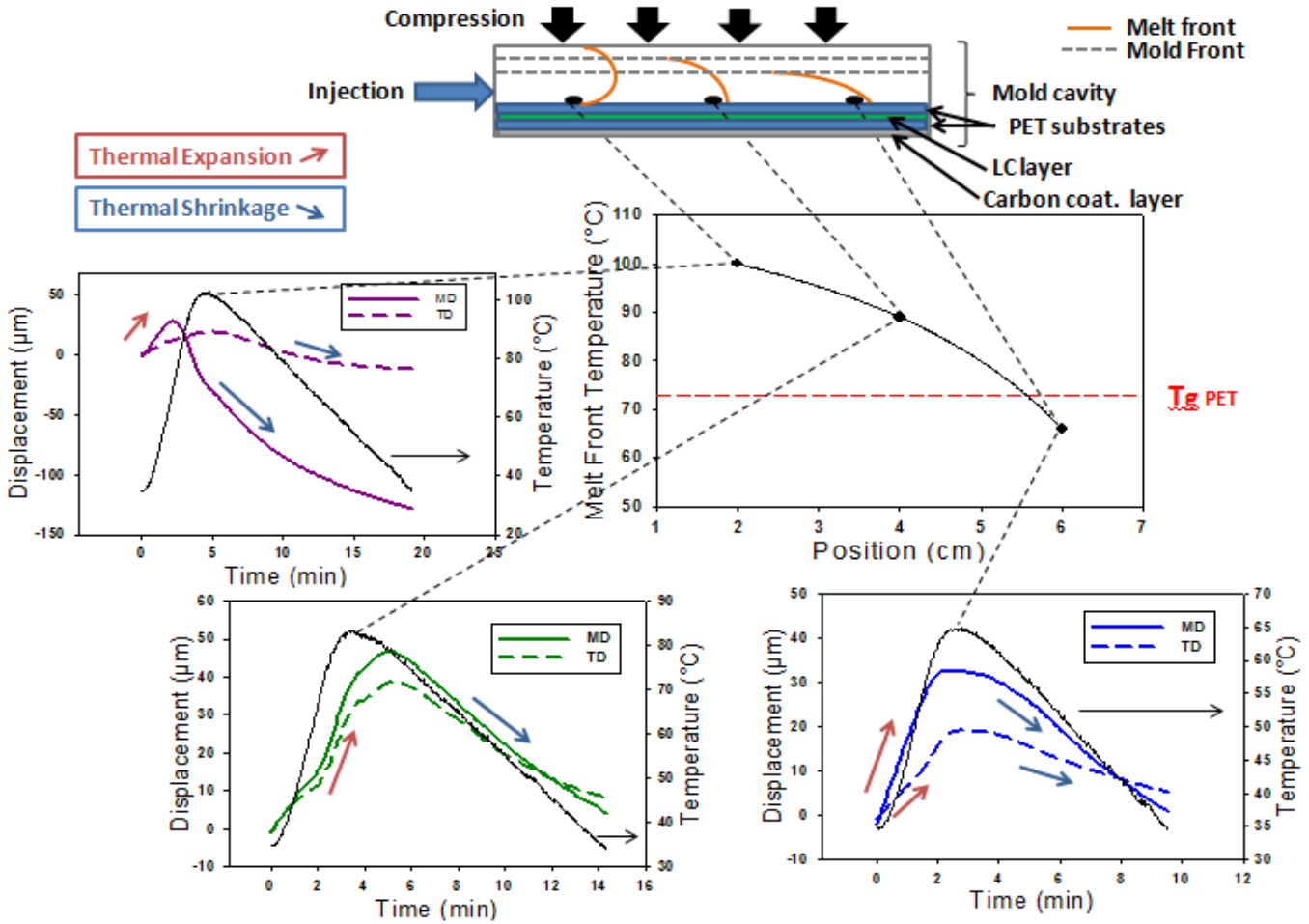

Figure 3.11. Complex expansion/shrinkage behavior of top display substrate –melt facing side- zones creating delamination.

The substrate expands upon melt contact heating if temperature rises above 90°C and upon cooling it shrinks as shown in TMA results (Figure 3.11). This creates different expansion/shrinkage behavior along display length as shown on peak temperature versus position on display graph. The temperature profiles experienced at each of the points from close to gate to flow end result in not only differences between them but also differences on the machine direction to the transverse direction of single point as well. At high temperature profile history point close to gate location, the machine direction is greater than the transverse direction shrinkage as the thermal peak point exceeds the glass transition temperature of PET. If the expansion/shrinkage behavior at the flow end with lower temperature profile is placed into the same scale graph as the high temperature profile point near the gate, the shrinkage value would be extremely low, and therefore, a higher degree of delamination and warpage is expected and observed near the gate location than cavity end. Warpage in single side encapsulated displays can be reduced in two different ways: first is by setting the mold B temperature higher as shown on Table 3.2. Second is by using a post-processing by heating the injected side on a hot plate (HP) of 60°C after the injection molding process. This post-processing creates a symmetrical cooling effect by diminishing the cold metal wall and hot insulating plastic wall effect (Figure 3.12).

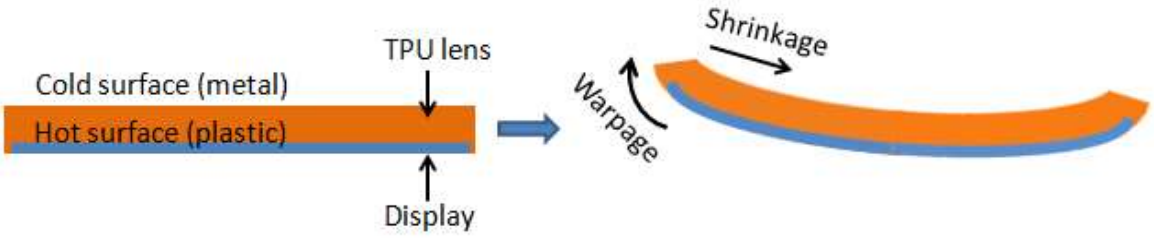

Figure 3.12. Warpage development on encapsulated part.

Table 3.4. Hot plate treatment effect on the overall radius of curvature of single-side 1 mm and 1.5mm lens encapsulated parts with high viscosity lens injection at standard processing conditions.

Lens thickness	FICM* (mm)	FICM+HP** (mm)
1mm	49.92±1.11	60.50±2.13
1.5mm	72.50±1.37	84.26±2.25

*FICM: Film Injection Compression Molding
**FICM+HP: Film Injection Compression Molding + Hot Plate

Table 3.4 shows the increase in the radius of curvature of the displays placed on HP after injection which indicates that the displays were more flat, and had less warpage than the single side lens injection molded displays without annealing post-processing.

Changing the substrate material of display from PET to PEN also results in reduced warpage results with higher radius of curvature values (Figure 3.13 (a)). This behavior is expected as PEN has a higher Tg (121°C) than PET (72°C), and therefore, PEN is experiencing lower thermal expansion shrinkage values at same temperature profile (Figure 3.14). The radius of curvature increases, warpage decreases as the display insert and lens thickness increases as seen on Figure 3.13(a) and (b) respectively. In regular film insert injection molded samples, this behavior is observed as warpage increases with increasing film and decreasing lens thickness unless the film insert is annealed [29]. For the display assembly, the substrates are thermally annealed around 200°C, warpage reversal phenomenon occurs in this case and the warpage decreases with

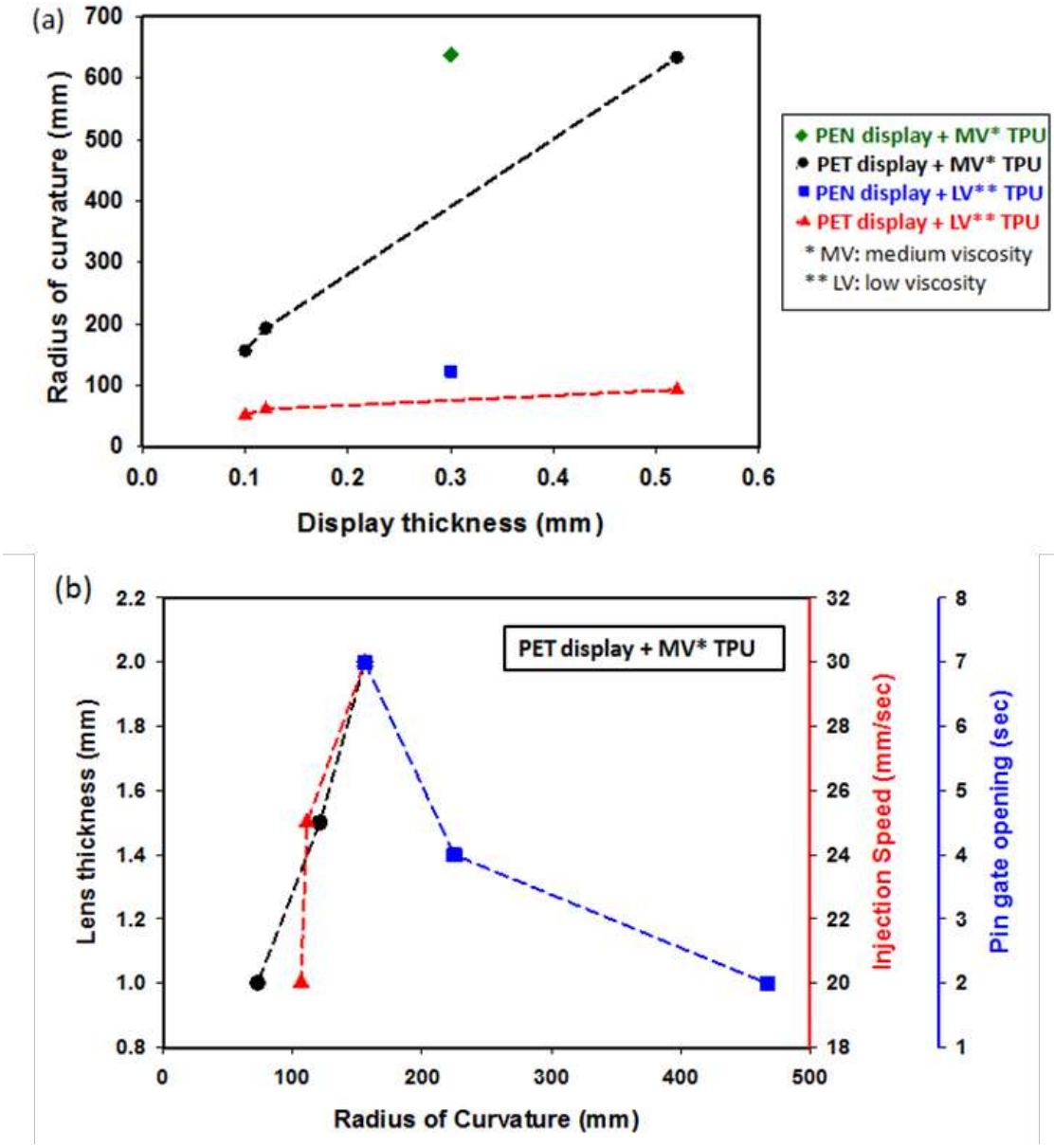

Figure 3.13. (a) Radius of curvature of PET and PEN displays with different thicknesses and lens material grade (b) Effect of lens thickness, injection speed and pin gate opening on the radius of curvature.

increasing display insert thickness. As also supported by previously reviewed results, thinner the lens, the lower is the pressure exerted during injection which increases the shrinkage on the part. Additionally, the lower the thermal insulation, the faster the parts cools down and has not time to relax the residual stresses which causes higher warpage. Processing parameters also affect the radius of curvature (Figure 3.13(b)). Lower warpage is observed at higher injection speeds. The melt flowing faster into the cavity, the frozen skin layer is thinner and there is less thermal gradient through the thickness of the part. This effect combined with slightly higher pressure results in lower warpage. The warpage dependence on injection speeds is not always inversely proportional. Very high

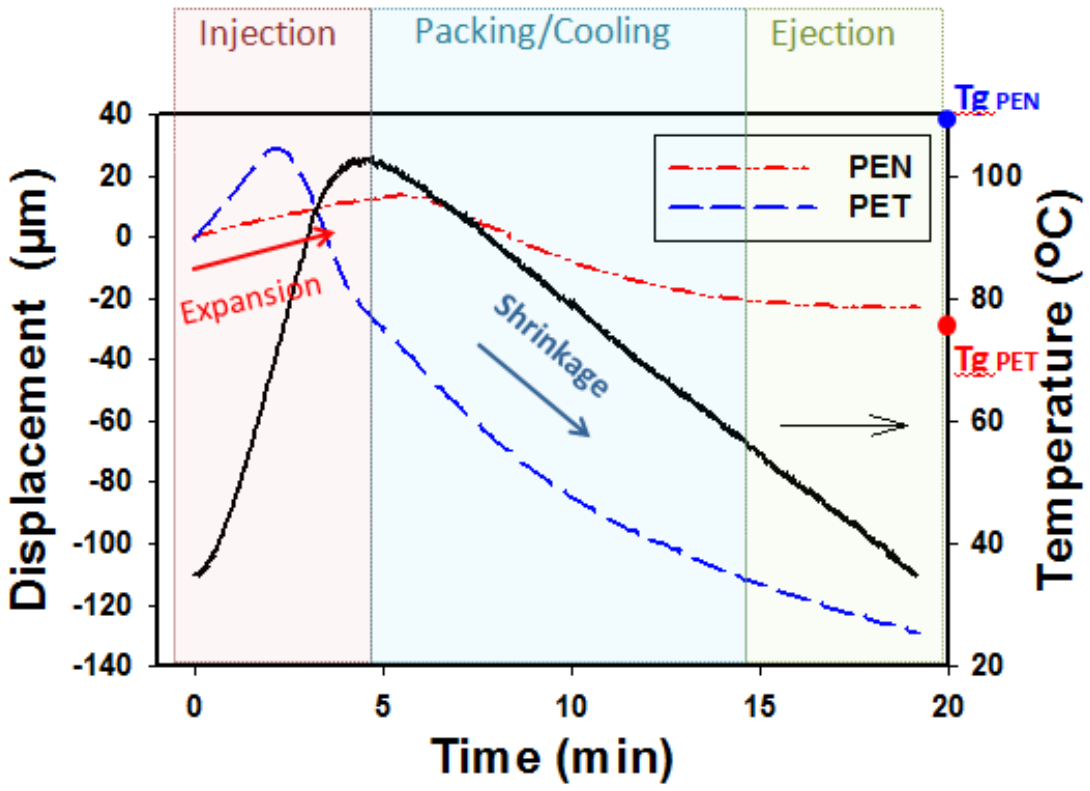

Figure 3.14. Substrate type comparison for displacement behavior.

injection speeds can also create high orientation of polymer chains in the flow direction compared to the transverse direction which, in turn, causes a differential shrinkage and higher warpage. In this case, more uniform cooling and pressure effect apparently overcomes the orientation effect.

Shorter pin gate opening cycle selection is a plus, as more cycles can occur during a designated time injection step (filling + packing) as opposed to a longer pin gate cycle setting (Figure 3.15). While compression continues along with injection, the amount of melt material getting into the cavity as well as the pressure ratio is lower at shorter pin opening cycles. This will reduce the residual stresses and shrinkage for each proceeding cycle and in return cause lower warpage (Figure 3.13(b)).

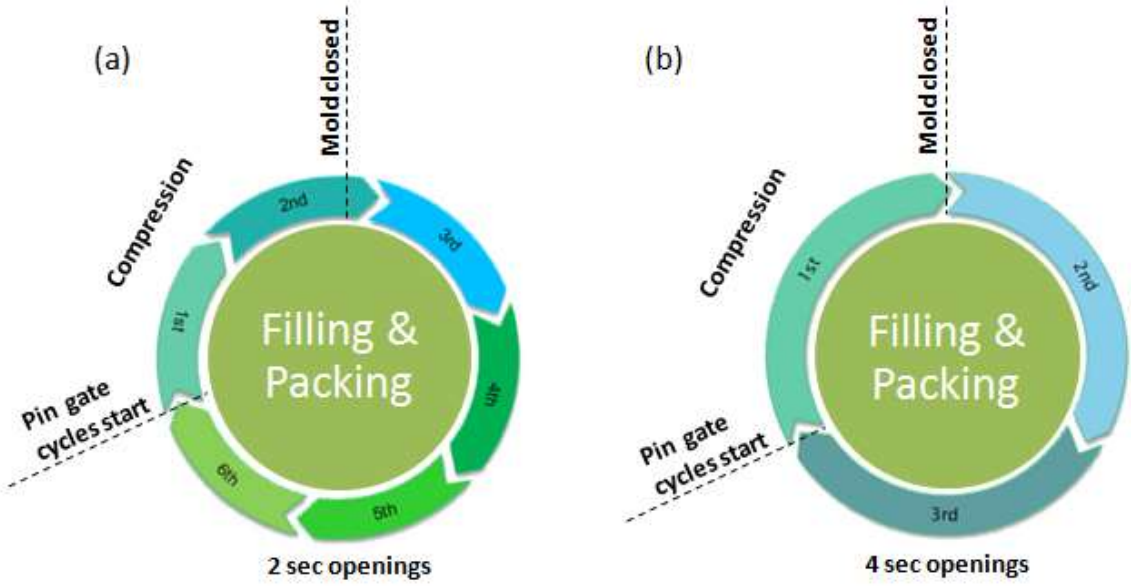

Figure 3.15. Injection compression molding short (a) and long pin gate cycles (b).

Table 3.5. Summary of radius of curvature results.

Run	Radius of curvature (cm)			Average	S/N
	1	2	3		
1	47.6	41.7	47.3	45.6	33.1
2	56.3	53.4	54.8	54.9	34.8
3	81.3	85.3	104.2	90.3	39.0
4	73.0	65.6	90.3	76.3	37.4
5	74.3	66.4	60.9	67.2	36.5
6	54.9	55.8	55.2	55.3	34.8
7	82.6	85.8	100.9	89.8	39.0
8	85.7	86.8	94.9	89.1	38.8
9	83.8	82.7	96.9	87.8	38.8
10	77.3	85.6	104.2	89.0	35.6
11	65.5	55.9	61.0	60.8	38.2
12	77.0	78.6	91.1	82.2	34.7
13	52.3	52.6	58.6	54.5	37.7
14	80.5	72.7	77.5	76.9	36.0
15	61.9	64.4	63.7	63.3	37.5
16	80.4	72.7	72.0	75.0	37.3
17	79.1	69.0	75.2	74.5	37.4
18	85.7	77.4	83.6	82.2	38.3

The summary of radius of curvature and S/N ratio results are given on Table 3.5 and 3.6, and Figure 3.16 respectively. The ranking in terms of the most influential factor to the least is also given on Table 3.6 showing the most effective factor to be mold temperature. The optimal process parameter combination for this application therefore is 1L2, 2L3, 3L3, 4L3, 5L3, 6L2, 7L3 and 8L3. The graphs in Figure 3.15 are plotted for the ease of understanding the Table 5 results and rankings. Using these optimum process parameters, the radius of curvature was increased by 16 % from the highest result obtained in the design of experiment run 3.

Table 3.6. Response table for S/N

#	Parameter	Mean S/N Ratio			Rank
		Level 1	Level 2	Level 3	
1	Melt Temperature (°C)	36.9	37.1	-	8
2	Mold Temperature (°C)	36.6	36.2	38.3	1
3	Injection Speed (mm/sec)	36.7	36.8	37.5	5
4	Packing Pressure (psi)	36.8	36.5	37.8	3
5	Packing Time (sec)	36.4	37.1	37.5	6
6	Cooling Time (sec)	36.2	37.6	37.3	4
7	Compression Position (mm)	37.0	36.8	37.3	7
8	Pin Gate Open Time (sec)	36.9	36.0	38.1	2

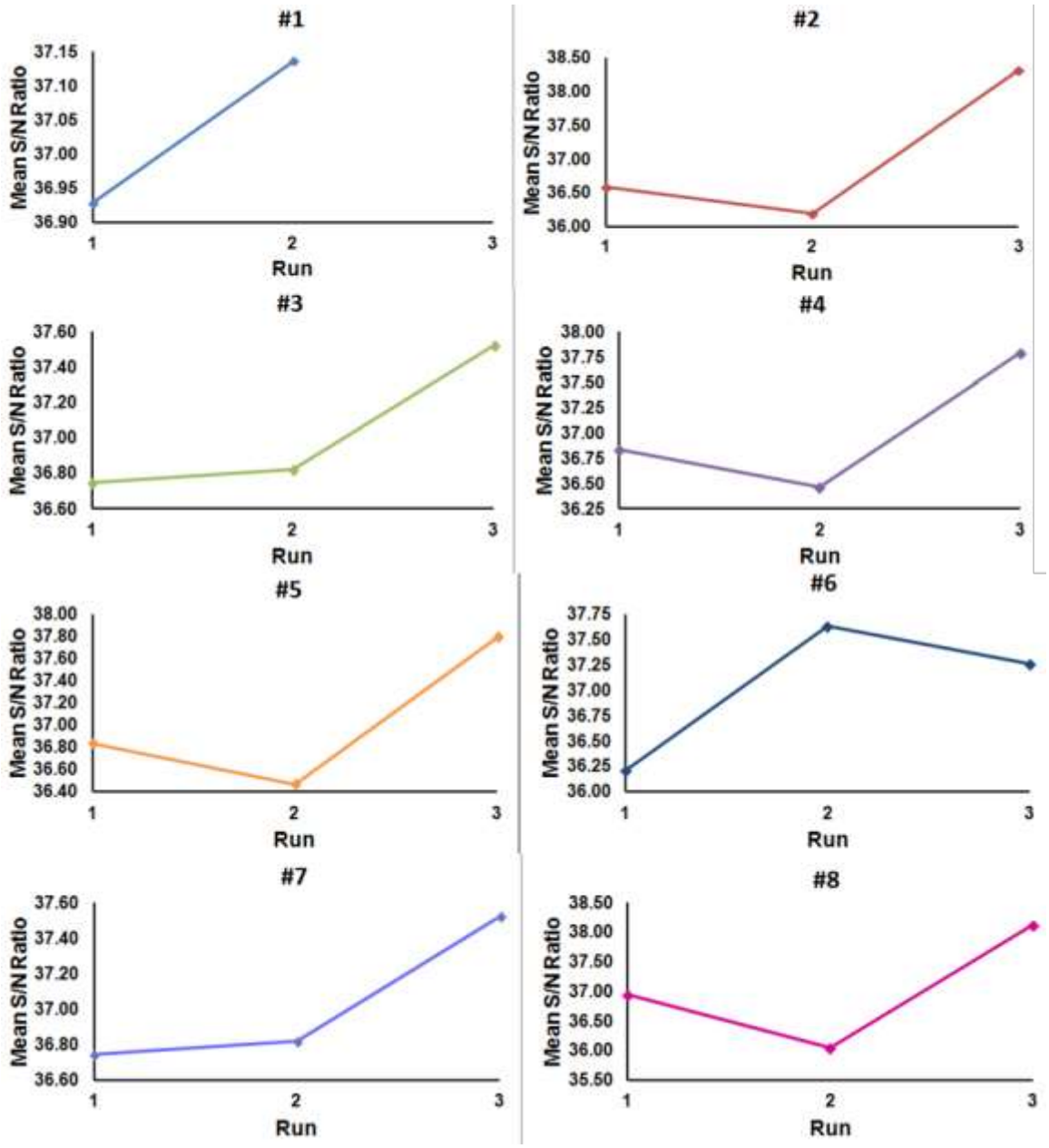

Figure 3.16. S/N ratio response diagrams.

Table 3.7. Successful switchable displays from FICM trials.

Gate/Lens Type		Center gated/Rigid		Edge gated/Rigid	Edge gated/Flexible
Encapsulation Type		Single	Double	Single	Single
Film Insert Type	PET Display*	☑		☑	
	PEN Display**	☑		☑	☑
	Laminated Display***	☑	☑	☑	

*2milPET+LC+2milPET layers (0.1mm display)
**5milPEN+LC+5milPEN layers (0.3mm display)
***7milPET+2milPET+LC+2milPET layers (0.5mm display)

Successful switchable encapsulated displays obtained by this method were summarized in Table 3.7.

3.4. Conclusion

A new hybrid method was developed for encapsulating liquid crystal displays. This combination of the film insert and injection-compression molding methods required process optimization for reliable product results free of delamination and with significantly reduced warpage (more than 10 %). In order to accomplish this goal and avoid processing related problems such as warpage, the processing machine was highly instrumented as described and a design of experiment was established.

Overall, problems such as delamination and warpage were avoided or significantly reduced (16 %), and switchable lens encapsulated displays were obtained by setting process conditions as found in Taguchi method. Using post process annealing or increasing lens or display thickness were also shown as solutions to the warpage problem. The second side injection also prevents warpage as the thermal history is symmetrical on

both sides of the display in that case. Apart from process optimization, changing the display substrate from PET to PEN was also demonstrated to be an effective design modification to obtain delamination-free and reduced warpage parts supported by the thermomechanical behavior comparison of these two materials.

CHAPTER IV

HYBRID FILM INSERT INJECTION COMPRESSION MOLDING FLOW SIMULATIONS FOR LENS ENCAPSULATION OF FLEXIBLE DISPLAY SUBSTRATES

4.1 Introduction

Full color, reflective, bistable, lightweight and flexible cholesteric liquid crystal displays are introduced to the market offering numerous applications such as electronic skins with real time switchable colors for consumer device cases, walls and windows. They add a personalization feature to the application area and device by providing a discrete color with the advantage of lower power consumption. For the current use, plastic/glass film lenses are hand laminated on the displays with a pressure-sensitive optical adhesive for increased protection and ease of application. However, this process is a labor intensive process, increasing the production time and failing to encapsulate the edges of the displays as it involves only adhesion of the lens on the display. Therefore, there is a need for a more economically viable process to create fully protective display

encapsulations allowing use in rigid and flexible applications. The injection molding process can be considered as a good candidate for encapsulating the displays, although the process complexity is likely to cause challenges to be resolved. For this encapsulation applicaton, film-insert injection molding technique by-itself would generate over the limit pressure values on the delicate display elements. A new combination of film-insert injection (FIM) and injection compression molding (ICM) techniques were introduced. Process effects in transparent polyurethane lens encapsulation of cholesteric liquid crystal displays were investigated elsewhere [87].

In the past two decades, different numerical techniques and approaches have been developed separately for both injection compression molding and film insert injection molding [28, 30]. Their combination effects have not been studied numerically earlier. The compression technique lowers residual stresses on the part with even pressure distribution, and therefore, is widely used for optical applications. This method also has a high potential to diminish, and even eliminate the warpage problem that occurs during and after film insert injection molding process [87].

In the film-insert injection molding (FIM) process, the molten polymer is injected into the mold cavity where one side of the mold wall is insulated by a pre-attached film. FIM is a cost- and time-effective technique eliminating various post-processing procedures (screen printing, spray painting, laminations etc.) and improving surface quality as well as durability. Numerical analyses were conducted in order to understand the processing procedure and physical properties of the final parts produced with this technique. Kim et al. performed numerical analysis by using three dimensional finite element analysis with Moldflow equipped with part insert option and time-dependent

viscoelastic analysis were completed with ABAQUS stress analysis code [30]. Beak *et al*. used a mesh generation program, HyperMesh, to generate two dimensional finite elements for film and substrate domains and carried out the three dimensional analysis in Moldflow program [10]. For the flow analysis, under non-isothermal conditions during filling and post filling stages, Hele-Shaw model for compressible viscous fluid is used; rheological behavior of polymer melt is assumed to follow the modified Cross model with Williams-Landel-Ferry Equation, and PVT relationship is represented by Tait Equation [10]. The material is assumed transversely isotropic for long-term viscoelastic behavior. Generalized Kelvin model is selected as constitutive Equation for linear thermoviscoelastic material in stress analysis [10, 29-31].

Injection-compression molding processes also are used in manufacturing of high precision plastic optical parts such as lenses and disk substrates. Young *et al*. studied the shrinkage and residual stress simulation of injection compression molded pickup lens with large thickness variations [22]. Cross-WLF Equation for viscosity and modified Tait Equation for density were used to simulate the process. The surface profile deviation due to shrinkage is found to be mostly affected by mold temperature and compression time. Kwon et al. showed numerical birefringence distribution on injection compression center-gated disk using the Leonov viscoelastic fluid model [23, 88]. Park *et al*. used the same model for simulating the same process with the finite difference method and addition of the Tait Equation of state [32]. Chen *et al*. simulated the filling stage of stamping injection compression molding with a new numerical algorithm [25-28]. They found the measured cavity pressure and simulated pressure are in agreement and switch time changes the pressure profiles. The reduced and more uniform shrinkage in molded parts,

smaller birefringence at higher melt temperatures and lower mold closing velocity are reported. On the other hand, the flow rate and mold temperature is shown to have no significant effect on birefringence.

Due to the complicated nature of, and the unclear physical mechanism involved in, the newly introduced combination insert and injection compression technique, using only trial-and-error experimental techniques would be time consuming and limiting. The Moldex3D moldflow simulation software offers a modifiable user interface where combined injection molding modes (insert+compression) can be run together and changes in theoretical approaches and material data are possible as well. This study shows a feasible numerical approach for simulating insert injection compression molding using Moldex3D R12 simulation package. Flow front and frozen layer development, temperature and pressure profile data were generated and compared with the experimental data obtained from instrumented setup published elsewhere [87]. The simulation tool is proved to be a cost-effective technique to be used in similar application simulations.

4.2 Experimental

4.2.1 Geometry and Design

A prototyping mold was designed as shown on Figure 4.1 to be used both as film insert and injection compression mold. The mold had a female (Mold A) and a male (Mold B) part to prevent flashes during injection compression molding. Mold A consists of an interchangeable female cavity with inner edge vacuum vents for holding

the display on the cavity wall, and adjustable shims allowing the production of center or edge gated lens encapsulations with different thicknesses ranging from 0.5 mm to 1.5 mm. The vents on this side are also used with air compression to eject the sample at the end of process, instead of ejector pins that would potentially damage the device. Mold B consists of an interchangeable male core with Teflon squeeze insert to prevent

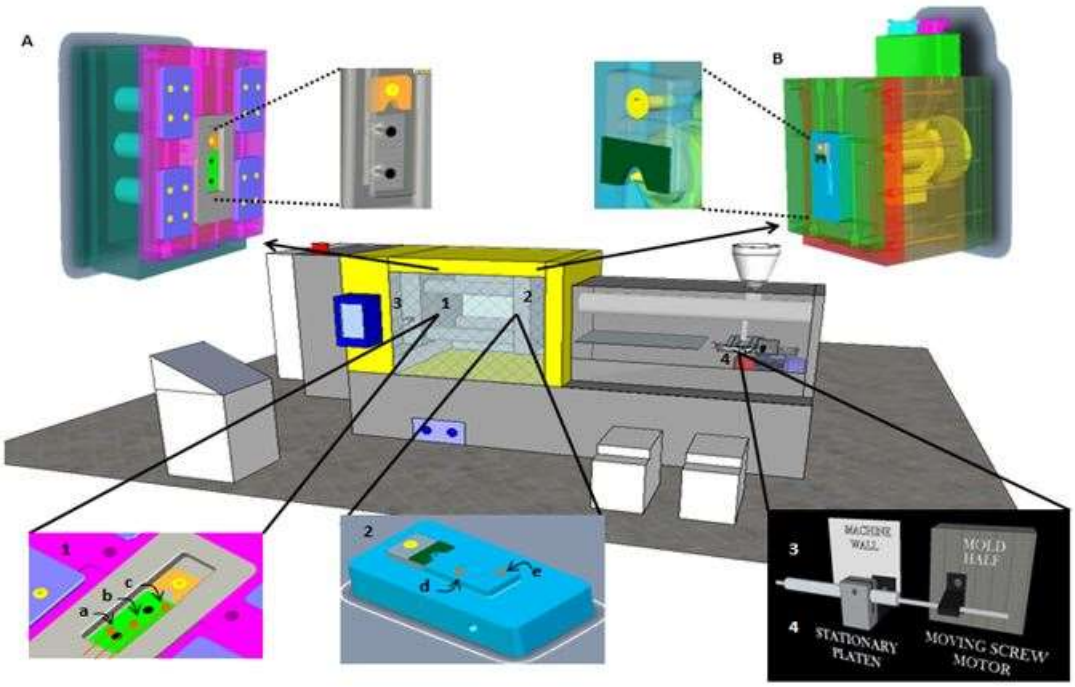

Figure 4.1. Film insert injection compression molding unit: (A) interchangeable cavity with inner edge vacuum/air compression vents and adjustable shims, (B) interchangeable core with Teflon squeeze insert and hydraulic 3-zone pin gated hot runner and the instrumentation of (1) thermal monitoring of the display with 3 thermocouples at the cavity side, (2) melt pressure monitoring with 2 pressure transducers and (3) mold and screw movement monitoring LVDTs.[87]

flash onto electronic circuit attachment of the display, and a hydraulic three zone pin gated hot runner. A P.E.T.S. hot runner system with flush mount small diameter pin

gate was used in the system. The center gated lenses were designed to be used in parts having logos in the center to close the gate mark. The PETS hot runner system allows the melt to be at lowest viscosity when it reaches the cavity to exert reduced flow pressure on displays. The mold temperatures can also be controlled with water mold heating/cooling units from Polymer Processing Equipment.

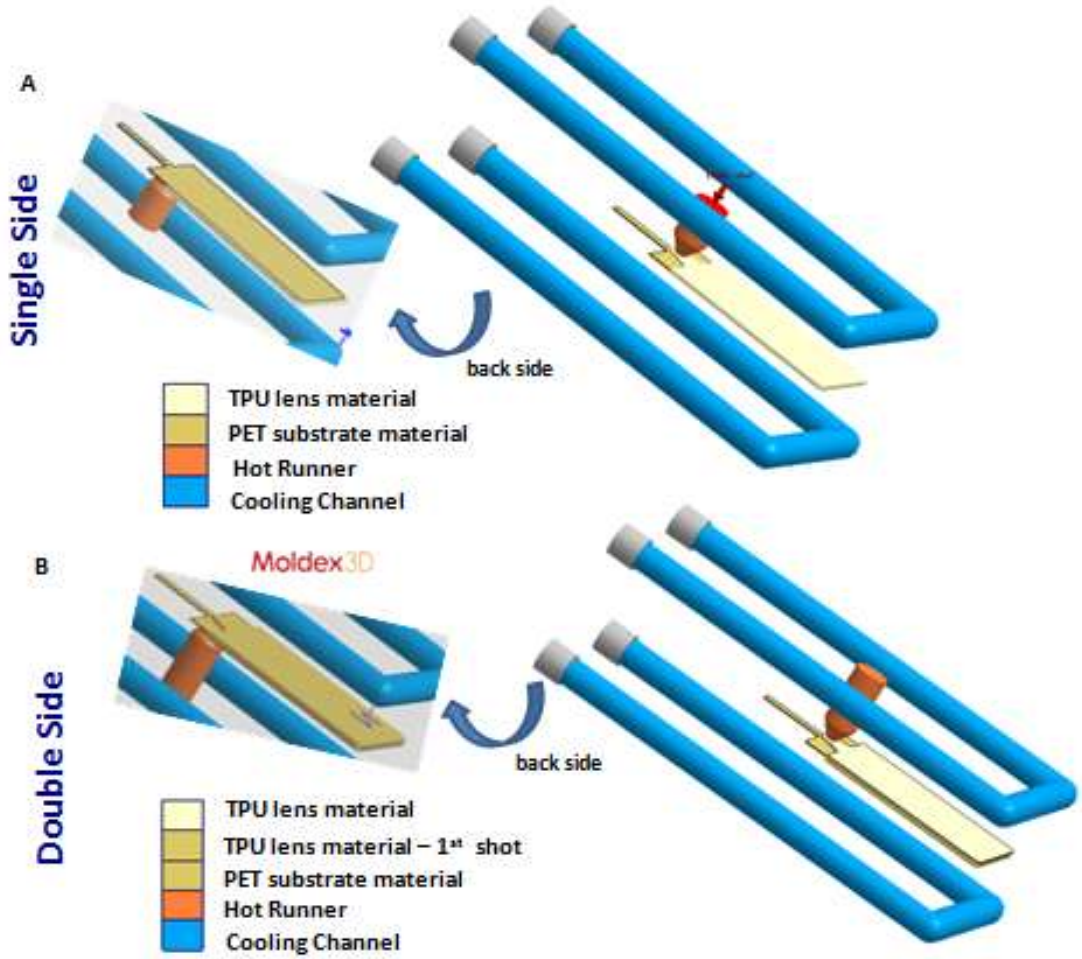

Figure 4.2. Model for (A) single and (B) double side encapsulated parts with hot runner and cooling channel design.

In this process, encapsulation was accomplished in two steps: first, injecting the TPU on the front of the display from an edge pin gate, and second, encapsulating the

back side of the display. The complete mold and part geometry was exported to Moldex3D software for flow simulation (Figure 4.2). The geometry includes "U-shaped" cooling channels on mold A and B sides, hot runner pin gate structure, 178 μm polyethylene terephthalate (PET) display substrate insert material as well as the encapsulating thermoplastic polyurethane (TPU) material. The insert is a PET film for the first shot and TPU lens and PET film combination in the second shot case. These

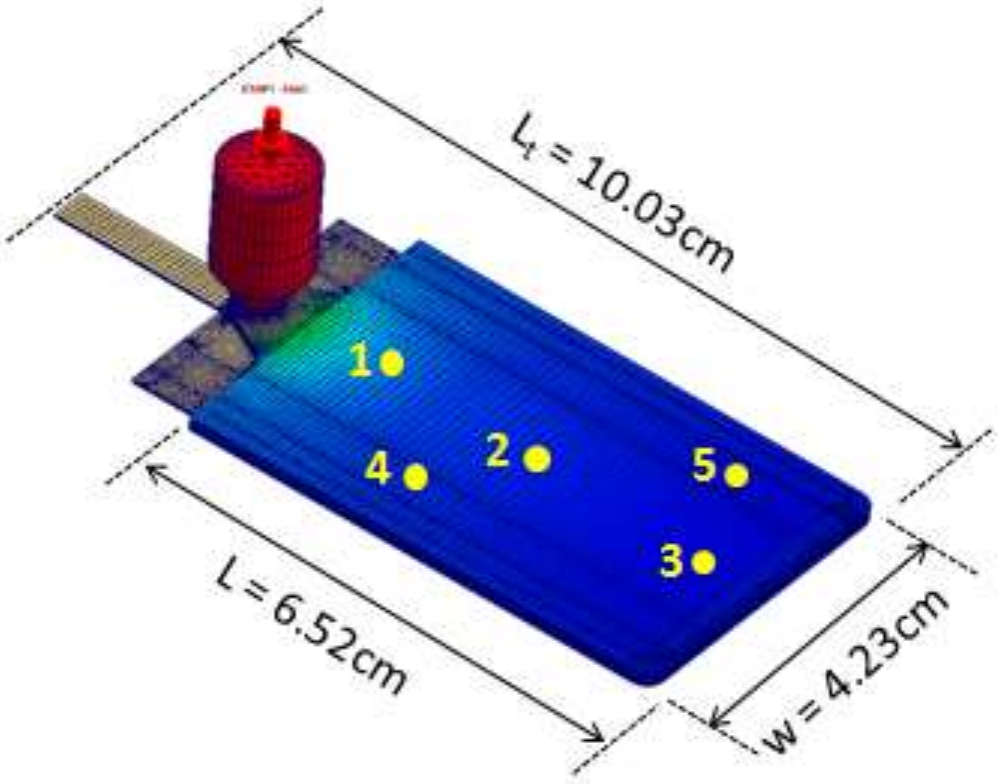

Figure 4.3. Solid mesh model and geometry for 1.5mm thick encapsulated part with sensor node locations : 1 to 3 temperature sensors, 4 and 5 pressure sensors.

exported geometries were meshed in Rhino 5.0 using Moldex3D mesh plug-in. The mixed hybrid mesh injected part and insert substrate consist of 47625 and 43085 elements respectively. Compression and optics boundary layers were also added to

apply Moldex3D R12 at injection compression molding (ICM) mode and to obtain optical results. Measuring nodes were setup as seen in Figure 4.3 to monitor temperature evolution at locations 1 through 3 and pressure at locations 4 and 5. The experimental equipment shown in Figure 1 also includes the same instrumentation at defined locations [87].

4.2.2 Model Equations

The simulation analysis consists of three main injection molding steps of filling/packing, cooling and warpage. In the filling/packings steps, the polymer melt is assumed to behave as Generalized Newtonian Fluid (GNF). The non-isothermal 3D flow motion can be mathematically described using the following equations:

$$\frac{\partial \rho}{\partial t} + \nabla \cdot \rho \mathbf{u} = 0 \tag{1}$$

$$\frac{\partial}{\partial t}(\rho \mathbf{u}) + \nabla \cdot (\rho \mathbf{u}\mathbf{u} - \boldsymbol{\sigma}) = \rho \mathbf{g} \tag{2}$$

$$\boldsymbol{\sigma} = -p\mathbf{I} + \eta(\nabla \mathbf{u} + \nabla \mathbf{u}^{\mathrm{T}}) \tag{3}$$

$$\rho C_P \left(\frac{\partial T}{\partial t} + \mathbf{u} \cdot \nabla T\right) = \nabla(\mathbf{k}\nabla T) + \eta \dot{\gamma}^2 \tag{4}$$

where t is time, ρ density, u velocity vector, σ total stress tensor, η viscosity, T temperature, C specific heat, k thermal conductivity and $\dot{\gamma}$ shear rate. The finite volume method (FVM) is applied to solve the transient flow field in three-dimensional geometry. During the cooling step, a three-dimensional, cyclic, transient heat conduction problem with convective boundary conditions on the cooling channels and

the mold base surfaces is involved [89]. The Modified-Cross model with Arrhenius temperature dependence is selected to describe viscosity of polymer melt:

$$\eta = \frac{\eta_0}{1+\left(\frac{\eta_0 \dot{\gamma}}{\tau^*}\right)^{1-n}} \tag{5}$$

$$\eta_0 = B\ exp\left(\frac{T_b}{T}\right) \tag{6}$$

where η_0 is zero shear viscosity, n power law index and τ^* critical shear stress characterizing transition shear stress from Newtonian range to pseudo-plastic region of the viscosity curve.

Equations 1 to 6 predict a satisfying pressure and velocity. However, in order to predict precisely residual stress and molecular orientation, the viscoelastic nature of the polymer needs to be considered. The White-Metzner Model modified from the Upper Convected Maxwell Model is used in this study:

$$\tau + \lambda\left(\frac{\partial \tau}{\partial t} + \mathbf{u}\cdot\nabla\tau - \nabla\mathbf{u}^T\cdot\tau - \tau\cdot\nabla\mathbf{u}\right) = \eta(\nabla\mathbf{u} + \nabla\mathbf{u}^T) \tag{7}$$

$$\lambda(T,\dot{\gamma}) = \frac{\eta(T,\dot{\gamma})}{G} \tag{8}$$

where τ is the stress and λ the relaxation time. The relaxation time and viscosity are both functions of temperature and shear rate.

Modified Tait Model 2 was chosen as PVT model to describe the change in compressibility of the material with melt temperature and applied pressure (Equations

9-15). Representing well both semi-crystalline and amorphous materials, this method is widely employed in all major CAE calculations.

$$\hat{V} = \hat{V_0}[1 - Cln(1 + P/B)] + \hat{V_t} \tag{9}$$

$$\hat{V_0} = b_{1S} + b_{2S}\bar{T}, if\ T \leq T_t$$

$$b_{1L} + b_{2L}\bar{T}, if\ T > T_t \tag{10}$$

$$B = b_{3S} \exp(-b_{4S}\bar{T}), if\ T \leq T_t$$

$$b_{3L} \exp(-b_{4L}\bar{T}), if\ T > T_t \tag{11}$$

$$\hat{V_t} = b_7 \exp(b_8\bar{T} - b_9P), if\ T \leq T_t$$

$$0, if\ T > T_t \tag{12}$$

$$\bar{T} = T - b_5 \tag{13}$$

$$T_t = b_5 - b_6P \tag{14}$$

$$C = 0.0894 \tag{15}$$

Where V is specific volume at temperature T and pressure P, V_0 specific volume on the zero gauge pressure, C the universal constant and B the pressure sensitivity of the material. A total of 13 model parameters ($b_{1S}, b_{1L}, b_{2S}, b_{2L}, b_{3S}, b_{3L}, b_{4S}, b_{4L}, b_5, b_6$) are implemented to describe changes at the PVT data around upper ($T > T_t$) and

lower temperature region ($T \leq T_t$) for the liquid (b_{xL}) and solid (b_{xS}) states of material, respectively.

The simulation package presents the warpage development after two major stages of packing and cooling separately. In-mould constraint effect is considered in simulation as a contact interface exists between the part surface and the mold wall. A deformation develops inside the rigid mold under constraints before the part is ejected. The in-mould constraint induced part warpage was calculated to enhance the analysis accuracy. After ejection, the part shrinks freely as it cools down in atmospheric conditions. The mechanical properties are assumed linear elastic and the governing equations to solve the displacement problem are the following equilibrium equations.

$$\nabla\sigma + F = 0 \tag{16}$$

$$\sigma = C(\varepsilon - \varepsilon^0 - \alpha\Delta T) + \sigma^F \tag{17}$$

$$\varepsilon = \frac{1}{2}(\nabla\mathbf{u} + \nabla\mathbf{u}^T) \tag{18}$$

where ε is the strain tensor, C elastic material stiffness, σ^F the initial stress to differentiate flow and thermally induced residual stress contributions and α coefficient of linear thermal expansion [90, 91].

4.2.3 Materials

The materials in this study are low and high viscosity flexible TPUs from Bayer and Lubrizol, respectively, and PET from Dupont Teijin films. Most of the material properties and values associated with models described in the previous section were

found in the Moldex3D software material database as indicated on Table 4.1. Missing thermal, mechanical and optical properties of the insert film and optical properties of the TPU were found in this study as shown on Table 4.2 by the following characterization experiments.

Table 4.1. Material property resources.

Information	Property	Model	Characterization	Reference
Viscosity	Viscosity vs. shear rate	Modified Cross Model	-	Moldex3D database
PVT	Specific volume vs. temperature	Modified Tait Model	-	Moldex3D database
Viscoelasticity	Shear modulus	White-Metzner Model	-	Moldex3D database
Heat capacity	Constant c_p	-	DSC	Moldex3D database
Thermal conductivity	Constant K	-	Thermal conductivity test instrument	Moldex3D database This study*
Mechanical properties	Elastic modulus –E Poisson`s ratio CLTE (coef. of linear thermal expansion)	-	Tensile tester " TMA	Moldex3D database This study*
Optical properties	Refractive index Stress optical coefficient	-	Abbe refractometer Mechano-optical device	This study*

The molecular weights of same hardness but different viscosity TPUs were obtained running through Waters Model 410 GPC in THF. The high viscosity TPU has a bimodal distribution and two molecular weights of 46020 and 58870g/mol whereas the low viscosity TPU has unimodal distribution of 26300g/mol molecular weight. Bohlin

(Malvern) RH7 Capillary Rheometer tests were conducted to generate viscosity profiles for these TPU materials (Figure 4.4). Critical surface tensions for low and high molecular weight TPUs were also found, extrapolating toluene and water contact angle versus surface tension Zismon plots, as 24 and 27 mJ/m^2.

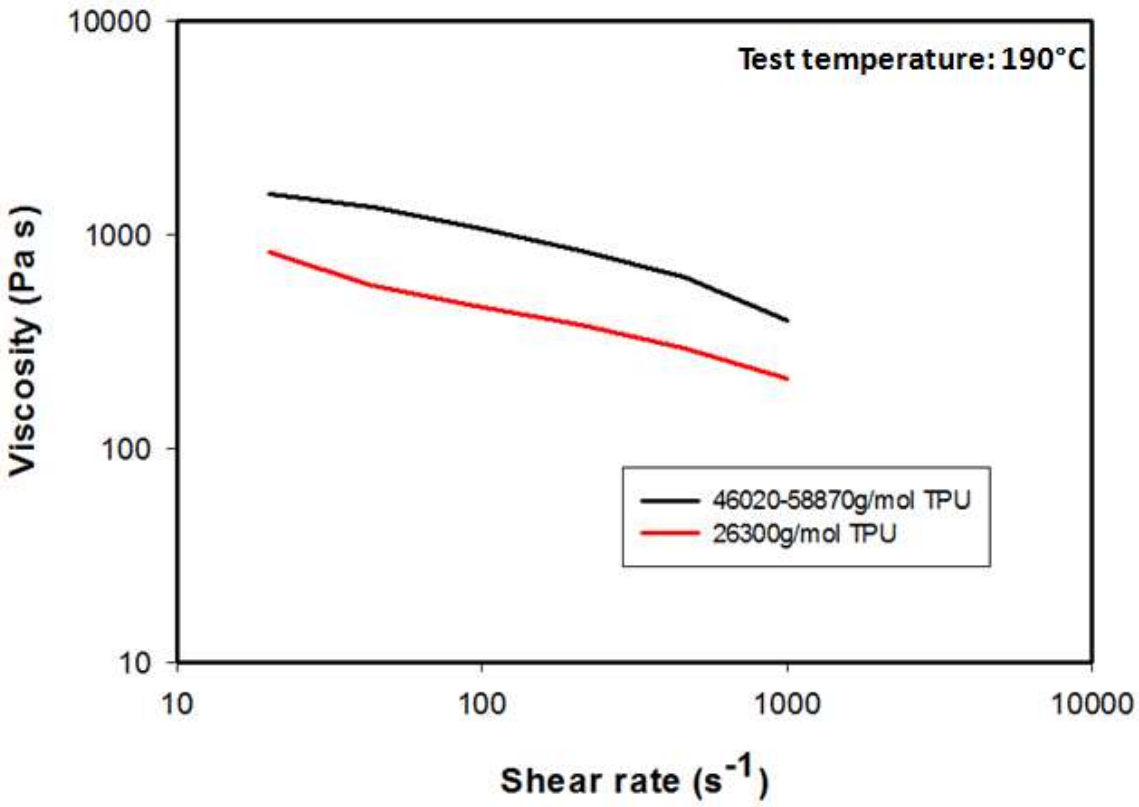

Figure 4.4. Rheological comparison of low (TPU) and high molecular weight (TPU-2) polyurethane.

Laser Comp`s FOX 50 Heat Flow Meter was used to calculate thermal conductivity of PET insert as well as the full display stack. Samples were cut in 5 cm diameter circles and 5 and 7 layers stacked together using heat sink grease to get stable heat flow readings. Two-thickness method tests were conducted in a 35 to 95°C

temperature range and the results are given on Figure 4.5. Thermal resistivity of the layers were taken into consideration to prevent loss of accuracy in calculations [92]. The equation used to calculate thermal conductivity, λ, is given below:

$$Q = q / S_{cal} = \Delta T / [(\Delta x/\lambda + 2R)\, S_{cal}] \quad (19)$$

where Q is electric signal in flow meter instrument, q heat flux, S calibration constant, ΔT temperature difference between top and bottom plate, and R contact resistivity.

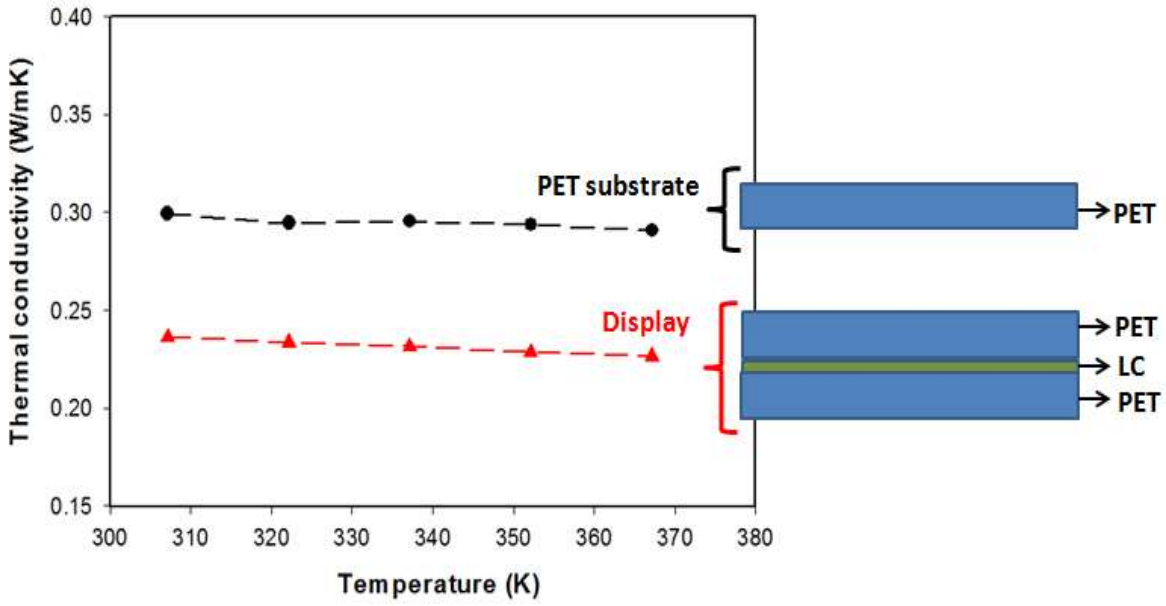

Figure 4.5. Constant thermal conductivity for PET inserts and display stack.

PET substrate`s Young`s modulus and poisson ratio values were obtained from data collected with in-house custom mechano-optical device [93]. Experiments were conducted at 15°C above PET glass transition temperature at 85°C with a stretch ratio of 1.5 and stretch rate of 10mm/min in machine direction. Stress versus strain curve

and the Poisson ratio time evolution is shown on Figure 4.6. The calculated values were added to the software material property list.

High viscosity TPU lens material was also tested in mechano-optical device for stretching ratio of 2 and rate of 10 mm/min at room temperature. The stress optical behaviors are given on Figure 4.7 along with initial diffraction patterns from Bruker AXS Dimension D8 X-Ray system with Cu Ka radiation at 45° chi (κ) angle and 180 seconds count. The stress optics law, equation 20, was applied to retrieve the stress optical coefficient from the initial linear portions of birefringence versus true stress plots in Figure 4.7.

$$\Delta n = \frac{R}{t} = C\ (\sigma_1 - \sigma_2) \tag{20}$$

where Δn is birefringence, R retardation, t thickness, C stress optical coefficient, and σ stress.

TA Instruments RSA3 DMA was used in TMA mode with constant 0.05N force applied on 3mm x 8mm PET samples during temperature ramp from room temperature to 180°C at 5°C/min ramp. The coefficient of thermal expansion (CTE) value was calculated using equation 21. Displacement versus temperature data was collected and the calculated CTE inserted in Table 4.2.

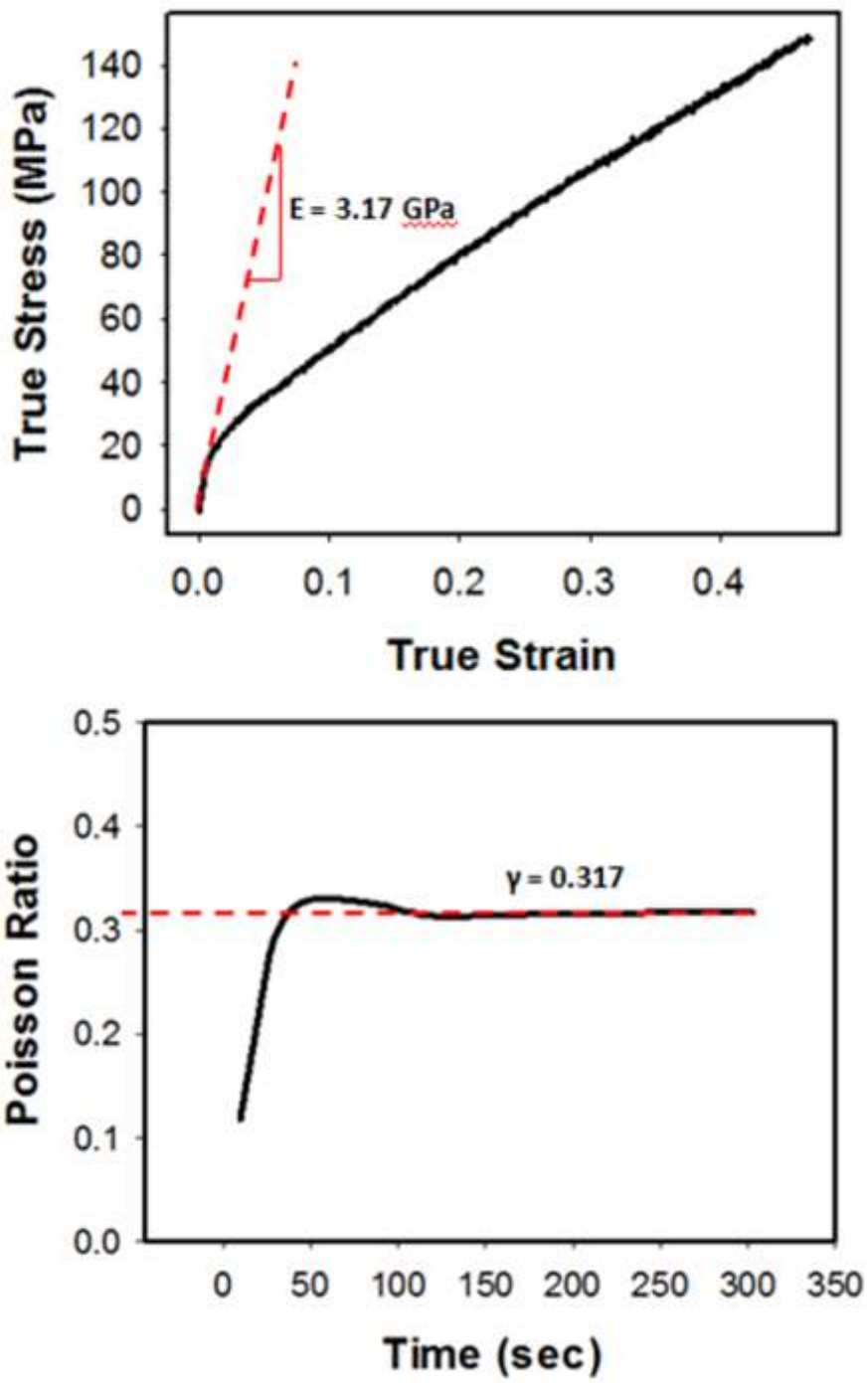

Figure 4.6. PET insert mechanical properties

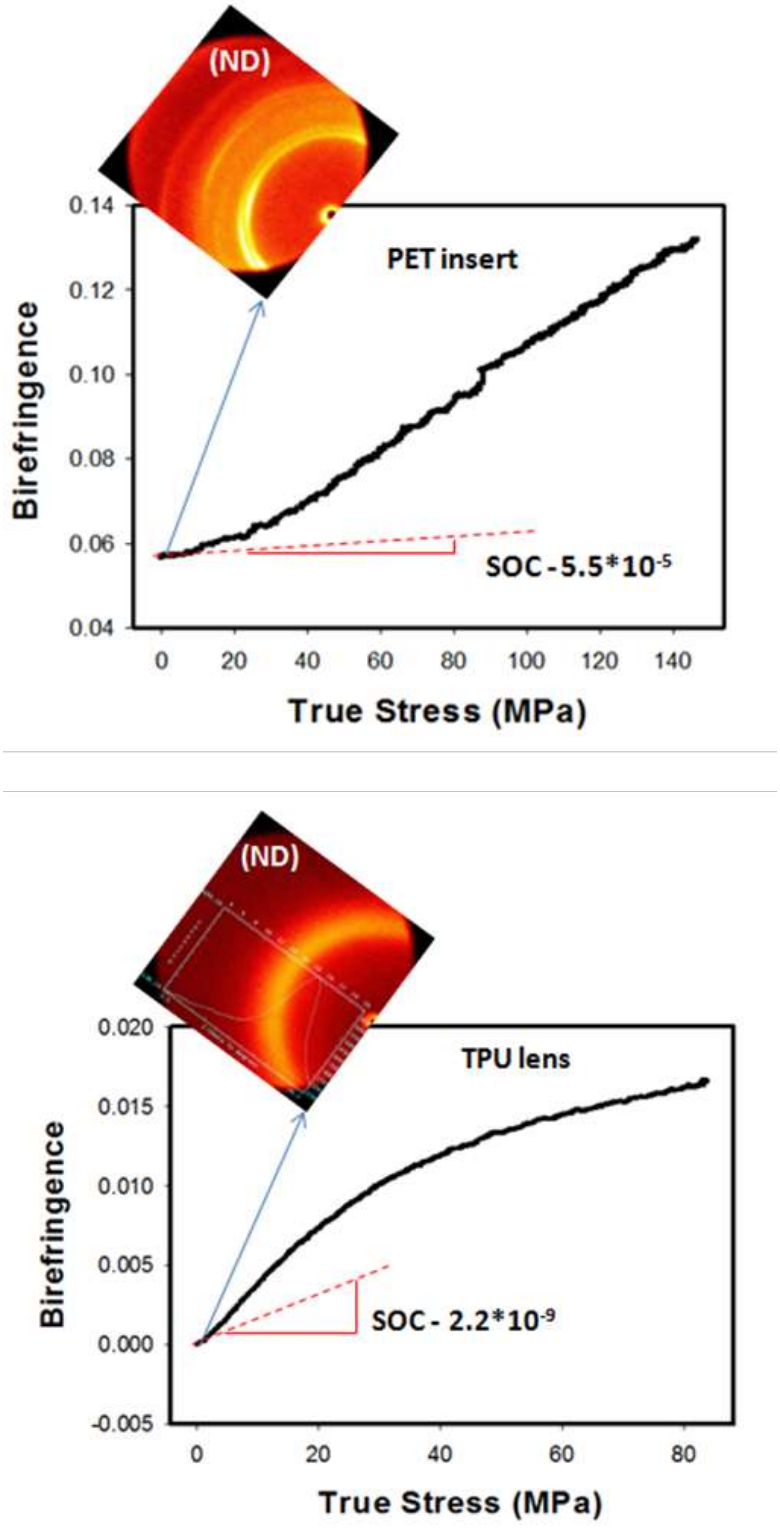

Figure 4.7. Mechano-optical properties of PET insert and high viscosity TPU lens materials with stress optical coefficient (SOC) values.

Table 4.2 PET insert and TPU lens materials properties.

Property/Material	PET	TPU	TPU-2
Heat Capacity, c_p (J/(kg.K))	1793 *	2100	1988
Thermal Conductivity (W/(m.K)	0.296 *	0.200	0.268
Shear modulus (kPa)	100	270	199
Elastic modulus (GPa)	3.17 *	2.00	1.43
Poisson Ratio	0.317 *	0.380	0.395
CLTE (1/K)	$5.00*10^{-6}$ *	$1.85*10^{-4}$	$2.36*10^{-4}$
Refractive index	1.5750 *	-	1.4962 *
Stress-optical coefficient (1/Pa)	$1.6*10^{-11}$ *	-	$2.2*10^{-9}$ *

*** Values obtained in this study**

$$\alpha = \Delta L/(L_0 * \Delta T) \tag{21}$$

where α is coefficient of thermal expansion, ΔL displacement, L_0 initial length, and ΔT final and initial test temperature difference.

4.2.4 Process Conditions

Three level processing conditions set for simulations are summarized on Table 4.3. The "standard conditions" designated on the table with an asterisk (*) were kept constant while others were systematically varied in ranges for various optimization experiments under Milacron Roboshot S2000i110B electric injection molding machine configuration included in software settings.

Table 4.3 Process conditions for single side 1.5 mm display encapsulation.

Parameters	Level 1	Level 2*	Level 3
Melt temperature (°C)	205	210	215
Mold temperature (°C)	50	60	70
Packing time (sec)	5	7	9
Cooling time (sec)	25	30	35
Compression gap (mm)	0.1	0.5	1

*Standard condition

4.3 Results and Discussion

Temperature profiles recorded at 1, 2 and 3 sensor node locations during Level 2 standard settings were compared to the experimental results for accuracy. Figure 8a shows simulated temperature profile. The first peak appears at node 1 being closest to the gate location, followed by nodes 2 and 3. As the material continues to flow towards the end of the cavity, the shear increases causing shear heating; therefore node 3 records the highest peak temperature. This behavior was confirmed by the experimental temperature profile (Figure 4.8b) recorded by thermocouples in the instrumented multi cavity mold described elsewhere [87]. The profiles recorded during injection and packing stages have some variations in terms of rise and decay speed (Figure 4.8c). The simulation results fail to exactly simulate the broad temperature profile observed in experimental case. The cooling behavior is very rapid and followed by leveling off at 70°C. However, the real

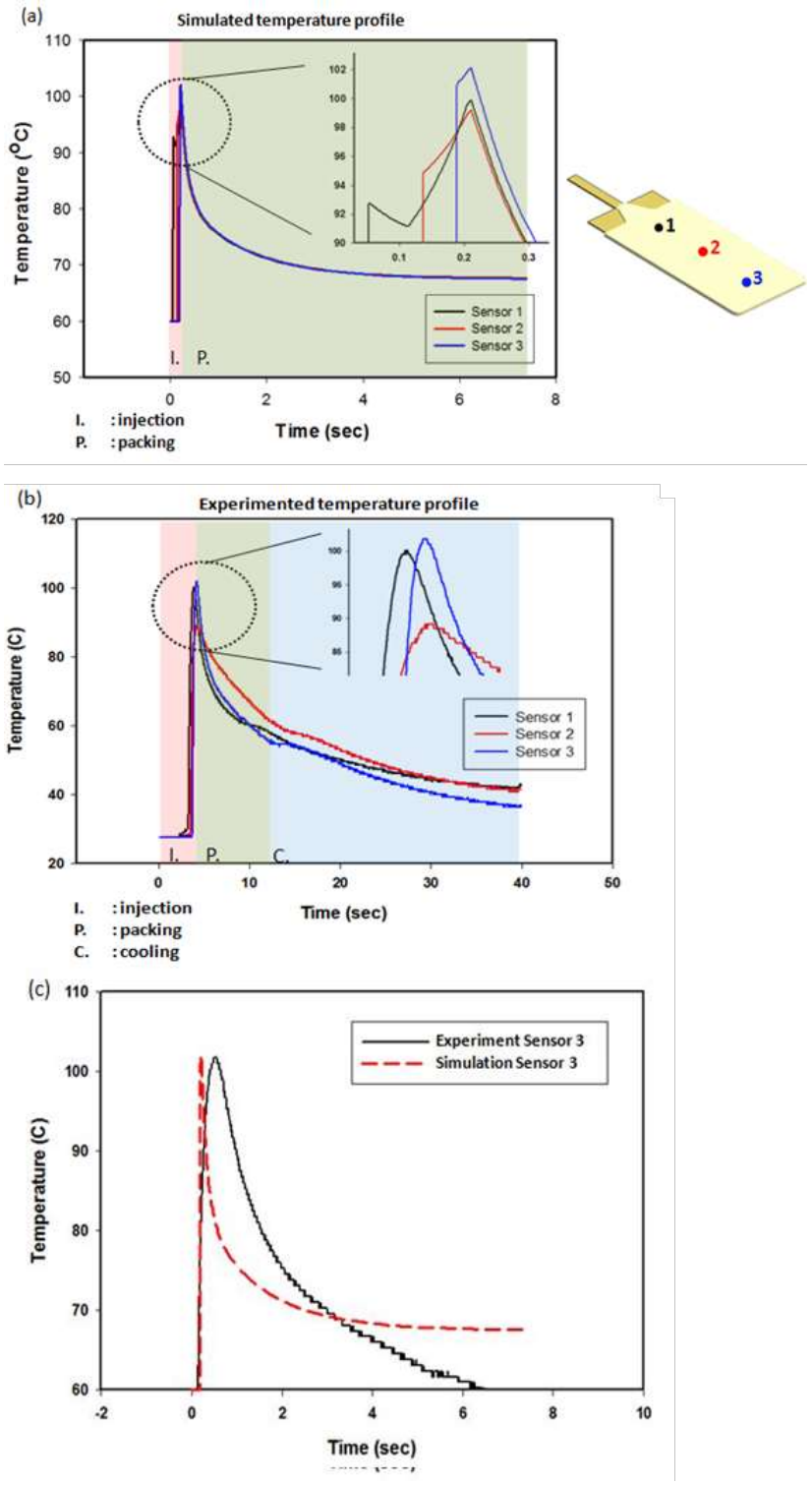

Figure 4.8. Simulated injection/packing (a) and experimental injection/ packing and cooling stages (b) temperature profiles at all instrumentation points. Direct top sensor point (1) data comparison between simulated and experimental (c).

cooling process has a much slower trend. The hot runner system, heating source on the cavity side, and the film insert, insulation on the core side makes cooling slower regardless of cooling channel use. The simulations assume ideal cooling system ignoring the hot runner heating effect which results in this faster cooling profile through the end of packing stage. However, the peak temperature values are in agreement for sensor 1 and 3 as seen from Figure 4.8 zoomed sections of (a) and (b). Direct comparison for the peak values of sensor 3 is also given in Figure 4.8(c). Predefined hot runner pin gate opening setting in the simulation algorithm show the opening cycles during injection compression with two peaks. This effect, that occurs very fast, is not observed for temperature profiles in real cases. This sequential material inlet into the cavity can be more distinctive in higher viscosity material injection cases pressure profiles [87]. Sensor 2 peak point is overestimated by 10°C in simulations. Shear heating effect is calculated within the simulation, therefore as the material flows towards cavity end temperature increase. However, in the real experiment as the material flows into the cold mold cavity, it shows cooling as seen in thermocouple 2 temperature drop and later the shear heating effect was seen at location thermocouple 3.

Pressure profiles were recorded at sensor nodes 4 and 5 locations. On Figure 4.9a closer to gate location 4 starts rising slightly earlier than location 5 as expected from the flow direction and as seen on the magnified portions. The simulated node 4 profile, when compared to the pressure transducer in experimental setting in Figure 4.9b, reflects an agreement with pressure rising values during injection stage, but slightly overestimates the peak value. Further along the packing stage the pressure drop is a steeper exponentially decaying function. All that being noted, these variations were minor and

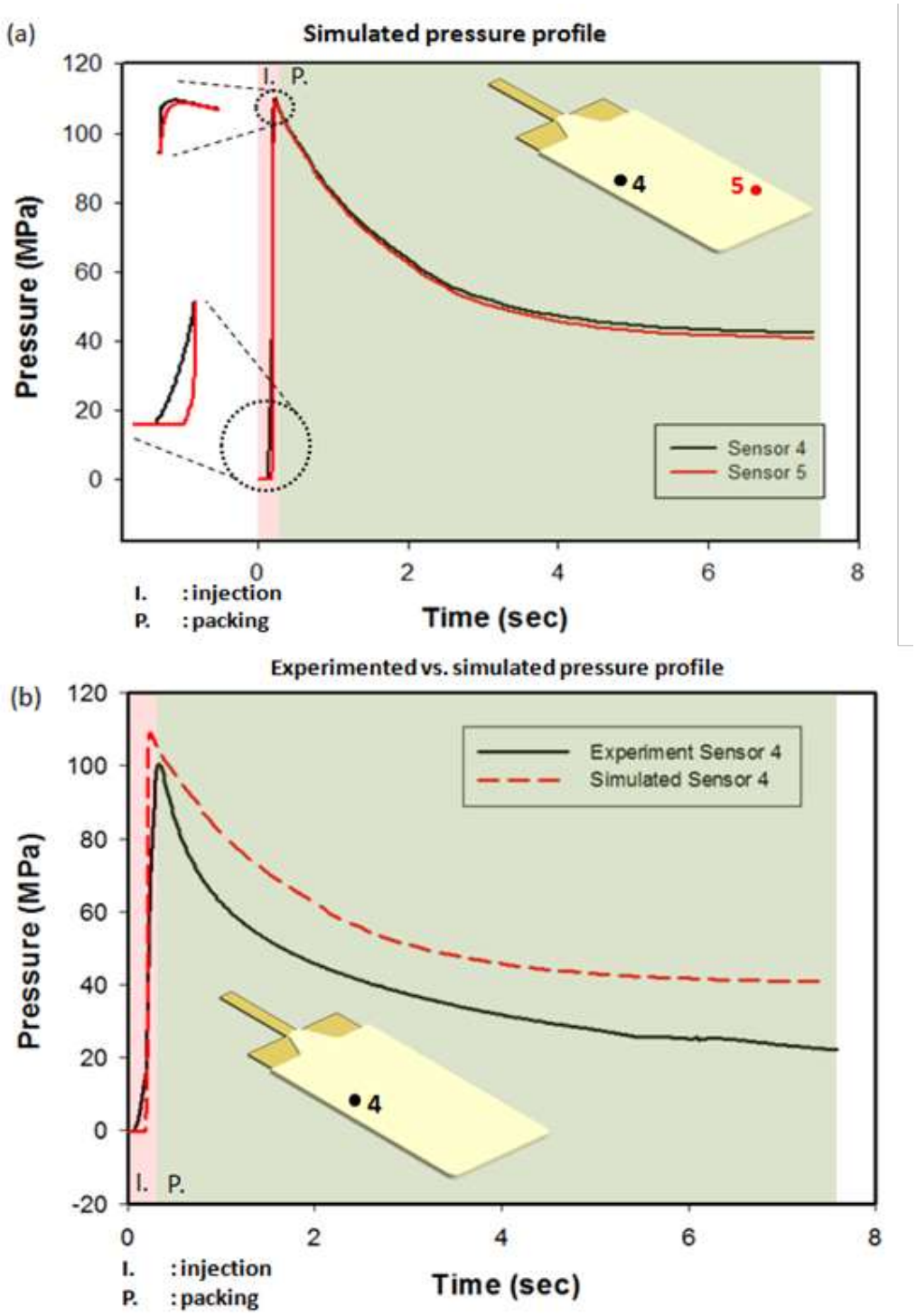

Figure 4.9. Simulation (a) and comparison with experiment (b) pressure profiles at instrumentation points.

the simulations overall were close to experimental results as seen on Figure 4.9b. The compression feature of this process also needed to be optimized. The compression gap settings had significant effect on the part and therefore became one of the main focuses in this study. The gap variation was able to entirely modify the melt flow front geometry as seen on Figure 4.10. Cavity with smaller compression gap was filled faster and the initially convex flow front was changing to a concave one after more than half of the cavity was full. At larger compression gap setting, heat flow front starting geometry does not change as expected from longer filling time and lower pressure values.

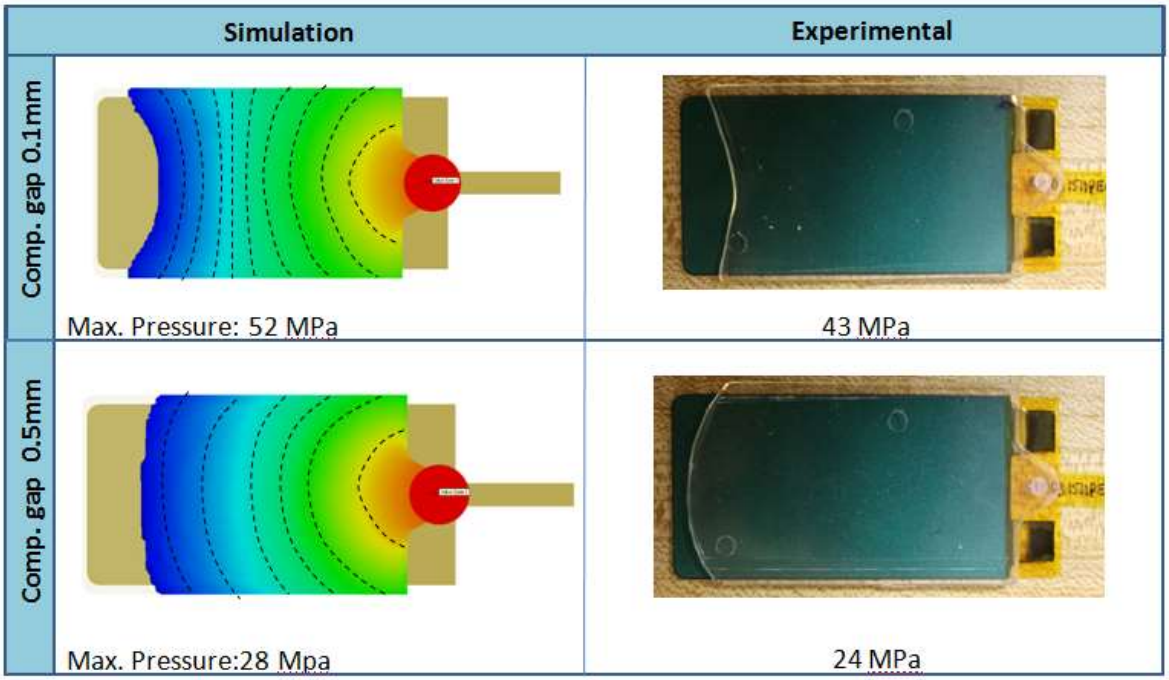

Figure 4.10. Melt front geometry change with different compression gaps experimental and simulation results.

These results are verified with the experimental cases creating short shots with controlled pin gate closure to prevent the entire shot size to flow in the cavity. The flow front profiles were also in agreement with experimental results. The main reason of this observation is the viscosity change of the material during filling. Compression gap distance setting has to be carefully optimized for flow property control. Although, high compression gap setting helps lower the pressure, it causes higher part warpage due to higher residual stresses generated by higher viscosity material flow towards cavity end during longer filling time. On the other hand, the flow front geometry change after the mid length of the part in lower gaps creates symmetrical warpage near gate and cavity end locations of the part with lower residual stresses from short time melt filling.

Injection molding technique creates complex orientation distribution and gradients that significantly affect mechanical and optical properties of materials. Experimental and simulation studies have been conducted on the details of frozen layer formation depending on local thermal history for traditional injection molding [94-97]. As the core mold wall is insulated with PET insert, to be lens encapsulated with injection compression technique, the frozen layer development is both asymmetric and more complex. Flow simulations were computed for 0.5, 1 and 1.5 mm first side (single) and 2 mm second side (double) geometries at Level 2 standard settings and lower compression gap in order to understand lens thickness, compression gap, and encapsulation side effect. The end of filling/packing stage simulated frozen layer profiles are shown in Figure 4.11. Frozen layer thicknesses (FLT) had to be evaluated separately for each effect on the PET insulated core side and cavity mold wall side as shown on Table 4.4. In all cases, melt facing cold wall side forms thicker frozen layer compared to insulated warmer insert case

as expected. Figure 4.11 a, b, c and e cases all show single side encapsulation frozen layer results. The main difference in these cases from the d, double side encapsulation, is that the mold and insert side layer thickness difference was very low (1-4µm) compared to the doubled frozen layer thickness on the double side. The second side encapsulation has a one side TPU encapsulated PET film as "insert", providing a higher insulation on the mold core side, and keeping the cavity side mold warm (~60°C) during injection does not help as much as in the other cases.

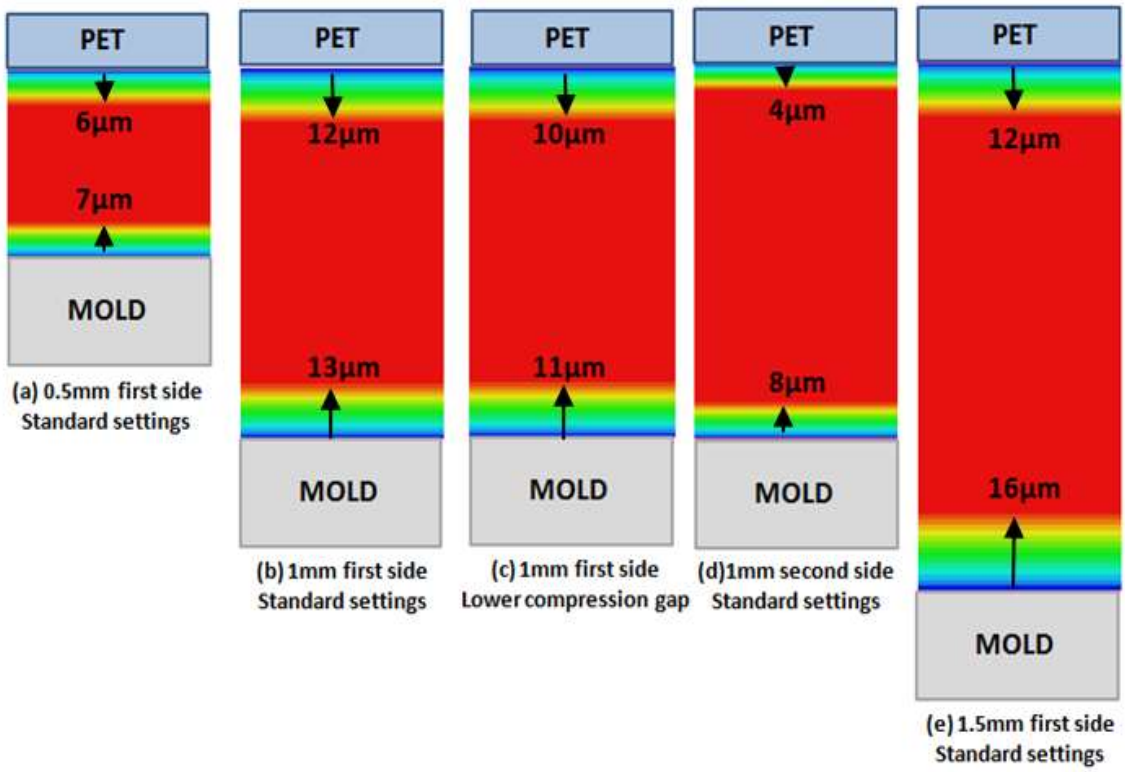

Figure 4.11. Frozen layer development for different encapsulation side (b,d), lens thickness (a,b,e) and compression settings (b,c).

Table 4.4 Mold core and cavity side FLT changes

Mold Side / Effect	**Insulated core side (PET insert)**	**Cavity side (Mold wall)**
Lens thickness	FLT increase from 0.5 to 1mm remains unchanged at 1.5mm	FLT increases with increase
Compression gap	FLT increase with increased gap from 0.1 to 0.5mm	FLT increases with increase
Encapsulation side	Significant FLT decrease on second side injection	FLT decreases at second side

*FLT- Frozen layer thickness

On Figure 4.12, the frozen layer ratio profiles are given to evaluate further the frozen layer development at different settings. Frozen layer ratios normalized by part thickness at current time step were plotted to compare each case's layer development more accurately. The asymmetries in frozen layer thicknesses on two different sides of the part are clearly seen in these graphical representations. Looking at Figure 4.12 a, b and e in this order, asymmetry increases with increasing lens thickness. Considering the ratio of the layer formed with respect to the injected material thickness, higher warpage values were expected from the thinner lens encapsulations (0.5mm). The thick frozen layer thickness insulates the warm inner core, constrains potential shrinkage during cooling, and thus causes high residual stresses on the part. This effect will be further discussed in this section.

Varying residual stresses in the parts are the main cause of uneven part shrinkage at top to bottom layer, and thus, of warpage. These residual stresses have two main components: flow-induced and thermally induced residual stresses. Above the melting temperature, the unstressed long polymer chains are at random-coil conformation and with injection process they are orientated along the flow direction due to complex combination of shear and extensional flow. At cold mold wall contact, a frozen layer forms, and as the material continues to solidify, all oriented polymer material portions that cannot relax have flow induced residual stress. The frozen layer on the part surface due to high shear stress stays highly oriented with high cooling rates. The residual stresses in these orientated structures cause warpage. The inner hot core insulated by frozen part layers has a higher degree of relaxation, and thus, lower orientation [98].

Part shrinkage starts with the cooling of outer surface layers, when the inner core is still in the molten state and can contract. However, when the core starts to cool down the fully frozen rigid outer layers constrain the contraction of the cooling core, resulting in thermally induced residual stress. Core side film insert insulation and cavity side cold mold wall structure leads to a thicker frozen layer on the colder cavity side. This usually results in a net bending moment towards the core side film insert with lower cooling rate. The biaxially oriented film insert material bares residual stresses. After film insert injection molding, if sample is annealed a reverse warpage phenomenon has been reported due to irreversible relaxation of biaxial molecular orientation in film. Before injection process pre-annealed films do not show this behavior when annealed after injection as the pre-annealing releases the biaxial residual stresses on the film thus have expected final warpage form [10, 29-31].

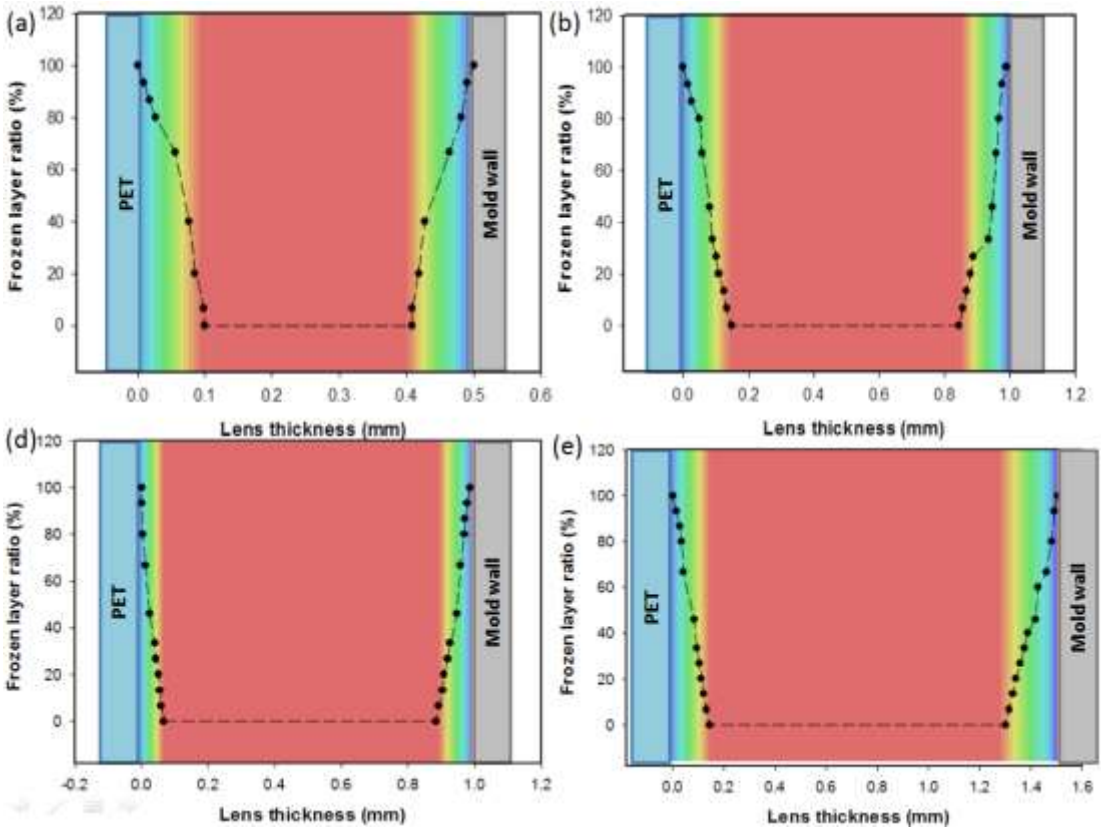

Figure 4.12. Frozen layer ratio along display length at the end of filling step.

Heat treated PET insert injection compression molded parts exhibited the same behavior as reported elsewhere [87]. The expected warpage from part bending moment towards the core side is also simulated and shown on Figure 4.13 A in this study. The slight overestimation of the simulated warpage value compared to the experimental values shown on Table 4.5 can be explained by the simulation assumptions and the narrower temperature profile mentioned earlier. Experimentally, the cooling after injection is slower compared to simulated case, therefore, residual stresses have time to relax during this stage which results in lower warpage. It is important to note that setting cavity side temperature higher than the core side results in more symmetrical frozen layer formation and lower warpage.

Table 4.5. Experimental and simulation warpage results (at standard condition for higher viscosity TPU)

Source (1mm first side)	Warpage (mm)
Experiment	2.83±0.5
Simulation	4.24

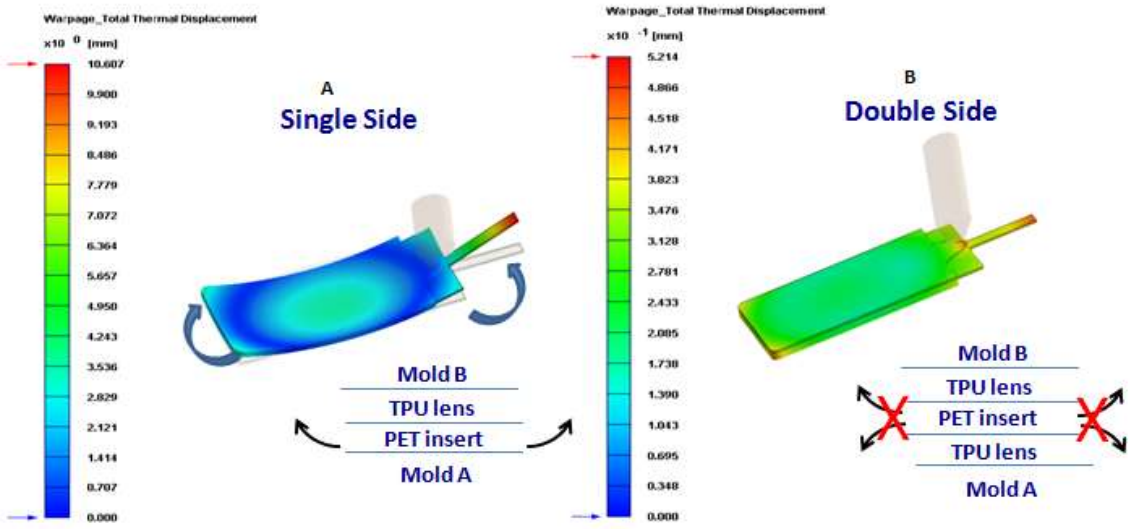

Figure 4.13. Warpage predictions for flexible grade lens encapsulation: (A) single and (B) double side cases.

Double side encapsulated part has very minimal warpage (~452µm) as the TPU injected part stresses cancel out each other being symmetrical on the front and the back of the insert as shown on Figure 4.13 B.

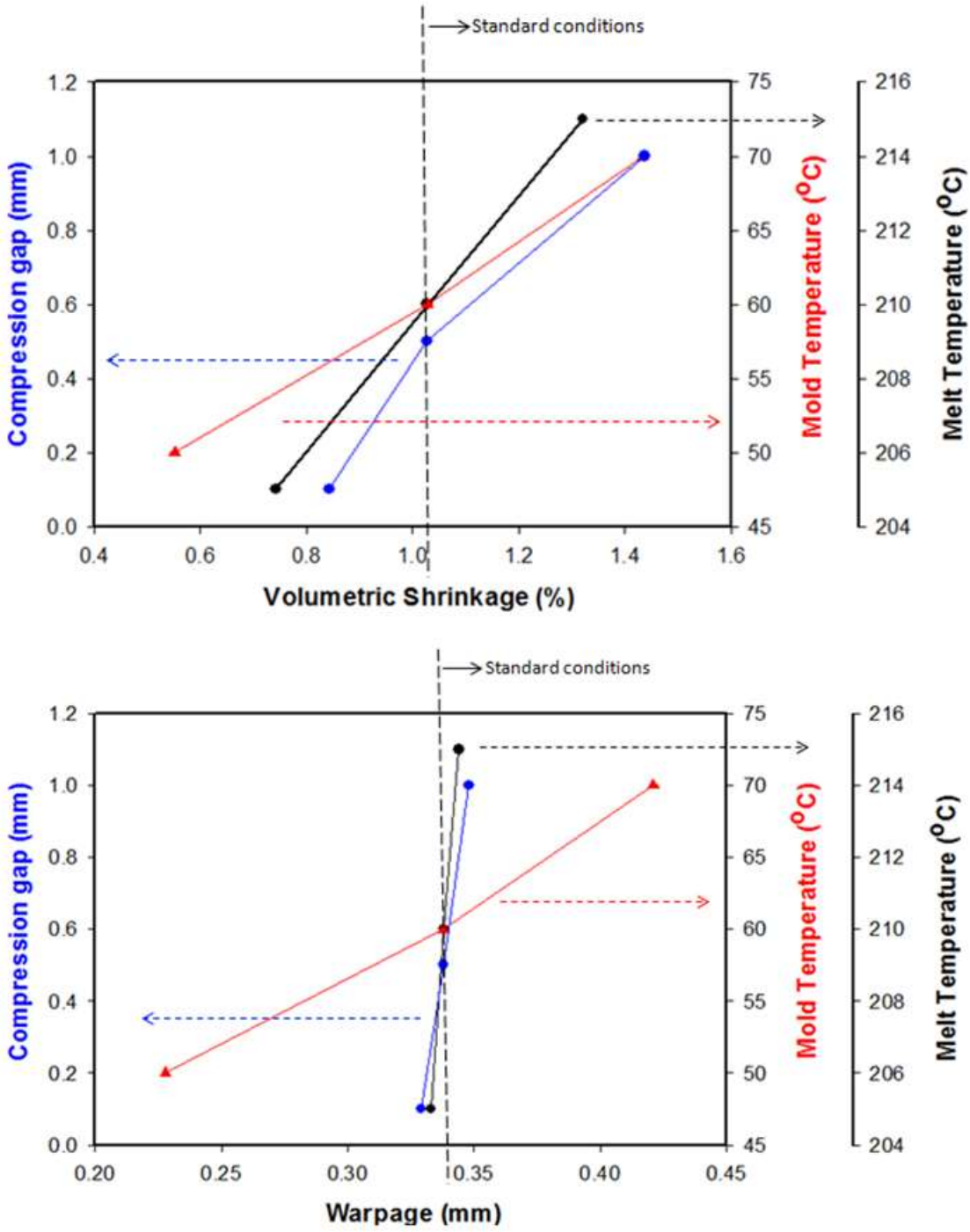

Figure 4.14. Process variables effect on volumetric shrinkage and warpage.

Shrinkage and warpage changes were evaluated for different process condition settings. Compression gap, mold temperature and melt temperature effects are shown on Figure 4.14. The trend was increasing shrinkage and warpage for increasing selected settings of compression gap, mold and melt temperature. The same behavior was reported for the traditional injection molding method [99]. Mold temperature changes caused the highest variation in warpage. These findings are in agreement with the design of experiments (DOE) results of which were presented elsewhere [87].

Low viscosity TPU lens material injected on the film insert had lower warpage compared to high viscosity TPU. Although, both of these materials are flexible (87 A Shore hardness), the root cause of warpage variation can be attributed to their different rheological behaviors as well as their critical surface tensions given in the material section. Lower molecular weight, lower viscosity material flows into cavity without causing high shear stress on part, therefore, had lower residual stresses and warpage as shown on Figure 4.15. The adhesion between the injected TPU material and PET substrate was another influential factor on final warpage. The PET has a higher critical surface tension than the TPUs. Surface tension match between the lens and the insert is dominated by molecular interactions. Dipole-dipole interactions and hydrogen bonding contributes to the adhesion between PET and TPU. Overmolding and PET/TPU blend studies also support this information [100, 101]. Comparing the two TPUs, the high viscosity material has slightly higher critical surface tension than the low viscosity one. The high molecular weight TPU`s long chains, flowing slowly in cavity, can form more hydrogen bonds at the interface with PET substrate. The surface energy match between PET insert and high viscosity TPU results in better adhesion with a higher degree of

adhesive forces. Moreover, the shrinkage on the PET layer due to the process thermal profile [87] contributes to the final warpage at a higher extent when adhesion is stronger between lens and insert. Therefore, the high viscosity TPU lens injected part showing higher total warpage than the low viscosity lens encapsulation is a combination effect of its higher viscosity and better adhesion.

Finally, optical properties were simulated using Moldex3D software. The stress optical constant was fed into the software to obtain an approximation for flow, and thermally induced birefringences Cross sectional birefringence distributions along flow direction and through thickness are given on Figure 16 for single and double side encapsulation cases. The through thickness distribution of flow induced birefringence for

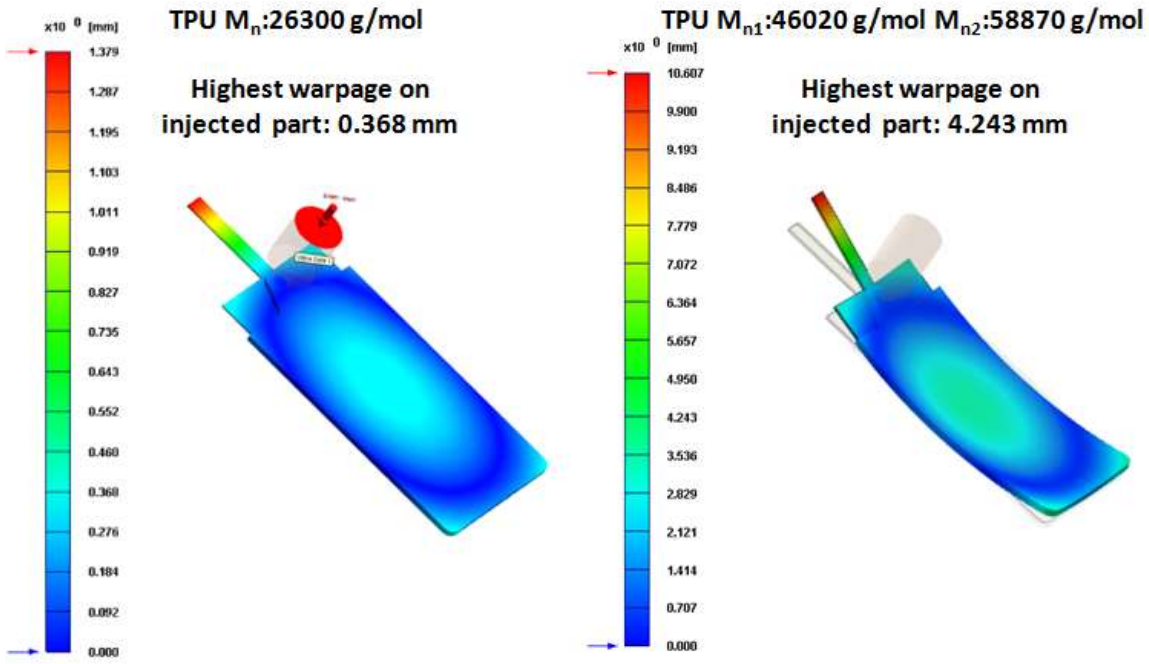

Figure 4.15. Warpage comparison between low and high viscosity TPU injections.

single and double side encapsulations show no differences, having the same process condition settings and comparable frozen layer development as well as residual stresses reported earlier in this section (Figure 4.16 left plots). The flow induced birefringence remains almost zero along the flow direction for both cases. Major differences were observed as expected in thermally induced birefringence at cross sections. The second side was injected on a thicker core side insulation consisting of a layer of PET and TPU lens material, and therefore, higher thermally induced birefringence values were observed near mold wall and film insert boundaries. This outcome was expected from the doubled frozen layer development of cold mold wall cavity side compared to the insulated core side. The filling velocity and shear rate decreases near mold wall and film insert as a result of frozen layer formation. As a result the flow gap narrows down creating a higher velocity and shear rate region at the proximity of the frozen layer, far from the mold wall and film insert. This through thickness flow behavior results in the given birefringence profile with asymmetric peak values at frozen layer boundaries. The asymmetry observed is caused by the thick insert insulated part. The slower cooling of hot core significantly lowers orientation resulting in birefringence minima near the center (closer to mold wall at 0.3 mm). The simulated profile agrees with the previously reported through thickness birefringence distributions in literature [102, 103].

Flow and thermal residual stress development contributions must be well understood for comparative evaluation of flow and thermally induced birefringences. In injection molding, flow induced stresses are due to molecular orientation during filling. Generally, frozen layer on the surface of mold cavity acts as a poor thermal conductor, so molecular orientation in hot core is allowed to relax in later post-filling stages. Usually,

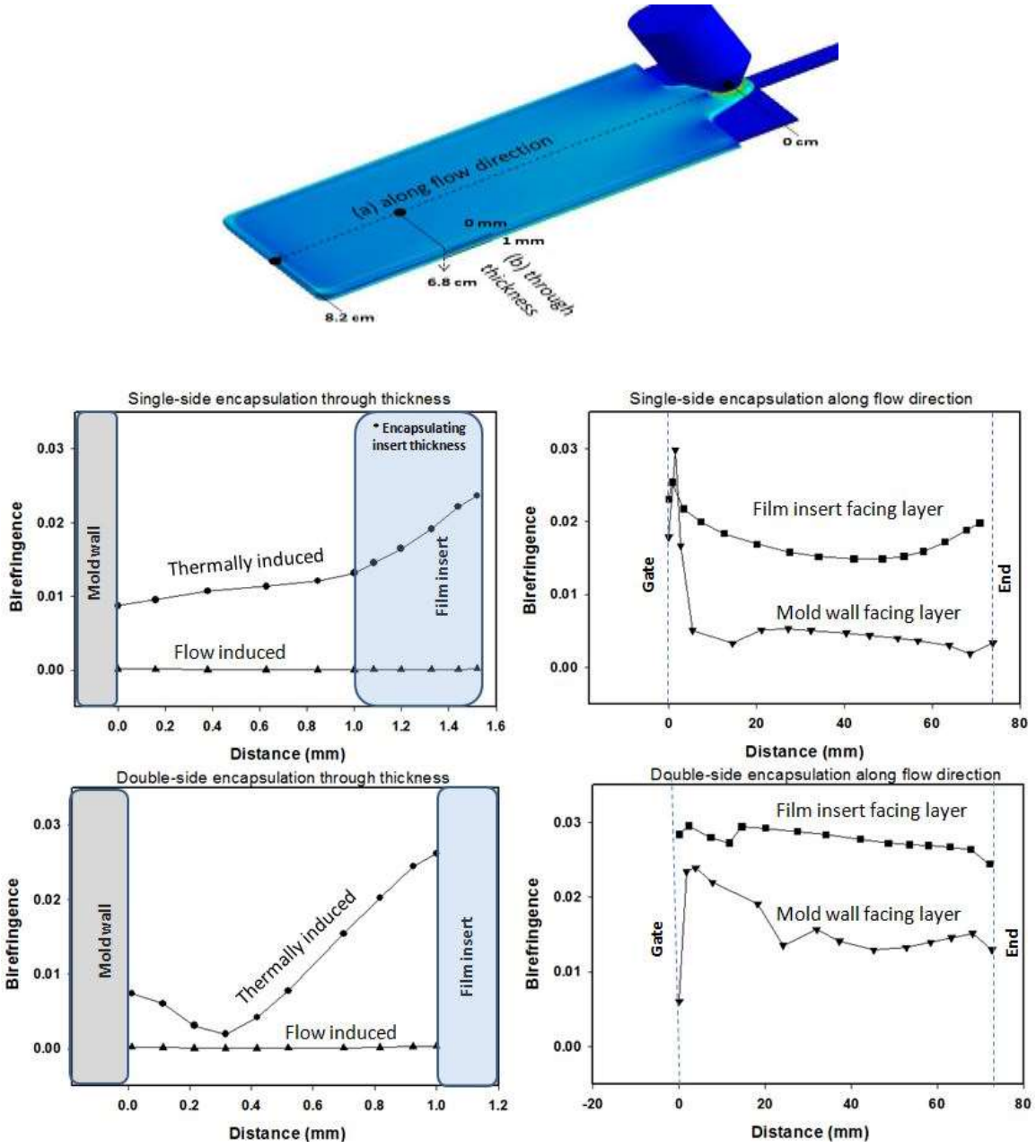

Figure 4.16. Birefringence predictions for 1mm TPU-2 lens encapsulation with data locations for total birefringence distribution on film insert (■) and mold wall (▼) facing layers as a function of (a) distance from gate and thermally (●) and flow (▲) induced birefringences (b) through lens thickness.

flow induced stresses are smaller than thermally induced stresses caused by non-equilibrium contraction during cooling. This effect is observed in distribution results given on Figure 4.16. However, for thin sample injection (e.g. lens thickness < 0.5mm), the part is cooled and frozen in a shorter period, and therefore, has no time for completely relaxed orientation.

The distribution of birefringence as a function of distance from the gate is plotted also on Figure 4.16 for film insert and mold wall facing layers of single and double side encapsulation. First near the gate, the birefringence increases and subsequently, starts to decay exponentially along the flow direction for single side case. This behavior can be explained by the high shear stress causing orientation near the gate and followed by decreasing flow rate towards the end of the cavity. The close to cavity end increases observed can be explained by high shear stress by increased melt viscosity. The back lens injection for double-side encapsulation parts, the close to gate maxima peak were broader compared to single-side encapsulations and did not go through significant exponential decay. This difference is due to insert side encapsulation geometry difference and thicker insulating insert layer presence with previously discussed frozen layer formation. The film insert facing layer birefringence values are higher than mold wall facing layer ones for both cases. The constraints in shrinkage on the insert layer obviously create higher residual stresses on this side. (Please see appendix for complete birefringence distributions parallel to the flow directions.)

Finally, on Figure 17 mold and melt temperature effects on birefringence distribution along melt flow are presented. Three different mold temperatures of 50, 60 and 70°C were set for comparing birefringence distribution on close to mold wall and

film insert side layers. No significant difference is observed on the mold wall side facing layer at different mold temperature settings on Figure 4.17 A. The higher mold temperature setting resulted in lower birefringence. This difference is more pronounced at inner layers as seen from the inner film insert facing layer distributions. When the mold temperature is increased, difference in cooling speed between surface facing the mold mold wall and the surface facing insulating film insert becomes smaller thus residual stresses decrease. On Figure 4.17B higher the melt temperature lower birefringence

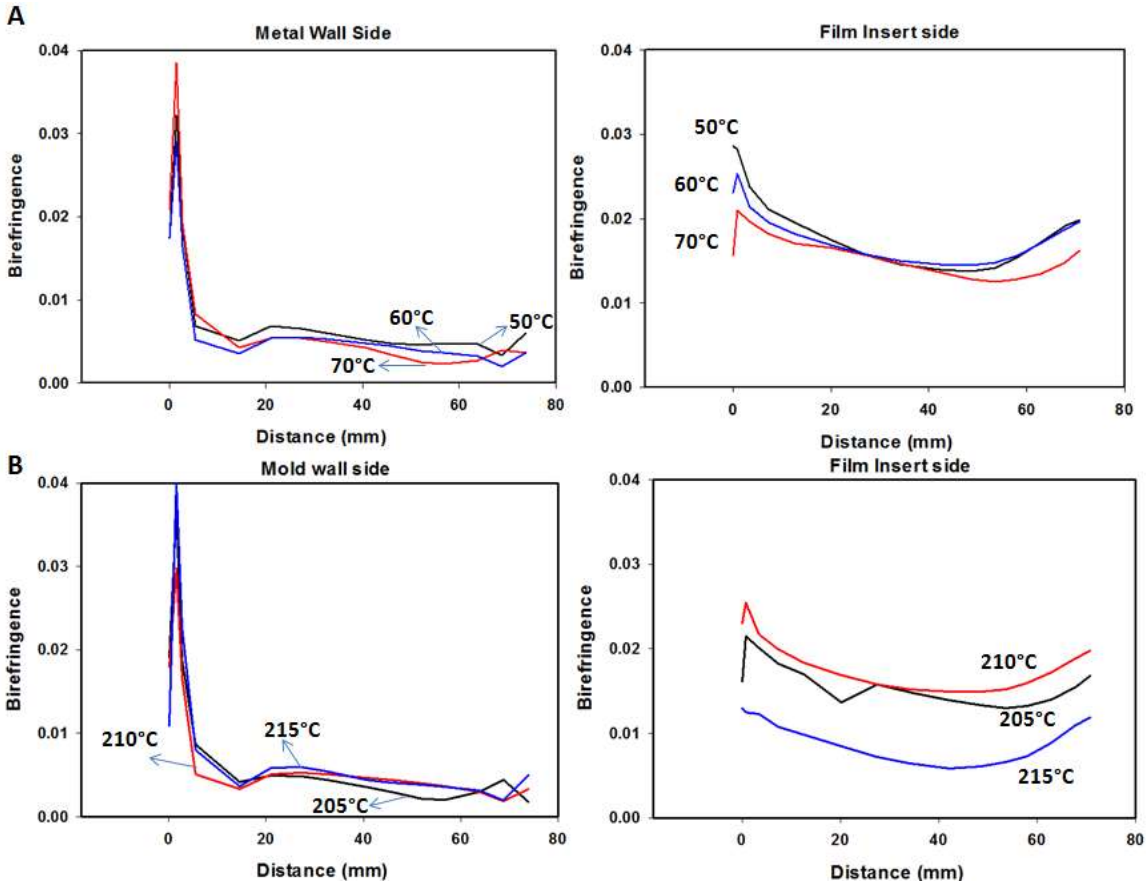

Figure 4.17. Single side encapsulation mold (A) and melt (B) temperature effects on birefringence distribution along flow direction from gate to end cavity.

distribution was more pronounced on the film insert facing side at 215°C compared to similar profiles on the mold wall facing layers with set melt temperatures of 205, 210 and 215°C. The peak birefringence values close to the gate area were due to higher packing pressures on that region.

4.4. Conclusion

In this study, film insert injection compression technique simulation was performed for the first time to compare results with our experimental findings and validate the Moldex3D tool for use in the display encapsulation applications. The real time temperature and pressure profiles, generated using the sensor nodes, were in agreement with the experimental in-mold instrumentation results. The frozen layer development was evaluated for lens thickness, encapsulation side and compression gap setting changes. The most drastic top and bottom frozen layer difference was caused by the second injection step for the double sided encapsulation due to the thick PET and TPU combination insert layer insulating core side of the mold. Smaller the lens thickness, higher the residual stresses observed. Although there were no significant frozen layer thickness differences with varying compression gap settings, it was found to modify the melt front profile from convex to concave when flow front is beyond half of cavity as evidenced by the experimental short shot samples. Compression gap, mold temperature and melt temperature settings were tested on three different levels and the mold temperatures were found to be the most influential factor on part warpage. This result was supported by the experimental DOE performed in another study for this technique [87]. Finally, cross sectional through thickness and along flow direction birefringence

distributions were compared for different side injection and process condition settings. The flow induced birefringence was found to be lower than the thermally induced birefringence for injected lenses as flow induced stresses have time to relax in later packing and cooling stages. The thermally induced birefringence development for second side encapsulation was reported to have significant difference on the thick PET and TPU insulated core side compared to the outer cold mold cavity side layers. Changing melt temperature and mold temperature affected the film insert facing layer more than the mold wall facing layer. At higher temperature settings, birefringence values decreased throughout the distribution on film insert facing side. This effect was expected for higher mold temperature settings as the cooling rate difference between mold facing layer and insert facing layer decreases. Also, for higher melt temperature settings, warmer melt cools down slower and the relaxation on the film insert insulated side is higher compared to the one at lower temperature settings.

Overall, this study shows that commercial Moldex3D software simulates close to real case results and can be used for different display insert encapsulation material injection compression molding technique. This effective processing method can replace the labor intensive, adhesion layer requiring lamination techniques in the future.

CHAPTER V

SHRINKAGE CONTROL ON POLYETHYLENE TEREPHTHALATE FILMS VIA REAL-TIME PROCESS OPTICAL MEASUREMENTS

5.1 Introduction

Thermal shrinkage control is very important for substrate films used in display electronics industry. Thermal expansion coefficient match of substrate layer with the display base material is desired to avoid delamination during thermal cycling tests performed to check device reliability. Most commonly these substrate materials are prepared through biaxial stretching followed by heat setting, typically by tenter frame processes for mass production in industry. In tenter frame process a polymer sheet is extruded from a flat die onto cooled rolls to quench it into amorphous state then stretched at 20-30°C above glass transition temperature (Tg) for machine direction orientation. Following this step, transverse direction orientation happens on the film carried into an oven held by tenterhooks. The long residence time in oven allows processing of slow

crystallization rate polymers such as polyethylene terephthalate (PET). The orientation in both directions can be independently controlled using this process.

Stress-induced crystallization and structural order establishment [104, 105], amorphous phase orientation [106, 107] at above Tg sequential biaxial drawing of PET has been studied and found that phenyl rings perpendicular to amorphous phase tend to become perpendicular to the draw direction. Structural and optical assessments has been established showing PET has a triclinic unit cell [50] and intrinsic birefringence for amorphous and crystalline phases [108].

Later on Cakmak et al [109, 110] used real-time birefringence to monitor the changes during crystallization of preoriented poly(ethylene terephthalate) poly(ethylene naphthalate), poly(ether imide), and poly(ether ether ketone) and poly(lactic acid) films. These studies revealed that low crystallization rate temperature annealing in relaxation followed by a rapid rise in birefringence that accompanies crystallization. This behavior is especially observed on low stretch ratio films. Structural changes were shown to be very fast for intermediate stretch ratios, whereas slow for high stretch ratios due to network formation above certain crystallinity.

Currently, PET retardation films for LCD applications are prepared with sequential biaxial stretching. Optical properties are tailored through the combination of deformation in machine (MD) and transverse (TD) directions at optimum stretching rate and temperature [66, 67].

The display substrate material candidates are also expected to meet many specifications for optical clarity, surface smoothness, good barrier as well as thermal performance especially minimal shrinkage. The later property can be minimized by

dimensional stabilization using heat setting [68]. Heat setting process relaxes residual stresses within the biaxially oriented parts. Processing conditions effect [69-74], morphology-orientation contribution [75, 76], to shrinkage as well as its kinetics [77] and models [78, 79] has been reported for various PET applications. However, none of these previously reported works to understand shrinkage are coupled with real-time mechano-optical property monitoring technique.

Understanding of detailed structural mechanisms during various stages of processes and monitoring of birefringence for ultimately controlling structural parameters real time is crucial for tight control shrinkage required applications. The purpose of this work is to investigate the real-time birefringence measurements during sequential biaxial stretching and heat setting combined with thermal analysis to shed light on controlled shrinkage properties of PET substrates.

5.2 Experimental

5.2.1 Materials

Commercial polyethylene terephthalate (PET) films were used in this study and were provided by M and G polymers. The films dissolved in phenol/tetrachloroethane 60/40 had intrinsic viscosity of 0.80dl/mg. Mark-Houvink relationship (Equation 1) is used to calculate the corresponding number average of 28500.

$$[\eta] = k \cdot \bar{M}_n^{a} \quad (1)$$

where k is 7.5×10^{-4} and a 0.68[208].

5.2.2 Methods

5.2.2.1 Biaxial Stretching System

Highly instrumented and customized biaxial stretching system is used in sequential biaxial stretching mode in this study. Real-time true stress, true strain, in- and out-of plane birefringence monitoring is possible with this unique system instrumented by our group [1]. The system includes a spectral birefringence instrument consisting of detectors and light sources located perpendicular and at 45° angle to the tested substrate. Figure 5.1 shows the dot pattern created on 14 cm x14 cm sample and tracked by CCD camera during process.

Film sample were inserted into unit heated to stretching temperature of 90°C for an hour to reach equilibrium. The sample was constrained from all four sides by regularly spaced and pneumatically activated clamps. Once, sample in and chamber and door closed, 10 minutes additional time to equilibrium was counted before stretching start. PET films are stretched with a rate of 1.5 mm/sec (0.0125 s-1). Different sequential biaxial stretching ratios of 1.5x1.5, 2x1, 2x1.5, 2x2, 2.5x1, 2.5x1, 2.5x1.5 and 3x1 and time slicing experiment on final ratio has been conducted. The sequential biaxial stretching is composed of two stages: first stretching in machine direction (MD) with constant sample width, where the transverse direction motor is not activated then, second stretching in the transverse direction (TD) with constant sample length, where machine direction motor is not

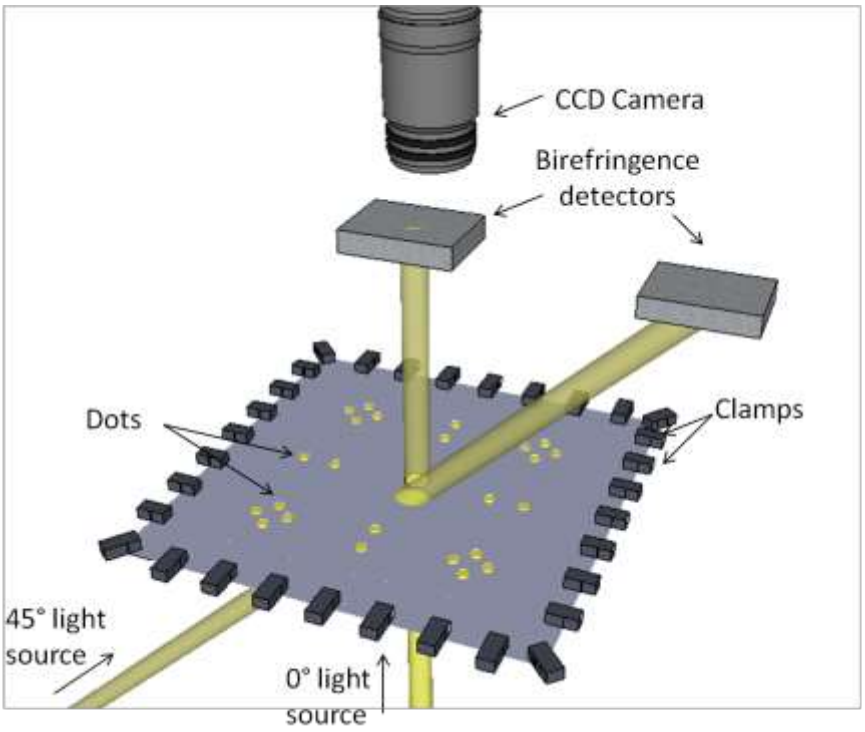

Figure 5.1 Instrumentation and sample with dot pattern attached to biaxial stretcher clamping unit.

activated. Samples were cooled down below T_g (72°C) before removal from the clamps after stretching.

The true stresses and true strains were calculated through the CCD camera dot separation assuming constant volume principle with changing thickness and area as below:

$$t_A = \frac{V}{Sep_x \, x \, Sep_y} \tag{2}$$

where, t_A is apparent film thickness, V constant film volume and Sep_x and Sep_y dot separation in x and y directions respectively. These separations multiplied

with film thickness provide film cross sections named CS_x and CS_y. From which the true stresses are calculated with the forces recorded at each direction $F_x(t)$ and $F_y(t)$.

$$\sigma_{Tx} = \frac{F_x(t)}{CS_x(t)} \tag{3}$$

$$\sigma_{Ty} = \frac{F_y(t)}{CS_y(t)} \tag{4}$$

Finally, the true strain is calculated as in equation 5 from L_o as the initial separation between the dots then ΔL is the difference in the dot position from frame to frame.

$$\varepsilon_t = ln\,(1 + \frac{\Delta L}{Lo}) \tag{5}$$

5.2.2.2 Heat Setting System

Heat setting experiments are carried out in the optical heat setting set up designed in our laboratories as shown in Figure 5.2. The films used for the heat setting process were stretched at the rate of $0.0125s^{-1}$ in sequential biaxial and uniaxial mode at 90°C. After stretching the samples were cooled quickly using both the in-unit cooling system and an external fan. Die cut samples as shown in upper right corner of Figure 5.2 were mounted to circular sample holder for all direction constrain then, inserted in oven guide rails.

Prepared samples were inserted into oven at desired heat setting temperature (170°C or 190°C) and time. Retardation measurements collected spectrometer

light detection through optical windows and sample. The in and out-of-plane birefringences are calculated as shown in equation 6 and 7 (Stein`s equation) using 0° and 45° retardations collected, respectively.

$$\Delta n_{12}(t) = \frac{R_o(t)}{d} \tag{6}$$

where, $R_0(t)$ is 0° retardation, d constant film thickness for heat setting and

$$\Delta n_{23}(t) = -\frac{1}{d(t)} \frac{\left[R_0(t) - R_{45}(t) \left(1 - \frac{Sin^2 45}{1.57^2} \right)^{0.5} \right]}{\frac{Sin^2 45}{1.57^2}} \tag{7}$$

$R_{45}(t)$ is 45° retardation, 1.57 average refractive index for the used PET.

When heat setting time complete, sample is pushed down the rails through a spring loaded bottom door into a cold water bath for rapid quenching.

5.2.3 Thermal Analysis

As cast film, stretched and heat set samples were thermally analyzed using a TA instrument Q800 dynamic mechanical analyzer in thermal mechanical analyzer mode and Q2000 differential scanning calorimeter.

5.2.3.1 Dynamic Mechanical Analysis (DMA)

A constant force of 0.05N applied on 7 mm length and 3.5 mm width cut samples for measuring dimensional changes as a function of temperature with a

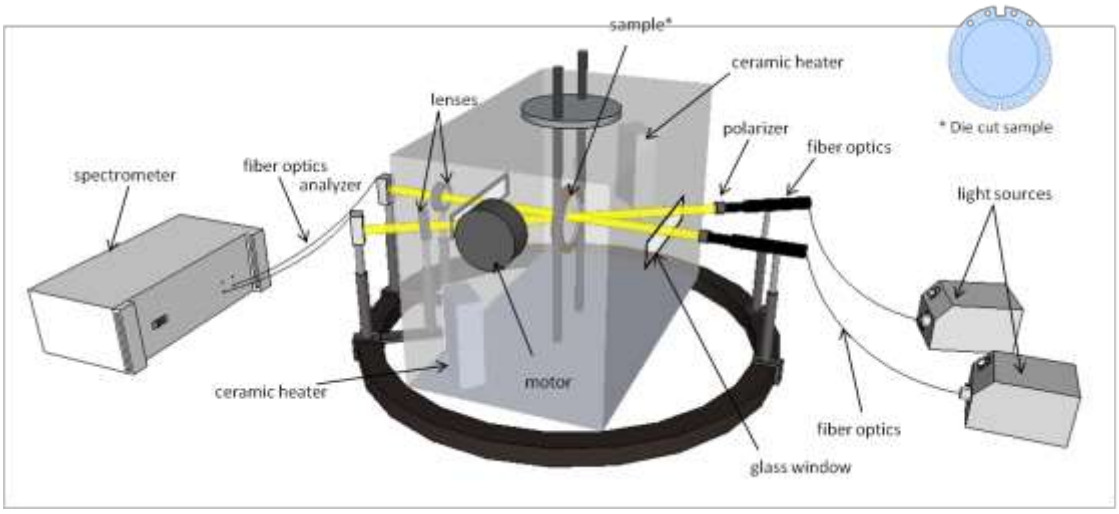

Figure 5.2. Multi-angle heat setting device setup.

heating cooling rate of 5°C per minute. The samples were heated up from 40 °C to 180°C and cooled back again to 40°C. Percent shrinkage values were calculated using the ratio of length difference (Δl) to the initial length (l) of the sample as below:

$$\text{Shrinkage } \% = \frac{\Delta l}{l} * 100 \qquad (8)$$

5.2.3.2 Differential Scanning Calorimetry (DSC)

Around 8mg of films were placed in aluminum sample holders and crimped. The samples were heated from 20°C to 280°C at the rate of 20°C/min. The glass transition temperature, T_g, the cold crystallization temperature, T_{cc} and the melting point, T_m are determined from the heat flow charts for each sample. Area

under the cold crystallization peak, ΔH_{cc}, and under the melting peak, ΔH_m are determined and the percentage of crystallinities are calculated using Equation 9 in order to evaluate the effect of the stretching conditions on the crystallinity.

$$\text{Crystallinity } \% = \frac{\Delta H_m - \Delta H_{cc}}{\Delta H_m^{\circ}} x100 \qquad (9)$$

where, ΔH_m° is heat of fusion of 100% crystalline PET, which is 120 J/g [111].

5.2.2 Structure Analysis

5.2.3.1 Wide Angle X-ray Scattering (WAXS)

The WAXS patterns were obtained using a Bruker AXS Dimension D8 X-Ray system with Cu Ka radiation and 180 seconds count**.** The X-ray samples were prepared from the as cast, stretched and heat set films by cutting into strips then stacking them to get 2 mm thick samples. The X-ray patterns were taken through two orthogonal directions: the normal direction (ND) to the film surface to give the through view and through the machine direction (MD) to get the edge view setting the sample stage at $2\theta=0°$, $\phi=0°$ and $\chi=90°$ to get the best possible view for the crystallographic diffractions.

5.3 Results and Discussion

5.3.1 Real-time Mechano-Optical Behavior

The real-time mechano-optical behavior of uniaxial constant width (UCW) and biaxially stretched sample at 90°C are presented in this section.

Temporal in and out-of-plane birefringence evolutions are given in Figure 5.3 for different stretch ratios. At first stage with the MD stretching, both the in plane and out of plane birefringences are increasing. Starting the second stage with the TD stretching, the in-plane birefringence decreases, while the out of plane birefringence continues to increase for 2x2 and 2x1.5 samples. The effect of the TD stretching on the out of plane birefringence is more significant compared to the effect on the in-plane birefringence as the higher slopes observed. This behavior is reported being a direct result for the chain orientation induced by the stretch in the TD direction [111].

The structural order of PET with respect to different stretch ratios were investigated through WAXS diffraction patterns combined in Figure 3. The triclinic PET unit cell has $(\bar{1}05)$ planes perpendicular to the chain axis, (100) planes parallel to the phenyl planes and (010) planes of 80° and 59° to the $(\bar{1}05)$ and (100) planes respectively. No sign of crystallinity observed until 2.5x1 stretching ratio in the WAXS patterns. The UCW samples with crystalline signs, 2.5x1 and 3x1 stretching have (010) planes aligned on the equator as expected from uniaxial drawing. The increase in transverse direction stretching causes spreading of diffractions as seen at 2.5x1.5 stretched sample. The phenyl rings aligns parallel to the film surface on those biaxial stretching modes. The

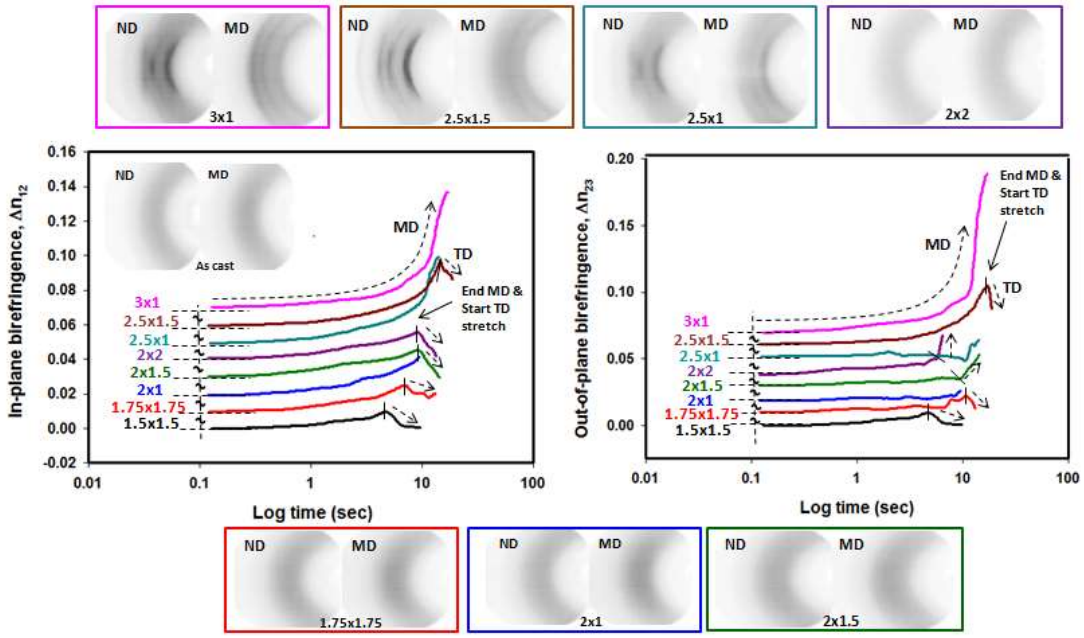

Figure 5.3. In-plane and out-of-plane birefringence evolution of sequentially biaxially stretched PETs -values shifted (~) in the Y-direction for illustration purposes.

final in and out-of-plane birefringence values are also higher for the higher stretching ratio samples supporting signs of crystallinity on WAXS patterns.

Mechanical response trends are given by the true stress-strain plots in the transverse and machine direction at different stretch ratios in Figure 5. 4. Plots are separated for UCW (left upper and lower graphs) and biaxial (right upper and lower graphs) results. At first stage with the MD stretching, the true strain (ε_{11}) increases as the monitored dot movement used for calculations is in MD as well. Later at second stage with the TD stretching, initially, the stress and strain drop while retraction happens then, increases again with further stretch. The material is rejecting to relax back with the TD

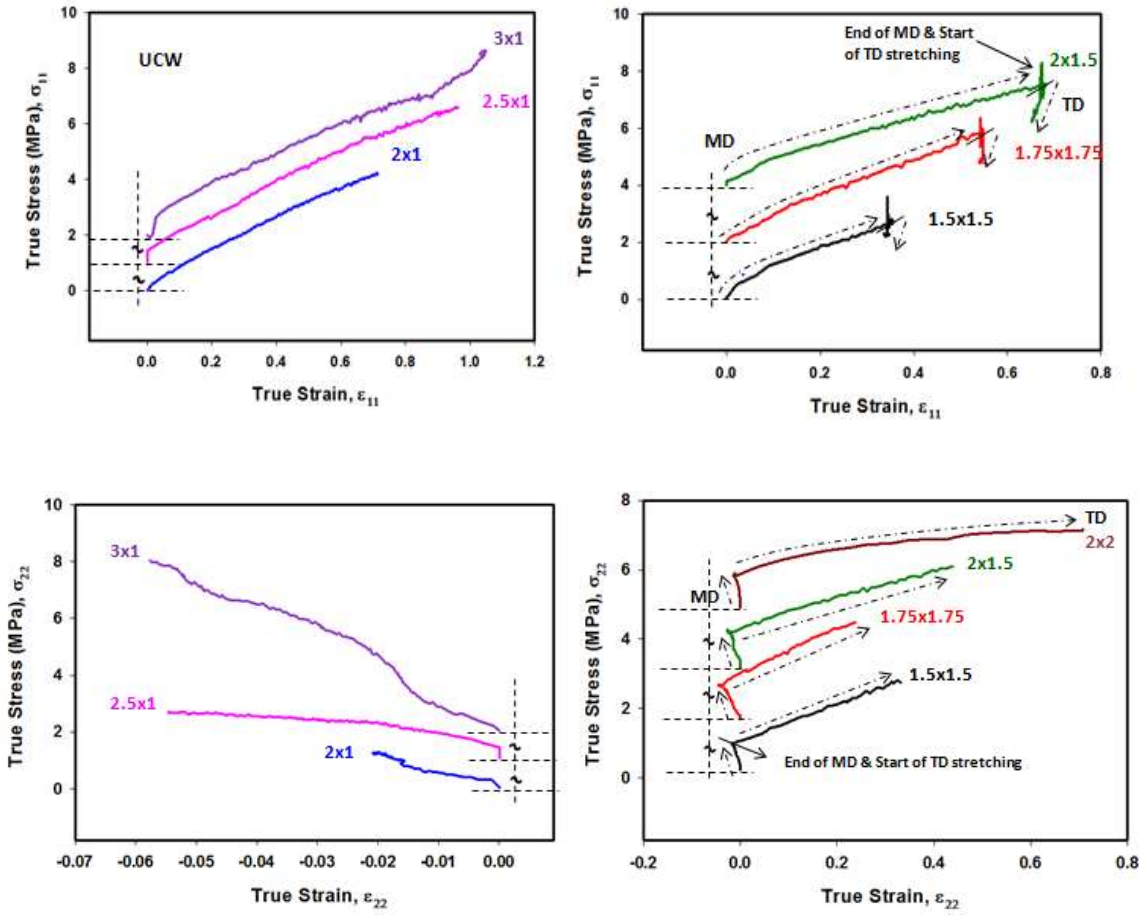

Figure 5.4. Stress-strain behavior of sequentially biaxially stretched PETs on machine (indicated by subscript 11) and transverse (indicated by subscript 22) direction results - values shifted (~) in the Y-direction for illustration purposes.

stretch and held constrain in MD. The retraction was observed as negative strain observed when graphs plotted for the TD true stress (σ_{11}) versus true strain (ε_{22}).

Stress-optical behavior is given in Figure 5.5 for UCWs of 2x1, 2.5x1 and 3x1. The stretching ratio effect is higher on in-plane birefringence compared to out-of-plane one at lower draw ratios whereas, at 3x1 the out-of-plane birefringence is as significant.

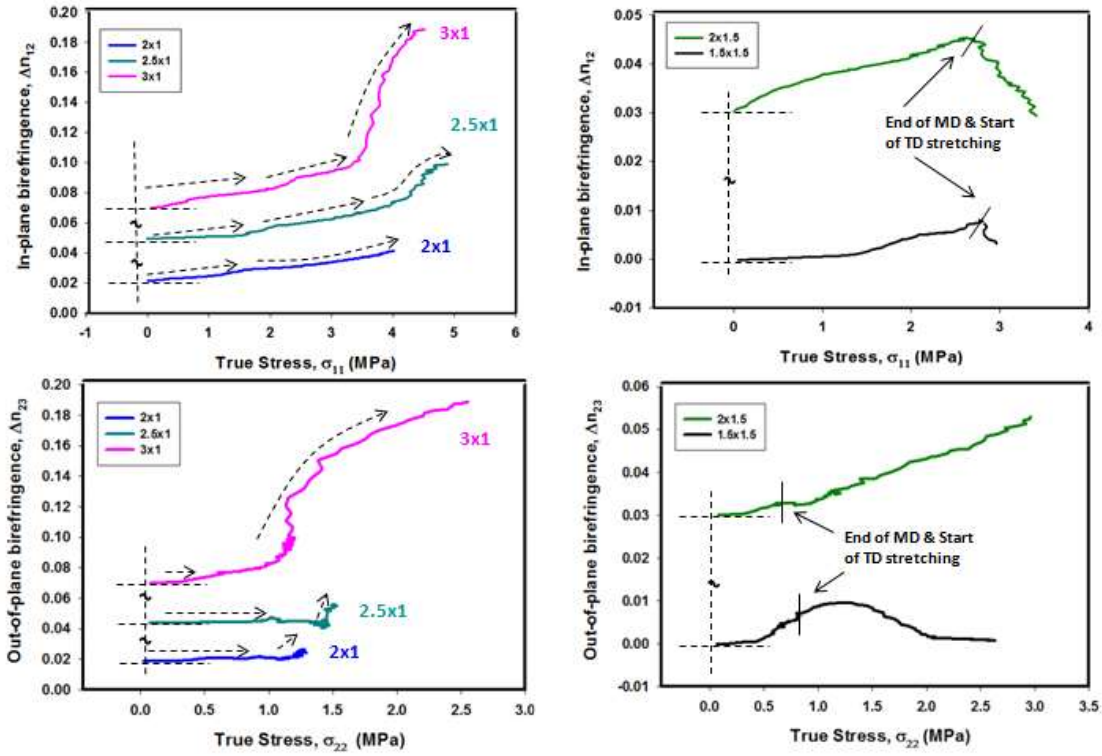

Figure 5.5. Stress optical behavior of sequentially biaxially stretched PETs

As also previously reported [1, 112], increase in MD stretching align chains planar in MD-TD plane and increase in TD stretching cause orientation in film plane with uniform distribution between the MD and TD directions. Considering the MD stretching pre-induces an orientation in TD direction, the balanced biaxial orientation will be achieved with a lower TD stretching ratio than the MD stretching ratio in sequential mode.

5.3.2 Optical Behaviour During Heat Setting

5.3.2.1. Heat Setting at 170^{o} C

In and out-of-plane birefringence evolution during heat setting of UCW and sequential biaxial stretch samples at 170°C are given in Figure 5.6 and 5.7. The heat setting of equal biaxially stretched samples of 1.75x1.75 and 2x2 had lower in-plane birefringence values. Although the 2x2 sample birefringence did not change throughout the process, the 1.75x1.75 birefringence decreased after a short induction period. The higher stretching ratios show slight increase after the induction period except the UCW sample of 2x1 stretching which goes through an initial increase followed by a decrease.

The wide-angle X-ray diffraction patterns for the heat set at 170°C samples are also shown in Figures. Higher intensity sharper diffraction peaks observed after heat settings compared to the as stretched sample patterns shown in Figure 5.3. At low stretching ratio of 1.75x1.75, no preferred orientation observed on the crystallization peaks. The film planarity increases with the increasing transverse direction stretching as well as heat setting. The (100) crystal plane which appears with weak diffraction patterns for as stretched samples, preferentially orients into the film plane with heat setting, showing sharper, higher intensity diffraction peaks. The non-existing $(\bar{1}05)$ plane patterns on as-stretched samples appear in the heat set sample samples also, as a result of orientation of the phenyl rings in the film plane.

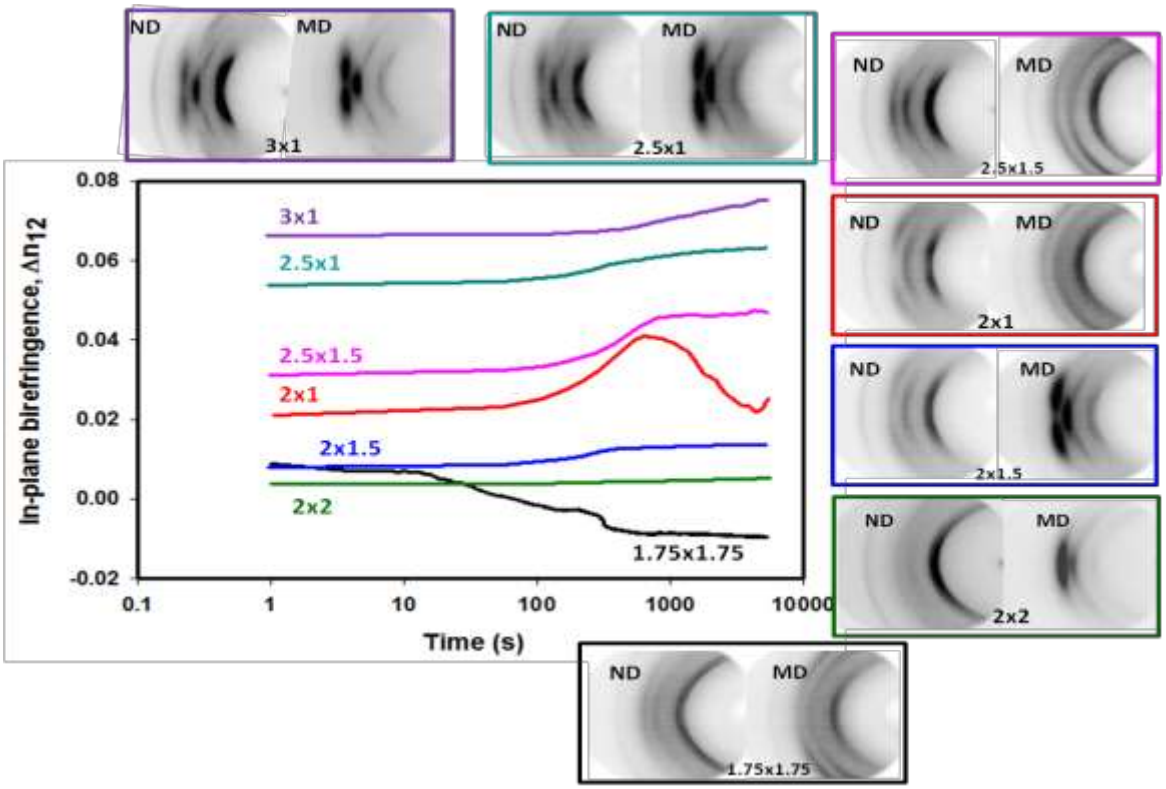

Figure 5.6. In-plane optical behavior during heat setting sequentially biaxially stretched PETs at 170°C.

For the out-of-plane birefringence distributions, the trends were more complicated therefore, evaluated in Figure 5.7 separately for sequential (left) and UCW (right) biaxially stretched samples. The 1.75x1.75 stretched sample show decreasing trends throughout the heat setting process: lower slope induction period followed by higher slope decrease and level off behavior after 10 minutes of heat setting. The higher stretch ratio samples show after induction period rapid decrease in birefringence. Separately, the 2.5x1.5 stretch sample has and increasing birefringence trend after 15 minutes of heat setting. Similar behavior from the UCW 2x1 and 2.5x1 samples was observed with higher stretching ratio having lower end birefringence. For

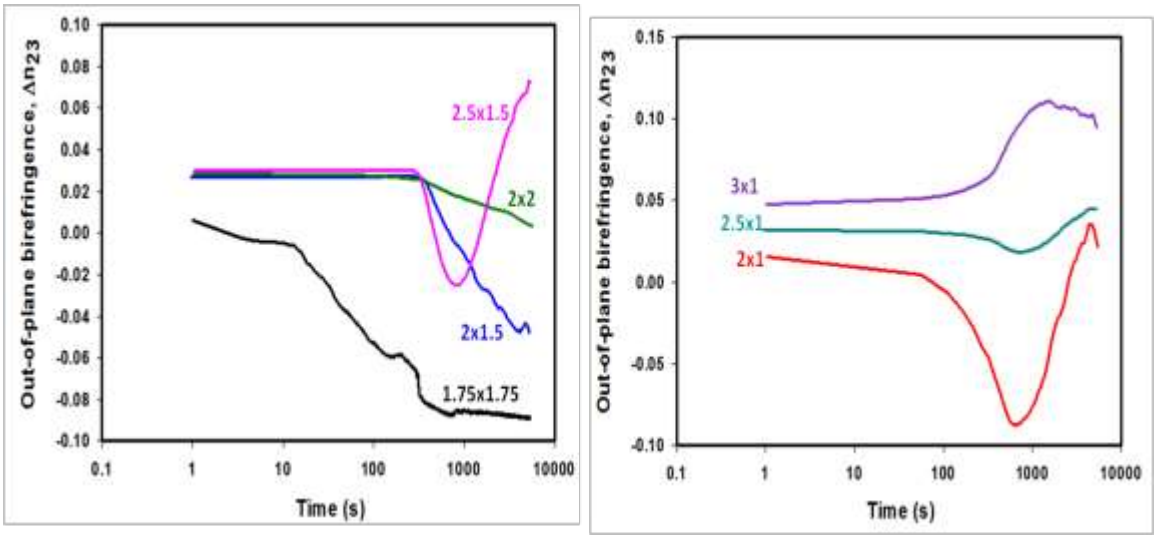

Figure 5.7. Out-of-plane optical behavior during heat setting sequentially biaxially stretched PETs at 170°C.

3x1 stretching, the induction period is followed by increase and level off after 15 minutes.

5.3.2.2. Heat setting at 190^{o} C

The in-plane birefringence results during 190°C heat setting shown in Figure 5.8 are similar to the ones at 170°C. The UCW sample birefringences were higher than the sequential biaxially stretched samples with increasing transverse direction stretching sample.

The out-of-plane birefringence trends during 190°C heat setting show two different trends for low (upper graph) and high (lower graph) stretching ratios in Figure 5.9. The lower stretching ratios had an induction then an increasing birefringence followed by decrease. The equal biaxial stretching samples 2x2 and 1.75x1.75 had higher birefringences compared to UCW 2x1 stretched sample. The complete reverse behavior to the low stretch ratio samples is seen for the ones with

high stretching ratios. The UCW stretched samples, 3x1 and 2.5x1 this time show higher birefringences than 2.5x1.5 sequential biaxially stretched sample.

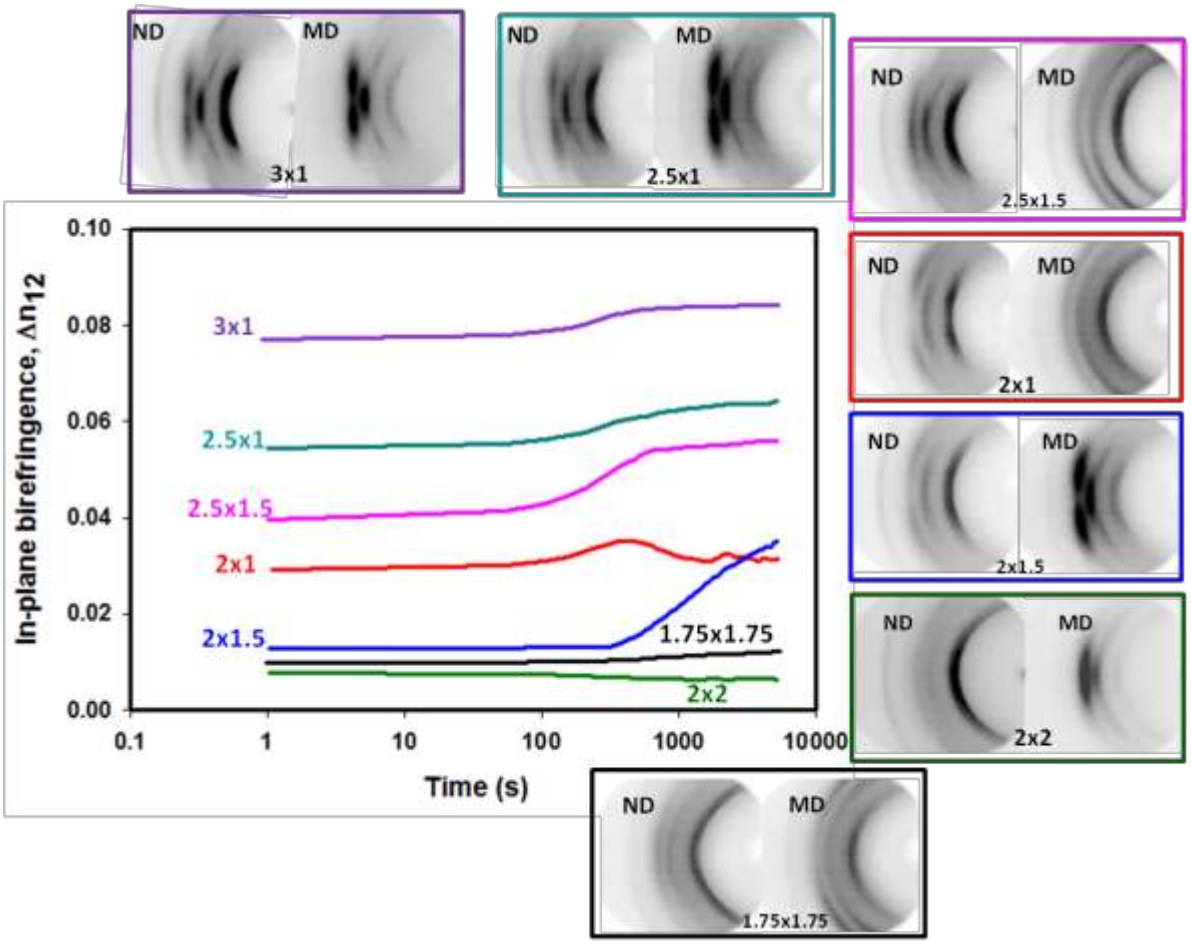

Figure 5.8. In-plane optical behavior during heat setting sequentially biaxially stretched PETs at 190°C.

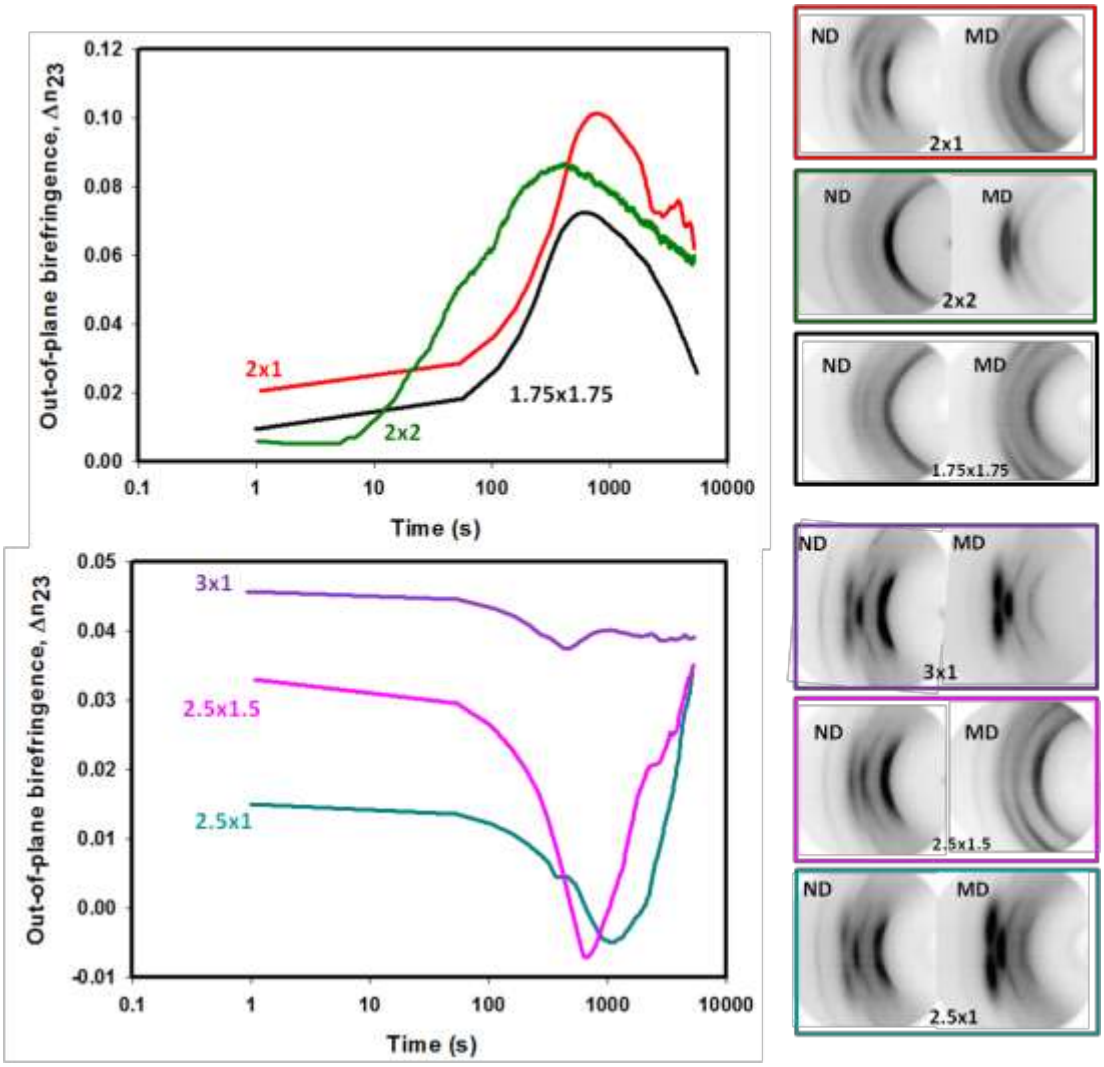

Figure 5.9. Out-of-plane optical behavior during heat setting sequentially biaxially stretched PETs at 190°C

5.3.2.3 Heat Setting Time-Slicing

The UCW 3x1 stretched samples are put through a periodic time-slicing study up to 9 hours to monitor structural evolution during 190°C. This stretching is selected being the highest stretch ratio with well-developed high crystalline domains. Birefringence time evolution is given in Figure 5.10 along with check points with different heat set checkpoints. The induction period is around 1 minute at which no

significant orientation observed. The increase of in-plane and decrease of out-of plane birefringence happens within the 15 minutes. Level off stage is follows up to 3 hours from which increases for both in and out-of plane birefringences. The WAXS diffraction patterns are shown on the figure for different heat set points from 3 seconds up to 9 hours. Increasing the heat setting time crystalline peaks got slightly higher intensity and sharpness. The contrast between crystalline and amorphous regions also increases as the amorphous hallo gets lighter as a sign due to the increasing transformation from the amorphous to the crystalline phase. The reflection of the $(\bar{1}05)$ ring becomes more pronounced with increasing planarity of the phenyl groups in the film plane as seen on the normal direction (ND) patterns. The $(\bar{1}10)$ and (100) diffraction planes can be defined on the machine direction (MD) patterns.

5.3.3 Thermal Characteristics

5.3.3.1 As Stretched Samples

DSC thermograms for sequentially biaxially stretched samples are given in Figure 5.11. The "as cast" film thermogram shows a glass transition temperature, T_g around 79°C, a cold crystallization temperature, T_{cc} around 153°C and a melting temperature, T_m around 252°C. The melting peak area increased with the increase in stretching ratio in MD and TD. At lower stretch ratios, the crystallization exotherm increased in area whereas, at higher stretch ratios decreased in area and even flattened moving towards lower temperatures for all stretching ratios. The glass transitions did not change at low ratio but, flattened and shifted to slightly higher temperatures at higher ratios.

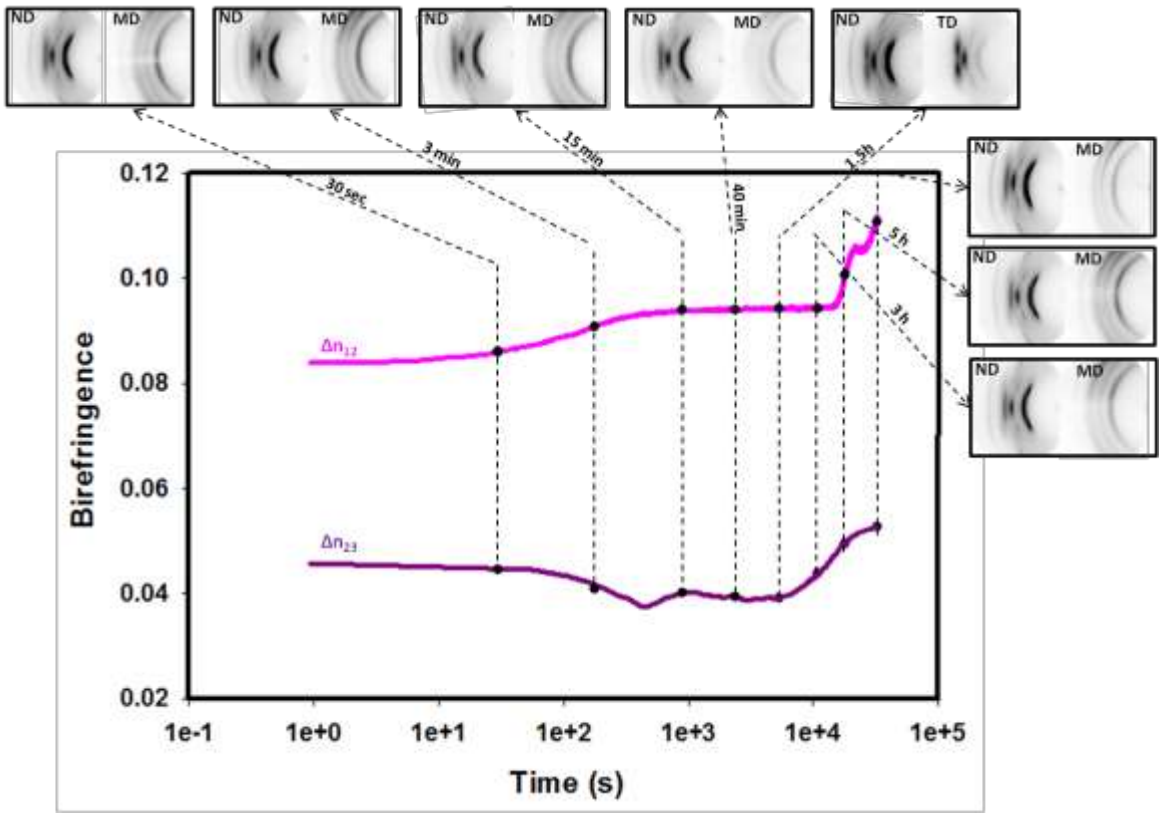

Figure 5.10. Optical behavior during heat setting 3x1 UCW PETs at 190°C and time slicing.

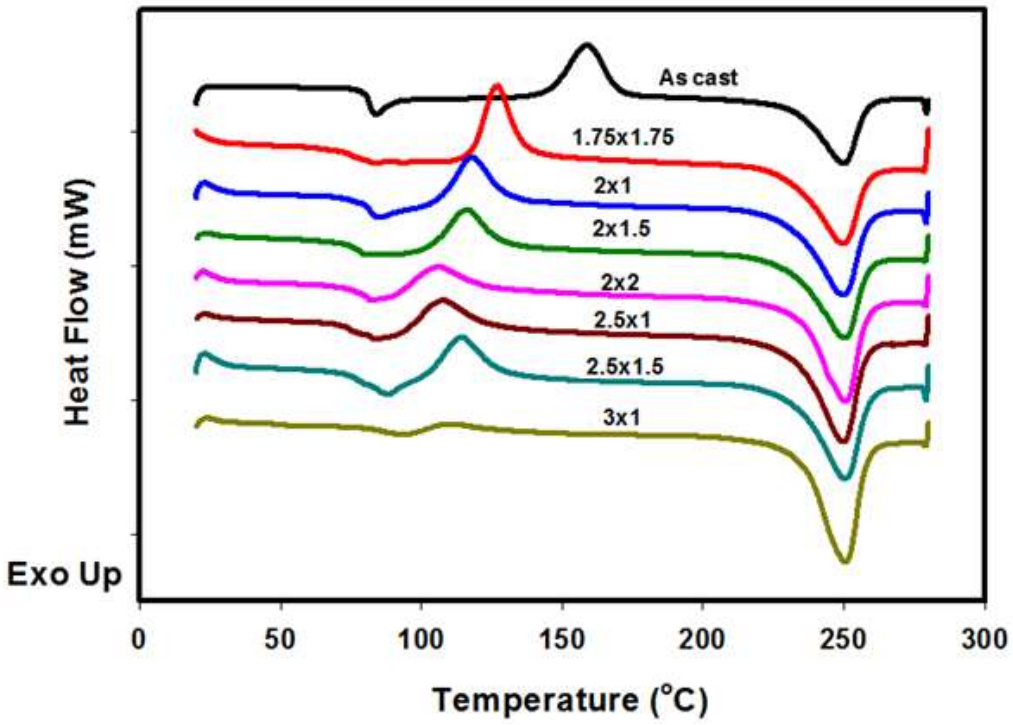

Figure 5.11. DSC thermograms of sequentially biaxially stretched samples.

5.3.3.2 Heat settings at 170°C

DSC thermograms for the 170 and 190°C heat set stretched samples are shown in Figures 12 and 13, respectively. The samples were stretched 20°C above glass transition temperature at 90°C. The glass transition endotherm is flat and spread over a wider temperature compared to as-stretched sample glass transition behavior. The cold crystallization exotherm appearing at 110°C -135°C for as-stretched samples, disappears for all stretch ratios after heat setting at 170°C. After heat setting, a secondary melting peak is established around 175°C for the newly formed crystalline structures with thermal crystallization. The position of the melting peak remains at 250°C with the stretch ratio or heat setting however, the area under the peak increases indicating the increase in crystallinity.

5.3.3.3 Samples heat set at 190°C

No changes observed on the DSC thermograms of samples heat set at 190°C (Figure 5.13) compared to the ones heat set at 170°C except the secondary melting peak appearing closer to the dominant melting endoterm due to higher temperature heat setting.

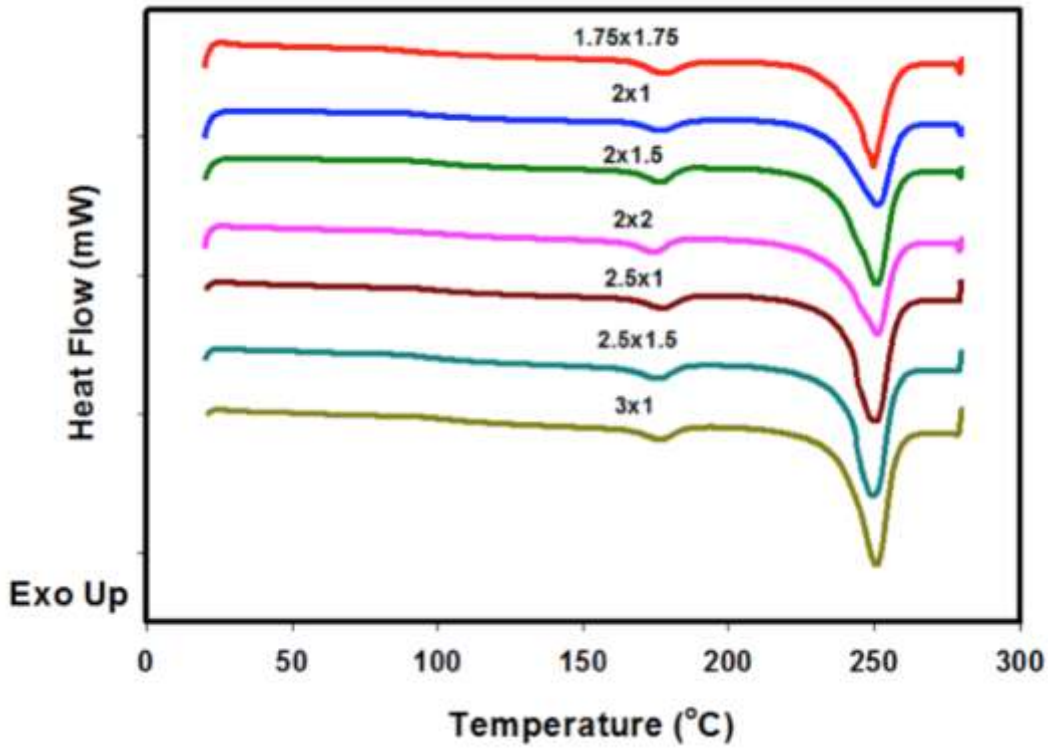

Figure 5.12. DSC thermograms of sequentially biaxially stretched and heat set at 170°C overnight samples.

The thermal analysis is used to quantify the crystallinity of the stretched and heat set samples at different stretch ratios. The crystallinity increases with increasing MD stretching ratio as seen on the Figure 5.14. The TD stretching effect is less pronounced below 1.5 ratio. At equal-biaxial stretching of 2x2, the crystallinity was increased to the same range of 2.5 series stretching. Different temperature heat setting effect on the crystallinity is not differentiating as both cases resulted in similar degrees of crystallization increasing with the stretch ratio. Heat setting increased the crystallinity of lower stretch ratio samples more than the higher ones as seen from tripled crystallinity of 1.75x1.75 stretch sample compared

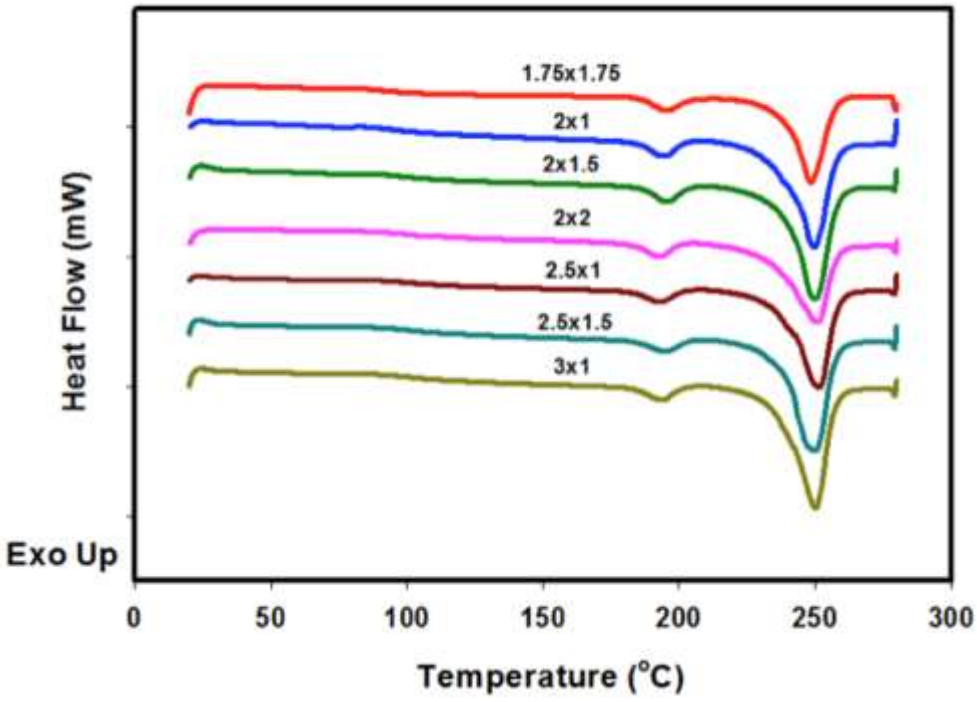

Figure 5.13. DSC thermograms of sequentially biaxially stretched and heat set at 190°C overnight samples.

to the increase in 3x1 stretch sample. The UCW stretching mode allows orientation in both directions as the unidirectional stretching is constraint by constant width,

however still the chain registration into crystalline domains are easier due to the major unidirectional draw. The relaxation in this sample is reduced by highly developed network in the machine direction therefore, results in higher crystallinity.

Figure 5.15 shows DSC thermograms of 3x1 as stretched, 170°C and 190°C heat set samples summarizing the above comparative observations.

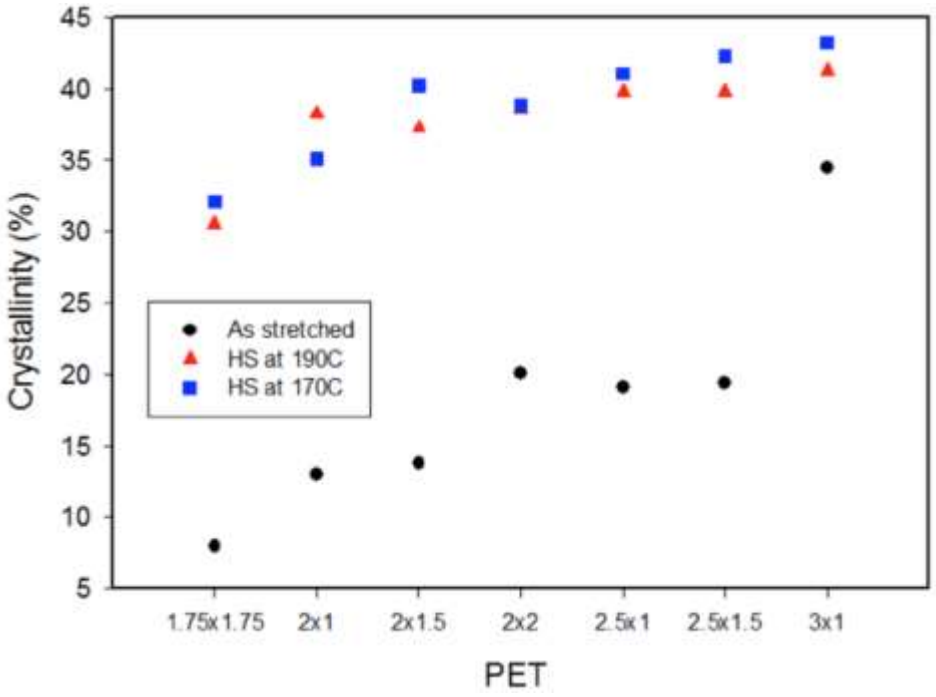

Figure 5.14. Crystallinity of sequential biaxially stretched and heat set samples.

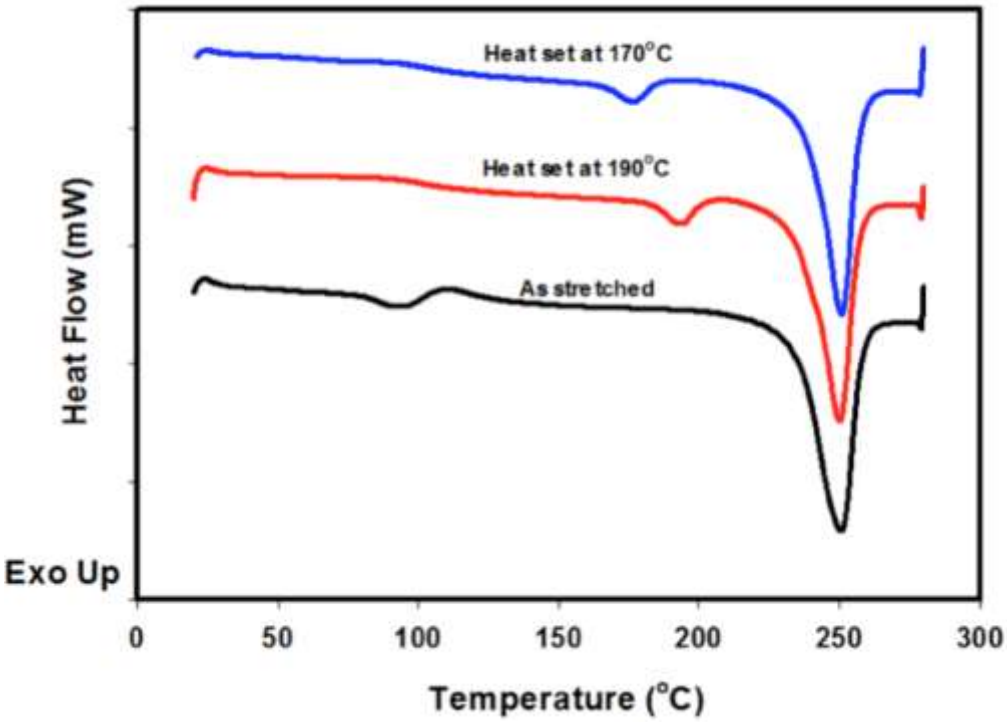

Figure 5.15. DSC thermograms of 3x1 sequentially biaxially stretched and heat set samples.

5.3.3.4. Time-slicing Study

The 3x1 samples heat set above 30 seconds do not show the cold crystallization exotherm as seen in Figure 5.16. The secondary melting endotherm appears after 3 minutes of heat setting at 190°C. Later, as the heat setting time increases, endotherm moves towards the dominant melting peak. The area under the melting endotherms varies at different heat setting times giving rise to the crystallinity percentages given in Figure 5.17. The crystallinity increase is seen within the first 30 seconds which remains almost constant for the following 1.5 hours followed by a drastic increase at 9 hours. The maximum crystallinity level observed was 47% after 9 hours. This behavior is in good agreement with the in-plane orientation behavior at which the initial increased is

followed by a leveling off behavior. In the industry, the goal is to keep the heat setting times as low as possible to minimize the production time, therefore for shorter times 3 minutes is where the sample attains the highest crystallinity of 39%.

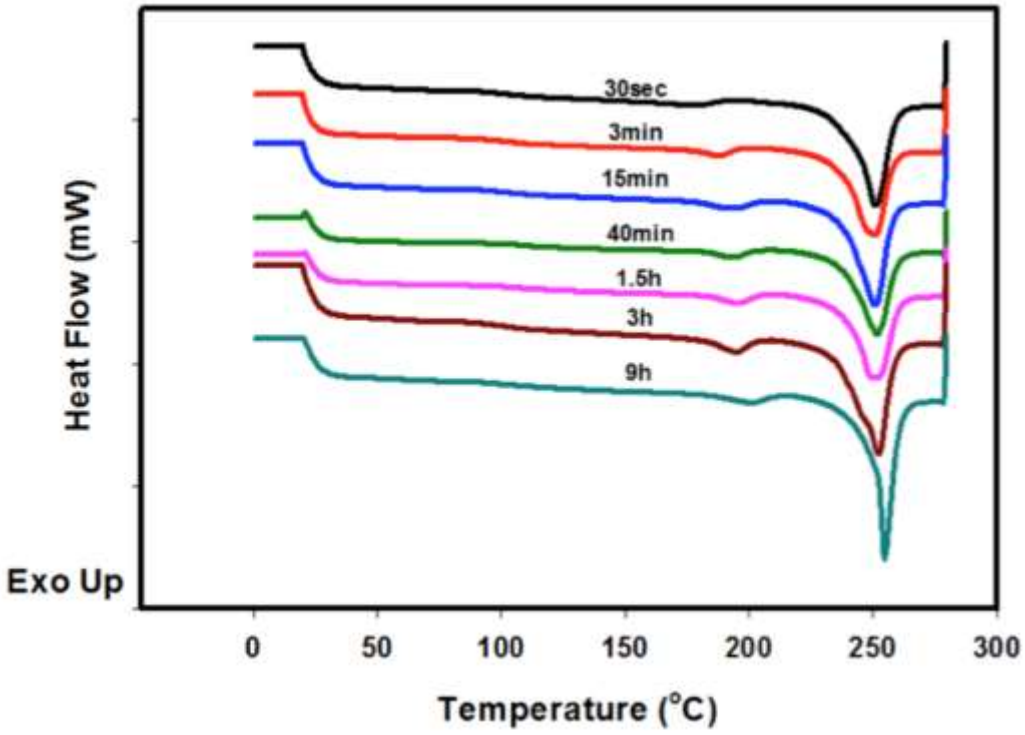

Figure 5.16. DSC thermograms of 3x1 sequentially biaxially stretched samples heat set at 190°C for different time frames.

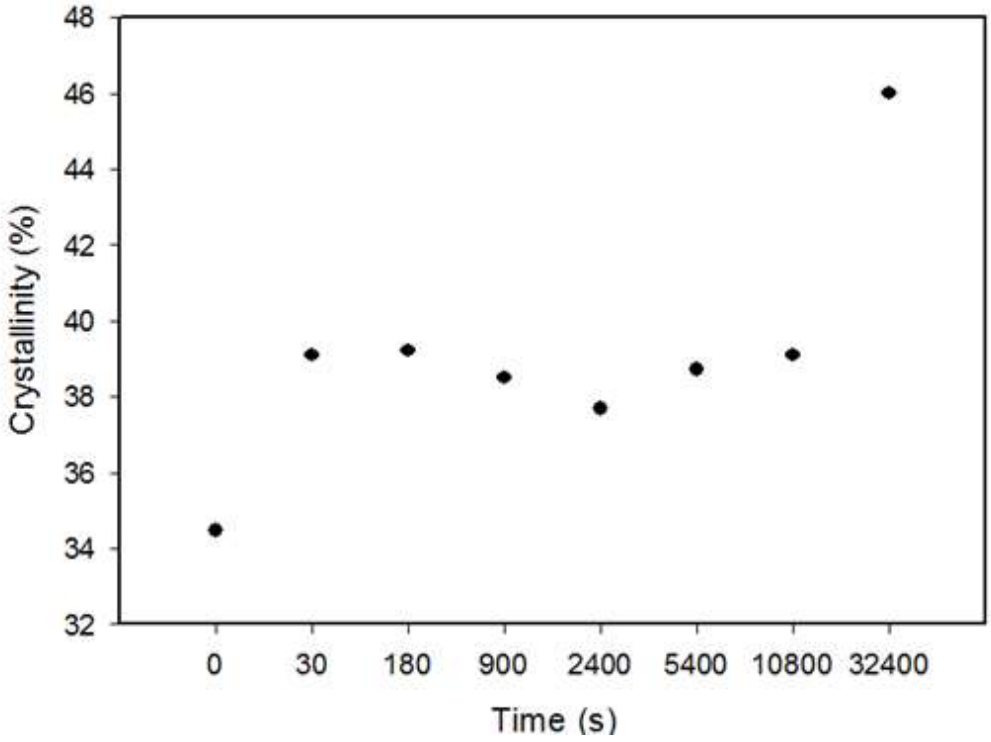

Figure 5.17. Crystallinity of sequentially biaxially stretched and heat set at 190°C samples for different time frames.

5.3.4. Shrinkage behavior

The TMA displacement data during the constant rate heating to 180°C and cooling back to room temperature was obtained and recalculated considering sample length as percent shrinkage and represented over time with given temperature change in the following Figures 5.18 to 5.21. Results are assessed separately for the machine direction and transverse direction shrinkage (also expansion when behavior in decreasing or negative shrinkage values) and its evolution with the heating/cooling cycle is divided into four main stages by vertical dashed lines:

- First (1), initial period up to 70-75°C.
- Second (2), after glass transition temperature behavior.

- Third (3), shrinkage kinetics or behavior change approaching higher temperatures.
- Final (4), shrinkage behavior during cooling stage.

These steps are studied below for as stretched and heat set samples at 170°C and 190°C as well as for the time-slicing samples quenched at different times during long heat setting experiment.

5.3.4.1 As stretched samples

For the TMA results of as stretched samples given in Figure 5.18, in stage 1, up to glass transition temperature, no expansion or shrinkage behavior observed on any stretch ratio. Later in stage 2, above the glass transition temperature the behaviors change depending on the stretch ratios.

- At lower stretch ratios, higher shrinkage rate is observed in both machine direction and transverse direction compared to higher stretch ratios.
- The UCW stretched samples also shrink less compared to the sequential biaxially stretched ones on both directions.

In the stage 3, after around 115°C shrinkage for lower stretch ratios (e.g. 1.75x1.75) levels off, whereas, for higher stretch ratios shrinkage decreases. In other words, the sample expands in machine direction. Step 3 behavior is different in transverse direction as the shrinkage continues to increase only at a slower rate than in the stage 2.

At the final stage of cooling, samples shrinkage is goes through only a minor increased compared to the heating shrinkages observed in earlier stages.

Overall, UCW high machine direction stretch ratio samples (e.g. 2.5x1, 3x1) having dimensionally stable crystalline network, goes through the lower shrinkage and expansion percentages compared to low stretch samples with tightly ordered ready to shrink entanglements. The higher shrinkage values on transverse direction compared to machine direction again is due to the ordered yet not stabilized chains. These structures are induced by contraction stress along constraint TD direction during MD stretching.

The sample shrinkage arises from the disorientation of oriented amorphous chains. UCW sample goes through higher shrinkage in machine direction and lower shrinkage in transverse direction compared to biaxially stretched samples (e.g. 2x1, 2x1.5, 2x2). This behavior is easily explained using structural models in Figure 5.19. The sample with tightly ordered entanglements in specific direction shrinks higher along that direction to relax when subjected to heating. The relaxation of ordered unstable structure and re-crystallization is possible via heat setting which reduces shrinkage values significantly.

5.3.4.2. Heat setting set at 170°C

Figure 5.20, the shrinkage evolutions for samples heat set at 170°C are given. In stage 1 no significant shrinkage observed on any sample. Later in stage 2, after glass transition temperature samples expand in machine direction whereas shrinks

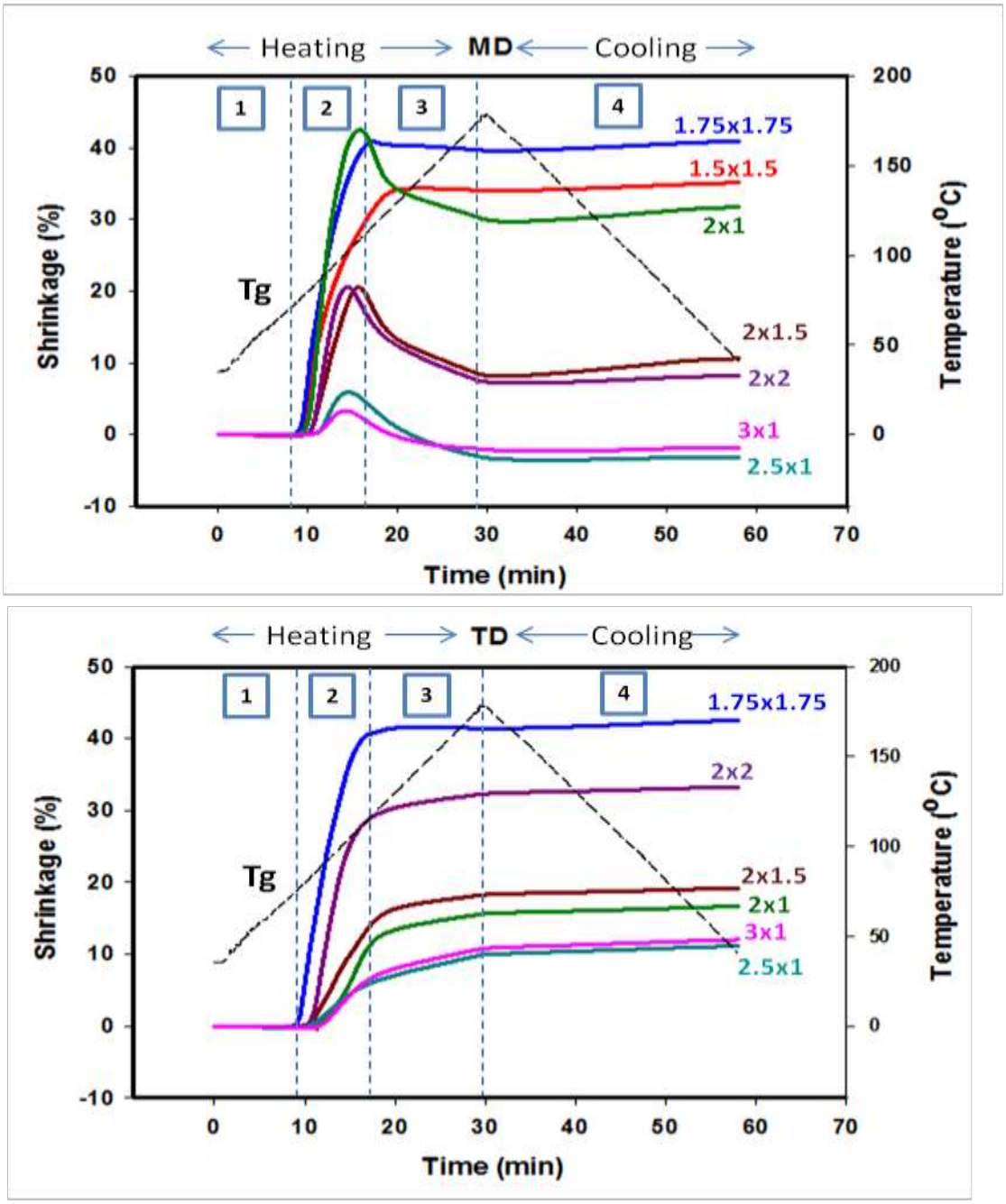

Figure 5.18. TMA results of sequentially biaxially stretched samples.

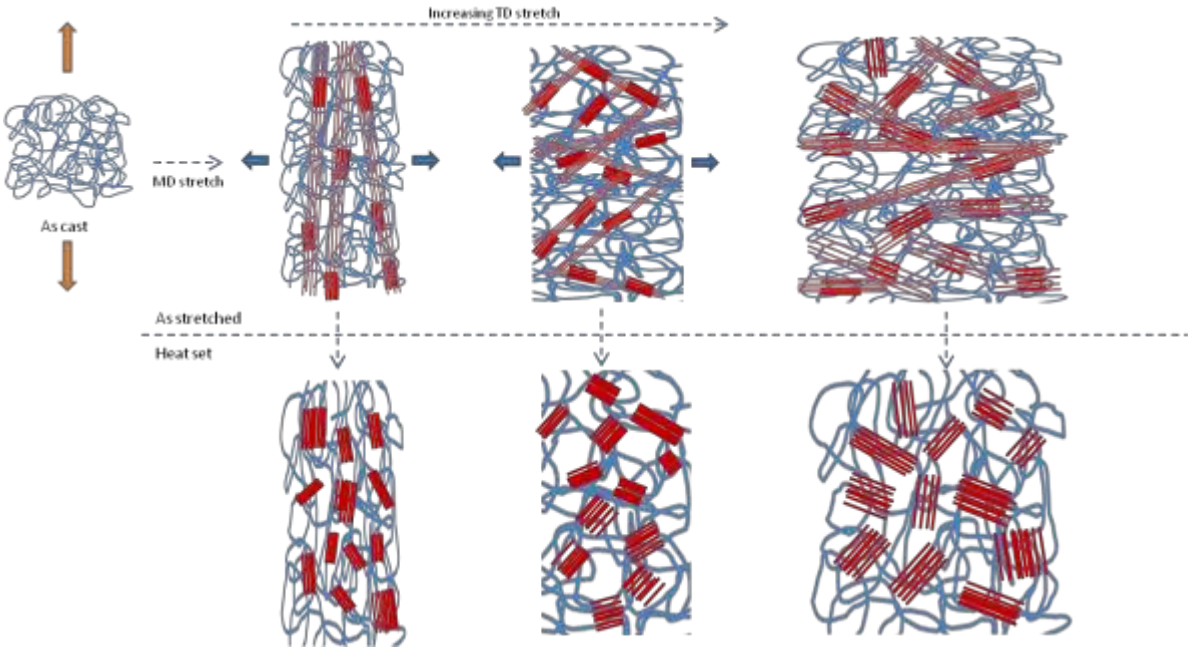

Figure 5.19. Structural models for increasing transverse direction stretch and subsequent heat setting.

in transverse direction for all stretch ratios except the 2x2 stretch sample which also shrinks in machine direction. In stage 3, the same reverse behavior observed between the machine and transverse direction appears with lower rate from 120°C to 160°C. After that point to the maximum 180°C changes with a much higher rate. It is important to note that these shrinkage and expansion changes are very low which makes hard to draw a conclusion from different stretch ratios effect. Finally, in stage 4 only shrinkage is observed on all samples in machine at a slightly lower rate of change than in transverse direction.

Overall, again the higher stretching ratio samples show the lowest changes compared to others in both direction. The shrinkage percentages are overall much lower in this heat set case (max. 4%) compared to as-stretched sample (max. 43%). The samples already have gone through the shrinkage and relaxation procedures

during heat setting and have mostly eliminated the residual stresses build up due to the stretching process.

5.3.4.3 Heat setting at 190°C

In Figure 5.21, the shrinkage evolutions for samples heat set at 190°C are given. In stage 1 only minor expansion behaviors observed in machine direction of 1.75x1.75 and 2.5x1.5 stetched and heat set samples seen whereas, all others in same and transverse direction remained unchanged. No vertical dashed line separation placed in between stages 2 and 3 this time as behavior changes were observed at different temperatures depending on the stretching ratio. An overall expansion behavior is observed at these stages in all stretching ratios except 1.75x1.75. The transition from lower rate of change to higher rate one happened at much higher temperatures for high stretch ratios such as 3x1 and 2.5x1 but also for equibiaxial stretching of 2x2. Finally, at stage 4 similar shrinkage increasing behavior observed for all samples. Again, the lowest shrinkage and expansion percentages are observed on the highest UCW samples.

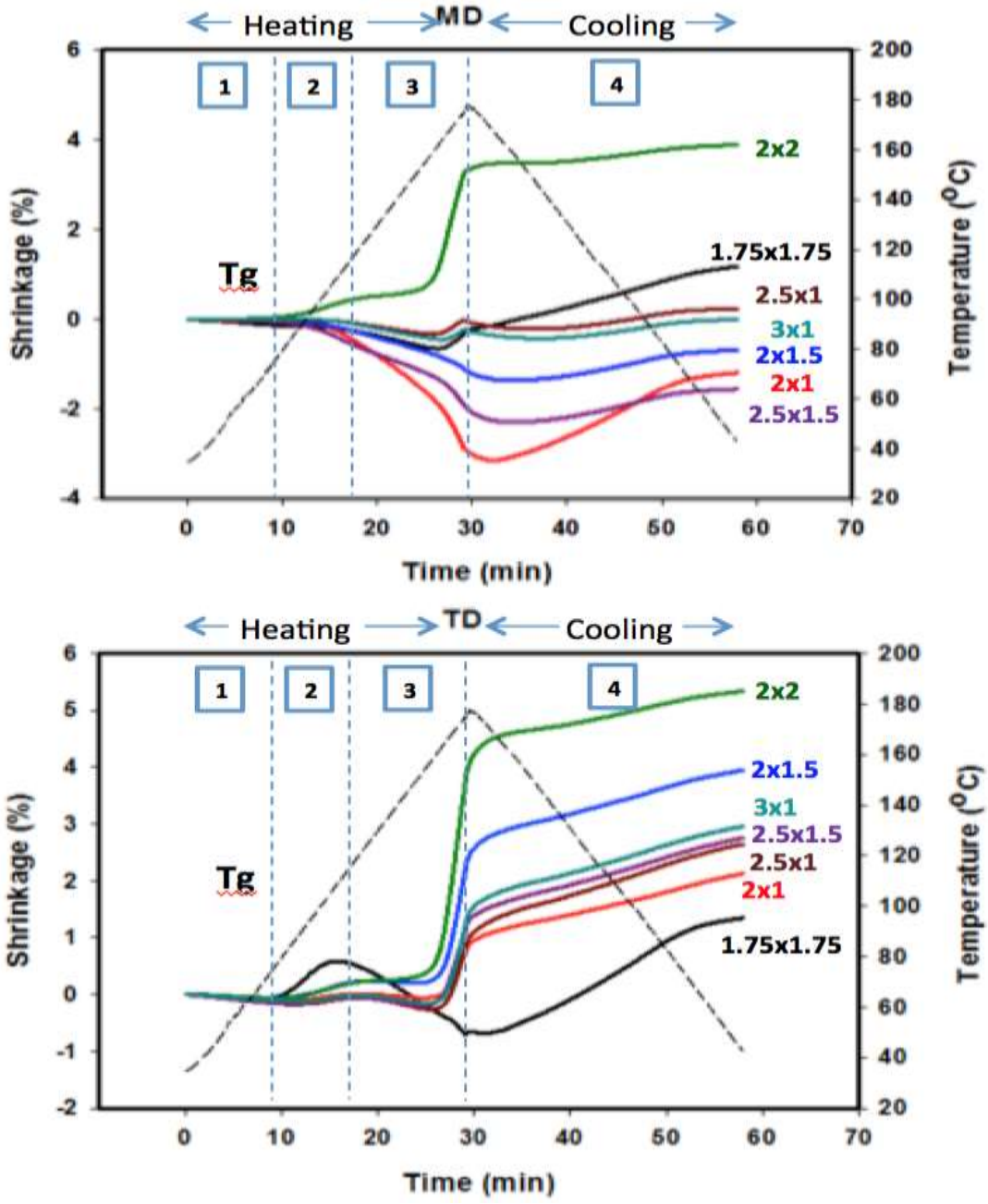

Figure 5.20. TMA results of sequentially biaxially stretched and heat set at 170°C samples.

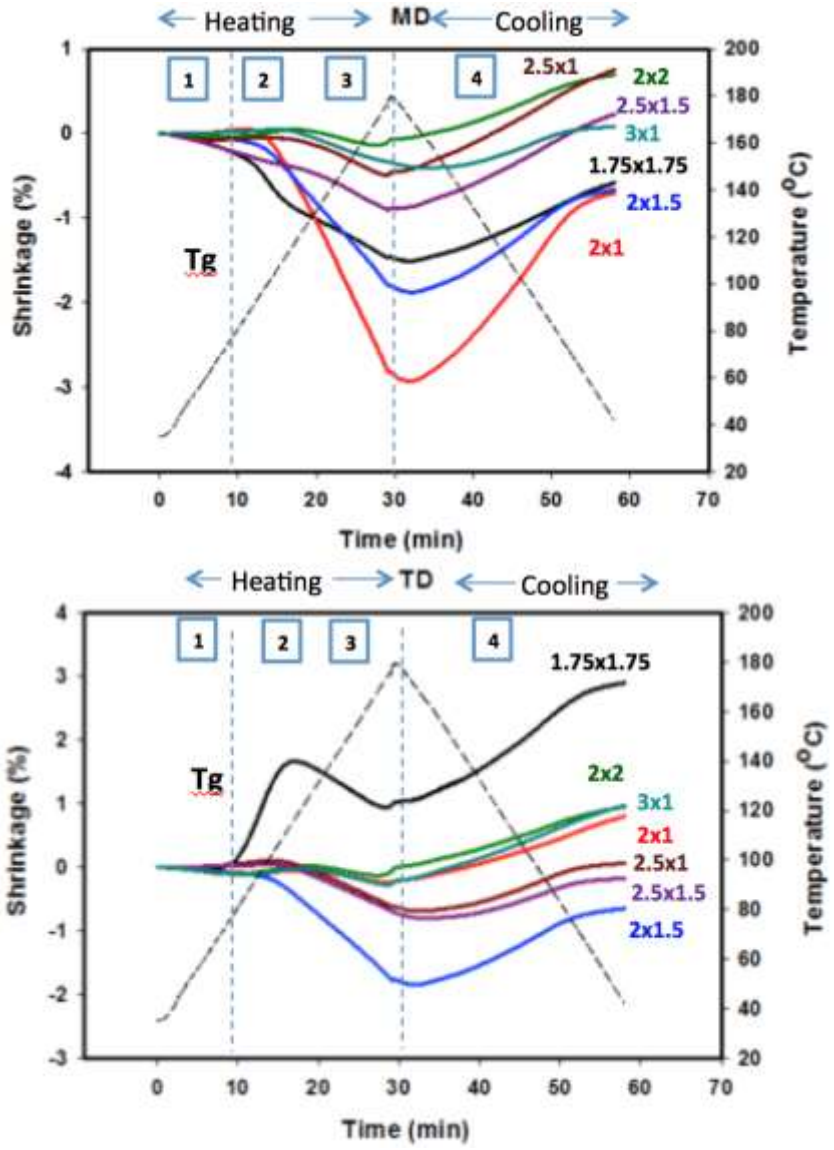

Figure 5.21. TMA results of sequentially biaxially stretched and heat set at 190°C samples.

5.3.2.1.4 Time-slicing study

The time slicing study for 3x1 stretched than 190°C heat set samples are tested for shrinkage behavior to evaluate the heat setting time effect and plotted in Figure 5.22. There is a significant trend difference between 3 minutes to 15 minutes which can be also confirmed by the previously observed orientation change. The trend for 3 hours and 15 minutes samples match closely for which the in and out-of-plane birefringence as well as percent crystallinity values were the same. The heating expansion/shrinkage transition points did not seem to have a trend with increasing heat setting time. Although, the shrinkage and expansion values were extremely low for all samples below 1%, nearly eliminated shrinkage was for the 9 hours heat set sample.

5.4 Discussion

The UCW and sequential biaxial stretching mechano-optical and structural characterization results are in good agreement with the previously reported work [112]. Later, preoriented PET films put through heat setting at 170°C and 190°C has shown induction, relaxation, melting and crystallization behaviors. The induction period is where the sample reaches thermal equilibrium in chamber and does not go through significant changes. Following the induction period, first easily crystallizing chains orient and a rapid change of in and out-of-plane birefringence is observed. The in- plane

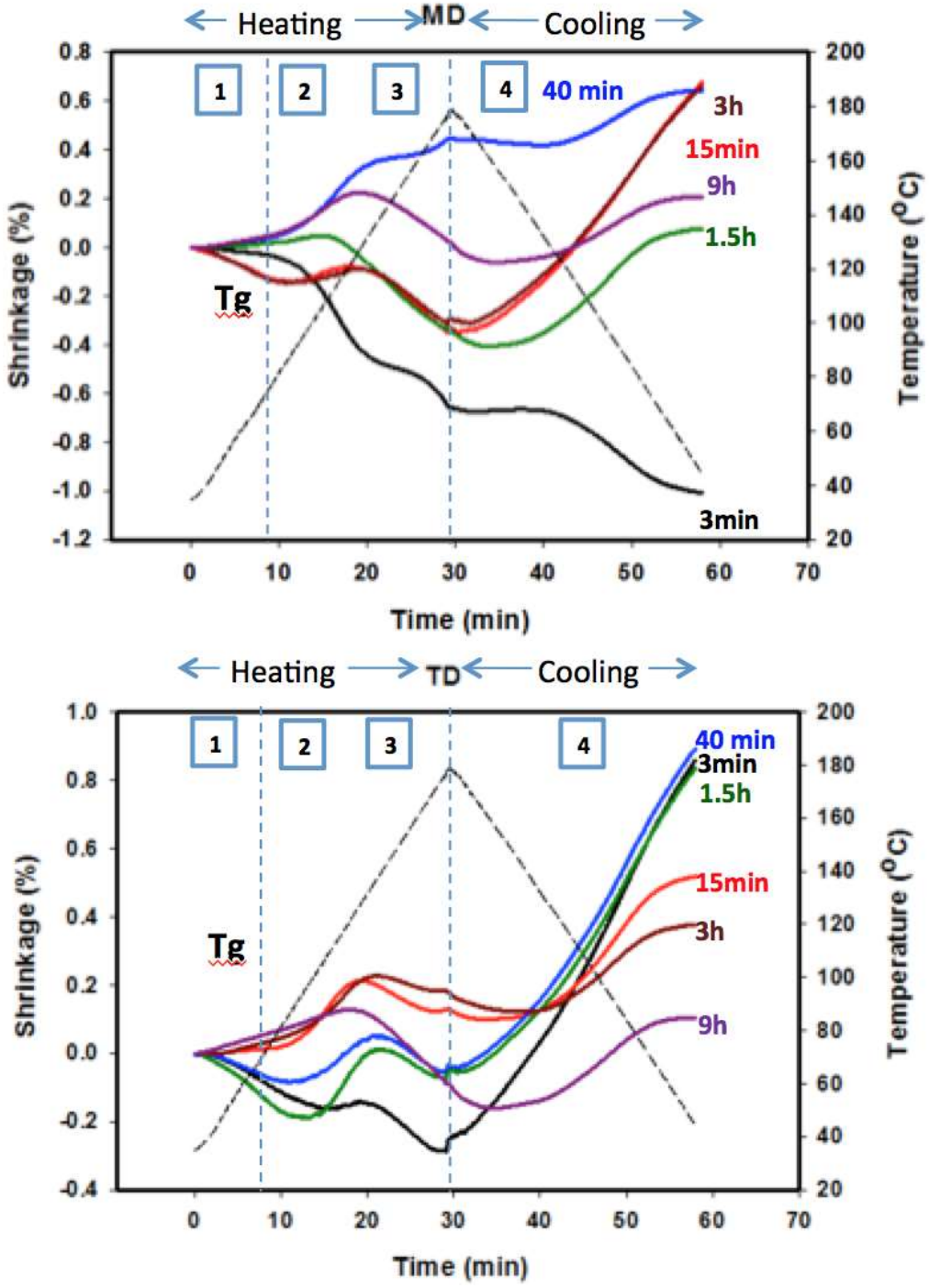

Figure 5.22. TMA results time-slicing of 3x1 sequentially biaxially stretched and heat set at 190°C samples.

birefringence levels off after changes but the out-of-plane birefringence increase or decrease at different rates depending on the sample stretching history. Overall, the rapid changes where shown to happen within the first 15 minutes of heat setting for high stretch ratio samples which can be applied for industrial products. Further, crystallization and solid network formation can happen at longer heat setting periods up to 9 hours. This behavior is expected as the longer times allow chains to relax, melt and recrystallize completely.

Several thermal property changes are observed with heat setting such as disappeared crystallization peak and appearance of the secondary melting peak for the newly formed crystals above heat setting temperature. Time slicing studies demonstrated also that long heat setting times the melting endotherms became narrower which shows uniform crystal size distribution compared to wider distributions at short times.

At lower stretch ratios such as 1.75x1.75 the relaxation dominates birefringence decrease during heat setting at 170°C. However when heat setting temperature set to higher 190°C, the increase in out-of-plane birefringence is followed by relaxation. The established state of orientation cannot be supported as no physical or crystalline network exists at those low stretch ratio samples which results in relaxation of oriented chains. Only thermal nucleation process causes crystallization in those films. The same behavior is observed for low stretch UCW of 2x1 sample as still the supporting network not in place. Other stretching ratios at different heat setting temperatures demonstrate either no change or very minor increase than level off behavior for the in-plane birefringence. Whereas, for the out-of plane birefringence of intermediate stretch ratios there is an initial reduction in orientation which indicates partial relaxation of oriented amorphous chains

followed by rapid orientation increase. The relaxed chains under lowest energy confirmation can register into crystalline domains increasing sample birefringence by increased crystallinity. The time-slicing studies show also that there is slight crystallinity decrease before the birefringence increase at long time heat setting. This shows that also partial melting contributes to reformation of metastable crystalline phases shown by the formation of secondary melting endotherms.

The final and the maximum shrinkage/expansion values are shown below in Figures 5.23 through 5.25. Before the heat setting process the shrinkage results are heavily dependent on the shrinkage ratios. Increasing the machine and transverse direction stretch decreases both the maximum and final shrinkage in machine direction of the film as expected from the formation solid physical network at high stretch ratios. However, the transverse direction shrinkage values depend on the stretching mode rather than, the stretching ratio. The sequential biaxial stretching mode, especially equibiaxial stretching, results in high maximum and final shrinkage values compared to the UCW stretching. During the UCW stretching the orientation is not only on the machine direction as keeping constant width stress is also generated in transverse direction. Same way, during equal biaxial stretching there is more residual stress generated during stretching in transverse direction as they go through two phases of orientation: first, with machine direction stretching than, during the transverse direction stretching. The heat setting temperature effect on shrinkage and expansion behavior is found to be minor: samples heat set at 190°C show slightly lower final shrinkage values on the TD.

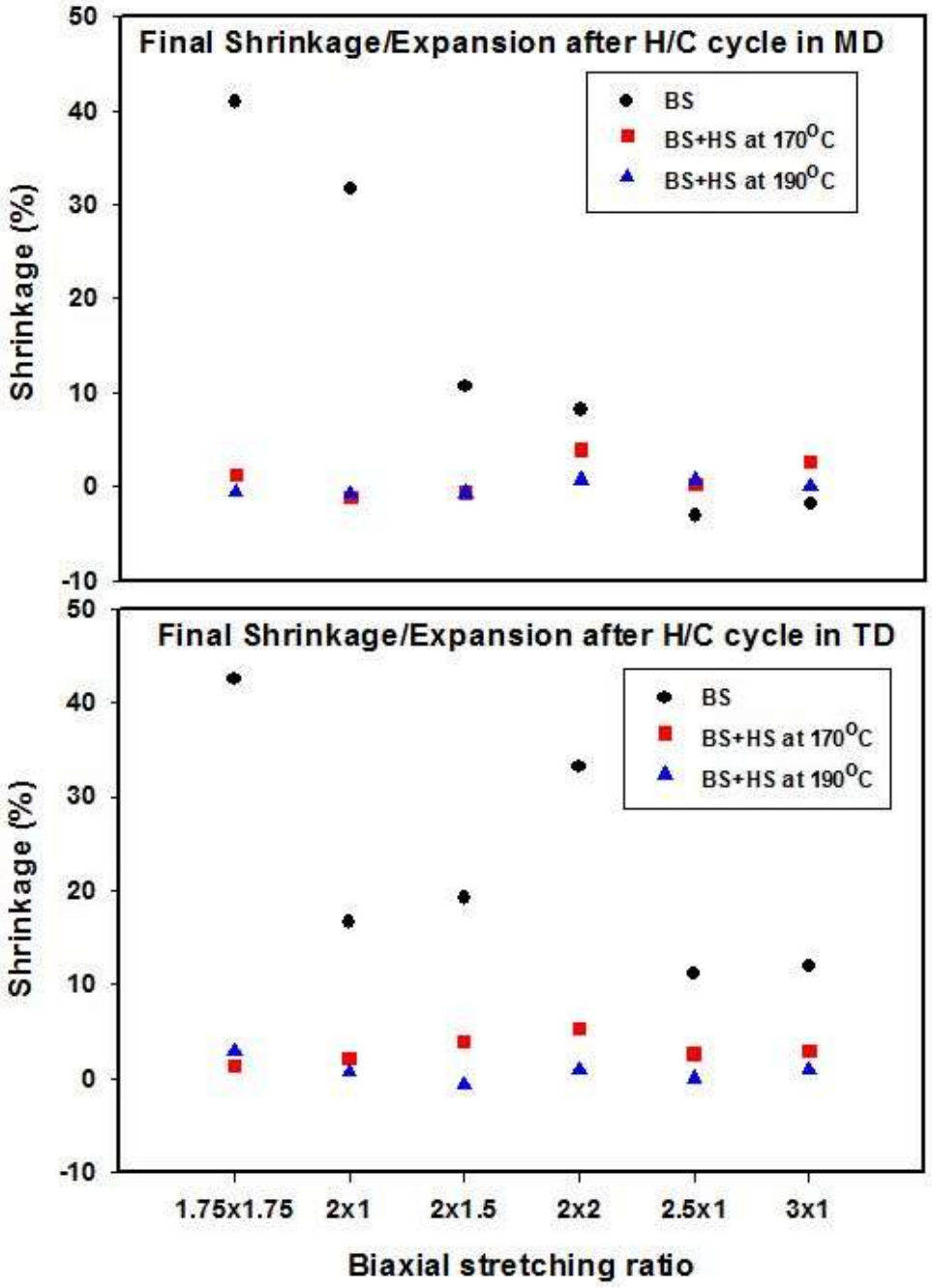

Figure 5.23. Final shrinkage values in MD and TD of different biaxially stretched and heat set samples after H/C.

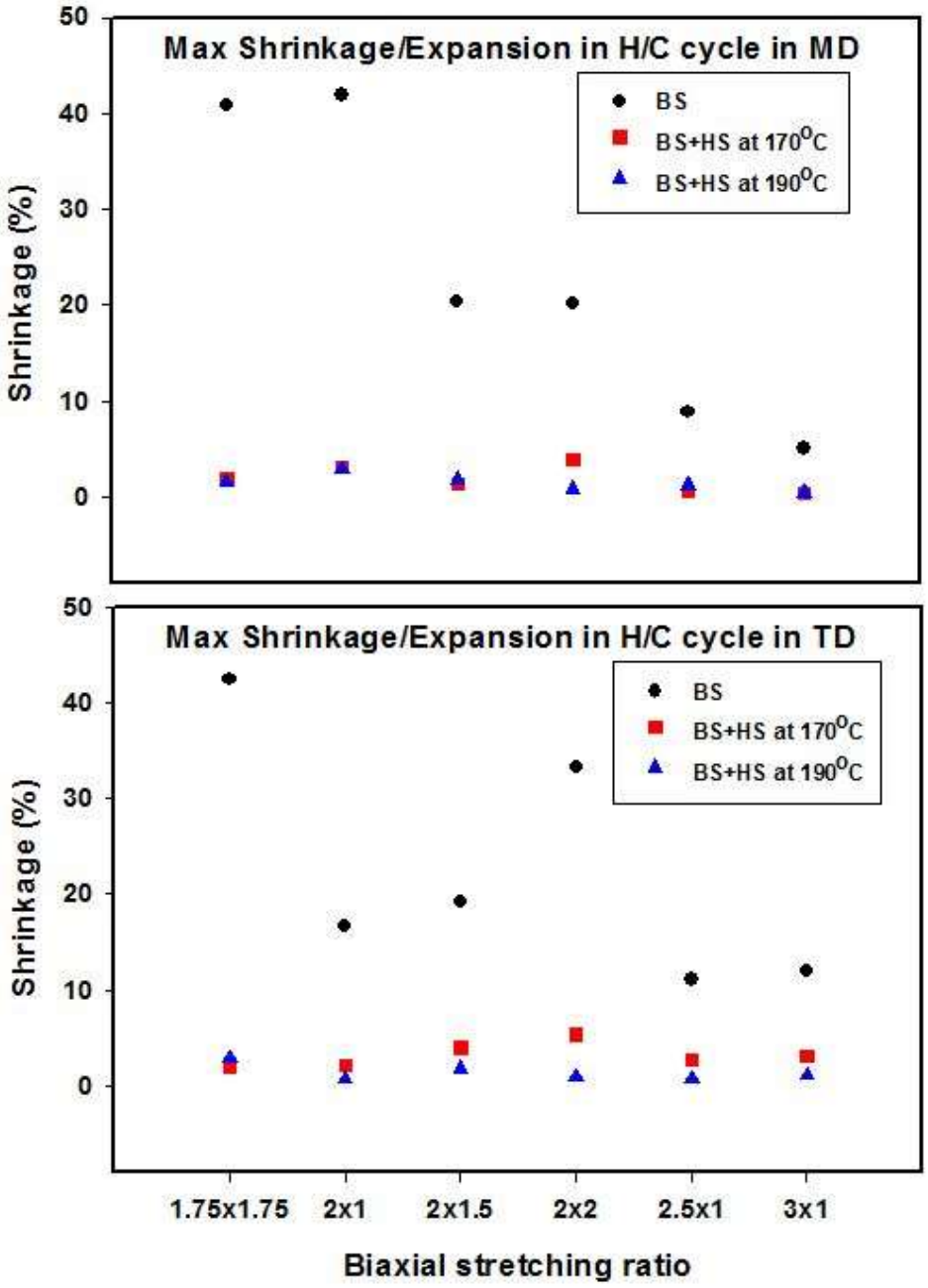

Figure 5.24. Maximum shrinkage values in MD and TD of different biaxially stretched and heat set samples during H/C.

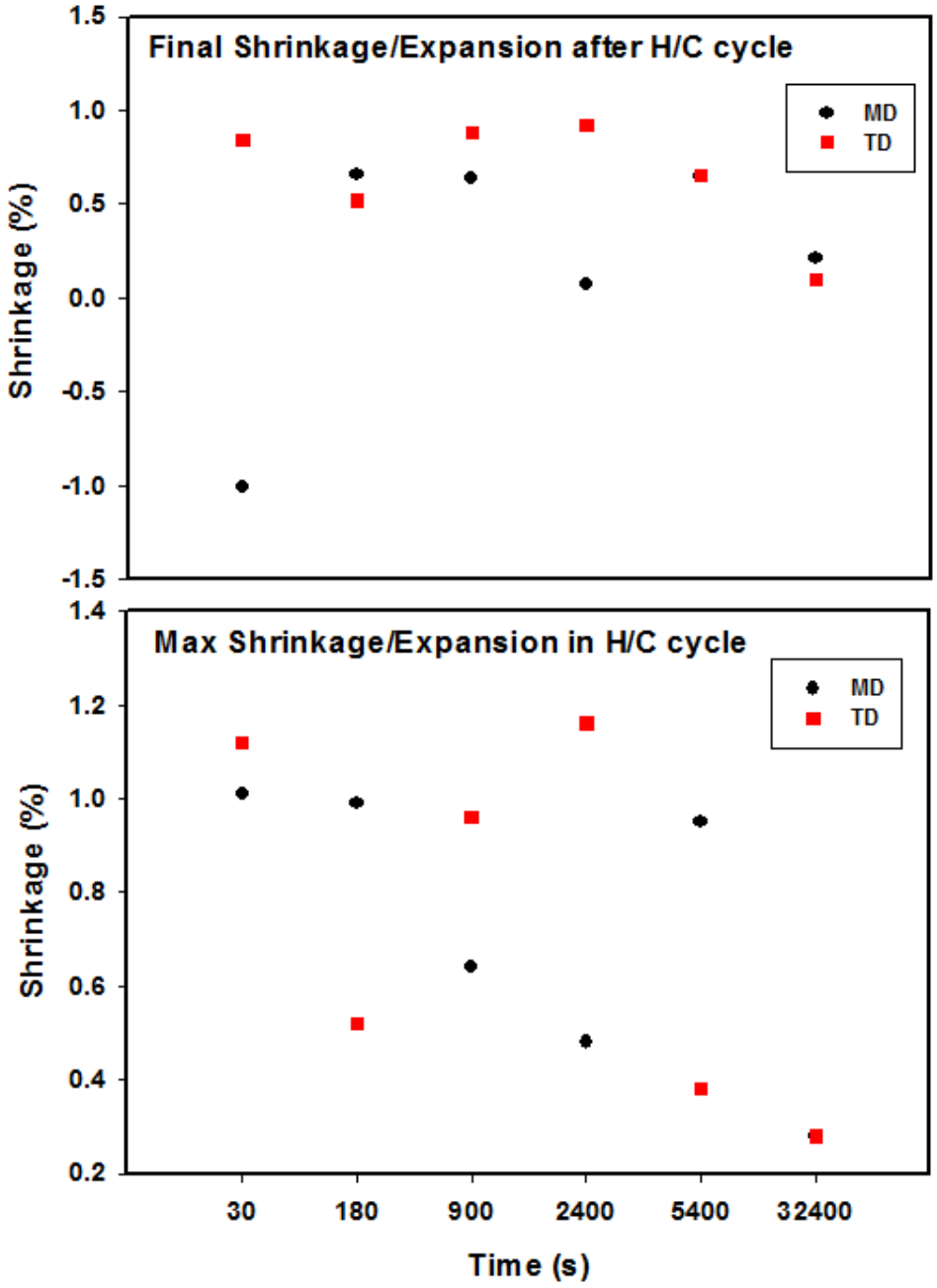

Figure 5.25. Maximum shrinkage values in MD and TD of 3x1 biaxially stretched and heat set (for different time intervals) samples during H/C.

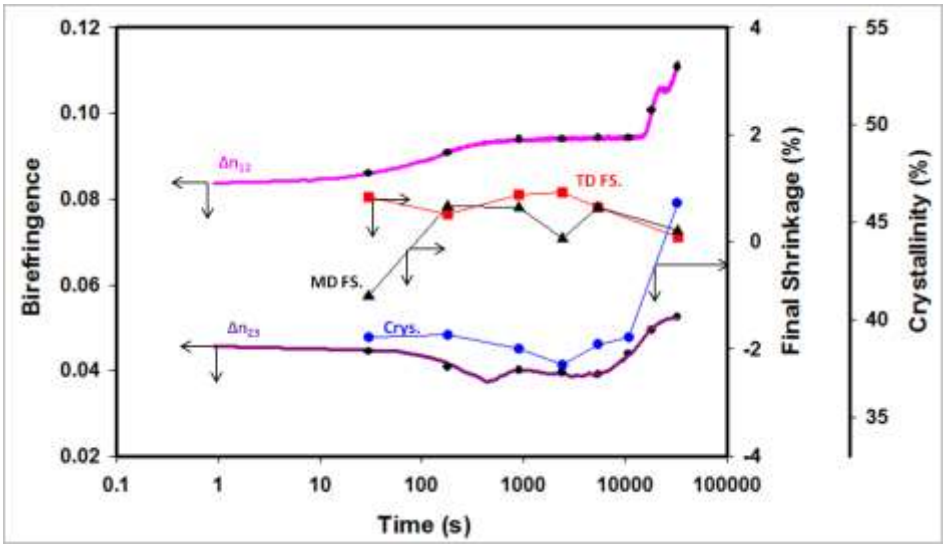

Figure 5.26. Complete time-slicing study results including in (Δn_{12}) and out-of-plane (Δn_{23}) birefringences, machine (MD FS.) and transverse (TD FS.) direction final shrinkage and crystallinities (Crys.) for 3x1 biaxially stretched and heat set samples.

The heat setting process minimizes the final and maximum shrinkage and expansion behavior regardless of stretching ratio. Lowest shrinkage and expansion profiles are obtained from the 3x1 as expected by the existence of the physical network structure enabling support for the recrystallization after relaxation during heat setting process. Further assessment of the time-slicing study for the 3x1 sample revealed minimization of the MD and TD shrinkage behavior difference occurs at very long heat setting process around 9 hours where the final shrinkage expansion values as well as maximum ones matches in both direction (Figure 5.25). In Figure 5.26, the time slicing-study data is summarized combining birefringence, crystallinity and shrinkage results. It can be also clearly seen that the MD to TD direction shrinkage control can be also managed at short time heat setting (*e.g.* 3 minutes).

5.5 Conclusions

The use of heat stabilized PET in electronics industry is very common. Understanding the failure modes caused by the shrinkage deviations not only within the sample in MD and TD but also compared to other laminated materials is crucial and controlled shrinkage developments depending on application is a must. This study shows that, based on application, the shrinkage and expansion behavior of PET films prepared can be controlled by using real-time biaxial stretching and heat setting optical property tracking devices. The optimum samples with reduced final and maximum shrinkage/expansion values as well as MD to TD variations are obtained by using 3x1 UCW stretched and heat set at 190°C for different time frames. The advantage of working with higher stretch ratio is to have effective heat setting process resulting in crystallinity increase and also faster process results as desired from the industry. Increase in the heat setting time did not show complete level off as reported earlier Although, the chain population capable of crystallizing decreases overtime, the slow-crystallizing chains still shows further reorganization increasing crystallinity.

CHAPTER VI

REAL-TIME TRACKING OF SEGMENTAL ORIENTATION BY RHEO-OPTICAL PROPERTIES IN PEO BASED POLYURETHANE(UREA)S: DEGREE OF SOFT SEGMENT ORDERING EFFECT

6.1 Introduction

The multicomponent, hard and soft segment structures of polyurethanes offer unique mechanical properties. Even though these segments are semi-continuous, it was found that they exhibit distinctly different orientation response to deformation [43, 46, 113-133]. First, Rinke [124] and Oertel [122] studied the stretched elastic polyurethane using offline X-ray diffraction. Later, Cooper and Tobolsky used a torsional testing apparatus to find the origin of enhanced modulus on plasticizer loaded polyurethane films [117]. Studies followed with Bonart`s WAXD and SAXS experiments on orientation assessment under tensile deformation [115, 116], Cooper and coworkers reports on temperature dependence of mechano-optical behavior [120, 134] and orientation behavior of different segments using offline infrared dichroism [43, 113, 126]. Each segment

behavior in polyether-based polyurethanes was monitored following stretching in step increments and relaxation. They found that hard segment orientation was highly dependent on strain history while the soft segments orientation generally was insensitive [43]. Desper and Schneider found three different modes of microstructural deformation in uniaxial stretching of three different types of polyurethanes [119]. Amine-cured polyurethanes (PU) showed shear deformed soft segments whereas hard segments perpendicular to the chain axis tilted away from stretching direction. Diol-cured PU exhibited soft segments orienting in while hard segments normal to the tension direction. However, triol cured polyurethanes showed either rotation or translation in irregular microstructural constituents during deformation. Although, many other publications exist on the effect of deformation to structural orientation assessment through offline measurements [46, 47, 121, 123, 127], they provide limited understanding on the real-time material response. Therefore, the real-time studies have gained importance being able to capture deformation effects more accurately.

Siesler *et al*. developed instrumentation to measure the synchronized real-time mechanical and FTIR spectroscopic changes of polymers during uniaxial deformation and relaxation [128-130, 133, 135, 136]. They studied the strain-induced crystallization behavior of thin polyurethane films during uniaxial deformation and relaxation. The engineering stress and strain were measured in their work and the following similar studies. More recently, Yeh and co-workers, including Siesler, investigated segmental orientation of polyurethane(urea)s during cyclic elongation and recovery with real time WAXD, SAXS by synchrotron radiation and time resolved FTIR [133]. Their study showed that at lower strain levels hard segment lamellar stacks of which long axis

perpendicular to chain axis tilted towards the stretching direction later, at higher strain rates, they break down, and align parallel the stretching direction. Sauer et al. studied orientation development and morphology changes during deformation of thermoplastic elastomers with PTMO soft and nylon 12 hard segments using SAXS, AFM, birefringence and DSC [125]. These results were in agreement with Yeh *et al*.`s work [133] and supported by the un-deformed and deformed samples AFM images. Blundell *et al*. reported monodisperse and randomized hard segment length structural contributions using SAXS during polyurethane deformation [114]. Versteegen *et al*. investigated morphology change of copoly(ether urea)s with uniform hard segments at deformation along with temperature effects [132].

The real-time true stress and stress optical behavior of PUU was published first by our group [118]. Thus, the local true mechanical response of the material was presented along with optical results. More recently, Unsal *et al*. evaluated the real time-true stress and true strain along with birefringence behavior of PUUs substantiated with offline AFM, SAXS and WAXD studies at critical deformation levels [131]. A novel integrated measurement system combining the previously reported custom-built uniaxial stretcher [3, 118, 131] with custom-built ultra-rapid scan polarized FT-IR (URS-FT-IR) in our group [3]. For the first time in that study, the segmented caprolactone based polyurethanes deformation and orientation behavior was monitored by coupling the mechanical (true stress-true strain), optical (birefringence), and spectrometric (IR dichroism) information at very high speeds for long experiment times. The primary focus of this research is to expand that real-time study on the dynamical structural evolution of segmented PEO based PUUs with different soft segment molecular weights and hard

segment percentage contents during their uniaxial deformation including stretching and relaxation.

6.2 Experimental

6.2.1 Materials

The polyurethane(urea) samples with hard segments consisting of bis(4-isocyanatocyclohexyl)methane (HMDI) and 2-methyl-1,5-diaminopentane (MDAP or Dytek) and soft segments consisting of poly(ethylene oxide) (PEO) oligomers was kindly synthesized and provided by Yilgor`s Polymer Research and Technology Lab at Koc University. Details on PEO molecular weight, mixing ratios and resulting hard segment length from stoichiometry as well as general chemical structure are given in Table 6.1. All three grades consisted of 30 % hard segment.

Table 6.1. Three different PUU composition details.

	PEO M_w	PEO/HMDI/Dytek	Hard segment length (g/mol)
PEO2-UU30	2K	1/2.6/1.6	868
PEO4.6-UU30	4.6K	1/5.5/4.5	1966
PEO8-UU30	8K	1/9.9/8.9	3632
Chemical Structure	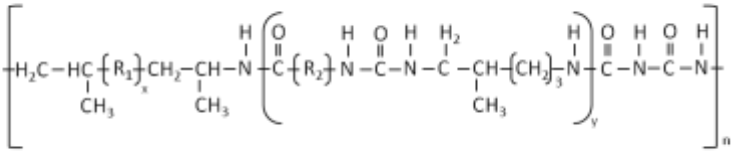		

R_1: PEO, R_2: dicyclohexylmethane radical, x: soft segment repeat units, Y: hard segment repeat units

6.2.2 Sample Preparation

8% PUU solution is prepared with THF/IPA (1:1) for each composition. The prepared solutions were poured into a commercial 3-inch wide, double blade assembly Dr. Blade coater set to 208 µm gap. Motorized drawdown coater Cheminstruments, EZ Coater EC-200 is used to coat material over glass substrate designed for real-time drying properties. Detailed setup for this process pictured our previous publication [2]. After drying procedure, around 20 µm samples were cut using a die cutter to obtain geometry shown in Figure 6.1 for the real-time uniaxial stretching orientation properties measurement system. The dumb-bell shaped samples had 40 mm stretching length between the holding grips and 42 mm width at the center.

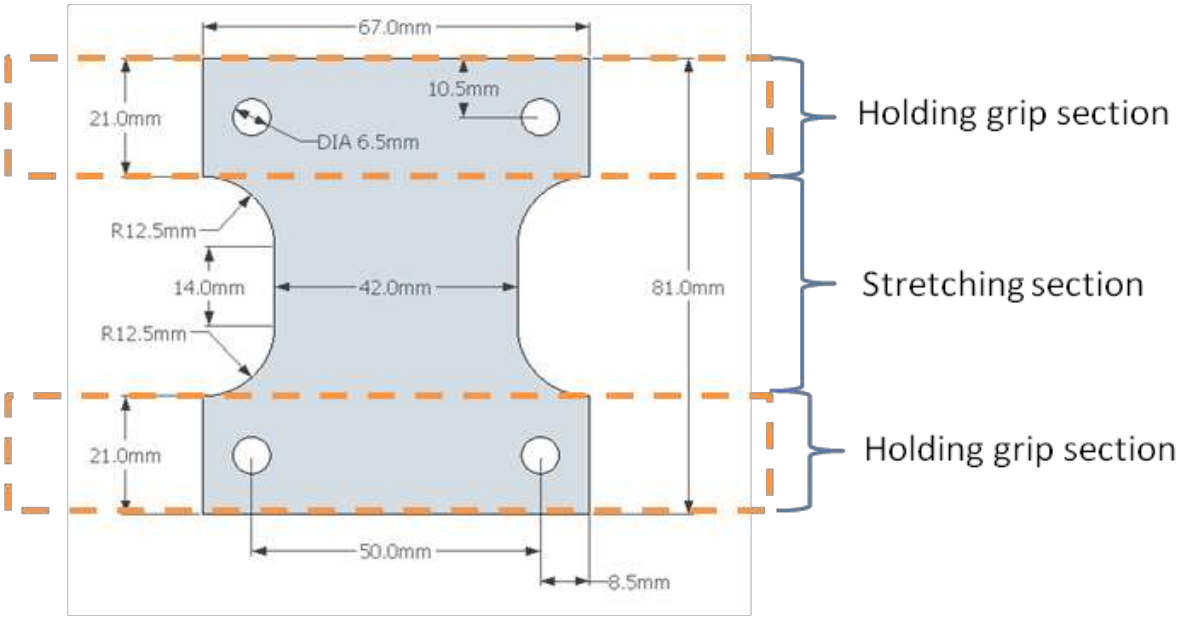

Figure 6.1. Sample geometry for orientation property measurement system.

6.2.3 Real-Time Material Property Tracking Methods

6.2.3.1 Real-Time Drying Properties Measurement System

The prepared sample is placed on the sample platform of real-time drying property measurement system shown in Figure 6.2. We monitored temporal changes in physical parameters during the drying behavior of the PUU solutions. This instrument can follow properties such thickness, weight, film temperature, in-plane and out-of-plane birefringence during solidification of films through solvent evaporation: further details on the system is given elsewhere [2]. The air speed was set to 0.5 m/s and the drying properties were recorded at room temperature, 23 °C, and 30 % humidity.

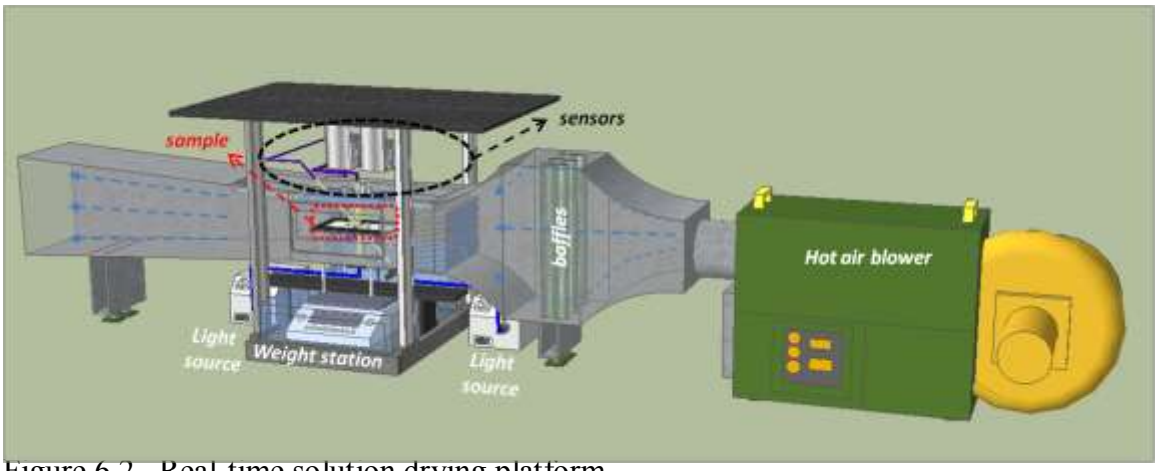

Figure 6.2. Real-time solution drying platform

6.2.3.2 Real-Time Uniaxial Stretching Orientation Properties Measurement System

Figure 6.2 geometry cut 20 μm PUU thin films were tested for real-time spectral birefringence, true stress and true strain, structural feature changes using an integrated ultra-rapid-scan polarized FT-IR spectrometer (URS-FT-IR) to the mechano-optical system given in Figure 6.3. Further, details on this instrument are given elsewhere [3]. The samples were stretched with stretching rate of 50 mm/min, 300 % strain and an after stretch holding time of 30 min at room temperature.

The dichroic ratio (D) is calculated from the parallel (A //) and perpendicular (A □) polarized IR absorbance values as given in Equation 1. The polarized IR absorbance values were obtained by integrating the peak area for selected chemical groups of (NH) and (CH) in hard and soft segments, respectively.

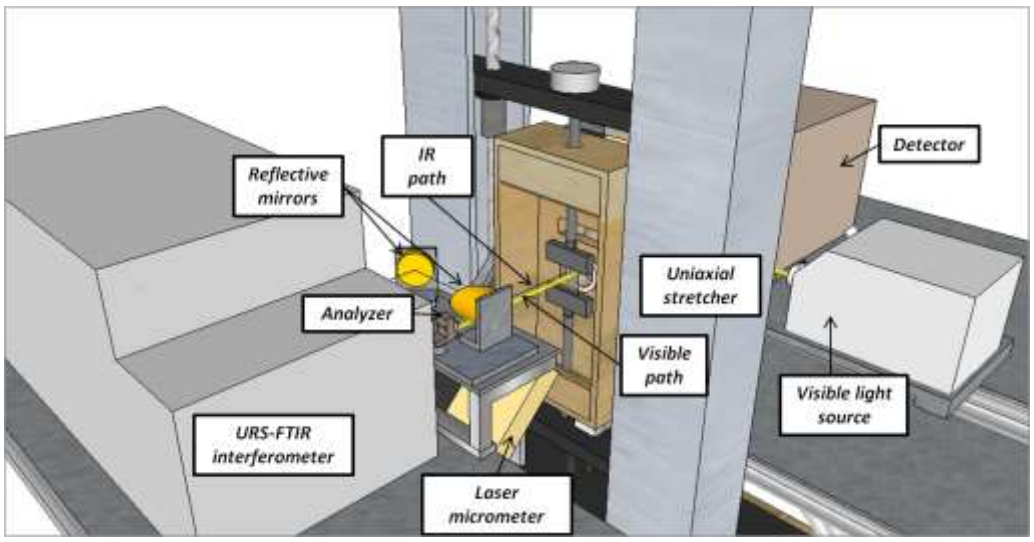

Figure 6.3. Real-time rheo-optical measurement platform.

Corresponding wavenumbers and transition moment angles are given in Table 6.2. Orientation functions (f) calculation for the selected groups was as given in Equation 2 and 3.

$$D = \frac{A_{\parallel}}{A_{\perp}} \quad (1)$$

$$f = \frac{(D-1)(D_0+2)}{(D+2)(D_0-1)} \quad (2)$$

$$D_0 = 2\cot^2\psi \quad (3)$$

ψ is the transition moment angle of a specific vibration with respect to polymer chain [136].

Table 6.2. Wavenumbers and transition moment angle for selected chemical groups in PUU [35, 36].

	Wavenumber (cm^{-1})	Transition moment angle , ψ (°)
ν (NH)	3320	90
ν (CH_2)	2935	90

6.2.4 Characterization Techniques

6.2.4.1 Atomic Force Microscopy (AFM)

The height and phase images of as-cast samples were obtained by using a Bruker Nanoscope V operating at quantitative mapping (QNM) mode with SCANASYST-AIR probe with 650 nm cantilever thickness, 115 µm length, 25

μm width, and 70 kHz frequency. DMT modulus images obtained in order to differentiate hard and soft segment separation.

6.2.4.2 Differential scanning calorimetry (DSC)

DSC experiments were performed using TA Instruments, DSC Q2000. Around 8 mg of as-cast films were placed in aluminum sample holders and crimped. Samples were heated to 220 °C to erase thermal history, then cooled to -90 °C at 10 °C/min and subsequently heated to 220 °C at the same rate in nitrogen atmosphere.

6.3 Results and Discussion

6.3.1 Drying and Film Formation

Real-time weight, thickness and surface temperature data for PEO based PUU systems are presented on Figure 6.4 and 6.5. Initial fast solvent evaporation occurs evidenced by the rapid weight and thickness decrease. During this period, the temperature of the film increased by 2 °C due to slowing down of evaporative cooling effect as the remaining THF/IPA solvent is depleted. After a critical time a drying front is established at the upstream (towards the air blower side) and is propagated downstream. The thickness wave(s) associated with this front evidenced by 10 μm bump between 200 and 450 seconds detected by the middle laser thickness device. Following the passage of the front around 450 seconds, the solvent evaporation rate substantially is decreased as evidenced by temporal changes in weight and the change

in temperature slows down. Partially dried sample at the end of this process contains around 44 % solvent by weight.

The PEO4.6-UU30 system resulted in similar drying trend. The weight level off point was at the same location of 450 seconds although; the thickness change was less than the low molecular weight case. This behavior is validated by the higher bound solvent content of 66 % by weight in partially dried samples.

In both cases, the in and out-of-plane birefringences are very low showing slight increase during drying process.

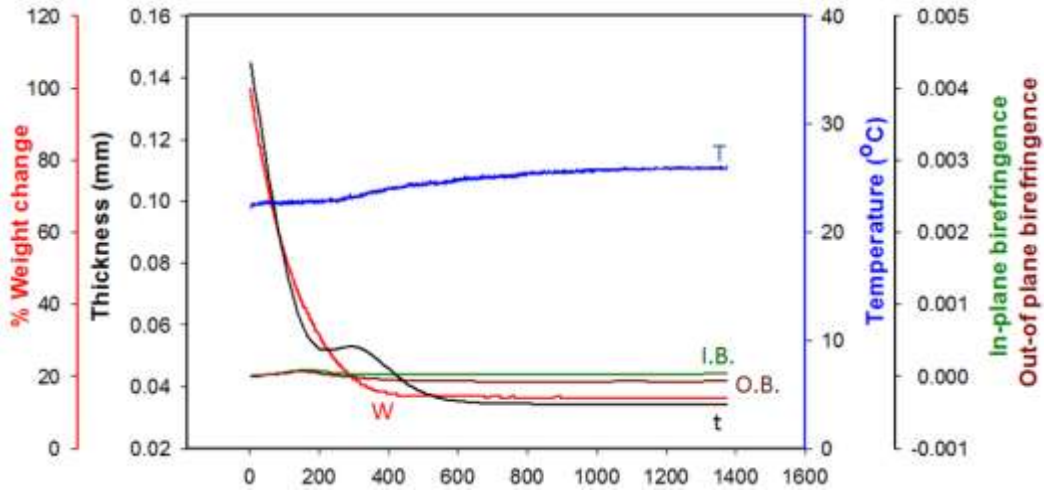

Figure 6.4. Real-time drying results for PEO2-UU30 solution in THF IPA mixture. (Weight change -W-, thickness -t-, temperature -T-, in-plane -Δn_{12}- and out-of-plane birefringence -Δn_{23}-)

6.3.2 As-Cast Film Structure

Depending on the chemical structure, segment length and order of soft and hard segments, polyurethanes can be semi-crystalline or amorphous. The glass transition commonly found between -120 and -50 ^{o}C for soft and at room temperature for hard segments. The melting temperature for soft segment, if semi-crystalline is also observed around room temperature and that of the hard segment around 120 ^{o}C and above depending on degree of short/long range ordering to microcrystalline regions [43, 134]. The soft and hard segment thermal transitions in fixed hard segment content (30 %) and varying soft segment length PUs were investigated from the second heating curves where cooling prehistory effects were erased. All thermal transition temperatures and enthalpies obtained from these curves are indicated on Table 6.3.

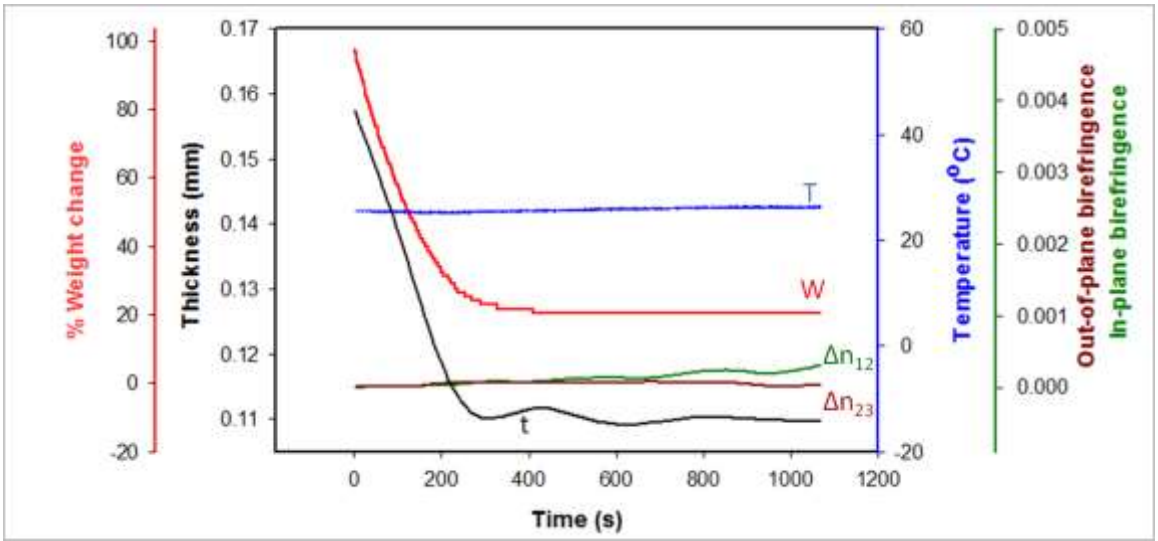

Figure 6.5. Real-time drying results of PEO4.6-UU30 solution in THF IPA mixture. (Weight change -W-, thickness -D-, temperature -T-, in-plane birefringence -Δn_{12}- and out-of-plane birefringence -Δn_{23}-)

In PU structures, hard domain segregation leads to higher melting temperature and enthalpy. Second heating curves did not show well defined hard segment melting endotherm. The values in Table 6.3 for the PEO4.6-UU30 and PEO8-UU30 are the ones retrieved from the first heating curve. For this case, hard segment lower melting temperatures in long soft segment samples, PEO4.6-UU30 and PEO8-UU30, are due to suppression of the well-ordered hard domains. No high temperature well-defined melting endotherm observed due to absence of long range order microcrystalline region in the 30 % hard segment content PUs. The short range crystalline ordering of soft segments appears as fairly broad endotherms on Figure 6.6. The higher soft segment melting temperatures for PEO4.6-UU30 and PEO8-UU30 compared to PEO2-UU30 one are due to enhanced soft segment chain crystallization. The lower glass transition temperatures than pure PEO (-52 °C) is an indication for lower amorphous soft segment quantity.

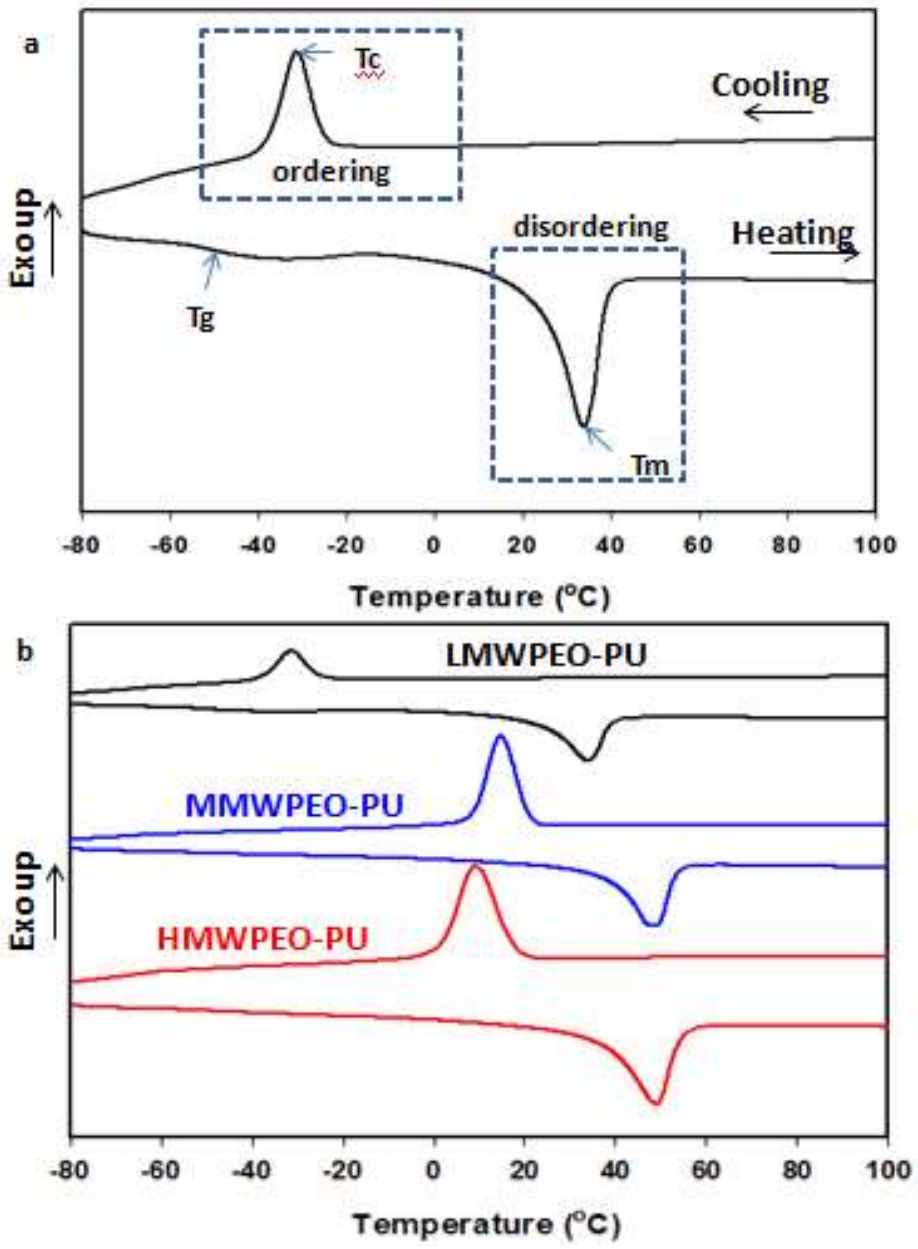

Figure 6.6. DSC second cooling and heating thermograms for PEO2-UU30 (a, b), PEO4.6-UU30 (b) and PEO8-UU30 (b) showing soft segment melting (disordering) and crystallization (ordering).

Table 6.3. Thermal transition temperatures and enthalpies of PUs

	PEO2-UU30	PEO4.6-UU30	PEO8-UU30
Tg,ss (°C)	-51	-60	-59
Tm,ss (°C)	32	46	47
ΔHm,ss (J/g)	46	71	74
Tc,ss (°C)	-30	15	10
ΔHc,ss (J/g)	19	61	66
Tm,Hs* (°C)	-	145	125
ΔHm,Hs* (J/g)	-	4.8	6.6

ss: soft segment Hs: hard segment
g: glass transition c: crystallization
m: melting transition *: obtained from first heating curve

Different soft segment length structures results in varying tendencies to crystallize and phase segregate. The soft segment composition is shown to affect crystallinity in soft and hard segments in previous studies [137, 138]. The higher extent of soft domain crystallization on longer soft segment length samples have shown enhanced phase segregation evidenced by AFM pictures on Figure 6.7. The hard and soft segments of PEO2-UU30 are not discernible on the AFM DMT modulus image possibly because of the phase mixing of the hard and soft segments (Figure 6.7a). Phase mixing stems from H-bonding between C-O-C parts of ether domains and N-H of urethane or urea groups. The relatively low sizes of soft and hard segments also enhance phase mixing since these domains do not have the required size to crystallize.

In PEO4.6-UU30, the DMT Modulus image shows a distinct microphase separation between the lighter colored, rod-like hard segment rich parts and the

surrounding softer matrix (Figure 6.7b). The rods have diameters around 17-30 nm. This percolated nano-stranded morphology of hard segments shows us that hard domains with higher sizes can crystallize, although the H-bonding between hard and soft domains still exists. By increasing the soft segment molecular weight of the polymer but keeping the hard segment wt % constant, we also elongate the hard segments of the polymer chains composed of bis(4-cyclohexylmethane)diisocyanate (HMDI) and 2-methyl-1,5-diaminopentane (MDAP or Dytek). This difference in morphology can easily be followed by AFM images.

As given above, the ratios of PEO to diisocyanate and diamine differ with increasing molecular weight of the poly(ethylene oxide) oligomer used. This difference in ratios results in changes of hard and soft segment lengths in polymer chains. In PEO2-UU30, for example, a hard segment of 868 g is present in one mol of repeating unit of the polymer chain. In PEO4.6-UU30, the amount of hard segment raises upto 1966 g per one mole of polymer chain repeating unit. Such an increase in weight, and thus length, results in crystallizable soft domains. And, in PEO8-UU30 3632 g of hard segment is present in one mole of repeating unit of polymer chain which gives the hard domains the possibility to crystallize further.

In PEO8-UU30, hard segments again appear as bright lines in DMT modulus image (Figure 7c). The rod-like morphology of hard segments persists and the diameter of the fibrils also grows (30-35 nm) due to further elongation of hard domains.

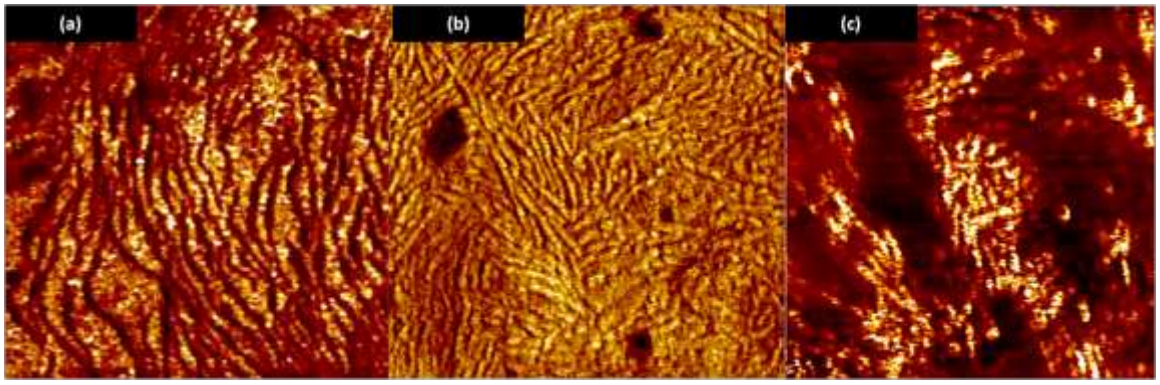

Figure 6.7. AFM DMT modulus images (1μmx1μm) for (a) PEO2-UU30 (b) PEO4.6-UU30 and (c) PEO8-UU30

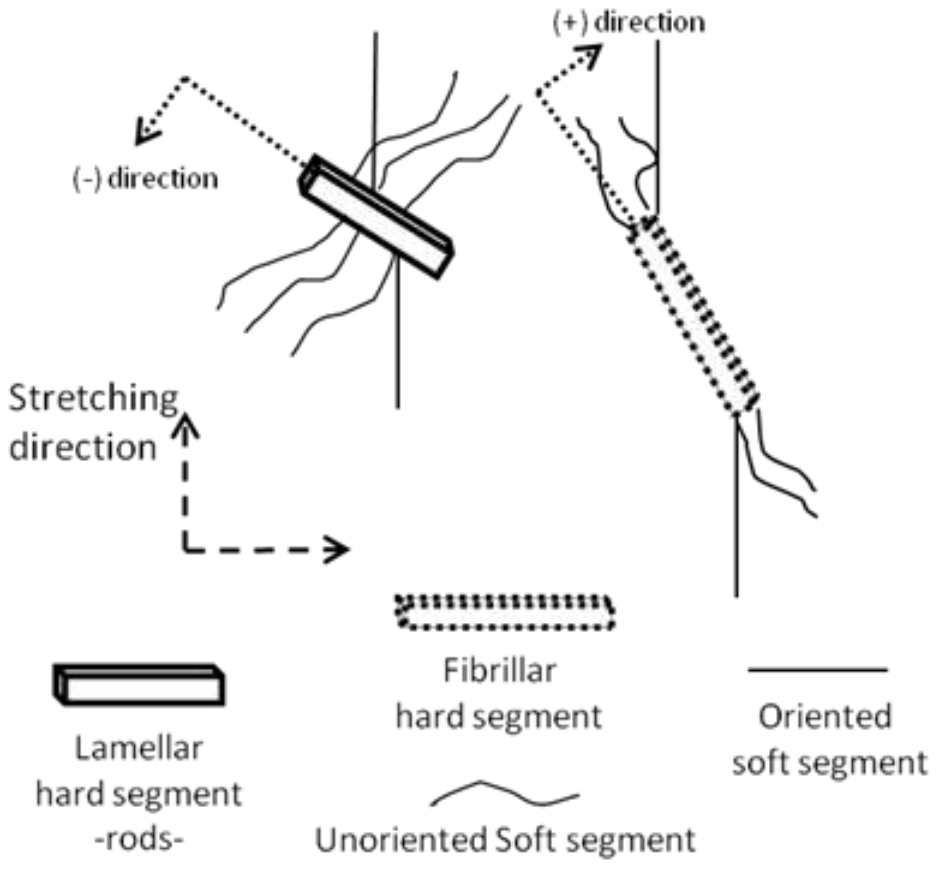

Figure 6.8. Orientation behavior of lamellar and fibrillar hard segment domains in PUUs

Given the initial morphologies of synthesized PUUs with low hard segment concentration, there are two specific hard segment morphologies. One is the lamellar morphology with long axis perpendicular to the chain axes and second is the fibrillar structures parallel to the chain axes. Lamellar domains tend to orient perpendicular to the chain stretching direction indicated as negative, (-) direction whereas, fibrillar domains orient parallel with the extension direction indicated as positive, (+) direction in Figure 6.8.

6.3.3 Spectral Orientation and Mechano-Optical Behavior During Uniaxial Stretching And Relaxation

6.3.3.1 Low Molecular Weight PEO Based PUU (PEO2-UU30)

Dried and die cut samples parallel polarization absorbance changes are shown on Figure 6.9 waterplot as a function of time for the 2650–3600 cm^{-1} region during stretching and holding. Stretching end, holding start point is marked with arrows for each chemical group absorbance. The absorbance decrease with stretching goes through rapid increase with holding and then levels off. The NH stretching vibration in the urethane linkage were used to characterize the orientation of hard segments and the asymmetric CH_2 stretching is used to describe the soft segments with absorptions appearing around 3320 cm^{-1} and 2935cm^{-1}, respectively.

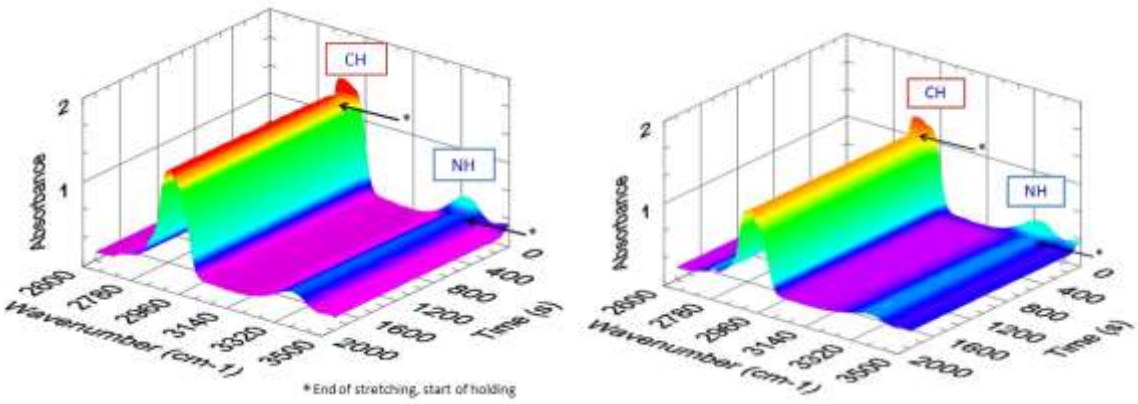

Figure 6.9. Time evolution of parallel (left) and perpendicular (right) spectra for PEO2-UU30 during initial 90 seconds of stretching followed by holding for 30 minutes.

The transition moment angles were taken to be 90° for both vibrations indicated by Zbinden [35] and Fraser [36]and shown in Table 6.1. The orientation functions were calculated for each segment under these assumptions and plotted against time along with stress, Hencky strain and birefringence changes on the overall sample as shown in Figure 6.10. The first 90 seconds was the stretching and the following 30 minutes was holding period separated by dashed line.

Although similar orientation behaviors have been observed for hard and soft segments, their kinetics was different during the experiment. The orientation behavior of each segment is sectioned into three distinct regions separated by vertical dashed lines on Figure 6.11 during stretching.

At low strain levels (I), both hard segment (-NH region) and soft segment (-CH_2 region) orientation is very low, perpendicular to the chain direction (in negative direction) as seen in Figure 6.11 and 6.12. The hard segment orients towards normal to the stretching direction at a slightly higher extent than soft segment at this region where the birefringence starts increasing. Strain hardening

onset at 39 % strain (see Figure 6.11-II) is the starting point for the second region where the soft segment orientation remains unchanged, but hard segment negative orientation continues. At second region of strain hardening marked by Figure 6.11-III (55 % strain), both fibrilar hard and soft segment chains start orienting towards the stretching direction. During stretching, birefringence follows increasing trend with a rate change after strain hardening. This behavior is also plotted against Hencky strain on Figure 6.12 for better understanding of different regimes and transitions. Before strain hardening, the birefringence goes through a transition region at Figure 6.12-II where soft segment orientation ceases and hard segment negative orientation slows down.

The birefringence remains unchanged during relaxation (Figure 6.11-IV). However, the orientation for soft and hard segment fallows the same increasing orientation behavior until the end of fast initial relaxation. Thereafter, hard segments goes through a slight relaxation followed by increasing orientation whereas, soft segment orientation continues to increase at a slower degree. As previously reported in literature, stress induced ordering of partially crystalline region may have happen during this stage [131]. With stress levelling off, both segment orients in negative direction again. This behavior is due to a long range order in the system. The AFM morphologies, discussed previously, was showing co-continuous soft and hard segment structure therefore, the highly comparable stretching and holding behavior was expected.

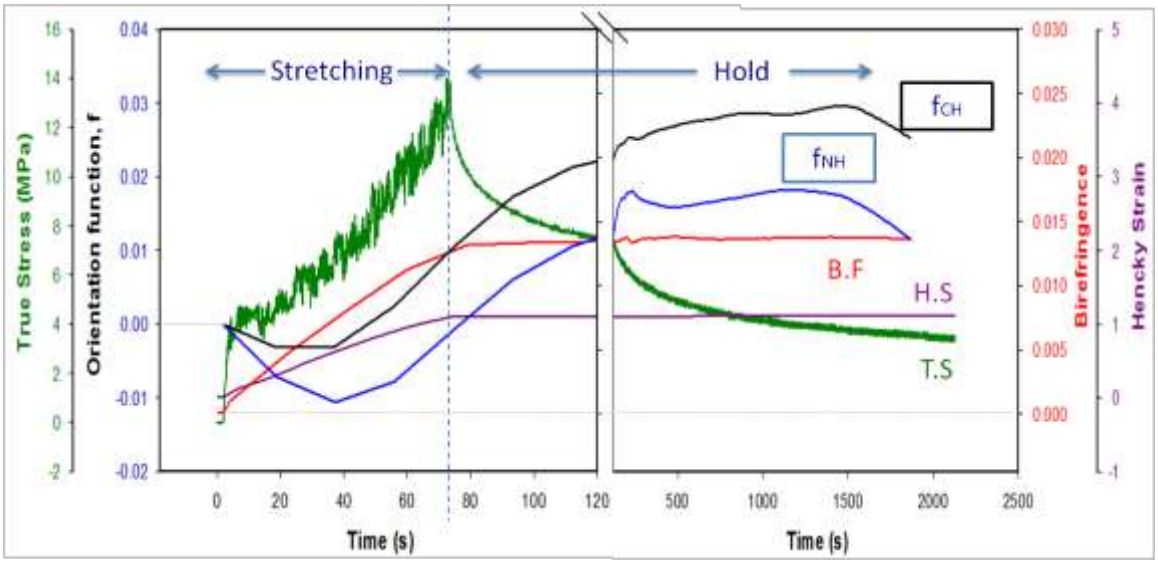

Figure 6.10. True stress (T.S), Hencky strain (H.S), birefringence (B.F), and orientation function (f) for PEO2-UU30 film calculated by IR dichroism versus time (s) stretching and holding stages marked with the vertical dashed line.

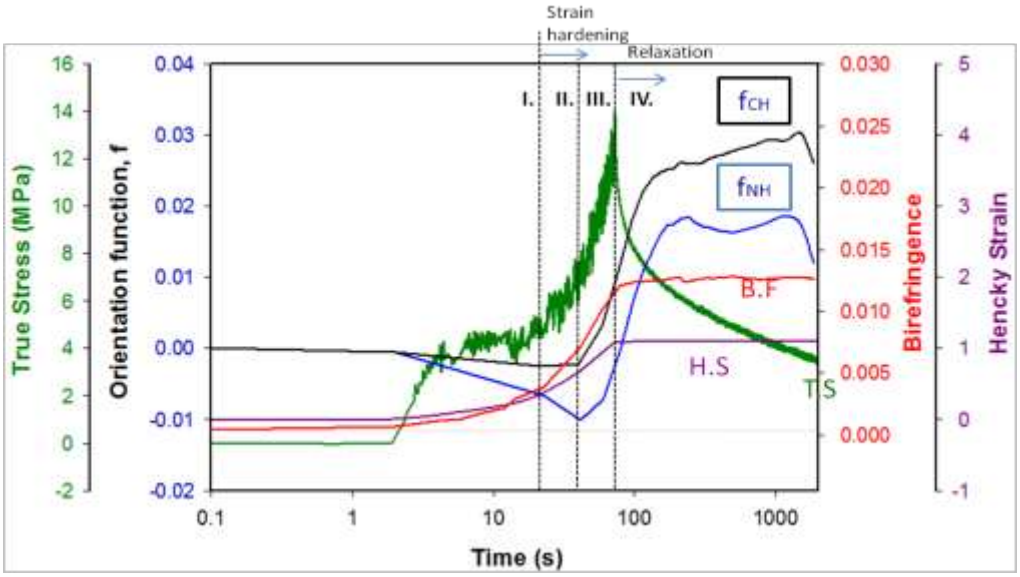

Figure 6.11. True stress (T.S), Hencky strain (H.S), birefringence (B.F), and orientation function (f) for PEO2K-UU30 film calculated by IR dichroism versus time (s).

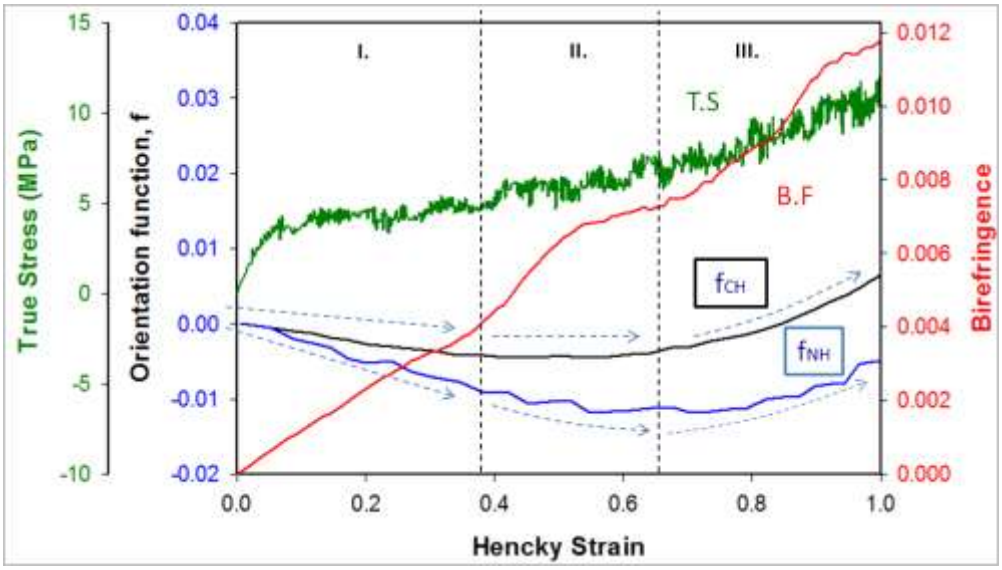

Figure 6.12. Rheo-optical behavior of PEO2-UU30 and strain hardening (marked by vertical dashed line)

6.3.3.2 Mid-Molecular Weight PEO Based PUU (PEO4.6-UU30)

Parallel polarization absorbance changes are shown on Figure 6.13 as a function of time for the 2650–3600 cm^{-1} region during stretching and holding of PEO4.6-UU30. The waterplot characteristics were similar to PEO8-UU30 results described earlier with absorbance decrease during stretching fallowed by a rapid increase and levelling off along the holding period.

Initially with stretching both hard and soft segments orientation increase positively in stretching direction with a faster soft segment response as seen on Figure 6.14. The rheo-optical data is plotted in Figure 6.15 for the stretching stage. At low strain levels, the birefringence remains unchanged, no orientation in hard segments and slight orientation of soft segments towards stretching direction

are observed. With the strain hardening at around 25 % strain, the birefringence increases driven by soft segment orientation as the hard segment orientation remains nearly unchanged until 75 % strain. The second dashed line marks the rapid stress-strain ramp beginning. At this point birefringence transition zone ends, the hard segment orientation starts to increase in stretching direction, soft segment orientation still being higher. In Figure 6.14 during relaxation indicated by hold section, soft segments goes through a continuous orientation decrease and levels off with the stress whereas the hard segment orientation continues to increase and later levels off the same way. After 3 minutes of relaxation the hard and soft segment orientation crosses over while former increases and later decreases.

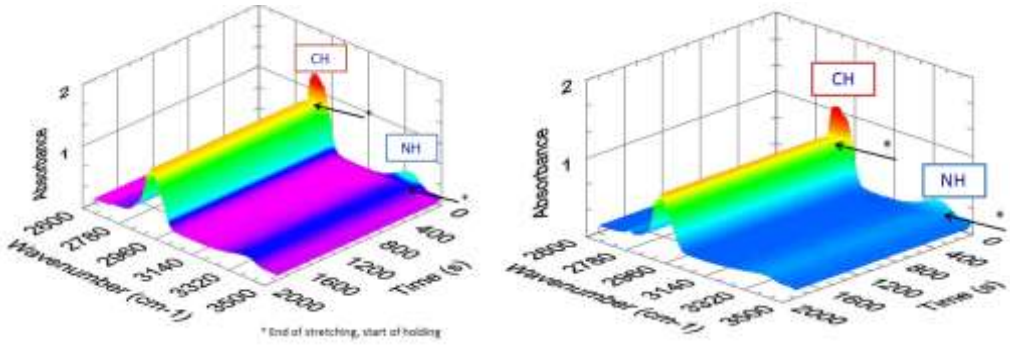

Figure 6.13. Time evolution of parallel (left) and perpendicular (right) spectra for PEO4.6-UU30 during initial 90 sec of stretching followed by holding (next 30min).

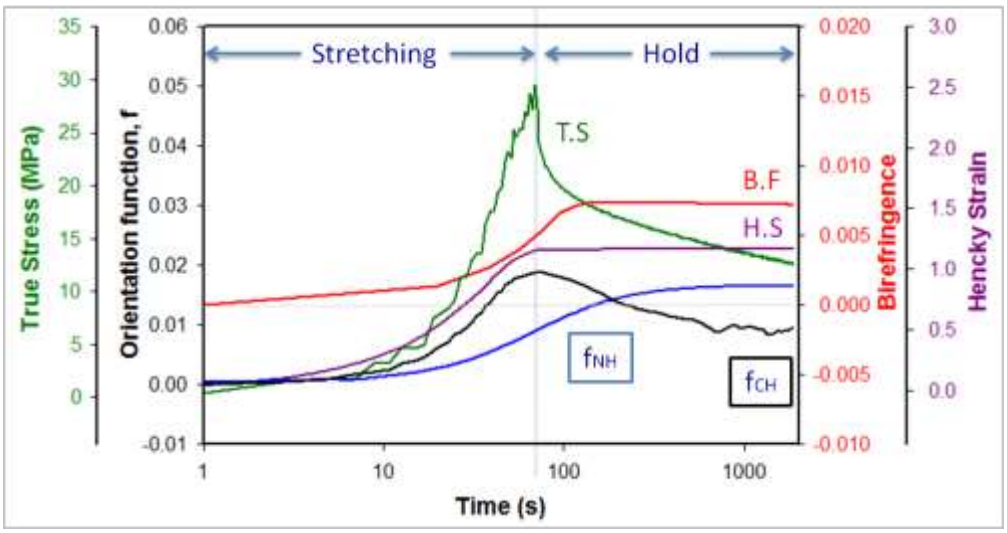

Figure 6.14. True stress (T.S), Hencky strain (H.S), birefringence (B.F), and orientation function (O.F) for PEO4.6-UU30 film calculated by IR dichroism versus time (s) -stretching and holding stages marked with the dashed line-

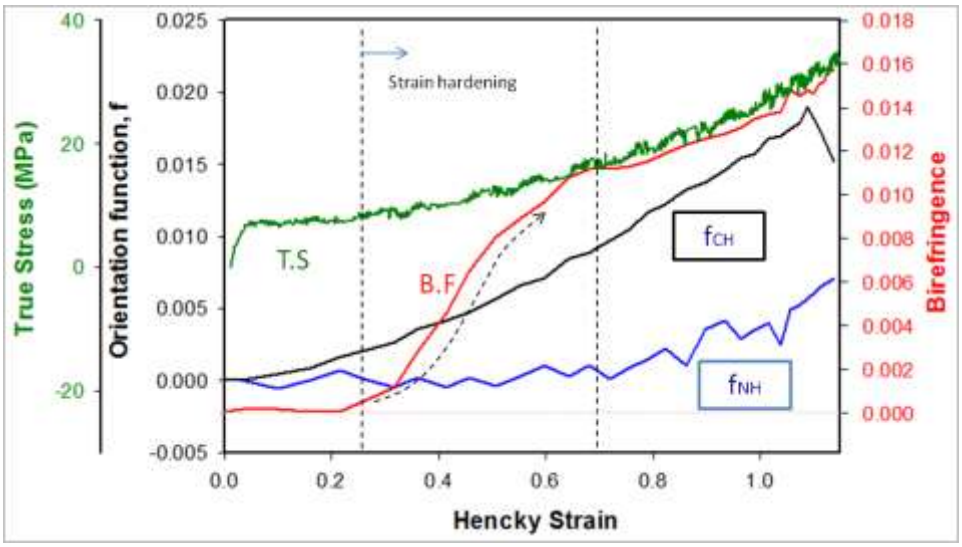

Figure 6.15. Rheo-optical behavior of PEO4.6-UU30 and strain hardening (marked by 1st dashed line) and True stress (T.S), birefringence (B.F) of the mid-molecular weight soft segment PUU overall film and orientation function (f) of the hard (NH absorption bands) and soft (CH_2 absorption bands) segments versus Hencky strain during stretching.

Figure 6.16 shows in-plane birefringence versus true stress profiles for PEO2-UU30 and PEO4.6-UU30 stretched to three times its length and subsequently relaxed by a constrained hold time of 30min. Both medium and low molecular weight PEO based PUU exhibits similar linear stress optical behavior. Further along stretching, the birefringence goes through a rapid increase and a non-linear transition region, followed by another lower increase. PEO4.6-UU30 exhibits higher true stress and birefringence compared PEO2-UU30. Longer soft segment length systems were reported to strain crystallizes [131]. In this case, the soft segments supported by hard segments in co-continuous at PEO2-UU30 responds to strain with higher degree orientation exhibiting less significant transition zone followed by steeper birefringence rise compared to PEO4.6-UU30.

During the holding stage where there is significant stress relaxation, birefringence remains constant for PEO4.6-UU30 and displays increasing behavior for PEO2-UU30. The segment mobility for PEO2-UU30 is higher having close to room temperature soft segment melting point. Going through significant stress relaxation, the increase in birefringence can be explained by rendering pf short soft segments. Whereas, for the PEO4.6-UU30 case no strain induced crystallization observed is an indication of the strong physical network before stretching hard segments physical crosslinking sites among distributed soft segment matrix [115-117]. This explanation is confirmed by higher true stress attained by PEO4.6-UU30 compared to PEO2-UU30.

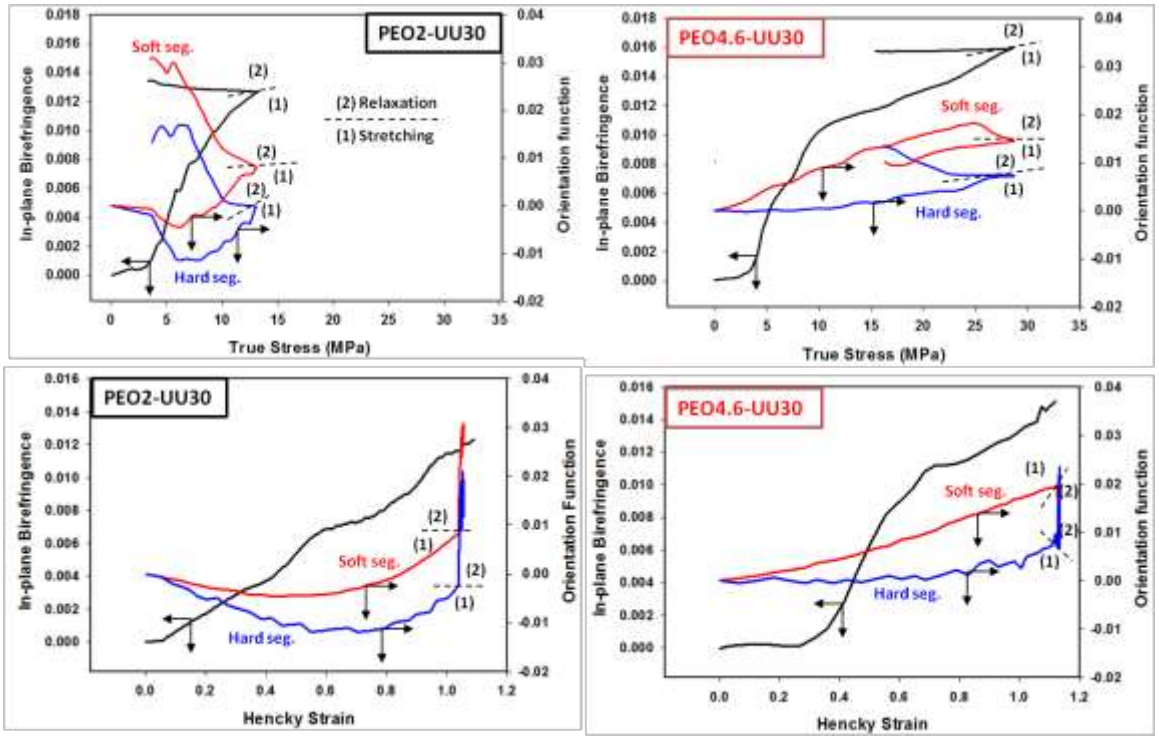

Figure 6.16. Birefringence and orientation function (soft segment in red, hard segment in blue) versus true stress and true strain for PEO2-UU30 and PEO4.6-UU30(transition from stretching to holding stages are indicated by short dash lines).

Stress and strain optical constants for PEO2-UU30 and PEO4.6-UU30 are determined from the initial linear portion of birefringence versus true stress and hencky strain curves given in Figure 16 using stress-optical law and given in Table 6.4.

Table 6.4. Stress and strain optical constants of PUUs.

	Stress optical constant (MPa^{-1})	Strain optical constant
PEO2-UU30	$2.7x10^{-4}$	$9.8x10^{-4}$
PEO4.6-UU30	$6.5x10^{-5}$	$2x10^{-3}$

6.3.3.3 High Molecular Weight PEO Based PUU (PEO8-UU30)

Parallel polarization absorbance changes are shown on Figure 6.17 as a function of time for the 2650–3600 cm^{-1} region during stretching and holding for PEO8-UU30. The waterplot for hard segment NH group and soft segment CH group spectral characteristics in this case does not show any significant changes during stretching or holding compared to previous systems.

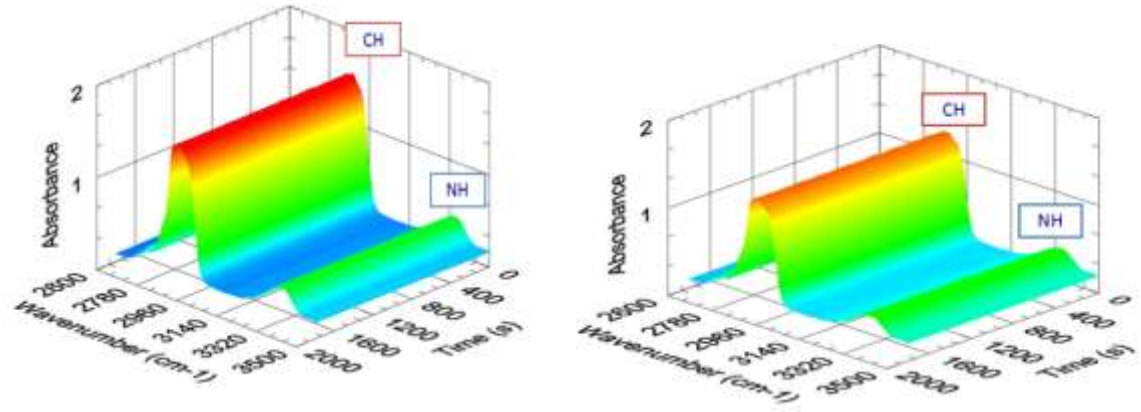

Figure 6.17. Time evolution of parallel (left) and perpendicular (right) spectra for PEO8-UU30 initial 90 sec of stretching followed by holding (next 30min).

No soft segment orientation detected during stretching of PEO8-UU30. The hard segment exhibited an increasing negative orientation fallowed by positive orientation with the relaxation as seen in Figure 6.18. Hard segment orientation increase started with the relaxation stage. This behavior can be explained by the stretching potential energy converting to rearrangement and orientation of hard segments in soft segment pool. These trends were very similar to PEO8-UU30 however; the orientation function values are significantly smaller and towards the end of the holding stage holes detected on stretched films. In this case, small hard

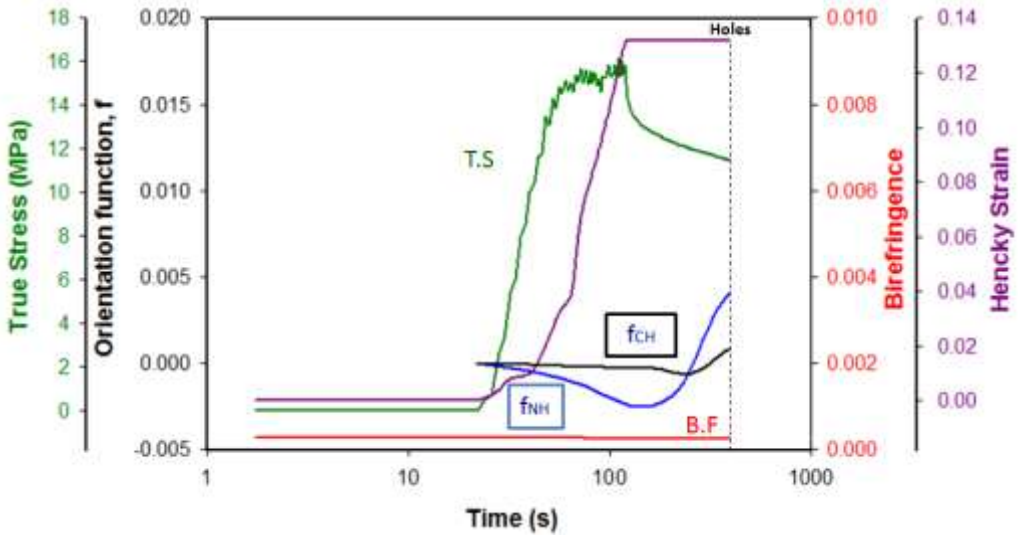

Figure 6.18. True stress (T.S), birefringence (B.F) of PEO8-UU30 film and orientation function (f) of the hard (NH absorption bands) and soft (CH_2 absorption bands) segments versus Hencky strain during stretching.

segment orientation is only observed which had no effect on overall birefringence. The birefringence stayed constant throughout the experiment.

6.3.4. Summary

Figure 6.19 summarizes obtained rheo-optical results of characterized polyurethanes. The stretching and relaxation behaviors are separated into regimes by key points. These marked key points are represented with models to explain the segment orientations in exaggerated manner as the orientation functions are significantly small. The model representations include fibrillar and lamellar hard

segment structures as well as orientated and unoriented soft segment chains. Initially, hard segments are distributed in a pool of soft segments.

At low deformation levels, the PEO4.6-UU30 shows lower strain optical constant compared to the PEO2-UU30. The PEO2-UU30 soft and hard segments, both exhibit negative chain orientation with stretching due to their pre-existing co-continuous morphology. The hard segment orientation is slightly higher than the soft segment one. The transition to positive orientation region is indicated between points B to C where non-linear mechano-optical behavior is observed. After the C onset point, the rapid reverse segment orientation continues till the end of stretching. The soft segments directly respond to stretching with linear increase in positive chain orientation as a function of strain whereas, hard segments orientation function values remains zero before the onset of positive orientation at point E for PEO4.6-UU30. This behavior of hard segments was explained as the compensation of positively orienting small fibrillar hard segments by the negatively orienting lamellar hard segment domains [128]. There is slight positive orientation between E and F in hard segment and continuous in soft segments marks onset of birefringence increase. A final regime between F and G is observed where both segments exhibit positive chain orientation.

During holding, the materials relax and the birefringence increase after D with continuous positive chain orientation for both segments. This behavior is shown to be due to strain-induced crystallization during relaxation in similar materials [131]. After point G, the birefringence remains constant where positive chain orientation of hard segments is compensated by the decrease in orientation of flowing soft segments. The

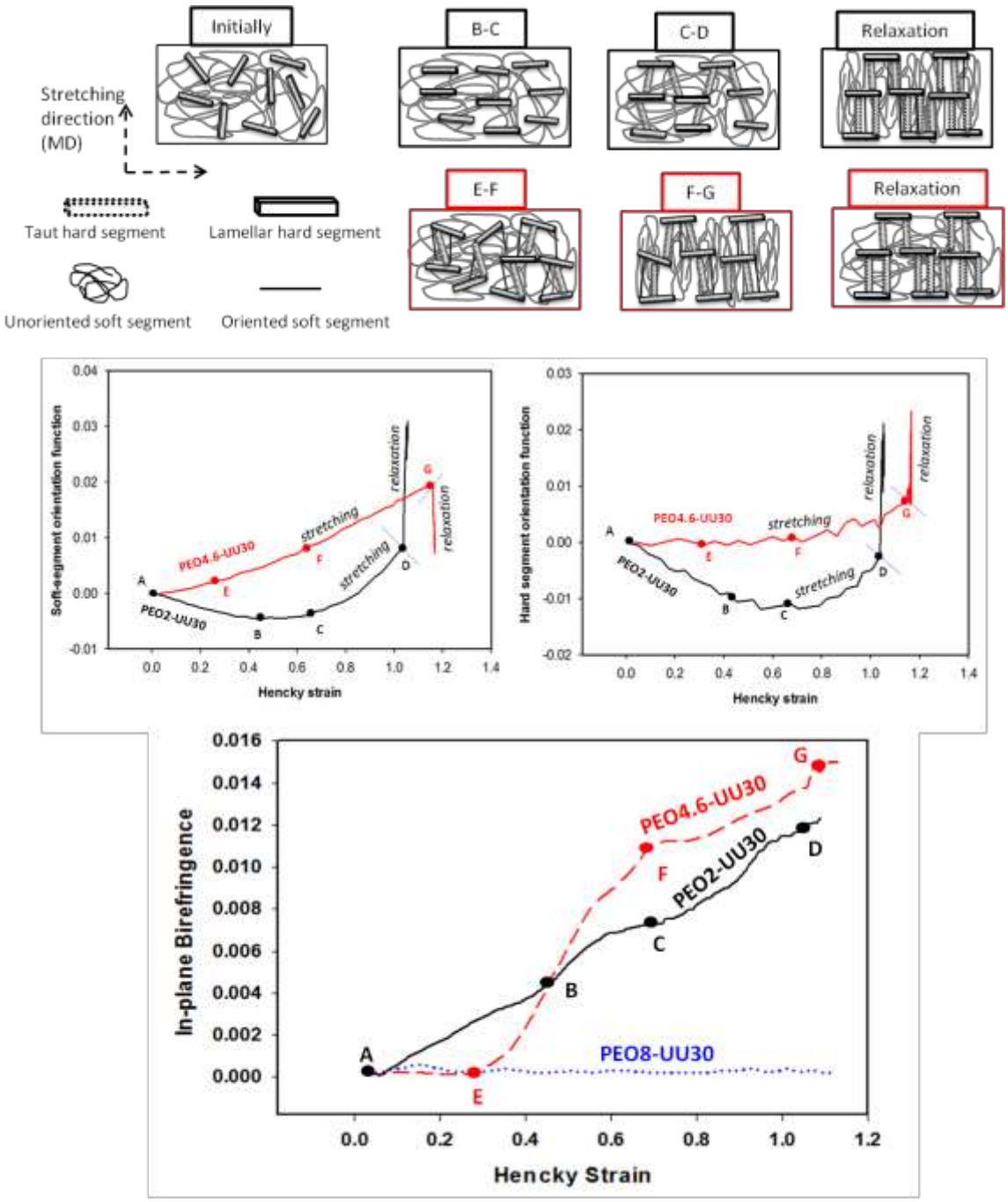

Figure 6.19. Strain induced birefringence during stretching represented by models depicted based on the hard and soft segment orientation functions obtained for all PEO based PUU systems.

reorganization of hard segments, after extensive disruption at elongation, was not enough to drive soft segment reorganization due to phase segregated structure in PEO4.6-UU30.

6.4 Conclusions

The orientation behavior of segment specific chemical groups of NH and CH were investigated for low (PEO2-UU30), mid (PEO4.6-UU30) and high (PEO8-UU30) molecular weight PEO based polyurethane(urea)s. The initial high molecular weight PEO based PUU morphologies have shown well define interfaces phase separated segments whereas, co-continuous morphology is observed on low molecular weight PEO based PUU . This is explained by PEOs hydrogen bonding characteristics preventing, to some extent, phase segregation. The bonding interaction results in increased phase mixing. Longer PEO content material, due to the lack in hydrogen bonding interaction sites which are occluded in crystal region, has more incompatibility between hard and soft segments therefore result in higher degree of microphase separation. The mechano-optical and specific chemical group orientation results were in agreement with this initial structural assessment. The mid molecular weight PEO based system (PEO4.6-UU30) have shown the highest true stress when compared to the other samples as expected from percolated nano-stranded morphology of crystallized hard segments with still existing H-bonding between hard and soft domains. The segment specific chemical group orientation study revealed that the relaxation and reorganization behavior within the system is closely dependent on the initial morphology. The hard and soft segment response to

stretching is similar with a higher hard segment orientation even at lower strain levels when co-continuous structure present. The relaxation stage after stretching results in strain induced reorientation. Whereas, for the phase segregated structure with distinct soft and hard segment phases the low strain level orientation is localized in the soft segment regions until the connection with the hard segments drive orientation in chain axis towards the stretching direction. This network transition is also marked by the mechano-optical behavior change from high-strain optical constant to lower-strain optical constant. In this case, the soft segment reorganization was not driven.

CHAPTER VII

CONCLUSION

For the first time, film-insert injection compression molding process was introduced to encapsulate cholesteric liquid crystal displays with flexible and rigid lens for full protection of displays to replace the currently used time consuming hand lamination technique. For this purpose, a new interchangeable cavity instrumented hot runner mold was designed and constructed. This complex method was carefully optimized considering challenges arising from an insert multilayer display with 90+% liquid crystal content as well as different thermal expansion coefficients between the layers and the lens material as a high potential of delamination and warpage. Concerning the desired physical properties including transparency, low melt viscosity and melting temperature as well as a wide range of hardness grades from soft (flexible) to hard (rigid), three different hardness grades of thermoplastic polyurethanes were found to be the best candidates for this lens application. During proposed lens encapsulation, the pressure changes were evaluated with screw and mold movements using position detection via displacement transducers attached to track the mold closure and screw forward motion. The quality of encapsulation and shrinkage related problems, as well as their elimination, were all discussed. Display substrate material selection criteria for lowered warpage were defined with supporting thermal characterizations. Among the process parameters, tested

also by applying the design of experiments with Taguchi method, mold temperature was found to be the most influential parameter on warpage, followed by pin gate opening time, packing pressure, and cooling time.

Hybrid display insert injection-compression molding process simulations were assessed for encapsulating liquid crystal display substrates with flexible and rigid lenses. While this process replaces the PSA-lens or cover glass lamination technique that fails to fully protect the display parts, still remains complex and requires optimization of multiple process conditions. Flexible display substrate encapsulation flow simulations are completed in Moldex3D R12 software to help pre-visualize the changing process parameters affecting part quality. Solid mesh model including compression and optics boundary layers was generated with Rhino 5 software Moldex3D plug-in tool. This study also discusses frozen layer formation and birefringence development. The experimental and simulation results for temperature and pressure profiles as well as melt front were found to be in good agreement. It can be safely concluded that the multi-component injection compression molding module of Moldex3D is an effective tool to avoid trial-and-error method experiments.

Real-time optical properties during biaxial stretching and heat setting of PET were investigated to elucidate its shrinkage behavior during heating/cooling cycle after production process. Mechanical and thermal effects on birefringence trends were combined with X-ray diffraction and differential scanning calorimetry (DSC) analysis to identify film structure-property relationships. Shrinkage trends were obtained using thermal meachanical analysis (TMA) in machine and transverse directions of the films. The sample with tightly ordered entanglements in specific direction shrunk higher along

that direction to relax when subjected to heating. The relaxation of ordered unstable structure and re-crystallization was possible via heat setting which reduced shrinkage values. The optimum samples with reduced final and maximum shrinkage/expansion values as well as MD to TD variations were obtained by using 3x1 UCW stretched and heat set at 190°C for different time frames. Effective heat setting process was shown to result in crystallinity increase and also faster process results as desired from the industry.

Real-time segment specific rheo-optical properties of three polyurethane(urea)s (PUU) grades with hard segments consisting of bis(4-isocyanatocyclohexyl)methane (HMDI) and 2-methyl-1,5-diaminopentane (MDAP) and soft segments consisting of poly(ethylene oxide) (PEO) oligomers were investigated. All PUUs had 30% by weight hard segment content. Three different molecular weight PEO oligomers were used for synthesis resulting in soft segment length variation among samples. Low molecular weight PEO based PUUs have shown phase mixing whereas, mid and high molecular weight PEO based ones phase segregation of hard and soft segments in AFM studies. Each grade exhibited different rheo-optical behavior consisting of multiple regimes discussed in detail and shown in model. The initial morphology governed the segment specific orientation at low and high strain values. Co-continuous structures resulted in similar hard and soft segment response even at lower strain levels and relaxation stage resulted in strain induced reorientation of soft-segments. Whereas, for the phase segregated structures, soft segment orientation was found at low strain levels. Later, the connection with the hard segments have driven orientation in chain axis towards the stretching direction marked by the rheo-optical behavior change from high-strain optical constant to lower-strain optical constant.

REFERENCES

1. M. Hassan, M.C., *A NEW INSTURMENT TO MONITOR THE TRUE STRESS-TRUE STRAIN-BIREFRINGENCE BEHAVIOR DURING MULTIAXIAL DEFORMATION AND ANNEALING OF PET FILMS*. Antec, 2003. **3**: p. 1583-1587.

2. Unsal, E., et al., *Real-time measurement system for tracking birefringence, weight, thickness, and surface temperature during drying of solution cast coatings and films*. Review of Scientific Instruments, 2012. **83**(2).

3. Unsal, E., et al., *Rapid integrated rheo-optical and polarized Fourier-transform infrared spectrometry measurement system for polymer films undergoing chemo-mechanical changes*. Review of Scientific Instruments, 2013. **84**(7).

4. Tadmor, Z. and C.G. Gogos, *Principles of Polymer Processing*. 2006: Wiley.

5. Pötsch, G.M.W., *Injection molding : an introduction*. 2008, Munich; Cincinnati: Carl Hanser Publishers ; Hanser Gardner Publications.

6. Osswald, T.A., L.S. Turng, and P.J. Gramann, *Injection Molding Handbook*. 2008: Carl Hanser Publishers.

7. Bryce, D.M., *Plastic Injection Molding: Manufacturing Process Fundamentals*. 1996: Society of Manufacturing Engineers.

8. Kamal, M.R.A.J.-F. *Injection molding technology and fundamentals*. 2009.

9. Olmsted, B.A. and M. Davis, *Practical Injection Molding*. 2001: Taylor & Francis.

10. Baek, S., et al., *Effect of processing conditions on warpage of film insert molded parts*. Fibers and Polymers, 2008. **9**(6): p. 747-754.

11. Taketa, J.A., *Mold with removable and replaceable core and cavity inserts*, 1975, Google Patents.

12. Isayev, A.I., *Injection and compression molding fundamentals*, ed. M. Dekker. 1987, New York: Wiley.

13. *Technical Brochure for Demag Plastic Group Injection Compression Molding*. [cited 2012 May 2]; Available from: http://www.sumitomo-shidemag.eu/fileadmin/user_upload/Downloads/Technologien_Download/TP_InjectionCompressionMoulding_gb.pdf

14. Lee, L.J., et al., *Flow Analysis of Sheet Molding Compounds in Compression Molding*. International Polymer Processing, 1991. **6**(1): p. 61-72.

15. Yang, S.Y. and M.Z. Ke, *Experimental study on the effects of adding compression to injection molding process*. Advances in Polymer Technology, 1995. **14**(1): p. 15-24.

16. Avery, J., *Injection molding alternatives : a guide for designers and product engineers*. 1998, Munich; Cincinnati, Ohio: Hanser ; Hanser/Gardner.

17. Klepek, G., *Manufacturing Optical Lens by Injection Compression Molding*. Kunstsoffe, 1987. **77**: p. 13.

18. Yang, S.Y. and Y.C. Chen, *Experimental study of injection-charged compression molding of thermoplastics*. Advances in Polymer Technology, 1998. **17**(4): p. 353-360.

19. Yang, S.Y. and L. Lien, *Experimental Study on the Injection Compression Molding of Parts with Precision Contours*. International Polymer Processing, 1996. **11**(2): p. 188-190.

20. Chen, C.M. and W.B. Young, *The Effects of Compression Pressure on Injection Compression Molding*. International Polymer Processing, 2000. **15**(2): p. 176-179.

21. Shin, J.W., D.C. Rhee, and S.J. Park, *Experimental study of optical disk birefringence*. Annual Technical Conference - Society of Plastics Engineers, 1997. **56**: p. 1753.

22. Young, W.-B., *Effect of process parameters on injection compression molding of pickup lens*. Applied Mathematical Modelling, 2005. **29**(10): p. 955-971.

23. Kwon, T.H., K.Y. Yoon, and S.W. Kim, *2nd Technical Report to KOSEF* 1996.

24. Park, S.J., et al., *Numerical Analysis of Injection/Compression Molding Process for Center-Gated Disc*. Annual Technical Conference - Society of Plastics Engineers, 1998: p. 1756.

25. Chen, S.C., Y.C. Chen, and H.S. Peng, *Simulation of injection–compression-molding process. II. Influence of process characteristics on part shrinkage*. Journal of Applied Polymer Science, 2000. **75**(13): p. 1640-1654.

26. Chen, S.C., et al., *Simulation of injection-compression mold-filling process*. International Communications in Heat and Mass Transfer, 1998. **25**(7): p. 907-917.

27. Chen, S.-C., et al., *Simulations and Applications of Injection-Compression Molding*. Journal of Reinforced Plastics and Composites, 1999. **18**(8): p. 724-734.

28. Chen, S.-C., et al., *Simulation of injection-compression molding process, Part 3: Effect of process conditions on part birefringence*. Advances in Polymer Technology, 2002. **21**(3): p. 177-187.

29. Kim, S.Y., et al., *Effects of film and substrate dimensions on warpage of film insert molded parts*. Polymer Engineering & Science, 2010. **50**(6): p. 1205-1213.

30. Kim, S.Y., et al., *Prediction of residual stress and viscoelastic deformation of film insert molded parts*. Polymer Engineering & Science, 2008. **48**(9): p. 1840-1847.

31. Kim, S.Y., S.H. Lee, and J.R. Youn, *Warpage of Film Insert Molded Parts and Optimum Processing Conditions*. International Polymer Processing, 2010. **25**(2): p. 109-117.

32. Kim, I.H., et al., *Numerical modeling of injection/compression molding for center-gated disk: Part I. Injection molding with viscoelastic compressible fluid model*. Polymer Engineering & Science, 1999. **39**(10): p. 1930-1942.

33. Merquinsa. *Polyurethane Types*. [cited 2012 May 7]; Available from: http://www.merquinsa.com/whats/FPPUtypes1.pdf.

34. Merquinsa. [cited 2012 May 7th]; Available from: http://www.merquinsa.com/

35. Zbinden, R., *Infrared spectroscopy of high polymers*. 1964: Academic Press.

36. Fraser, R.D.B., *Interpretation of Infrared Dichroism in Axially Oriented Polymers*. The Journal of Chemical Physics, 1958. **28**(6): p. 1113-1115.

37. Chalmers, J.M. and N.J. Everall, *Qualitative and Quantitative Analysis of Plastics, Polymers and Rubbers by Vibrational Spectroscopy*, in *Handbook of Vibrational Spectroscopy*. 2006, John Wiley & Sons, Ltd.

38. Buffeteau, T. and M. Pézolet, *Infrared Linear Dichroism of Polymers*, in *Handbook of Vibrational Spectroscopy*. 2006, John Wiley & Sons, Ltd.

39. *Scientific, T.F. FT-IR vs. Dispersive Infrared. Technical Note: 00128 2010* [cited 2012 May 9th]; Available from: http://www.thermo.com/eThermo/CMA/PDFs/Product/productPDF_21615.pdf.

40. Griffiths, P.R., B.L. Hirsche, and C.J. Manning, *Ultra-rapid-scanning Fourier transform infrared spectrometry*. Vibrational Spectroscopy, 1999. **19**(1): p. 165-176.

41. Yang, H., P.R. Griffiths, and C. Manning, *Improved data processing by application of Brault's method to ultra-rapid-scan FT-IR spectrometr*. Appl. Spectrosc., 2002. **56**(10): p. 1281-1288.

42. Pellerin, C., M. Pézolet, and P.R. Griffiths, *Time-Resolved Infrared Spectroscopic Studies of Poly(ethylene terephthalate) Deformation*. Macromolecules, 2006. **39**(19): p. 6546-6551.

43. Estes, G.M., R.W. Seymour, and S.L. Cooper, *Infrared Studies of Segmented Polyurethane Elastomers. II. Infrared Dichroism*. Macromolecules, 1971. **4**(4): p. 452-457.

44. Bistričić, L., et al., *Mechanical properties and linear infrared dichroism of thin films of polyurethane nanocomposites*. Journal of Applied Polymer Science, 2008. **108**(2): p. 791-803.

45. Versteegen, R.M., et al., *Properties and Morphology of Segmented Copoly(ether urea)s with Uniform Hard Segments*. Macromolecules, 2005. **39**(2): p. 772-783.

46. Lin, S.B., et al., *Segmental orientation studies of polyether polyurethane block copolymers with different hard segment lengths and distributions*. Colloid and Polymer Science, 1985. **263**(2): p. 128-140.

47. Graff, D.K., et al., *Static and Dynamic FT-IR Linear Dichroism Studies of Plasticization Effects in a Polyurethane Elastomer*. Macromolecules, 1999. **32**(21): p. 7147-7155.

48. *Polyethylene Terephthalate*. [cited 2014 30 June]; Available from: http://www.icis.com/v2/chemicals/9076423/polyethylene-terephthalate.html.

49. Fakirov, S., *Structure and Properties of Polymers*. 1985, Sofia Press: Sofia. p. 214.

50. de P. Daubeny, R. and C.W. Bunn, *The Crystal Structure of Polyethylene Terephthalate*. Proceedings of the Royal Society of London. Series A. Mathematical and Physical Sciences, 1954. **226**(1167): p. 531-542.

51. Cakmak, M., *Influence of Processing Conditions on Structure and Physical Properties of Biaxially Stretched Engineering Thermoplastics*, in *Film Processing*, T. Kanai, Editor. 1999, Hanser Publishers: Munich. p. 281-313.

52. Fakirov, S., E.W. Fischer, and G.F. Schmidt, *Unit cell dimensions of poly(ethylene terephthalate)*. Die Makromolekulare Chemie, 1975. **176**(8): p. 2459-2465.

53. Jadhav, J.Y.K., S. W., *Polyesters, thermoplastic, Encyclopedia of Polymer Science and Engineering*. Vol. 12. 1988, New York: John Wiley and Sons.

54. Simov, D., et al., *Effect of thermal treatment on the thermomechanical properties of of poly(ethylene terephthalate) fibers*. Vyssokomol Soedin, 1973. **A15**.

55. Holdsworth, P.J. and A. Turner-Jones, *Melting behavior of heat crystallized poly(ethylene terephthalate)*. Polymer, 1971. **12**: p. 195.

56. Illers, K.H., *Heat of fusion and specific volume of poly(ethylene teraphtalate) and poly(butylene teraphtalate)*. Colloid and Polymer Science, 1980. **258**: p. 117.

57. Cobbs, W.H.J. and R.L. Burton, *Crystallization of Polyethylene Terephthalate*. Journal of Polymer Science, 1953. **10**: p. 275.

58. Jeziorny, A., *Parameters characterizing the kinetics of the non-isothermal crystallization of poly(ethylene terephthalate) determined by DSC*. Polymer, 1978. **19**.

59. Yeh, G.S.Y. and P.H. Geil, *Strain-induced crystallization of polyethylene terephthalate*. Journal of Macromolecular Science, Part B, 1967. **1**(2): p. 251-277.

60. Campbell, G.A. and T. Kanai, *Film Processing: Overview and Introductory Rheology*, in *Film Processing*, T. Kanai, Editor. 1999, Hanser Publishers: Munich. p. 1-10.

61. Kazuo, Y., *Saturated Polyester Resin Handbook*. 1989: Nikkan Kogyo Shimbun, Ltd.

62. Spruiell, J.E., D.E. McCord, and R.A. Beuerlein, *The Effect of Strain History in the Crystallization Behavior of Bulk Poly(ethylene terephthalate)*. Trans. Soc. Rheology, 1972. **16**: p. 535.

63. Gorlier, E., J.M. Haudin, and N. Billon, *Strain-induced crystallisation in bulk amorphous PET under uni-axial loading*. Polymer, 2001. **42**(23): p. 9541-9549.

64. Terada, T., et al., *Oriented crystallization of poly(ethylene terephthalate) under uniaxial stretching*. Macromolecules, 1982. **15**(4): p. 998-1004.

65. Hannon, M.J. and J.L. Koenig, *Infrared studies of cryogenic transitions in poly(ethylene terephthalate)*. Journal of Polymer Science Part A-2: Polymer Physics, 1969. **7**(6): p. 1085-1099.

66. M. Yamazaki, K.A., K. Miyagi, T. Asada, and S. S. K. Akatani, *Development of COP retardation film for liquid crystal display by successive biaxial stretching method*. Seikei Kakou, 2007. **19**(8): p. 473-475.

67. King, J.-S., et al., *Effect of backbone on the biaxial retardation of polyimide films in uniaxial stretch*. Materials Chemistry and Physics, 2007. **103**(1): p. 35-40.

68. MacDonald, W.A., et al., *P-17: Plastic Displays - New Developments in Polyester Film for Plastic Electronics*. SID Symposium Digest of Technical Papers, 2003. **34**(1): p. 264-267.

69. Sharma, S.K. and A. Misra, *The effect of stretching conditions on properties of amorphous polyethylene terephthalate film*. Journal of Applied Polymer Science, 1987. **34**(6): p. 2231-2247.

70. Maruhashi, Y. and T. Asada, *Structure and properties of biaxially stretched poly(ethylene terephthalate) sheets*. Polymer Engineering & Science, 1996. **36**(4): p. 483-494.

71. Gupta, V.B., J. Radhakrishnan, and S.K. Sett, *Effect of processing history on shrinkage stress in axially oriented poly(ethylene terephthalate) fibres and films*. Polymer, 1994. **35**(12): p. 2560-2567.

72. Haworth, B., Z.W. Dong, and P. Davidson, *Characterisation of shrinkage in oriented PET films and containers by thermomechanical analysis (TMA)*. Polymer International, 1993. **32**(3): p. 325-335.

73. Karagiannidis, P.G., A.C. Stergiou, and G.P. Karayannidis, *Study of crystallinity and thermomechanical analysis of annealed poly(ethylene terephthalate) films*. European Polymer Journal, 2008. **44**(5): p. 1475-1486.

74. Vallat, M.F., D.J. Plazek, and B. Bhushan, *Effects of thermal treatment of biaxially oriented poly(ethylene terephthalate)*. Journal of Polymer Science Part B: Polymer Physics, 1986. **24**(9): p. 2123-2134.

75. Murthy, N.S., et al., *Measurement of amorphous orientation in poly(ethylene terephthalate) fibers by X-ray diffraction and its significance*. Journal of Applied Polymer Science, 1997. **64**(7): p. 1363-1371.

76. Gohil, R.M., *Morphology-property relationships in oriented PET films: A role of in-plane crystalline orientation distribution on the film properties*. Journal of Applied Polymer Science, 1993. **48**(9): p. 1635-1648.

77. Pakhomov, P.M., et al., *The molecular mechanism of shrinkage of polyethylene terephthalate*. Polymer Science U.S.S.R., 1983. **25**(3): p. 672-679.

78. Shih, W.K., *Shrinkage modeling of polyester shrink film*. Polymer Engineering & Science, 1994. **34**(14): p. 1121-1128.

79. Bhatt, G.M. and J.P. Bell, *Thermal shrinkage of oriented semicrystalline poly(ethylene terephthalate)*. Journal of Polymer Science: Polymer Physics Edition, 1976. **14**(4): p. 575-590.

80. Leong, Y.W., et al., *The effect of molding conditions on mechanical and morphological properties at the interface of film insert injection molded polypropylene-film/polypropylene matrix*. Polymer Engineering & Science, 2004. **44**(12): p. 2327-2334.

81. Tim A. Osswald, L.-S.T., Paul J. Gramann, *Injection Molding Handbook*. 2nd Edition ed. 2008: Carl Hanser Publishers.

82. Rybtz, R.A. and P.V. TYandeff, *Coatings of polymers and plastics*. 2003, New York: Marcel Dekker.

83. Lubrizol. *Estane ALR TPU*. 2009 [cited 2013; Available from: http://www.lubrizol.com/Engineered-Polymers/Products/EstaneALR.html.

84. Jacques, M.S., *An analysis of thermal warpage in injection molded flat parts due to unbalanced cooling*. Polymer Engineering & Science, 1982. **22**(4): p. 241-247.

85. Lee, B.H. and B.H. Kim, *Optimization of Part Wall Thicknesses to Reduce Warpage of Injection-Molded Parts Based on The Modified Complex Method*. Polymer-Plastics Technology and Engineering, 1995. **34**(5): p. 793-811.

86. Huang, M.C. and C. Tai, *The effective factors in the warpage problem of an injection-molded part with a thin shell feature*. Journal of Materials Processing Technology, 2001. **110**(1): p. 1-9.

87. Nugay, I.I. and M. Cakmak, *Instrumented Film-Insert Injection Compression Molding for Lens Encapsulation of Liquid Crystal Displays*. 2014: p. Submitted to Displays Journal.

88. Kwon, T.H., K.Y. Yoon, and S.W. Kim, *1st Technical Report to KOSEF* 1995.

89. Chang, R.-y. and W.-h. Yang, *Numerical simulation of mold filling in injection molding using a three-dimensional finite volume approach*. International Journal for Numerical Methods in Fluids, 2001. **37**(2): p. 125-148.

90. Zheng, R., R.I. Tanner, and X. Fan, *Injection Molding: Integration of Theory and Modeling Methods*. 2011: Springer. 188.

91. R12, M.D. *Online Help*. 2013 [cited 2013; Available from: http://help.plastics-u.com/online-help/.

92. Holman, J.P., *Thermal Contact Resistance*, in *Heat Transfer*, J.P. Holman, Editor. 1997, McGraw-Hill, Inc.: New York. p. 56-59.

93. Kanuga, K. and M. Cakmak, *The effect of blend composition on deformation and stress-optical behavior of PEN/PEI blends using online mechano-optical technique*. M..Annual Technical Conference - Society of Plastics Engineers, 2004. **2**(62): p. 2168-2172.

94. Shibaya, M., et al. *Relationship between Structure and Properties of PBT Injection Moldings in the Thickness Direction*. in *ANTEC*. 2003. Nashville.

95. Viana, J.C., *Development of the skin layer in injection moulding: phenomenological model*. Polymer, 2004. **45**(3): p. 993-1005.

96. Pivsa-Art, S., et al., *Effect of Specimen Thickness In PC/ABS Spiral Flow Injection Molding*, in *ANTEC*2006, Society of Plastics Engineers: Charlotte. p. 1123-1127.

97. Pontes, A.J., M.J. Oliveira, and A.Z. Pouzad. *Studies on the Influence of the Holding Pressure on the Orientation and Shrinkage of Injection Molded Parts*. in *ANTEC*. 2002. San Francisco.

98. Hsiung, C.M. and M. Cakmak, *Detailed Investigations of Structural Layering Phenomena in Injection Molded Thermotropic Liquid Crystalline Polymers*. International Polymer Processing, 1993. **8**(3): p. 255-270.

99. Berins, M., *Plastics Engineering Handbook Of The Society Of The Plastics Industry*, ed. S.o.t.P. Industry. 1991: Springer. 869.

100. Mace, J.M. and J. Moerenhout, *Multilayer polymer system comprising at least one engineering thermoplast layer and at least one soft touch composition layer, and compositions to be used therefore*, 1998, Google Patents.

101. Samios, C.K., K.G. Gravalos, and N.K. Kalfoglou, *In situ compatibilization of polyurethane with poly(ethylene terephthalate)*. European Polymer Journal, 2000. **36**(5): p. 937-947.

102. Isayev, A.I. and C.A. Hieber, *Toward a viscoelastic modelling of the injection molding of polymers*. Rheologica Acta, 1980. **19**(2): p. 168-182.

103. Shyu, G.D., *Birefringence and Residual Stresses in Molded Articles of Amorphous Polymers*. 1993: University of Akron, Department of Polymer Engineering.

104. Chandran, P. and S. Jabarin, *Biaxial orientation of poly (ethylene terephthalate). Part II: The strain–hardening parameter*. Advances in Polymer Technology, 1993. **12**(2): p. 133-151.

105. Chandran, P. and S. Jabarin, *Biaxial orientation of poly(ethylene terephthalate). Part I: Nature of the stress—strain curves*. Advances in Polymer Technology, 1993. **12**(2): p. 119-132.

106. Faisant de Champchesnel, J.B., et al., *Amorphous phase orientation in biaxially drawn poly(ethylene terephthalate) films*. Polymer, 1997. **38**(16): p. 4165-4173.

107. Vigny, M., J.F. Tassin, and G. Lorentz, *Study of the molecular structure of PET films obtained by an inverse stretching process Part 2: crystalline reorganization during longitudinal drawing*. Polymer, 1999. **40**(2): p. 397-406.

108. Cakmak, M., et al., *Small angle and wide angle x-ray pole figure studies on simultaneous biaxially stretched poly(ethylene terephthalate) (PET) films*. Polymer Engineering & Science, 1987. **27**(12): p. 893-905.

109. M. Cakmak, T.F.S., And G. Kokturk A.M. Cunha And S. Fakirov *Structure Development During Polymer Processing*. 2000, The Netherlands: Springer.

110. Venkatesvaran, H. and M. Cakmak, *Kinetics of structural evolution during crystallization of preoriented PET as followed by dual wavelength photometric birefringence technique*. Polymer Engineering & Science, 2001. **41**(2): p. 341-357.

111. Guan, J.Y., L.-H. Wang, and R.S. Porter, *Planar deformation of amorphous poly(ethylene terephthalate) by stretching and forging*. Journal of Polymer Science Part B: Polymer Physics, 1992. **30**(7): p. 687-691.

112. Hassan, M., *Novel True Stress-True Strain-Birefringence Measurement Systems for Real Time Measurement During Multiaxial Deformation and Heat Setting of Polymer Films: "Application on PET Films"*, 2004, University of Akron.

113. Allegrezza Jr, A.E., et al., *Segmental orientation studies of block copolymers: 2. Non-hydrogen bonded polyurethanes*. Polymer, 1974. **15**(7): p. 433-440.

114. Blundell, D.J., et al., *Real time SAXS/stress–strain studies of thermoplastic polyurethanes at large strains*. Polymer, 2002. **43**(19): p. 5197-5207.

115. Bonart, R., *X-ray investigations concerning the physical structure of cross-linking in segmented urethane elastomers*. Journal of Macromolecular Science, Part B, 1968. **2**(1): p. 115-138.

116. Bonart, R., L. Morbitzer, and G. Hentze, *X-ray investigations concerning the physical structure of cross-linking in urethane elastomers. II. Butanediol as chain extender*. Journal of Macromolecular Science, Part B, 1969. **3**(2): p. 337-356.

117. Cooper, S.L. and A.V. Tobolsky, *Properties of linear elastomeric polyurethanes*. Journal of Applied Polymer Science, 1966. **10**(12): p. 1837-1844.

118. Curgul, S., et al., *Effect of Chemical Composition on Large Deformation Mechanooptical Properties of High Strength Thermoplastic Poly(urethane urea)s*. Macromolecules, 2004. **37**(23): p. 8676-8685.

119. Desper, C.R., et al., *Deformation of microphase structures in segmented polyurethanes*. Macromolecules, 1985. **18**(12): p. 2755-2761.

120. Estes, G.M., et al., *Mechanical and optical properties of block polymers I. Polyester-urethanes*. Polymer Engineering & Science, 1969. **9**(6): p. 383-387.

121. Kornfield, J.A., et al., *Deuteron NMR measurements of order and mobility in the hard segments of a model polyurethane*. Macromolecules, 1991. **24**(17): p. 4787-4795.

122. Oertel, H., *Textil*. Praxis, 1964. **19**: p. 820.

123. Reynolds, N., et al., *Structure and deformation behaviour of model poly(ether-urethane) elastomers, 1. Infrared studies*. Macromolecular Chemistry and Physics, 1994. **195**(8): p. 2855-2873.

124. Rinke, H., *Elastomeric Fibers Based on Polyurethanes*. Angewandte Chemie International Edition in English, 1962. **1**(8): p. 419-424.

125. Sauer, B.B., et al., *Morphology and orientation during the deformation of segmented elastomers studied with small-angle X-ray scattering and atomic force microscopy*. Journal of Polymer Science Part B: Polymer Physics, 2002. **40**(16): p. 1727-1740.

126. Seymour, R.W., A.E. Allegrezza, and S.L. Cooper, *Segmental Orientation Studies of Block Polymers. I. Hydrogen-Bonded Polyurethanes*. Macromolecules, 1973. **6**(6): p. 896-902.

127. Siesler, H.W., *Rheo-Optical Fourier-Transform Infrared Spectroscopy of Polymers 14. Segmental Orientation and Strain-Induced Crystallization of a Poly(Ether Urethaneurea) Elastomer*. Berichte der Bunsengesellschaft für physikalische Chemie, 1988. **92**(5): p. 641-645.

128. Siesler, H.W., *Rheo-optical fourier transform IR spectroscopy of polyurethane elastomers*. Polymer Bulletin, 1983. **9**(8-9): p. 382-389.

129. Siesler, H.W., *Rheo-optical fourier transform IR (FTIR) spectroscopy of polyurethane elastomers*. Polymer Bulletin, 1983. **9**(10-11): p. 417-478.

130. Siesler, H.W., *The characterization of polymer deformation by rheo-optical fourier-transform infrared spectroscopy*. Makromolekulare Chemie. Macromolecular Symposia, 1992. **53**(1): p. 89-103.

131. Unsal, E., et al., *Real time mechano-optical study on deformation behavior of PTMO/CHDI-based polyetherurethanes under uniaxial extension*. Polymer, 2009. **50**(19): p. 4644-4655.

132. Versteegen, R.M., R.P. Sijbesma, and E.W. Meijer, *Synthesis and Characterization of Segmented Copoly(ether urea)s with Uniform Hard Segments*. Macromolecules, 2005. **38**(8): p. 3176-3184.

133. Yeh, F., et al., *In-Situ Studies of Structure Development during Deformation of a Segmented Poly(urethane−urea) Elastomer.* Macromolecules, 2003. **36**(6): p. 1940-1954.

134. Seymour, R.W., et al., *Rheo-optical studies of polyurethane block polymers*. Journal of Polymer Science Part A-2: Polymer Physics, 1972. **10**(8): p. 1521-1527.

135. Siesler, H.W., *Rheo-optical fourier transform IR (FTIR) spectroscopy of polyurethane elastomers*. Polymer Bulletin, 1983. **9**(12): p. 557-562.

136. Siesler, H.W., *Rheo-optical Fourier-Transform infrared spectroscopy: Vibrational spectra and mechanical properties of polymers*, in *Analysis/Networks/Peptides*. 1984, Springer Berlin Heidelberg. p. 1-77.

137. Korley, L.T.J., et al., *Effect of the degree of soft and hard segment ordering on the morphology and mechanical behavior of semicrystalline segmented polyurethanes*. Polymer, 2006. **47**(9): p. 3073-3082.

138. Waletzko, R.S., et al., *Role of Increased Crystallinity in Deformation-Induced Structure of Segmented Thermoplastic Polyurethane Elastomers with PEO and PEO−PPO−PEO Soft Segments and HDI Hard Segments.* Macromolecules, 2009. **42**(6): p. 2041-2053.